Creep and Shrinkage Behavior of Concrete in Segmental Bridge Applications

by

Grant Malachi Cooper

A thesis submitted to the Graduate Faculty of
Auburn University
in partial fulfillment of the
requirements for the Degree of
Master of Science

Auburn, Alabama
December 12, 2020

compressive strength, elastic modulus, compliance,
predictions, field work, laboratory testing

Approved by

Anton K. Schindler, Chair, Professor and Director of Highway Research Center
Robert W. Barnes, Associate Professor of Civil Engineering
James S. Davidson, Professor of Civil Engineering

ABSTRACT

The objective of this study is to accurately predict creep and shrinkage behavior of concrete in the I-59/I-20 segmental bridge located in downtown Birmingham, Alabama. In order to quantify creep and shrinkage, four different sample dates distributed throughout the segment casting schedule were selected to collect concrete specimens for testing. Concrete specimens were loaded at 7 days, 28 days, 91 days, and 182 days for creep testing. Shrinkage testing began for concrete specimens as soon as specimens were exposed to drying after initial curing. All concrete specimens were cured using increased temperatures for the first 24 hours after casting. Creep and shrinkage measurements were collected at set time intervals for the duration of the project from April 10, 2018 to September 30, 2020. In order to accurately predict creep and shrinkage, six commonly used models were evaluated in this project: ACI 209, AASHTO LRFD 2017, GL 2000, B3, CEB MC 1990, and CEB MC 2010. Measured and predicted values were compared using statistical analyses to determine which model most accurately predicted the test data.

It was determined that the April 10, 2018 specimens exhibited the largest amount creep and shrinkage; however the percentage of total segments cast with similar concretes is very small. Likewise it was shown that concrete used for casting the April 16, 2019 specimens produced the smallest amount of creep and shrinkage, where a much larger percentage of total segments were cast with similar concretes. A similar trend was found for each sample date across all loading ages for creep; however, creep significantly decreased as the loading age increased. Statistical analyses determined that the GL 2000 Model most accurately predicted creep and shrinkage combined for all specimens tested during the project. Several empirical parameters were adjusted in the calibration of the GL 2000 Model to improve the creep and shrinkage prediction accuracy of the concrete cast in segments of the Birmingham I-59/I-20 segmental bridge. After calibration, the Modified GL 2000 significantly improved the creep and shrinkage predictions. In addition the CEB MC 1990 Model was calibrated, which allows for improved estimates of creep and shrinkage in some commonly used bridge analysis software.

ACKNOWLEDGMENTS

I will start by most importantly giving praise to my Lord and Savior, Jesus Christ. Graduate school is something I would have never considered if it were not for the blessings The Lord instills in me every day. Secondly to my Mom, I say thank you for always believing in me and always being there for me in this academic journey. From the day I started at Auburn as an undergraduate student, you always hold an open ear to all of my troubles and always provide concise and calming advice. I express my gratitude to my extended family for always pushing me to keep up the good work and to always strive for excellence.

This thesis would not be possible without the continued guidance and support from my graduate school advisor, Dr. Anton Schindler. I greatly appreciate the answers to so many "quick" questions in countless emails and weekly meetings which expanded my understanding of so many structural engineering topics ten-fold. I express my appreciation to Dr. Barnes for throwing one-off questions my way to not only challenge but also teach me. In addition, I say thank you to Dr. Davidson for the countless hours of classroom instruction in addition to serving on my thesis committee.

I give a special thank you to the laboratory technician at Auburn University, Rob Crosby. Rob not only sacrificed countless hours to collect samples, record strain measurements, and load frames, but also became one of my closest friends in Auburn. I also say thank you to Christian, Wu, and Matt for always being willing to assist with anything that I may have asked. In addition, I say thank you to Daniel Richey for providing me with a jumpstart into this project.

This research project would not have been possible without several key contributors. First, I thank the Highway Research Center for its financial contributions to this project and providing me with this opportunity. Secondly, I say thank you to ALDOT, Volkert Engineering, Corven Engineering, and Johnson Brothers Construction for the support provided throughout this project; specifically from ALDOT Mr. DeJarvis Leonard and Mr. Tim Colquitt, from Volkert Engineering Mr. Adam Patterson and Mr. Lloyd Pitts, and from Corven Engineering Mr. Eric Johnson. Lastly, I say thank you to Adam Dye for his support with all field visits to collect specimens.

TABLE OF CONTENTS

CHAPTER 3: METHODOLOGY

LIST OF TABLES

LIST OF FIGURES

CHAPTER 1: INTRODUCTION

1.1 PROJECT BACKGROUND

With segmental bridge construction being at the forefront of modern day bridge design, uncertainties arise about certain concrete behavioral aspects, including volumetric changes. These volumetric changes have been studied by many researchers to better understand how different concrete properties and characteristics correlate with them. The research project described in this thesis is being conducted to assist with the previous knowledge of creep and shrinkage of concrete in segmental bridge applications, specifically for the State of Alabama. The I-59/I-20 interchange in Birmingham, Alabama is undergoing replacement to better suit traffic needs for the city. The replacement includes a segmental bridge–shown in Figure 1-1–containing 2316 typical precast segments that cover over one million square feet of deck area. The bridge consists of 172 spans with the longest span reaching 165 feet.

Figure 1-1: Birmingham I-59/I-20 Interchange amid segmental bridge construction

1.2 RESEARCH OBJECTIVES

This study focused on accurately predicting the creep and shrinkage of concrete used in segments of the I-59/I-20 segmental bridge in Birmingham, Alabama. These are the primary objectives of this research study:

- Quantify the creep and shrinkage behavior of concrete sampled from the Birmingham I-59/I-20 precast segmental bridge project.
- Predict the creep and shrinkage of concretes with the same properties and characteristics of concretes sampled and tested during this project using the models listed below:
    - ACI 209 (2008),
    - AASHTO LRFD (2017),
    - GL 2000 (Gardner and Lockman 2001),
    - B3 (Bazant and Baweja 2000),
    - CEB MC 1990 (CEB 1990), and
    - CEB MC 2010 (fib 2012).
- Calibrate the most accurate model for predicting creep and shrinkage to best represent the long-term volumetric changes that may occur in the Birmingham I-59/I-20 segmental bridge.

As a secondary objective to this study, the CEB MC 1990 Model was calibrated to most accurately predict creep and shrinkage in concrete specimens collected throughout the project duration for recommendations that may be implemented into commonly used bridge design software (i.e. Bridge Designer 2.)

1.3 RESEARCH SCOPE

This study was conducted to analyze the creep and shrinkage behavior of four different concrete mixture proportions collected from the Birmingham I-59/I-20 segmental bridge project between February 21, 2018 and August 9, 2019. The four sample collection dates were April 10, 2018, July 9, 2018, November 19, 2018 and April 16, 2019. For creep testing, loading ages of 7 days, 28 days, 91 days, and 182 days were evaluated for each of the aforementioned sampling dates. All specimens were collected on the jobsite and subjected to an elevated curing regime at the casting yard prior to returning to the laboratory at Auburn University to ensure collected concrete

specimens were the best representation of the concrete used in segments of the Birmingham I-59/I-20 bridge project.

All creep specimens were loaded at 40 percent of their ultimate compressive strength determined immediately prior to load application. Displacement measurements were taken at set time intervals to calculate creep strains. Shrinkage testing occurred by recording displacement measurements of unloaded concrete specimens subjected to drying at similar time intervals to creep testing. Lastly, all testing data were compared with predictions of creep and shrinkage from the models mentioned in Section 1.2. A statistical analysis was performed to evaluate model accuracy and determine which model would best be calibrated to predict the creep and shrinkage for the concrete mixtures in segments of the Birmingham I-59/I-20 segmental bridge.

1.4 THESIS ORGANIZATION

Many aspects of the behavior and construction of concrete segmental bridges are presented in Chapter 2. The chapter includes an overview of volumetric changes in concrete followed by the effects of volumetric changes in segmental bridge applications. A description of each creep and shrinkage prediction method is provided as well as an overview of previous studies related to creep and shrinkage of concrete in segmental bridge applications.

The experimental plan and procedures are covered in Chapter 3. The segmental bridge casting process and construction practices used in the Birmingham I-59/I-20 segmental bridge project are detailed in Chapter 4. The results from all testing are presented in Chapter 5. Results from creep and shrinkage testing are outlined, as well as fresh and hardened properties of the concrete specimens collected throughout this project.

All results from modeling creep and shrinkage are presented in Chapter 6. Comparison of these models as well as model calibration are covered in Chapter 7. Conclusions as well as recommendations for continued research are discussed in Chapter 8. All testing data and a full breakdown of the prediction models results are presented in Appendices A and B, respectively. The casting and erection dates for all segments used in the I-59/I-20 segmental bridge in Birmingham, Alabama are tabulated in Appendix C.

CHAPTER 2: LITERATURE REVIEW

2.1 INTRODUCTION

The first precast segmental bridge in the United States was completed in 1973 near Corpus Christi, Texas (Roberts et al. 1993). Segmental bridges offer many advantages to traditional concrete or steel girder construction, with one of the greatest benefits being increased span lengths. According to Roberts et al. (1993), in addition to being more economical, versatile, and aesthetically pleasing, segmental bridges offer the following benefits:

- The ability to meet strict horizontal or vertical curvature requirements—Linn Cove Viaduct shown in Figure 2-1 courtesy of Goins (2013),
- Erection methods that offer minimal disturbance to the underlying ground where environmentally sensitive areas or urban environments may exist,
- External post-tensioning which allows for
    - Thinner webs (reducing dead loads),
    - Easier installation and inspection of longitudinal tendons, and
    - Easier replacement of damaged tendons.

Figure 2-1: Curvature of the Linn Cove Viaduct (Goins 2013)

Modern precast segmental bridges are often viewed as an integration of multiple techniques and technologies that developed over time with the first technique being used in the early seventh century (Roberts et al. 1993). Important developments, described by Roberts et al. (1993), to reach the current form of precast segmental bridges are outlined as follows:

- Segmental construction that was first introduced in China for arch bridges around the seventh century, and history describes the next use of segmental construction method much later in Europe around the twelfth century,
- Box-shaped cross sections, which were first utilized in France for concrete arch bridges in 1899,
- Prestressed bridges, which were first implemented in France in 1912, and
- Post-tensioned segmental box girder bridges that were first built in Germany in 1950.

As with most post-tensioned concrete applications, it is important to understand the fundamentals of creep and shrinkage during segmental bridge design and construction. The purpose of this chapter is to not only describe and model the volumetric changes that occur in concrete, but also indicate how these changes may affect precast segmental bridges. A description of volumetric changes in segmental bridge design and construction is presented in Section 2.2. The groundwork for volumetric changes in concrete is presented in Section 2.3. The methods used by different models to predict volumetric changes are presented in Section 2.4. Lastly, an in-depth review of previous studies conducted on creep and shrinkage of CSC (Conventional Slump Concrete) in segmental bridge applications is presented in Section 2.5.

2.2 VOLUMETRIC CHANGES IN SEGMENTAL BRIDGE DESIGN AND CONSTRUCTION

It was important to understand not only how volumetric changes influence precast bridge applications, but also more importantly how these changes affect the post-tensioning for segmental bridges. According to Roberts et al. (1993), the first notable example of a prestressed bridge application was the three-arch Le Veudre Bridge over the Allier River in France, built by Eugene Freyssinet. Jacks were installed in the crest of the arch, and after considerable creep and shrinkage had occurred the jacks were used to push the two halves back to their original position (Roberts et al. 1993). This section focuses on historical and modern methods for design and construction of segmental bridges with an emphasis on accounting for volumetric changes of concrete.

2.2.1 Segmental Bridge Construction

Segmental concrete box-girder bridges are divided into two different types of segments: cast-in-place concrete segments or precast concrete segments. With precast segments, the segments are transported to the bridge location from a casting yard. For both segment types, match casting has been implemented in modern box-girder bridges where each segment is cast adjacent to the previous segment with shear keys for effective load transfer between segments (Gallaway 1975).

Precast segments can be erected by several different ways including: the balanced cantilever method, the span-by-span method, or the progressive placement method; however, all methods use a similar form of post-tensioning in which as each new segment is erected, a bar or cable is stretched between existing segments to secure the new unit until the either both spans or a single span is completed depending on the method (Gallaway 1975). For precast segmental bridge construction using the balanced cantilever method, segments are erected in cantilever extending two directions from a fixed pier location by successively adding one segment to each side at a time and post-tensioning each additional unit to the existing cantilever arms to form one continuous structure, as illustrated in Figure 2-2 (Gallaway 1975).

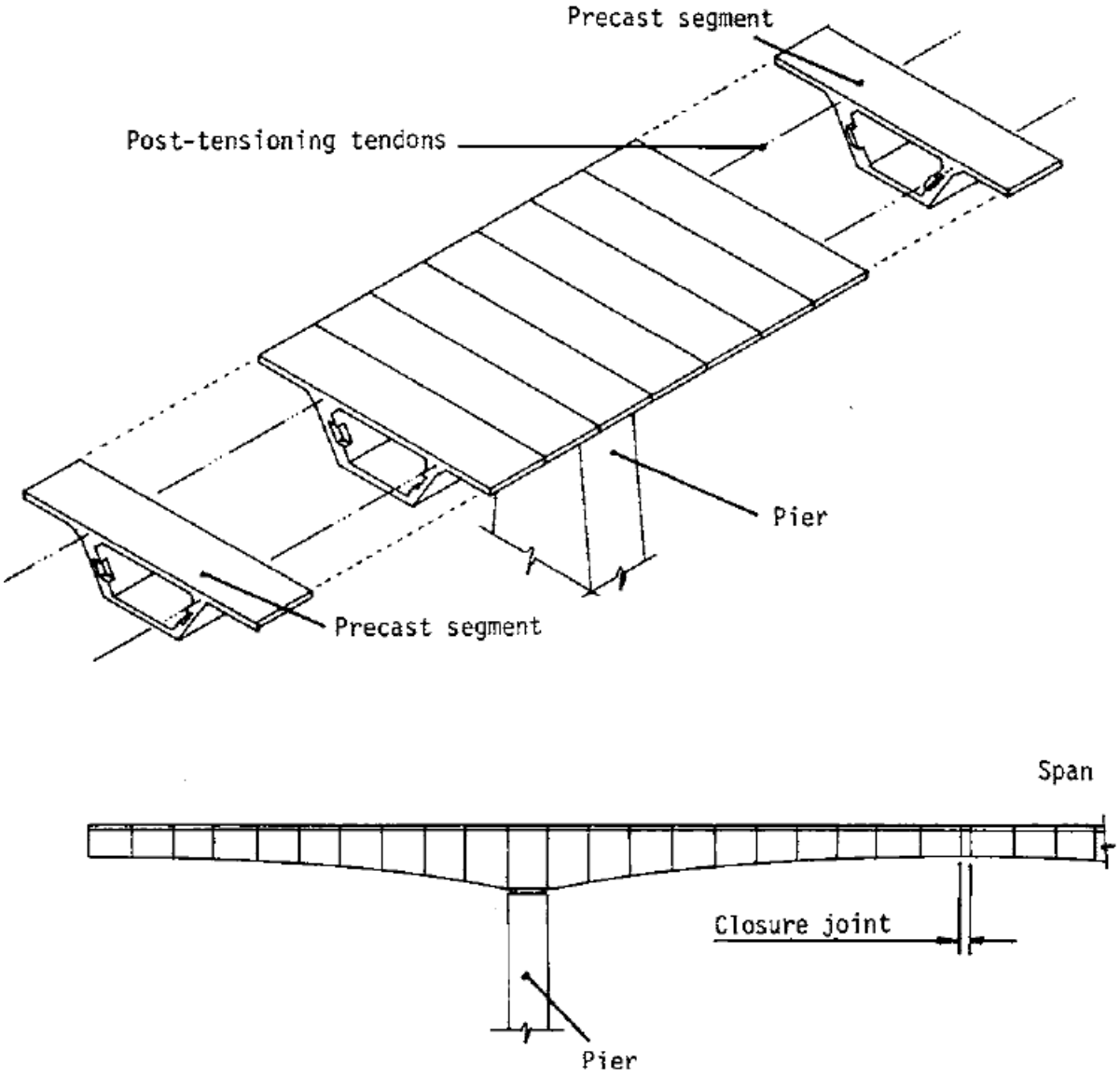

Figure 2-2: Erection of precast segments by use of balanced cantilever method (Gallaway 1975)

The balanced cantilever method is also used for cast-in-place segments; however, a system of false-work and soffits is erected under the bridge adjacent to the pier with which the formwork rests on (Gallaway 1975). As each segment is cast and initial post-tensioning is added, the formwork is removed and placed for the next segment to be cast as illustrated in Figure 2-3 courtesy of Gallaway (1975).

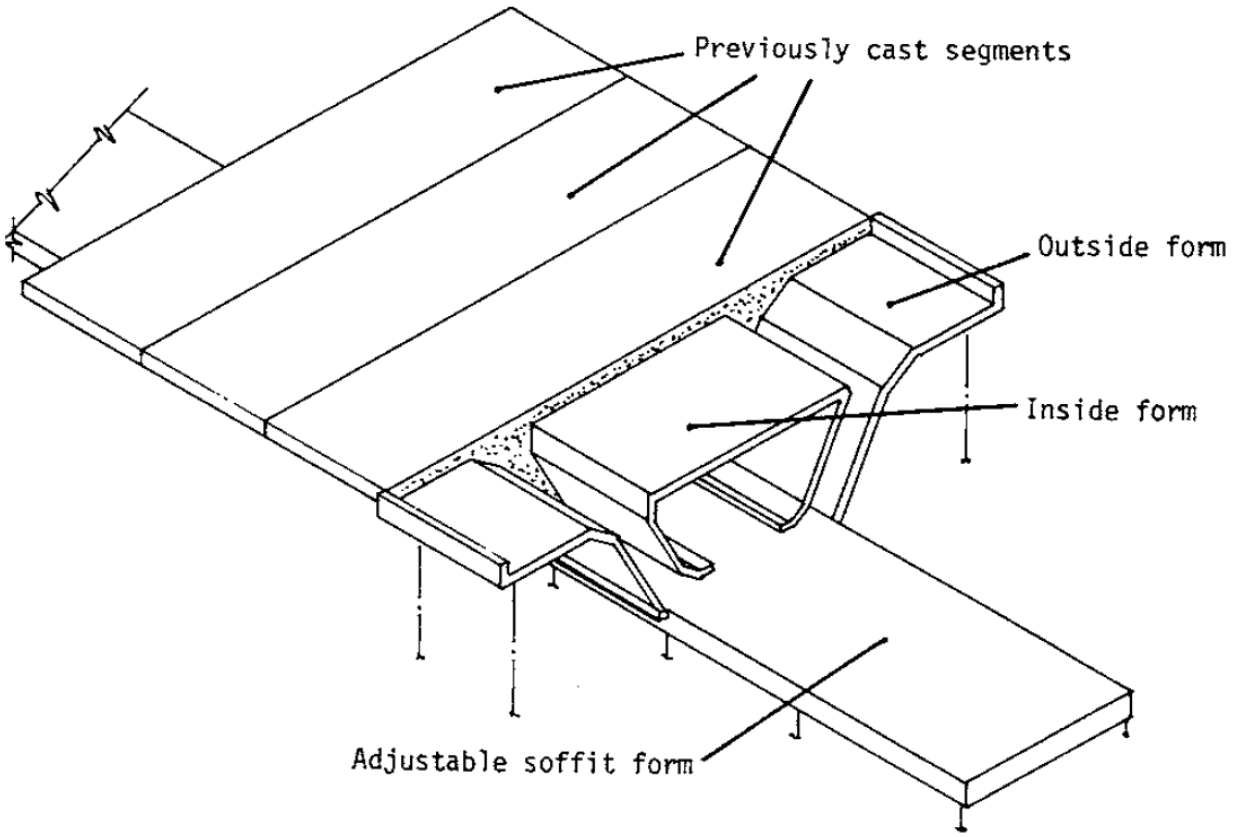

Figure 2-3: Cast-in-place method for constructing segmental concrete box-girder bridges (Gallaway 1975)

When precast segments are erected using the span-by-span method, post-tensioning occurs when an entire span is completed prior to the erection of the next span and is self-supporting; whereas with the progressive placement method, erection occurs beginning at one end of the bridge where segments are erected in sequential order (Padolny and Muller 1994). Prior to installation of any precast segments, a water resistant epoxy is applied to the surface of each segment to prevent potential distress due to moisture inside of the box-girder segments (Gallaway 1975).

2.2.2 Creep and Shrinkage in Segmental Bridges

It is important in the design of concrete structures to account for creep and shrinkage. Volumetric changes in concrete bridges can possibly cause major issues in calculated deflections and the specified camber along with moment distribution throughout the structure; however, creep and shrinkage vary depending on the type of bridge being erected, and thus must be considered

separately during the design phase (Podolny and Muller 1994). Libby (1976) provides detailed analysis of creep and shrinkage for segmental bridges constructed with the cantilever method:

> *"The cause of the redistribution of moment can be illustrated by considering two cantilever beams as shown in* [Figure 2-4]. *These beams are rendered continuous when the cast-in-place joint between them is constructed and the continuity tendons between the two cantilevers are installed. It should be apparent that if the two beams were not rendered continuous, the effect of creep would be to cause a deflection and a rotation of the ends of the beams with the passing of time. Because this rotation is resisted by the provision of continuity, a positive moment is created near midspan. The creep-caused positive moment is of significant magnitude and is accompanied with a reduction of the negative moment at the supports which is normally of negligible magnitude."*

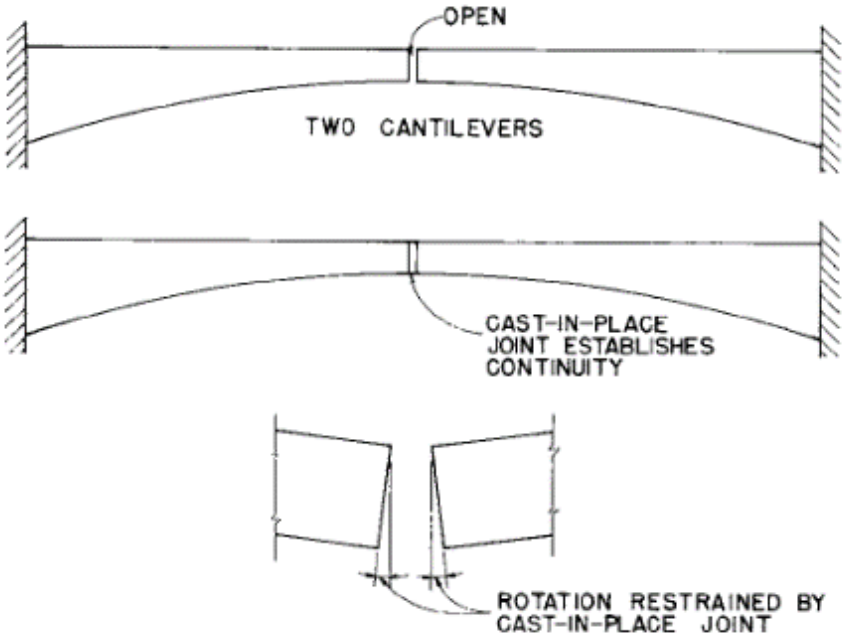

Figure 2-4: Two cantilever beams made continuous at their ends subsequent to construction (Libby 1976)

Prestressing force results in compression stresses induced in the concrete that contribute to creep and shrinkage. Creep and shrinkage may reduce the initial prestress by five percent to thirty percent in elastic tendons; whereas, if the prestressing is created by forces acting from rigid supports, a greater reduction should be considered (Rüsch et al. 1983). It is important to understand how not only a bridge may respond to different magnitudes of creep and shrinkage, but also how prestressing forces will influence the development of creep and shrinkage.

Muller (1969) published a paper explaining many of the mentioned topics of creep and shrinkage-induced moment distribution, where he provides example calculations based on a structure and estimated creep to cause a three percent reduction in negative and twenty percent increase in positive effective moment due to dead load. Most of the trouble in recent decades for segmental bridges is a result of higher than expected creep in concrete, inadequate anchorage, and poor understanding of construction loading (Roberts et al. 1993). Most modern bridge design software has the ability to estimate losses due to creep and shrinkage. It is important that during the bridge design phase creep and shrinkage be predicted effectively to reduce the need for potentially costly repairs.

2.3 VOLUMETRIC CHANGES IN CONCRETE

American Concrete Institute (ACI) Committee 209, Creep and Shrinkage in Concrete, is most often recognized as the reporting body in the United States to predict volumetric changes in concrete. ACI Committee 209 often references Comite Europeen du Beton (CEB) the European counterpart to ACI. In addition to the most recent CEB Model Code published in 2010, the CEB Model Code 1990 is also used to predict volumetric changes in concrete. Additional details for the two CEB Model Codes are described in Sections 2.4.5 and 2.4.6.

In general concrete behavior is a complex relation between stress, strain, and time; where concrete subjected to any sustained stress condition most often exhibits shrinkage and creep (CEB 1972). Creep, as summarized in Figure 2-5, is increase in strain with respect to time resulting from a constant applied external stress (Neville 2011).

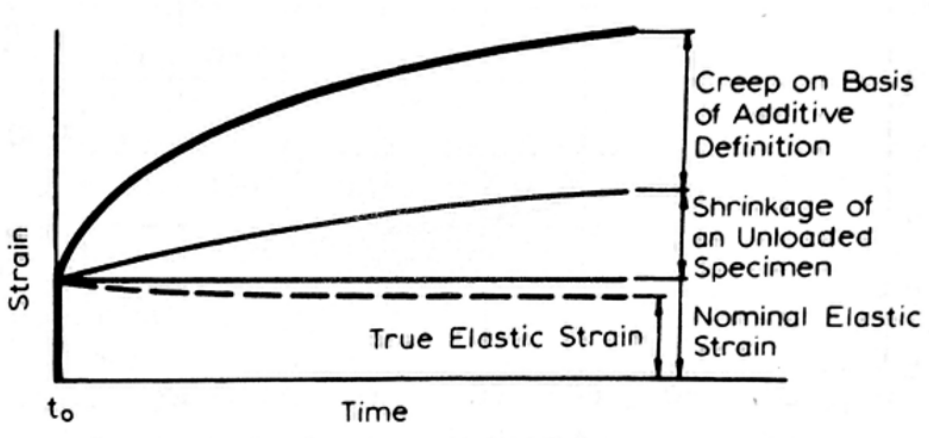

Figure 2-5: Volumetric changes of concrete under an applied external stress (Neville 2011)

ACI Committee 209 (1992) defines shrinkage as the decrease with time of concrete volume, where there are no external applied stresses. This shrinkage is often broken down as drying shrinkage, autogenous shrinkage, and carbonation shrinkage where the result is a dimensionless strain (in./in.) (ACI 209R 1992). The following subsections cover drying shrinkage, autogenous shrinkage, and creep, which are directly related to the research objectives.

2.3.1 Drying Shrinkage

According to Mehta and Monteiro (2014), the main driving force for volume change due to drying shrinkage is the removal of water from the hardened concrete due to a change in relative humidity. Concrete subjected to a relative humidity (RH) of 100% or fully saturated will have no drying shrinkage. Unrestrained concrete exposed to low relative humidity conditions causes drying shrinkage; however, in restrained concrete exposed to similar conditions the strain will be zero but tensile stresses will increase with time resulting in cracking.

In theory all moisture loss occurs in the hydrated cement paste, where several different factors acting simultaneously may influence the rate or magnitude of drying shrinkage and creep (Mehta and Monteiro 2014). Many of the same factors that influence drying shrinkage also influence creep including: time, humidity, material properties, mixture proportions, and geometry of the concrete element. The influence of these factors will be described in the following sections.

2.3.1.1 Effects of Time and Humidity on Drying Shrinkage

As moisture is lost from the hydrated cement paste, drying shrinkage gradually increases over time (Neville 2011). After studying long-term drying shrinkage testing, Troxell et al. (1958) found that approximately 20 to 25 percent of the 10-year shrinkage was developed in the first two weeks, 50 to 60 percent in the first three months, and 75 to 80 percent in the first year since concrete was exposed to drying.

For relative humidity the drying shrinkage strain is assumed to be zero at a RH of 100 percent, 200 micro-strain at 80 percent RH, and approximately 400 micro-strain at 45 percent RH according to data published by the Comite Euro-International du Beton (CEB 1970). According to Neville (2011), concrete located in dry (unsaturated) air shrinks, but concrete stored in an environment that is completely saturated or air with a relative humidity of 100 percent slightly swells over long periods of time.

2.3.1.2 Influence of Materials and Mixture Proportions on Drying Shrinkage

Since the majority of moisture-related volume change occurs in the hydrated cement paste, many studies have been completed in an attempt to relate the drying shrinkage strain to the volume fraction of the hydrated cement paste (Mehta and Monteiro 2014). Other contributing factors that have been proven to influence drying shrinkage are aggregate type and content, cement content, and water-cement ratio. Although some small comparisons can be made between drying shrinkage to aggregate gradation, maximum size, shape, or texture, the most important factor is modulus of elasticity of the aggregate (Mehta and Monteiro 2014). As the modulus of elasticity of the aggregate increases, the shrinkage of the concrete decreases (Mehta and Monteiro 2014).

The effects of cement content and water-cement ratio have an indirect relationship to drying shrinkage (Mehta and Monteiro 2014). The influence of cement content, water-cement ratio, and water content on the ultimate drying shrinkage is presented in Figure 2-6 adapted from Neville (2011).

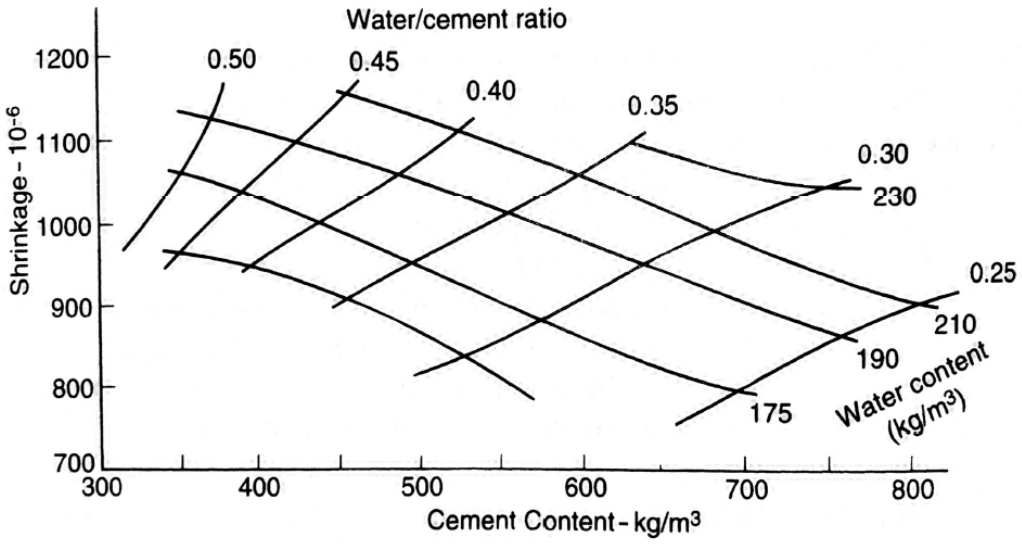

Figure 2-6: Influence of concrete cement characteristics on ultimate shrinkage (Neville 2011)

An increase in the cement paste volume correlates to a decrease in aggregate content therefore corresponding to an increase in moisture-dependent deformations according to Mehta and Monteiro (2014). This same relationship is understood for concrete strength where Mehta and Monteiro (2014) conclude, for a given cement content, an increase in water-cement ratio corresponding to a decrease in concrete strength will ultimately lead to an increase in drying

shrinkage. The relationship between 7-day compressive strength and water-cement ratio for a typical portland cement concrete mixture is presented in Figure 2-7 (Neville 2011).

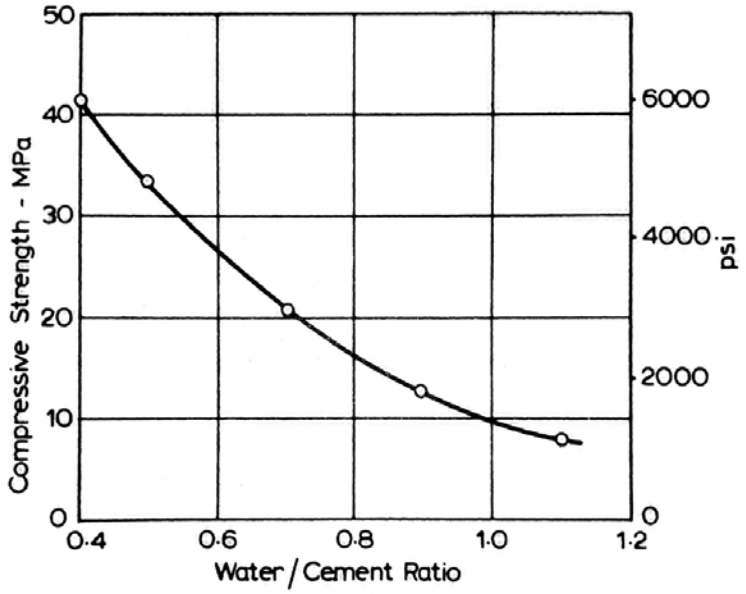

Figure 2-7: Relationship between compressive strength and water-cement ratio (Neville 2011)

Additional factors that may impact the amount of drying shrinkage in concrete include cement properties, supplementary cementing materials (SCMs), and chemical admixtures. The properties of cement have little influence on the drying shrinkage of concrete; however, drying shrinkage of concrete made with high-alumina cement develops more rapidly, but the magnitude is the same when compared to portland cement (Neville 2011). An increase in fly ash or ground granulated blast-furnace (GGBF) slag increases drying shrinkage at a constant water-cement ratio, where shrinkage may increase by up to 60 percent at very high slag contents (Neville 2011). The use of water-reducing admixtures in conventional slump content may cause a small increase in shrinkage; however, the effect is indirect because of the corresponding change in water and cement content within that are accompanied (Neville 2011).

2.3.2 Autogenous Shrinkage

Tazawa (1999) defines autogenous shrinkage as "the macroscopic volume reduction of cementitious materials when cement hydrates after initial setting [where it] does not include volume change due to loss or ingress of substances, temperature variation, application of an external force and restraint." Autogenous shrinkage occurs when no moisture movement is

permitted to and from the hydrated cement paste after initial set (Neville 2011). Autogenous shrinkage is expressed as a percentage of total volume reduction because it develops in three dimensions; however, autogenous shrinkage is often expressed as a dimensionless longitudinal strain (Tazawa 1999). The autogenous shrinkage mechanism and factors influencing autogenous shrinkage are detailed in the subsequent sections.

2.3.2.1 Understanding Chemical Shrinkage and Self-Desiccation

Chemical shrinkage is defined by Tazawa (1999) as "the phenomenon in which the absolute volume of hydration products is less than the total volume of unhydrated cement and water before hydration." The volume reduction with time for the comparison of chemical and autogenous shrinkage is presented in Figure 2-8.

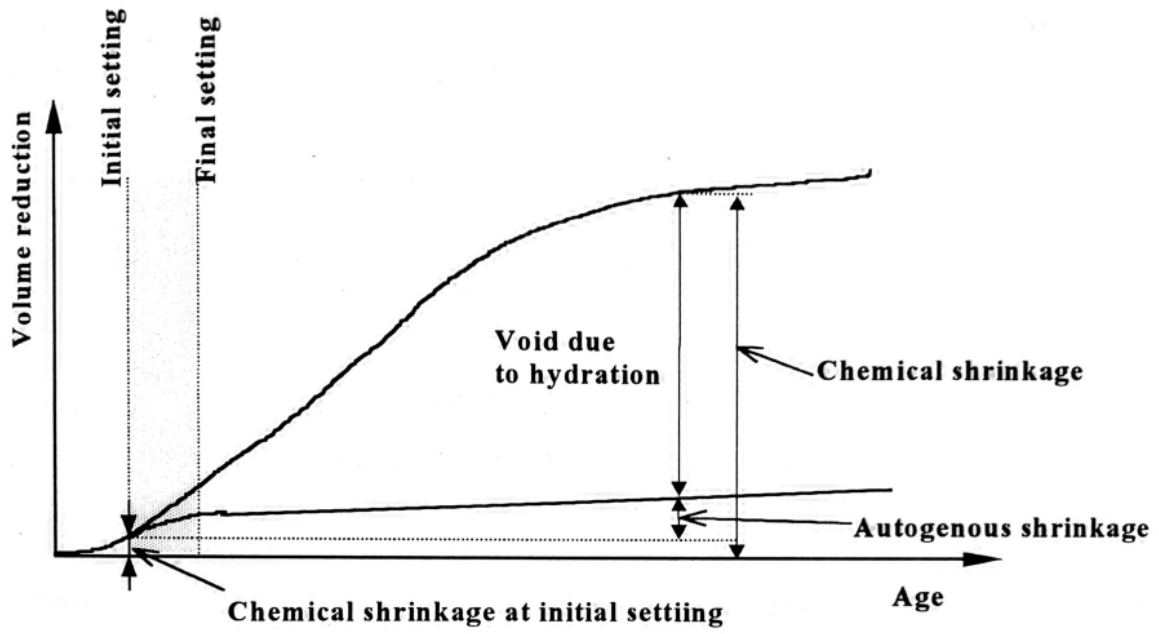

Figure 2-8: Relationship between chemical and autogenous shrinkage (Tazawa 1999)

Autogenous shrinkage is a small portion of the total chemical shrinkage, where chemical shrinkage is the reduction of the absolute volume of reactants and autogenous shrinkage is the reaction of the external volume since the solid skeleton is formed at initial set (Tazawa 1999). At initial set, chemical shrinkage produces voids within the hydrated cement paste, as shown in Figure 2-8 (Tazawa 1999).

Understanding microstructure within the hydrated cement paste is important for determining how autogenous shrinkage effects the shrinkage of hardened concrete. Ettringite is a

needlelike microstructure that forms on the surface of cement particles at initial hydration which creates a large volume of fine pores (Tazawa 1999). As cement particles hydrate further, calcium-silicate hydrate (C-S-H) is produced that also is filled with additional fine pores (Tazawa 1999). The process by which water is removed from capillary pores by the additional hydration of unhydrated cement particles is called self-desiccation (Neville 2011). In order to compare self-desiccation and pore micro structure, Tazawa (1999) concludes: "Self-desiccation is considered to be significant in the case of more amount of finer pores and less water in hardened cement body. In other words, the degree of self-desiccation is strongly related with microstructure formation."

2.3.2.2 Factors Influencing Autogenous Shrinkage

Although many factors may impact the extent of autogenous shrinkage, the main factors that influence autogenous shrinkage of concrete the most are: supplementary cementing materials (SCM's), chemical admixtures, and mixture proportions (Tazawa 1999). The influence of SCM's and expansive additives on autogenous shrinkage of concrete are as follows: silica fume and slag cement in general increase autogenous shrinkage and fly ash, limestone powder, treated silica powder, and expansive additives tend to reduce autogenous shrinkage (Tazawa 1999). The next major factor that influences autogenous shrinkage is concrete mixture proportions. Influence of cement type on autogenous shrinkage is as follows: in general low heat cements have the lowest amount of autogenous shrinkage and high-early strength cements tend to have the most autogenous shrinkage (Tazawa 1999). Typically as the water-cementitious material ratio or as the volume of aggregate is decreased the volume of hydrated cement paste increases which tends to result in an increase of autogenous shrinkage (Tazawa 1999).

2.3.3 Creep

The final volumetric change of concrete that will be discussed is a phenomenon called creep. Creep is defined by ACI Committee 209 (1992) as the time-dependent increase of strain in concrete under an applied stress. The creep strain is obtained by subtracting the initial elastic strain and shrinkage strain from the total strain from the applied stress. In order to quantify creep it is important to determine shrinkage in identical concrete due to the previously mentioned factors that influence both creep and shrinkage. Neville (2011) states "where a more fundamental approach is warranted, distinction will be made between creep of concrete under conditions of no moisture movement to

or from the ambient medium (true or basic creep) and the additional creep caused by drying (drying creep).” An illustration describing the distinction between basic creep and drying creep can be seen in Figure 2-9 adapted from Neville (2011). Creep is typically considered the sum of drying creep and basic creep for the following reasons: most concrete structures experience both drying and loading simultaneously as well as the majority of test data collected assumes the additive properties of creep and shrinkage (Neville 2011).

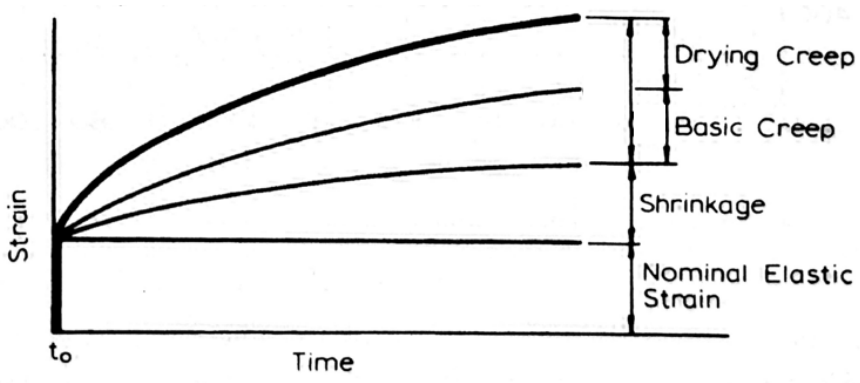

Figure 2-9: Two components of creep in concrete adapted from Neville (2011)

2.3.3.1 Compliance

Although creep is typically defined in strain units, creep can also be defined as compliance. According to ACI 209.2R (2008), compliance allows for a more accurate comparison of creep results because they are normalized based on applied loading. Compliance is useful because it is often difficult to separate early-age creep from the elastic strain in experimental results (ACI 209.2R 2008). Compliance is defined by ACI 209.2R (2008) as the ratio of total strain and stress resulting from an applied load shown in Equation 2.1:

$$J(t, t_o) = \frac{(\text{Elastic Strain} + \text{basic creep} + \text{drying creep})}{\text{stress}} \qquad \text{Equation 2.1}$$

Where,

$J(t, t_o)$ = compliance at age t caused by a unit uniaxial sustained load applied at age t_o(1/psi),

t = age of concrete (days), and

t_o = age of concrete at time of loading (days).

From this definition of compliance, at the instant a concrete element is loaded the creep strain will be zero; however, the compliance value will be the inverse of the modulus of elasticity at time of loading. The compliance function with the respect to concrete age, where the time-dependent behavior acts in addition to the instantaneous elastic deformation is illustrated in Figure 2-10, adapted from ACI 209.2R (2008).

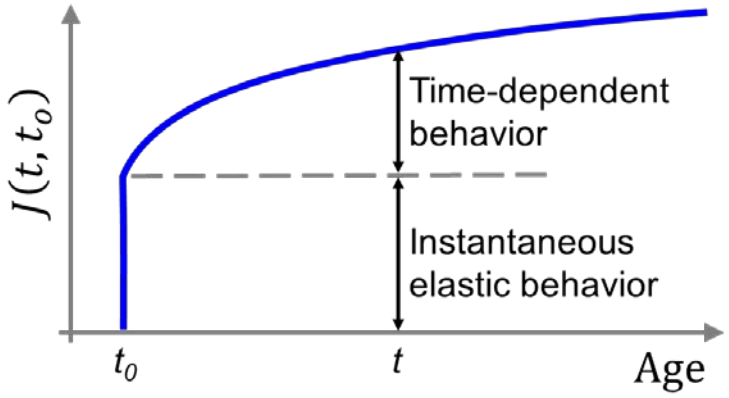

Figure 2-10: Compliance development schematic adapted from ACI 209.2R (2008)

2.3.3.2 Creep Mechanism

The majority of creep develops from the removal of absorbed water from the hydrated cement paste due to the application of stress (Mehta and Monteiro 2014). It has been proven that in concrete subjected to both drying and an applied stress greater than 40 percent of the concrete compressive strength, additional creep develops from microcracking in the interfacial transition zone due to the nonlinearity of the stress-strain relationship of concrete (Mehta and Monteiro 2014).

2.3.3.3 Factors Influencing Creep

As mentioned in Section 2.3.1 many of the same factors that influence drying shrinkage also influence creep. Although creep occurs within the hydrated cement paste, aggregate content in concrete has been shown to influence creep where an increase in aggregate content from 65 to 75 percent shows a noticeable decrease in creep of approximately 10 percent (Neville 2011). Many physical properties of aggregates have been studied in their relationship to creep; however, the most important property is aggregate modulus of elasticity where aggregates with a higher modulus of elasticity give more restraint for potential creep of the hydrated cement paste (Neville 2011). In conclusion, it is more convenient to relate aggregate type to creep based on the

combination of all properties as illustrated in Figure 2-11 (Neville 2011). Sandstone and limestone can be seen to have the highest and lowest creep respectively.

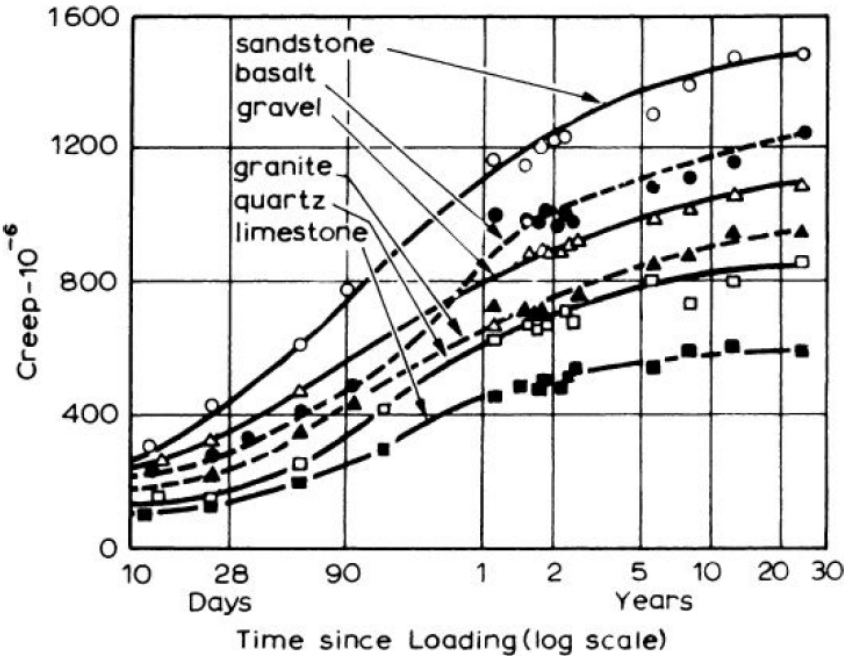

Figure 2-11: Creep based on different aggregate types (Neville 2011)

The same correlation holds true for creep, as discussed in Section 2.3.1.1 for drying shrinkage, which Mehta and Monteiro (2014) conclude for a given water-cement ratio, creep increases with increasing cement content due to larger volume of cement paste; however, in practice this may not always happen. The effect of water-cement ratio and cement content on creep is illustrated in Figure 2-12 adapted from Mehta and Monteiro (2014).

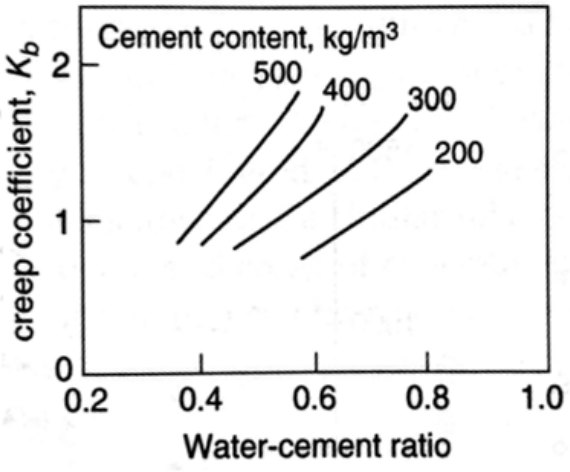

Figure 2-12: Effect of water-cement ratio and cement content on creep (Mehta and Monteiro 2014)

These same factors that influence creep also influence the concrete strength, as illustrated for water-cement ratio in Figure 2-7 (Neville 2011). According to Neville (2011), “the strength of concrete has a considerable influence on creep: within a wide range, creep is inversely proportional to the strength of concrete at the time of application of the load.” The compressive strength increases with maturity of concrete resulting in in a decrease in creep deformations (Neville 2011). This relationship between strength, maturity, and creep is important for later comparison.

Another important factor that influences creep is relative humidity of the ambient environment (Neville 2011). It has been shown for concrete that is loaded, a decreased relative humidity of the ambient environment will exhibit higher creep due to the free moisture inside of the concrete being released as compared to the same concrete exposed to a higher relative humidity (Neville 2011).

2.4 CREEP AND SHRINKAGE PREDICITON MODELS

The main objective of this research study is to accurately predict the creep and shrinkage of concrete in the Birmingham I-59/I-20 segmental bridge. The models evaluated in this report are most commonly used in either design or research studies (ACI 209.2R 2008). Each subsequent section provides details related to concrete properties and environmental conditions as well as the calculation methods for each model. The six models considered for this research project include:

- ACI 209 (2008),
- AASHTO LRFD (2017),
- GL 2000 (Gardner and Lockman 2001),
- B3 (Bazant and Baweja 2000),
- CEB MC 1990 (CEB 1990), and
- CEB MC 2010 (fib 2012).

As discussed in Section 1.2, the CEB MC 1990 Model is considered for the prediction of creep and shrinkage of concrete in the Birmingham I-59/I-20 segmental bridge. Although the most recent CEB Model Code was published in 2012, the creep and shrinkage models defined in the CEB MC 1990 are calibrated to most accurately predict creep and shrinkage in concrete specimens collected throughout the project duration for recommendations that may be implemented into commonly used bridge design software.

As presented in Section 2.2.3.1, compliance represents the initial-elastic and creep strain a concrete specimen experiences at a given time under an applied load. Most often models predict a creep coefficient to describe creep deformations; however, some models predict compliance directly. In general, the predicted compliance function is defined by ACI 209.2R (2008) as the ratio of total strain to stress resulting from an applied load shown in Equation 2.2.

$$J(t,t_0) = \frac{\varepsilon_{initial-elastic} + \text{predicted creep}(t,t_0)}{\sigma(t_0)} \qquad \text{Equation 2.2}$$

Where,

$J(t,t_0)$ = predicted compliance (1×10^{-6}/psi),

$\varepsilon_{initial-elastic}$ = predicted initial elastic strain (in./in.),

$\text{predicted creep}(t,t_0)$ = predicted creep strain (in./in.),

$\sigma(t_0)$ = uniaxial stress resulting from loading (psi),

t = age of concrete (days), and

t_0 = age of concrete at time of loading (days).

The simplified form of the predicted compliance function using the predicted creep coefficient is presented in Equation 2.3 (ACI 209.2R 2008).

$$J(t,t_0) = \frac{1 + \Phi(t,t_0)}{E_{cmto}} \qquad \text{Equation 2.3}$$

Where,

$\Phi(t,t_0)$ = predicted creep coefficient (unitless) and

E_{cmto} = predicted modulus of elasticity at time of loading (psi).

2.4.1 ACI 209 Creep and Shrinkage Prediction Method

The creep and shrinkage prediction method introduced by ACI 209R (1992) uses a development curve and ultimate values depending on several factors, such as concrete age at loading, curing conditions, mixture proportions, relative humidity, and ambient temperature. For both creep and shrinkage, an ultimate value is predicted where modification factors adjust this ultimate value according to the named parameters (ACI 209.2R 2008).

2.4.1.1 ACI 209 Creep Model

The ultimate creep coefficient is the ratio of ultimate creep strain to initial elastic strain resulting from the application of load. The ultimate creep coefficient Φ_u, with correction factors described in Equations 2.4 to 2.11, is calculated using Equation 2.2:

$$\Phi_u = 2.35\gamma_{c,to}\gamma_{c,RH}\gamma_{c,vs}\gamma_{c,s}\gamma_{c,\psi}\gamma_{sh,\alpha} \quad \text{Equation 2.4}$$

With,

$\gamma_{c,to}$ = the loading age correction factor defined as:

$$\gamma_{c,to} = 1.25t_o^{-0.118} \text{ (for moist-curing)} \quad \text{Equation 2.5}$$

$$\gamma_{c,to} = 1.13t_o^{-0.094} \text{ (for steam-curing)} \quad \text{Equation 2.6}$$

Where,

t_0 = age of concrete when load is applied (days), only to be used for concrete older than 7 days for non-accelerated curing and older than 1-3 days for steam-curing.

$\gamma_{c,RH}$ = the ambient relative humidity correction factor defined as:

$$\gamma_{c,RH} = 1.27 - 0.67h \text{ (for } h > 40\%) \quad \text{Equation 2.7}$$

Where,

h = ambient relative humidity expressed as a ratio.

$\gamma_{c,vs}$ = the volume-to-surface area ratio correction factor defined as:

$$\gamma_{c,vs} = (2/3)\left[1 + 1.13\exp\left(-0.54(v/s)\right)\right] \quad \text{Equation 2.8}$$

Where,

v/s = volume-to surface area ratio (in.)

$\gamma_{c,s}$ = the slump correction factor defined as:

$$\gamma_{c,s} = 0.82 + 0.067s \quad \text{Equation 2.9}$$

Where,

s = observed slump (in.)

$\gamma_{c,\psi}$ = the fine aggregate percentage correction factor defined as:

$$\gamma_{c,\psi} = 0.88 + 0.0024\psi \quad \text{Equation 2.10}$$

Where,

ψ = ratio of fine to total aggregate by weight (%)

$\gamma_{sh,\alpha}$ = the air content correction factor defined as:

$$\gamma_{sh,\alpha} = 0.46 + 0.09\alpha \geq 1.0 \quad \text{Equation 2.11}$$

Where,

α = air content (%)

After determining the modified ultimate creep coefficient, the next step is to develop the creep coefficient at any age after loading, $\Phi(t, t_o)$, which can be calculated using Equation 2.12:

$$\Phi(t, t_o) = v_t \Phi_u \quad \text{Equation 2.12}$$

With,

v_t = the concrete age time-ratio parameter defined as:

$$v_t = \frac{(t - t_o)^{\psi}}{d + (t - t_o)^{\psi}} \quad \text{Equation 2.13}$$

Where,

$(t - t_o)$ = duration of time after loading (days),

d = constant for member shape and size taken as 10, and

ψ = constant for member shape and size taken as 0.6.

The time dependent portion in determining creep, as demonstrated in Equation 2.13, is only applicable to concretes with an age at loading of 7 days for non-accelerated curing and 1-3 days for steam-curing. The predicted creep strain for a desired time after loading is calculated using Equation 2.14:

$$\text{predicted creep } (t, t_i) = \Phi(t, t_o) \times \varepsilon_{initial-elastic} \quad \text{Equation 2.14}$$

Where,

$\Phi(t, t_o)$ = creep coefficient for a considered duration of loading, t, and

$\varepsilon_{initial-elastic}$ = initial elastic strain at loading due to load application.

As presented in Equation 2.3, compliance predictions require the modulus of elasticity of the concrete at time of loading. For ACI 209.2 (2008) the elastic modulus at loading can be determined using Equation 2.15:

$$E_{cmto} = 33\gamma_c^{1.5}\sqrt{f_{cmto}} \qquad \text{Equation 2.15}$$

Where,

γ_c = unit weight of concrete (lb/ft^3) and

f_{cmto} = mean concrete compressive strength at loading (psi).

2.4.1.2 ACI 209 Shrinkage Model

The shrinkage prediction model proposed by ACI 209 (2008) shares many of the same characteristics as the creep prediction model, in which a standard ultimate value is modified using correction factors described in Table 2-1 and Equations 2.17 to 2.22 depending on conditions altered from the standard. Equation 2.16 is used to calculate the ultimate shrinkage strain, ε_{shu}, for modified parameters:

$$\varepsilon_{shu} = 780\gamma_{sh,tc}\gamma_{sh,RH}\gamma_{sh,vs}\gamma_{sh,s}\gamma_{sh,\psi}\gamma_{sh,c}\gamma_{sh,\alpha} \times 10^{-6} \qquad \text{Equation 2.16}$$

With,

$\gamma_{sh,tc}$ = the initial moist-curing correction factor presented in Table 2-1:

Table 2-1: Shrinkage correction factors for initial moist-curing (ACI 209.2R)

Curing Duration t_c (days)	$\boldsymbol{\gamma_{sh,tc}}$
1	1.20
3	1.10
7	1.00
14	0.93
28	0.86
90	0.75

$\gamma_{sh,RH}$ = the ambient relative humidity correction factor defined as:

$$\gamma_{sh,RH} = \begin{cases} 1.4 - 1.02h & \text{for } 0.40 \le h < 0.80 \\ 3.0 - 3.00h & \text{for } 0.80 < h \le 1.00 \end{cases} \qquad \text{Equation 2.17}$$

Where,

h = ambient relative humidity expressed as a ratio

$\gamma_{sh,vs}$ = the volume-to-surface area ratio correction factor defined as:

$$\gamma_{sh,vs} = 1.2\exp\left(-0.12(v/s)\right) \quad \text{Equation 2.18}$$

Where,

v/s = volume-to surface area ratio (in.)

$\gamma_{sh,s}$ = the slump correction factor defined as:

$$\gamma_{sh,s} = 0.89 + 0.041s \quad \text{Equation 2.19}$$

Where,

s = observed slump (in.)

$\gamma_{sh,\psi}$ = the fine aggregate percentage correction factor defined as:

$$\gamma_{sh,\psi} = \begin{cases} 0.30 + 0.014\psi & \text{for } \psi \leq 50\% \\ 0.90 + 0.002\psi & \text{for } \psi > 50\% \end{cases} \quad \text{Equation 2.20}$$

Where,

ψ = ratio of fine to total aggregate by weight (%)

$\gamma_{sh,c}$ = the cement content correction factor defined as:

$$\gamma_{sh,c} = 0.75 + 0.00036c \quad \text{Equation 2.21}$$

Where,

c = cement content (lb/yd^3)

$\gamma_{sh,\alpha}$ = the air content correction factor defined as:

$$\gamma_{sh,\alpha} = 0.95 + 0.008\alpha \geq 1.0 \quad \text{Equation 2.22}$$

Where,

α = air content (%)

After determining the modified ultimate shrinkage strain, the next step is to develop the function for shrinkage strain at any age after loading, $\varepsilon_{shu}(t, t_c)$, which can be calculated using Equation 2.23:

$$\varepsilon_{shu}(t, t_c) = v_t \varepsilon_{shu}$$ Equation 2.23

With,

v_t = the concrete age time-ratio parameter defined as:

$$v_t = \frac{(t - t_c)^{\alpha}}{f + (t - t_c)^{\alpha}}$$ Equation 2.24

Where,

$(t - t_c)$ = duration of time since drying commenced (days),

f = constant for member shape and size taken as 35 for 7 days of moist-curing and 55 for 1 to 3 days of steam-curing, and

α = constant for member shape and size taken as 1.

2.4.2 AASHTO LRFD 2017 Creep and Shrinkage Prediction Method

AASHTO LRFD (2017) is the current set of requirements that ALDOT follows in design for many infrastructure projects but specifically bridge design and construction. Studies conducted by Tadros (2003) and Rizkalla et al. (2007) influenced the method by which the AASHTO LRFD 2017 Model predicts creep and shrinkage. Although AASHTO has published a revised set of specifications in AASHTO LRFD 2020, this study focuses on the 2017 version. All references for creep and shrinkage can be found in C5.4.2.3 of the AASHTO LRFD Bridge Design Specifications (2017).

2.4.2.1 AASHTO LRFD Creep Model

The AASHTO LRFD Model for predicting creep uses an ultimate creep coefficient that can be compared to the compressive strain due to loading to calculate creep strains. The function used to predict the creep coefficient, $\psi(t, t_i)$, can be seen in Equation 2.25. In addition, the model uses several factors detailed in Equations 2.26 to 2.29 to account for the following:

- Member size,
- Ambient relative humidity,
- Concrete strength, and
- Time development.

$$\psi(t, t_i) = 1.9 k_s k_{hc} k_f k_{td} t_i^{-0.118}$$ Equation 2.25

With,

k_s = the volume-to-surface area ratio correction factor defined as:

$$k_s = 1.45 - 0.13(v/s) \geq 1.0 \qquad \text{Equation 2.26}$$

Where,

v/s = volume-to-surface area ratio (in.)

k_{hc} = the ambient relative humidity factor defined as:

$$k_{hc} = 1.56 - 0.008H \qquad \text{Equation 2.27}$$

Where,

H = average annual ambient relative humidity (%)

k_f = the concrete strength factor defined as:

$$k_f = \frac{5}{1 + f'_{ci}} \qquad \text{Equation 2.28}$$

Where,

f'_{ci} = Concrete compressive strength at time of initial loading (ksi). If concrete age at time of initial loading is unknown at design time, f'_{ci} may be taken as 0.8 f'_c (ksi).

k_{td} = the time development factor defined as:

$$k_{td} = \frac{t}{12\left(\frac{100 - 4f'_{ci}}{f'_{ci} + 20}\right) + t} \qquad \text{Equation 2.29}$$

Where,

t= Maturity of concrete (days), defined as difference between the age being considered for creep calculations and the age at when the structure was loaded.

t_i = the age of concrete at time of load application (days).

The AASHTO LRFD Model specifies that the value of t in the time development function may be taken as the chronological age if an accelerated curing method is used. Tadros (2003) found that for high-strength concretes with low water-cement ratios, ultimate values had little to no differences. To calculate compliance, AASHTO LRFD (2017) predicts the modulus of elasticity at the time of loading using Equation 2.30:

$$E_{cmto} = 120{,}000 K_1 w_c^2 f_c'^{1/3}$$ Equation 2.30

Where,

K_1 = correction factor for aggregate source taken as 1.0,

w_c = unit weight of the concrete (kcf), and

f_c' = compressive strength of concrete for use in design (ksi).

2.4.2.2 AASHTO LRFD Shrinkage Model

The AASHTO LRFD Model predicts shrinkage with nearly the same factors as for predicting creep. The function for shrinkage strain can be calculated using Equations 2.31 to 2.33:

$$\varepsilon_{sh}(t, t_c) = k_s k_{hs} k_f k_{td} (0.48 \times 10^{-3})$$ Equation 2.31

With,

k_s = the same as Equation 2.25,

k_{hs} = the ambient relative humidity factor defined as:

$$k_{hs} = 2.00 - 0.014H$$ Equation 2.32

Where,

H = average annual ambient relative humidity (%),

k_f = the same as Equation 2.28,

k_{td} = the shrinkage time development factor defined as:

$$k_{td} = \frac{t}{12\left(\frac{100 - 4f_{ci}'}{f_{ci}' + 20}\right) + t}$$ Equation 2.33

Where,

t = the chronological age of concrete from the time when drying begins to the time at which shrinkage is to be evaluated.

AASHTO LRFD (2017) states that if concrete is exposed to drying before 5 days of curing have elapsed, all shrinkage strains should be increased by 20 percent to ensure accurate results.

2.4.3 GL 2000 Creep and Shrinkage Prediction Method

The GL 2000 Model was developed and published by Gardner and Lockman (2001). The GL 2000 Model allows for the prediction of creep and shrinkage for some concrete mixture proportion inputs. Gardner and Lockman (2001) state that the method can be used regardless of the chemical admixtures or SCMs that are present. In addition the model uses relative humidity, element size, and strength at loading; however, the main difference between other models is that the 28-day compressive strength is required to predict creep and shrinkage at varying time intervals. Gardner and Lockman (2001) state, "All equations for computing creep and shrinkage were developed in terms of the mean concrete strength f_{cm} that was reported in the experimental investigations. Supplementary subscripts are used to differentiate mean strength from characteristic, or specified, strength and age."

In order to better represent concrete age for concretes exposed to accelerated curing conditions, Gardner and Lockman (2001) propose the use of the Arrhenius equivalent age method to determine concrete maturity. The Arrhenius function, shown in Equation 2.34, for determining concrete maturity was assumed to have an activation energy of 45,000 J/mol (ASTM C 1074 2018). Activation energy was based on the type and quantity of both portland cement and SCMs that were used in the approved mixture proportions.

$$t_e = \sum_{0}^{t} \exp\left[-\frac{E_a}{8.3144}\left(\frac{1}{273 + T_c} - \frac{1}{273 + T_r}\right)\right]\Delta t \qquad \text{Equation 2.34}$$

Where,

t_e = equivalent age of concrete (days),

t = chronological concrete age (days),

E_a = activation energy (J/mol),

T_c = average temperature during time interval, Δt, (°C), and

T_r = reference curing temperature (20°C).

2.4.3.1 GL 2000 Creep Model

The GL 2000 Model focuses on predicting compliance at desired concrete ages based on the 28-day creep coefficient. The function for the GL 2000 compliance model can be seen in Equation 2.35 (Gardner and Lockman 2001):

$$J(t, t_0) = \frac{1}{E_{cmto}} + \text{specific creep}(t, t_0) \quad \text{Equation 2.35}$$

With,

E_{cmto} = the modulus of elasticity at time of loading (psi) defined as:

$$E_{cmto} = 500{,}000 + 52{,}000\sqrt{f_{cmt}} \quad \text{Equation 2.36}$$

Where,

f_{cmt} = mean concrete compressive strength at time of loading (psi)

specific creep(t, t_0) = function to relate creep to the elastic modulus defined as:

$$\text{specific creep } (t, t_0) = \frac{\phi_{28}}{E_{cm28}} = \frac{\phi(t, t_0)}{E_{cm28}} \quad \text{Equation 2.37}$$

Where,

ϕ_{28} = 28-day creep coefficient,

$\phi(t, t_0)$ = creep coefficient function, and

E_{cm28} = concrete modulus of elasticity at 28 days (psi).

The creep coefficient is calculated with Equation 2.38. The first two terms of the function account for basic creep strains. The last term of the function is for drying creep strains.

$$\phi(t, t_0) = \phi(t_c)\left[2\left(\frac{(t - t_0)^{0.3}}{(t - t_0)^{0.3} + 14}\right) + \left(\frac{7}{t_0}\right)^{0.5}\left(\frac{t - t_0}{t - t_0 + 7}\right)^{0.5} + 2.5(1 - 1.086h^2)\left(\frac{t - t_0}{t - t_0 + 77(v/s)^2}\right)^{0.5}\right] \quad \text{Equation 2.38}$$

With,

t = the equivalent age of concrete (days),

t_0 = the equivalent age of concrete at loading (days),

h = the relative humidity expressed as a ratio,

v/s = the volume-surface area ratio (in.), and

$\phi(t_c)$ = the correction for concrete that is loaded after drying defined as:

$$\phi(t_c) = \begin{cases} 1 & \text{if } t_0 = t_c \\ \left[1 - \left(\frac{t_0 - t_c}{t_0 - t_c + 77(v/s)^2}\right)^{0.5}\right]^{0.5} & \text{if } t_0 > t_c \end{cases} \quad \text{Equation 2.39}$$

Where,

t_c = equivalent age of concrete when drying begins (days).

2.4.3.2 GL 2000 Shrinkage Model

Shrinkage strains for the GL 2000 Model are modeled as the ultimate shrinkage strain times correction factors based on the time of drying and the relative humidity of the concrete. The GL 2000 shrinkage strain function is defined in Equation 2.40:

$$\varepsilon_{sh}(t, t_c) = \varepsilon_{shu}\beta(h)\beta(t - t_c) \quad \text{Equation 2.40}$$

With,

ε_{shu} = the ultimate shrinkage strain defined as:

$$\varepsilon_{shu} = 1000k\left(\frac{4350}{f_{cm28}}\right)^{0.5} (\times 10^{-6}\text{in./in.}) \quad \text{Equation 2.41}$$

Where,

f_{cm28} = compressive strength at 28-days (psi)

$$k = \begin{cases} 1.0 & \text{Type I Cement} \\ 0.75 & \text{Type II Cement} \\ 1.15 & \text{Type III Cement} \end{cases}$$

$\beta(h)$ = the relative humidity correction factor defined as:

$$\beta(h) = 1 - 1.18 \times h^4 \quad \text{Equation 2.42}$$

Where,

h = relative humidity expressed as a ratio

$\beta(t - t_c)$ = correction factor for age of concrete since drying begins defined as:

$$\beta(t - t_c) = \left[\frac{(t - t_c)}{(t - t_c) + 77(v/s)^2}\right]^{0.5} \quad \text{Equation 2.43}$$

Where,

t_c = equivalent age of concrete when drying begins (days)

2.4.4 B3 Creep and Shrinkage Prediction Method

The B3 Model for predicting creep and shrinkage was developed, with the intention of improving the ACI 209 Model, and published by Bazant and Baweja (2000). The B3 Model parameters are confined to those listed in Table 2-2 (Bazant and Baweja 2000). The B3 Model functions are considered valid for concretes cured for at least one day, and can be applied to different portland cement mixture proportions by using interpolation.

Table 2-2: Material Parameters for the B3 Model (Bazant and Baweja 2000)

Parameter	Range
Water-Cement Ratio, w/c	$0.35 \leq w/c \leq 0.85$
Aggregate-Cement Ratio, a/c	$2.5 \leq a/c \leq 13.5$
Compressive Strength (psi)	$2500 \leq f_c' \leq 10{,}000$
Cement Content (pcf), c	$10 \leq c \leq 45$
Service Stress	Up to $0.45 f_c'$

In addition to the parameters listed above, the B3 Model accounts for the maturity of the concrete by use of the equivalent-age maturity method. The B3 Model has two maturity functions shown in Equations 2.44 and 2.45 to determine equivalent age before and after loading, respectively. The maturity function prior to loading is based on an activation energy of 42,000 J/mol. After loading the equivalent-age is based on an indirect activation energy based on the concrete's physical properties as shown in Equation 2.46.

$$t_0' = \sum_{i=1}^{n} \exp\left[\frac{U_h}{R} \times \left(\frac{1}{T_o} - \frac{1}{T}\right)\right] \Delta t_i \qquad \text{Equation 2.44}$$

Where,

t_0' = equivalent-age at loading (days),

U_h/R = 5000°K,

T_o = reference absolute temperature (293°K),

T = absolute temperature during time period, Δt_i, (°K), and

Δt_i = number of days where temperature T prevails.

$$t' = \sum_{i=1}^{n} \exp\left[\frac{U_c}{R} \times \left(\frac{1}{T_o} - \frac{1}{T}\right)\right] \Delta t_i \qquad \text{Equation 2.45}$$

With,

t' = the equivalent-age of concrete after loading (days) and

U_c/R = the activation energy ratio (°K) defined as:

$$U_c/R = 110 w^{-0.27} {f_c}^{0.54} \qquad \text{Equation 2.46}$$

Where,

w = water content of the concrete (lb/ft^3) and

f_c = mean concrete compressive strength at 28 days (psi).

2.4.4.1 B3 Creep Model

Similarly to the GL 2000 Model, the B3 Model uses the compliance function $J(t', t_0')$ to predict creep for any loading duration. The compliance function is illustrated in Equation 2.47. The B3 Model uses three terms to predict the overall compliance function including: elastic strain, basic creep, and drying creep.

$$J(t', t_0') = q_1 + C_0(t', t_0') + C_d(t', t_0'\ t_c') \qquad \text{Equation 2.47}$$

Where,

q_1 = instantaneous strain due to unit stress (1×10^{-6}/psi),

$C_0(t', t_0')$ = compliance function for basic creep (1×10^{-6}/psi),

$C_d(t', t_0', t_c')$ = compliance function for drying creep (1×10^{-6}/psi),

t' = equivalent-age of concrete after loading (days),

t_0' = equivalent-age of concrete at loading (days), and

t_c' = equivalent-age of concrete when drying begins (days),

Instantaneous strain due to unit stress is calculated using Equation 2.48:

$$q_1 = 0.6 \times 10^6 / E_{cm28} \qquad \text{Equation 2.48}$$

With,

E_{cm28} = the elastic modulus of the concrete at 28 days (psi) defined as:

$$E_{cm28} = 57{,}000\sqrt{f_c} \qquad \text{Equation 2.49}$$

Basic creep compliance in terms of concrete age is found using Equations 2.50 to 2.59:

$$C_0(t', t_0') = R_T \left[q_2 Q(t', t_0') + q_3 \ln[1 + (t' - t_0')^{0.1}] + q_4 \ln\left(\frac{t'}{t_0'}\right) \right] (1 \times 10^{-6}/\text{psi}) \quad \text{Equation 2.50}$$

With,

R_T = the additional constant that adjusts the basic creep compliance function for concrete maturity defined as:

$$R_T = exp\left[\frac{U_c'}{R}\left(\frac{1}{T_o} - \frac{1}{T}\right)\right] \quad \text{Equation 2.51}$$

Where,

$$U_c' = 0.18 U_c \ (°\text{K}) \quad \text{Equation 2.52}$$

R = universal gas constant

$q_2 Q(t', t_0')$ = the aging viscoelastic compliance (1×10^{-6}/psi) defined as:

$$q_2 = 451.1 c^{0.5} {f_c}^{-0.9} \quad \text{Equation 2.53}$$

Where,

c = cement content (lb/ft^3)

$$Q(t', t_0') = Q_f(t_0') \left[1 + \left(\frac{Q_f(t_0')}{Z(t', t_0')}\right)^{r(t_0')}\right]^{-1/r(t_0')} \quad \text{Equation 2.54}$$

Where,

$$Q_f(t_0) = \left[0.086 (t_0')^{2/9} + 1.31 (t_0')^{4/9}\right]^{-1} \quad \text{Equation 2.55}$$

$$r(t_0) = 1.7 (t_o')^{0.12} + 8 \quad \text{Equation 2.56}$$

$$Z(t', t_0') = (t_o')^{-0.5} ln[1 + (t' - t_0')^{0.1}] \quad \text{Equation 2.57}$$

q_3 = the non-aging viscoelastic parameter (1×10^{-6}/psi) defined as:

$$q_3 = 0.29 (w/c)^4 q_2 \quad \text{Equation 2.58}$$

Where,

w = water content (lb/ft^3)

q_4 = aging flow compliance parameter (1×10^{-6}/psi) defined as:

$$q_4 = 0.14(a/c)^{-0.7} \quad \text{Equation 2.59}$$

Where,

a = aggregate content (lb/ft^3).

The additional creep due to drying can be calculated using Equations 2.60 to 2.69:

$$C_d(\,t', t_0', t_c') = \, q_5[\exp\{-8H(t')\} - \exp\{-8H(t_0')\}]^{1/2} \quad \text{Equation 2.60}$$

With,

q_5 = the drying creep compliance parameter (1×10^{-6}/psi) defined as:

$$q_5 = 7.57 \times 10^5 f_c^{-1} |\varepsilon_{sh\infty}|^{-0.6} \quad \text{Equation 2.61}$$

Where,

$$\varepsilon_{sh\infty} = \varepsilon_{s\infty} \frac{E(607)}{E(t_c' + \tau_{sh})} \quad \text{Equation 2.62}$$

With,

E_{cmt} = the modulus of the concrete at time, t, (psi) defined as:

$$E_{cmt} = E_{cm28}\left(\frac{t}{4 + 0.85t}\right)^{0.5} \quad \text{Equation 2.63}$$

$\varepsilon_{s\infty}$ = a constant strain (in./in.) defined as:

$$\varepsilon_{s\infty} = \, -\alpha_1\alpha_2\left[26w^{2.1} {f_c}^{-0.28} + 270\right] \quad \text{Equation 2.64}$$

Where,

$$\alpha_1 = \begin{cases} 1.0 & \text{for Type I Cement} \\ 0.85 & \text{for Type II Cement} \\ 1.1 & \text{for Type III Cement} \end{cases}$$

$$\alpha_2 = \begin{cases} 0.75 & \text{for Steam Cured} \\ 1.2 & \text{for Air Cured} \\ 1.0 & \text{for 100\% RH} \end{cases}$$

τ_{sh} = the shrinkage half-time (days) defined as:

$$\tau_{sh} = 190.8 t_0'^{-0.08} f_c^{-0.25} [2k_s(v/s)]^2 \quad \text{Equation 2.65}$$

Where,

$$k_s = \begin{cases} 1.00 & \text{for an infinte slab} \\ 1.15 & \text{for an infinite cylinder} \\ 1.25 & \text{for an infinite square prism} \\ 1.30 & \text{for a sphere} \\ 1.55 & \text{for a cube} \end{cases}$$

v/s = volume-surface area ratio (in.).

$H(t')$ and $H(t_0')$ = spatial averages for pore relative humidity defined as:

$$H(t') = 1 - (1 - h)S(t - t_c') \qquad \text{Equation 2.66}$$

$$H(t_0') = 1 - (1 - h)S(t - t_0') \qquad \text{Equation 2.67}$$

Where,

h = the ambient relative humidity expressed as a ratio

$$S(t' - t_c') = \tanh\left[\left(\frac{t' - t_c'}{\tau_{sh}}\right)^{0.5}\right] \qquad \text{Equation 2.68}$$

$$S(t' - t_0') = \tanh\left[\left(\frac{t' - t_0'}{\tau_{sh}}\right)^{0.5}\right] \qquad \text{Equation 2.69}$$

2.4.4.2 B3 Shrinkage Model

The B3 model predicts the mean shrinkage strain of the cross section at time of drying with Equation 2.70:

$$\varepsilon_{sh}(t', t_c') = -\varepsilon_{sh\infty} k_h S(t' - t_c') \qquad \text{Equation 2.70}$$

With,

$\varepsilon_{sh}(t', t_c')$ = the total shrinkage since drying begins (in./in.),

$\varepsilon_{sh\infty}$ = the ultimate shrinkage of the cross-section (in./in.),

k_h = the factor based on ambient relative humidity defined as:

$$k_h = \begin{cases} 1 - h^3 & \text{for} \quad h \le 0.98 \\ -0.2 & \text{for} \quad h = 1 \\ \text{Linear Interpolation} & \text{for} \quad 0.98 \le h \le 1 \end{cases} \qquad \text{Equation 2.71}$$

$S(t' - t_c')$ = the time dependent portion of drying shrinkage.

2.4.5 CEB MC 1990 Creep and Shrinkage Prediction Method

The CEB MC 1990 method was previously recommended by the Eurocode (CEB-FIP Model Code 1990) for predicting creep and shrinkage, without the 1999 updates for high-strength concrete, prior to the introduction of the Model Code 2010. The first Model Code for concrete structures was formed by two committees known as the European International Concrete Committee (CEB) and the International Federation of Prestressing (FIP). The Model Code was first published in 1978, and has been revised many times over the years with the intention of accounting for more research into concrete properties (fib 2012).

The CEB MC 1990 Model is applicable to most concrete mixture proportions and physical properties, where the model provides the ability to account for cement type, curing temperature, and load intensities (CEB 1990). Contrary to the B3 Model, the CEB MC 1990 Model is rather simple with known concrete properties; however, the CEB MC 1990 Model is in SI units so input parameters and results must be converted.

The CEB MC 1990 Model recommends the use of the equivalent-age maturity method to account for concretes cured at elevated temperatures. The function used to account for equivalent-age maturity, defined in Equation 2.72, is based on an activation energy of 33,000 J/mol. All concrete age inputs should be modified by this equivalent-age maturity function.

$$t' = \sum_{i=1}^{n} \exp\left[13.65 - \frac{4000}{273 + T}\right] \Delta t_i \qquad \text{Equation 2.72}$$

With,

t' = the temperature adjusted concrete age (days),

Δt_i = the number of days where a temperature T prevails (days), and

T = the temperature during the time period Δt_i (°C).

2.4.5.1 CEB MC 1990 Creep Model

The CEB MC 1990 Model is similar to the ACI 209 Model, where a creep coefficient is predicted that can be used to calculate both compliance and creep. In addition to the temperature adjusted equivalent-age maturity, the CEB MC 1990 Model also has an additional adjustment for the age at loading based on cement type of the concrete shown in Equation 2.73.

$$t_0' = t_{0,T}'\left[\frac{9}{2+\left(t_{0,T}'\right)^{1.2}}+1\right]^{\alpha} \geq 0.5 \text{ days} \qquad \text{Equation 2.73}$$

Where,

t_0' = the modified equivalent age of concrete at loading (days),

$t_{0,T}'$ = the temperature adjusted concrete age at loading (days),

$$\alpha = \begin{cases} -1 & \text{SL Cement} \\ 0 & \text{N and R Cement} \\ 1 & \text{RS Cement} \end{cases}$$

In accordance with the CEB MC (1990), for a typical concrete mixture, cement is classified as one of the following: slow-hardening, normal-hardening, rapid-hardening, or rapid-hardening high-strength cement. The function describing the creep coefficient, $\phi(t', t_0')$ presented in Equation 2.74, is calculated based on several different modified input parameters.

$$\phi(t', t_0') = \phi_0 \beta_c(t' - t_0') \qquad \text{Equation 2.74}$$

With,

ϕ_0 = the notional creep coefficient,

$\beta_c(t' - t_0')$ = the age development function,

t' = the equivalent age of the concrete at desired time (days), and

t_0' = the modified equivalent age of the concrete at loading (days).

The notional creep coefficient, ϕ_0, is dependent on the compressive strength of the concrete and relative humidity of the environment shown in Equation 2.75.

$$\phi_0 = \phi_{RH}\beta(f_{cm})\beta(t_0') \qquad \text{Equation 2.75}$$

With,

ϕ_{RH} = the creep coefficient based on ambient relative humidity defined as:

$$\phi_{RH} = 1 + \frac{1 - RH/100}{0.46(h/100)^{1/3}} \qquad \text{Equation 2.76}$$

Where,

$$h = 2A_c/u \text{ (mm)}, \qquad \text{Equation 2.77}$$

RH = relative humidity (%),

A_c = cross-section area in contact with the atmosphere (mm^2), and

u = perimeter of the member in contact with the atmosphere (mm).

$\beta(f_{cm})$ = the factor based on concrete strength defined as:

$$\beta(f_{cm}) = \frac{5.3}{(f_{cm}/10)^{0.5}} \qquad \text{Equation 2.78}$$

Where,

f_{cm}= mean concrete compressive strength at 28 days (MPa)

$\beta(t_0')$ = the loading-age factor for the notional creep coefficient defined as:

$$\beta(t_0') = \frac{1}{0.1 + (t_0')^{0.2}} \qquad \text{Equation 2.79}$$

The development of creep with time after loading, $\beta_c(t' - t_0')$, is found using Equation 2.80 and Equation 2.81 based on equivalent-age maturity of the concrete.

$$\beta_c(t' - t_0') = \left[\frac{t' - t_0'}{\beta_H + (t' - t_0')}\right]^{0.3} \qquad \text{Equation 2.80}$$

With,

β_H = the relative humidity factor defined as:

$$\beta_H = 150\left\{1 + \left(1.2\frac{RH}{100}\right)^{18}\right\}\frac{h}{100} + 250 \leq 1500 \qquad \text{Equation 2.81}$$

For the purpose of comparison in this research effort it is important to calculate compliance based on the predicted creep coefficient. Compliance is calculated for the CEB MC 1990 Model using Equation 2.82.

$$J(t', t_0') = \frac{1}{E_{cmto}} + \frac{\phi(t', t_0')}{E_{ci}} \qquad \text{Equation 2.82}$$

With,

$J(t', t_0')$ = the compliance function ($\times 10^{-6}$/psi),

$\phi(t', t_0')$ = the function to for creep coefficient,

E_{ci} = the modulus of elasticity of the concrete at 28 days (MPa) defined as:

$$E_{ci} = E_{co}[f_{cm}/10]^{1/3} \qquad \text{Equation 2.83}$$

Where,

$$E_{co} = \begin{cases} 28{,}500 & \text{Basalt, dense limestone} \\ 21{,}500 & \text{Quartizite} \\ 19{,}400 & \text{Limestone} \\ 15{,}100 & \text{Sandstone} \end{cases}$$

E_{cmto} = the modulus of elasticity at time of loading (MPa) defined as:

$$E_{cmto} = \beta_{cc}(t_0')^{0.5} E_{ci} \qquad \text{Equation 2.84}$$

Where,

$$\beta_{cc}(t_0') = \exp\left\{ s\left[1 - \left(\frac{28}{t}\right)^{1/2}\right]\right\} \qquad \text{Equation 2.85}$$

$$s = \begin{cases} 0.38 & \text{SL Cement} \\ 0.25 & \text{N and R Cement} \\ 0.20 & \text{RS Cement} \end{cases}$$

2.4.5.2 CEB MC 1990 Shrinkage Model

The CEB MC 1990 Model uses a notional shrinkage strain to calculate shrinkage at a desired time similarly to creep. The equivalent-age maturity function is also used to determine the shrinkage of concretes cured at elevated temperatures. The shrinkage function is shown in Equation 2.86.

$$\varepsilon_{cs}(t', t_s') = \varepsilon_{cso}\beta_s(t' - t_s') \qquad \text{Equation 2.86}$$

With,

$\varepsilon_{cs}(t', t_s')$ = the total shrinkage strain (in./in.),

t' = the equivalent age of the concrete at desired time (days),

t_s' = the equivalent age of the concrete when drying begins (days),

$\beta_s(t' - t_s')$ = the function used to represent shrinkage development defined as:

$$\beta_s(t' - t_s') = \left[\frac{(t' - t_s')}{350(h/100)^2 + (t' - t_s')}\right]^{0.5} \qquad \text{Equation 2.87}$$

ε_{cso} = the notional shrinkage strain (in./in.) defined as:

$$\varepsilon_{cso} = \varepsilon_s(f_{cm})\beta_{RH} \qquad \text{Equation 2.88}$$

Where,

$$\varepsilon_s(f_{cm}) = [160 + 10\beta_{sc}(9 - f_{cm}/10)] \times 10^{-6} \text{ (in./in.)} \qquad \text{Equation 2.89}$$

$$\beta_{RH} = \begin{cases} -1.55[1-(RH/100)^3] & \text{for } 40 \leq RH < 99\% \\ 0.25 & \text{for } RH \geq 99\% \end{cases} \qquad \text{Equation 2.90}$$

$$\beta_{sc} = \begin{cases} 4 & \text{SL Cement} \\ 5 & \text{N and R Cement} \\ 8 & \text{RS Cement} \end{cases}$$

2.4.6 CEB MC 2010 Creep and Shrinkage Prediction Model

As mentioned previously, the first European Model Codes were developed by two committees; however, with time the European International Concrete Committee (CEB) and the International Federation of Prestressing (FIP) combined to form the International Federation for Structural Concrete (FIB). The current version of the European Model Code was published in 2012, which is referred to as CEB MC 2010 (fib 2012). The creep and shrinkage prediction models of the CEB MC 2010 are closely related to those of CEB MC 1990.

For the objectives of this research effort it was important also predict creep and shrinkage using the current version of the CEB Model Code. It should be noted that there are some differences between the CEB MC 1990 and the CEB MC 2010 Models. CEB MC 2010 incorporates many of the same parameters for predicting creep; however, the major change comes in shrinkage development and factors to better predict the behavior of high-strength concretes. CEB MC 2010 incorporates autogenous shrinkage in addition into the base drying shrinkage. Although CEB MC 2010 uses different notation of variables the majority of the equations remain the same. For discussion of CEB MC 2010, changes to CEB MC 90 equations are outlined. The first major change in the CEB MC 2010 Model is in calculating the notional creep coefficient, where additional adjustments were made to the relative humidity factor shown in Equations 2.91 and 2.92 to better predict the creep for high-strength concretes.

$$\phi_{RH} = 1 + \frac{1 - RH/100}{0.1\sqrt[3]{h}} \qquad \text{for } f_{cm} \leq 35 \text{ MPa} \qquad \text{Equation 2.91}$$

$$\phi_{RH} = \left[1 + \frac{1 - RH/100}{0.1\sqrt[3]{h}}\alpha_1\right]\alpha_2 \qquad \text{for } f_{cm} > 35 \text{ MPa} \qquad \text{Equation 2.92}$$

With,

f_{cm} = the mean concrete compressive strength (MPa),

RH = the ambient relative humidity expressed as a ratio,

h = the notional member size (mm), and

α_1 and α_2 = constants for high-strength concretes defined as:

$$\alpha_1 = \left[\frac{35}{f_{cm}}\right]^{0.7} \quad \text{Equation 2.93}$$

$$\alpha_2 = \left[\frac{35}{f_{cm}}\right]^{0.2} \quad \text{Equation 2.94}$$

The second difference between the CEB MC 1990 and CEB MC 2010 is the factor that accounts for concrete strength with respect to the notional creep coefficient shown in Equation 2.95.

$$\beta(f_{cm}) = \frac{16.8}{(f_{cm})^{0.5}} \quad \text{Equation 2.95}$$

The final difference in calculating the notional creep coefficient is in β_H, the factor depending on the relative humidity and notional member size. Depending on the mean 28-day compressive strengths, Equation 2.96 and Equation 2.97 outline the coefficient.

$$\beta_H = 150\left\{1 + \left(1.2\frac{RH}{100}\right)^{18}\right\}\frac{h}{100} + 250 \leq 1500 \quad \text{Equation 2.96}$$
$$\text{for } f_{cm} \leq 35 \text{ MPa}$$

$$\beta_H = 150\left\{1 + \left(1.2\frac{RH}{100}\right)^{18}\right\}\frac{h}{100} + 250\alpha_3 \leq 1500\alpha_3 \quad \text{Equation 2.97}$$
$$\text{for } f_{cm} > 35 \text{ MPa}$$

Where,

$$\alpha_3 = \left[\frac{35}{f_{cm}}\right]^{0.5} \quad \text{Equation 2.98}$$

2.4.6.1 CEB MC 2010 Shrinkage Model

The major difference between CEB MC 1990 and CEB MC 2010 is in shrinkage prediction. CEB MC 2010 separates shrinkage into two components to account for both drying shrinkage and autogenous shrinkage. Equation 2.99 illustrates the two stages of shrinkage.

$$\varepsilon_{cs}(t', t_s') = \varepsilon_{cas}(t') + \varepsilon_{cds}(t', t_s') \quad \text{Equation 2.99}$$

Where,

$\varepsilon_{cs}(t', t_s')$ = total shrinkage strain,

$\varepsilon_{cas}(t')$ = autogenous shrinkage strain, and

$\varepsilon_{cds}(t', t_s')$ = drying shrinkage strain.

The autogenous shrinkage strain is calculated using Equation 2.100.

$$\varepsilon_{cas}(t') = \varepsilon_{cas0}(f_{cm})\beta_{as}(t') \qquad \text{Equation 2.100}$$

With,

$\varepsilon_{cas0}(f_{cm})$ = the notional autogenous shrinkage coefficient defined as:

$$\varepsilon_{cas0}(f_{cm}) = -\alpha_{as}\left(\frac{f_{cm}/10}{6 + f_{cm}/10}\right)^{2.5} \times 10^{-6} \qquad \text{Equation 2.101}$$

Where,

α_{as} = coefficient depending on cement class shown in Table 2-3

Table 2-3: Shrinkage coefficients based on cement type (fib 2012)

Cement Class	α_{as}	α_{ds1}	α_{ds2}
32.5 N	800	3	0.013
32.5 R, 42.5 N	700	4	0.012
42.5 R, 52.5 N, 52.5 R	600	6	0.012

In accordance with the CEB MC 2010, for concrete mixture proportions with normal-hardening cements (i.e. Type I) and rapid-hardening cements (i.e. Type III,) the strength class is defined as “N” and “R”, respectively. The numerical value associated with each class is based on the cement strength class (CEB 2010).

$\beta_{as}(t')$ = the time development function of autogenous shrinkage defined as:

$$\beta_{as}(t) = 1 - \exp\left(-0.2\sqrt{t'}\right) \qquad \text{Equation 2.102}$$

The drying shrinkage strain is calculated using Equation 2.103.

$$\varepsilon_{cds}(t', t_s') = \varepsilon_{cds0}(f_{cm})\beta_{RH}(RH)\beta_{ds}(t' - t_s') \qquad \text{Equation 2.103}$$

With,

$\varepsilon_{cds0}(f_{cm})$ = the notional drying shrinkage coefficient defined as:

$$\varepsilon_{cds0}(f_{cm}) = [(220 + 110\alpha_{ds1}) \exp(-\alpha_{ds2} f_{cm})] \times 10^{-6} \quad \text{Equation 2.104}$$

Where,

α_{ds1} and α_{ds2} = coefficient depending on cement type listed in Table 2-3

$\beta_{RH}(RH)$ = the function to account for relative humidity defined as:

$$\beta_{RH} = \begin{cases} -1.55[1 - (RH/100)^3] & \text{for } 40 \leq RH < 99\% \beta_{s1} \\ 0.25 & \text{for } RH \geq 99\% \beta_{s1} \end{cases} \quad \text{Equation 2.105}$$

Where,

β_{s1} = the coefficient accounting for self-desiccation in high-performance concrete defined as:

$$\beta_{s1} = (\frac{35}{f_{cm}})^{0.1} \leq 1.0 \quad \text{Equation 2.106}$$

2.5 PREVIOUS STUDIES RELATED TO CREEP AND SHRINKAGE OF CSC IN SEGMENTAL BRIDGE APPLICATIONS

Many research projects have been conducted have been conducted on volumetric changes of concrete at Auburn University for both conventional slump concrete (CSC) and self-consolidating concrete (SCC). This section outlines two of the most recent studies of creep and shrinkage conducted at Auburn University by Schindler et al. (2007) and Richey (2018). In addition, a study by Kamatchi et al. (2014), on long-term prestress losses and camber of box girder bridges resulting from creep and shrinkage, is reviewed for better a better understanding of the effects of creep and shrinkage in box girder bridges. Lastly a study of volumetric changes in the Chevire Bridge in France by Raphael et al. (2018) is analyzed.

2.5.1 Overview of Previous Studies Conducted at Auburn University

Schindler et al. (2017) and Richey (2018) both conducted research on volumetric changes in concretes typically used Alabama bridges, and tested similar concretes to accurately predict creep and shrinkage using prescribed models. Schindler et al. (2017) focused on laboratory testing to compare compliance values of CSC and SCC used in prestressed applications in Alabama. Richey

(2018) conducted research to determine the effects of different aggregate types on creep and shrinkage in concrete with mixtures proportions used in the Birmingham I-59/I-20 segmental bridge.

2.5.1.1 Evaluation of Volumetric Changes by Schindler et al. (2017)

This research study comprised of five concrete mixtures, one CSC mixture and four SCC mixtures that were mixed and were subjected to creep and drying shrinkage testing under controlled laboratory conditions at five different loading ages: 18 hours, 2 days, 7 days, 28 days, and 90 days. Initially the compliance values for the SCC mixtures were compared to the CSC mixture to determine behavioral differences. Upon data collection, measured compliance values for all of the concrete mixtures were compared to predicted values using six prediction models including: ACI 209, CEB 2010, GL 2000, B3, AASHTO LRFD, and NCHRP 628. Only comparison results from the ACI 209 and CEB 2010 Models are shown due to these models being the most accurate out of the six that were evaluated.

The CSC mixture was composed of only Type III cement and no SCMs. Each of the four SCC mixtures had varied amounts of Class C fly ash and Grade 120 slag cement. The four SCC mixtures were labeled as follows: high-strength with fly ash (SCC-HS-FA), moderate-strength SCC with fly ash (SCC-MS-FA), high-strength with slag cement (SCC-HS-SL), and moderate-strength with slag cement (SCC-MS-SL). The only other differences between mixture proportions was in the water-cement ratio. All loading ages were exposed to moist-curing conditions with the exception of the 18-hour loading age, which was subjected to an accelerated curing regime to replicated techniques used in prestressed plants.

For each of the mixtures, Schindler et al. (2017) conclude that the ACI 209 predicted compliance values the closest to the line of equality for the moist-cured specimens. Figure 2-8 provides a comparison of measured to predicted compliance values using the ACI 209 Model. For concrete with similar mixture proportions and curing regime ACI 209 predicts compliance values more accurately for the moderate-strength SCC mixtures rather than the high-strength mixtures (Schindler et al. 2017). From Figure 2-13, for the same curing method and similar strength, ACI 209 predicts more accurately for mixtures made with fly ash as compared to the mixtures made with slag cement (Schindler et al. 2017).

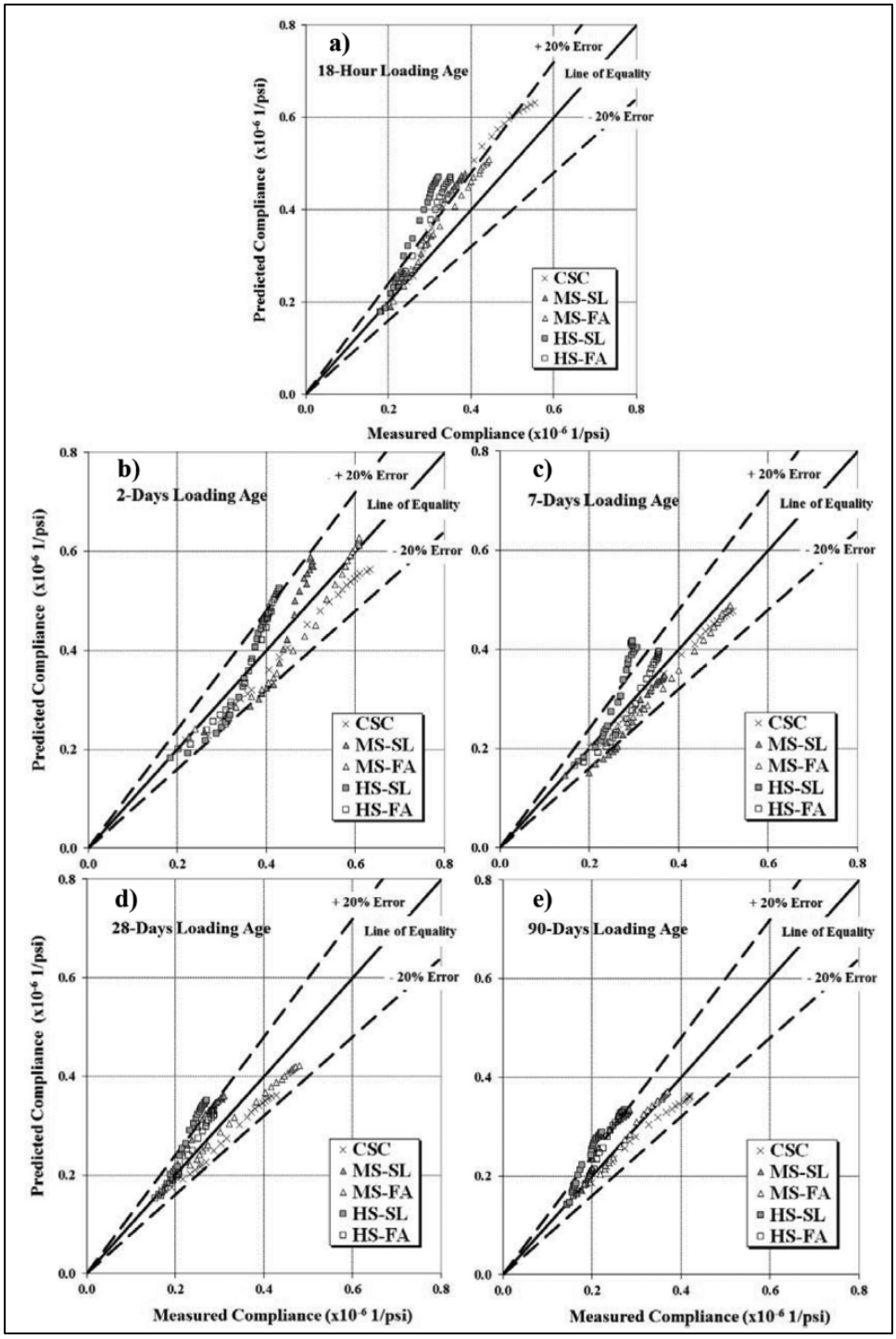

Figure 2-13: ACI 209 Predicted compliance values for all loading ages (Schindler et al. 2017)

As compared to predictions from the ACI 209 Model, Schindler et al. (2017) conclude that the CEB MC 2010 is much better at predicting compliance of concretes loaded at later ages. Results from compliance predictions using the CEB MC 2010 are shown in Figure 2-14, where

the compliance values for accelerated-cured CSC were not predicted accurately. According to Schindler et al. (2017), it can be concluded that for moist-cured specimens, CEB MC 2010 is more accurate in predicting the compliance of fly ash mixtures than it is for slag cement mixtures which can be seen in Figure 2-14.

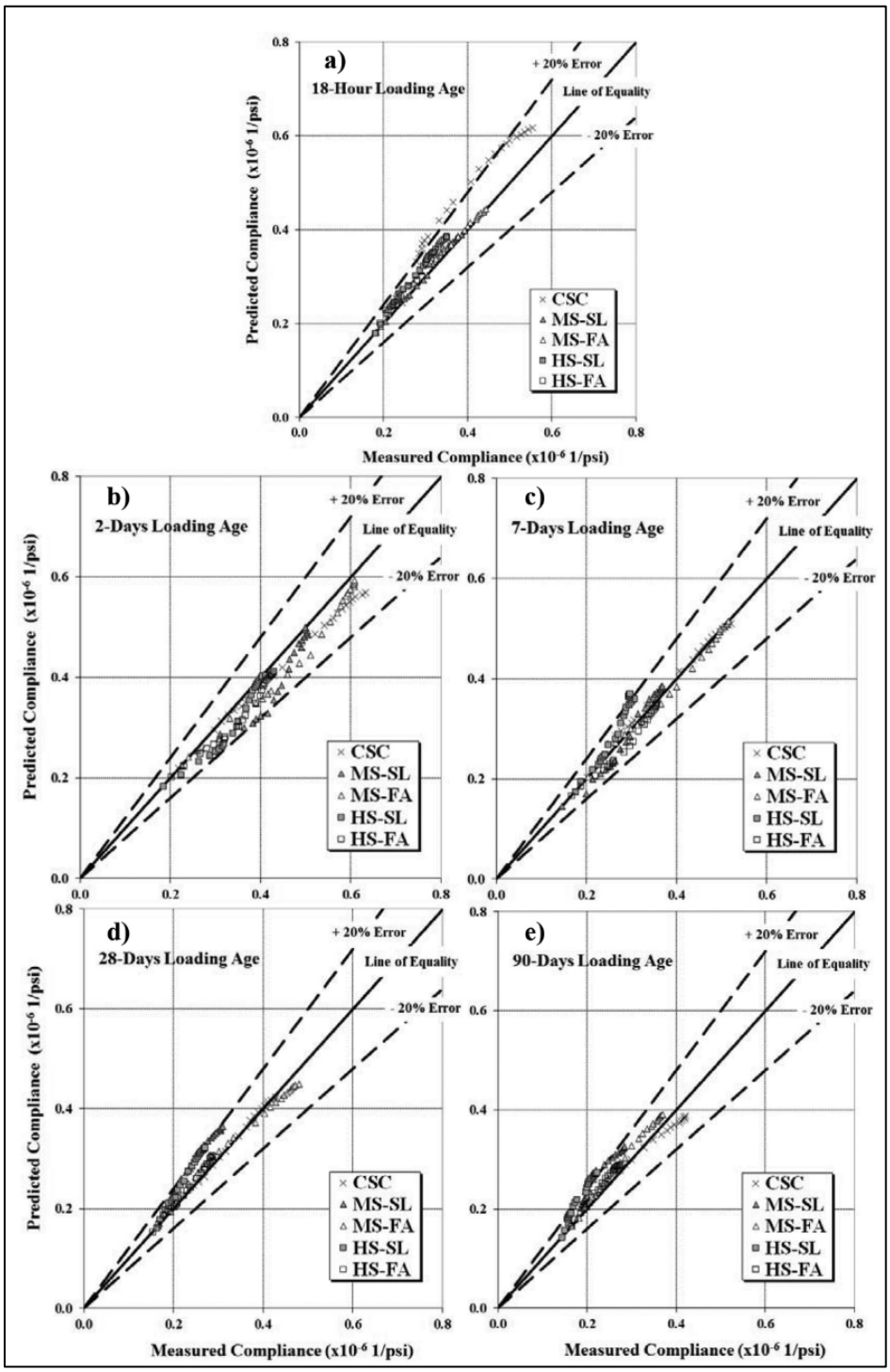

Figure 2-14: CEB MC 2010 predicted compliance for all loading ages (Schindler et al. 2017)

2.5.1.2 Effect of Aggregate Type on Volumetric Changes by Richey (2018)

In a research effort to study creep in shrinkage in the Birmingham I-59/I-20 segmental bridge, Richey (2018) performed mixing and testing in standard laboratory conditions on concretes with two different coarse aggregate types: limestone and quartzite. The goal of the research effort was to determine if changing aggregate type had any significant effect on volumetric changes occurring in concrete subjected to load for Alabama sourced materials. All mixture proportions were kept consistent for both mixtures except for the aggregate type, and an accelerated-curing regime was implemented to represent the curing methods used in segmental bridge casting.

Five models were used to predict both compliance and shrinkage including: ACI 209, AASHTO LRFD, CEB MC 2010, GL 2000, and B3 (Richey 2018). For all loading ages, the mixtures containing quartzite aggregate exhibited a higher compressive strength; however, the limestone mixtures exhibited higher modulus of elasticity (Richey 2018). The measured compliance values for the quartzite and limestone test specimens are presented in Figure 2-15 and Figure 2-16, respectively.

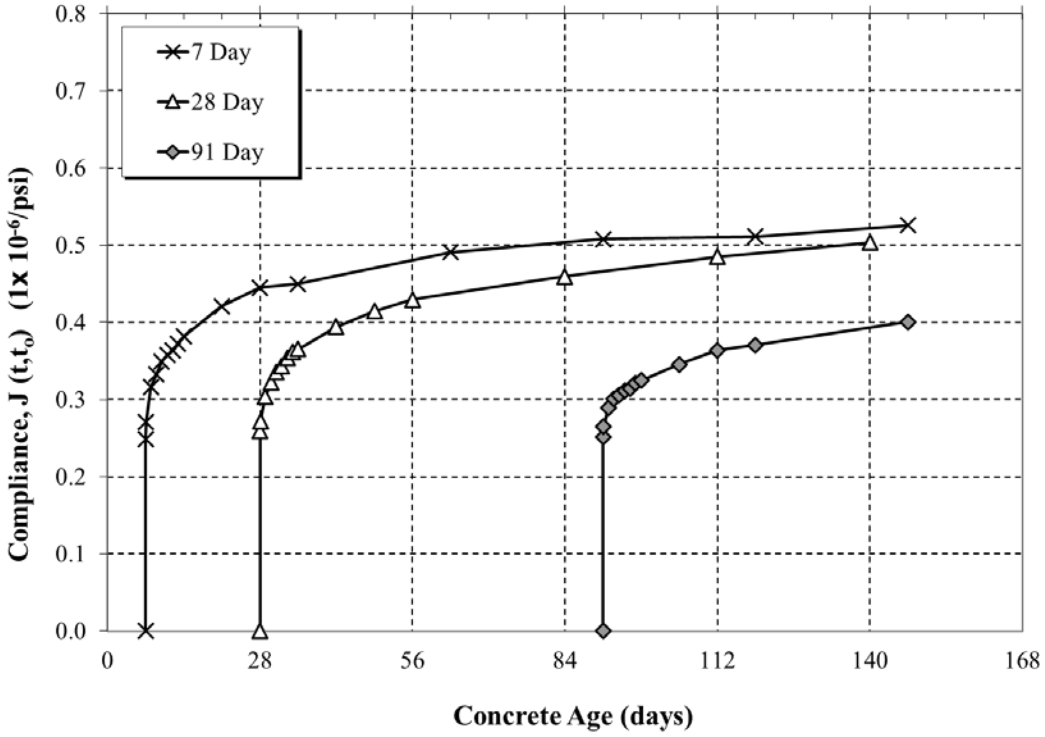

Figure 2-15: Compliance values for all loading ages of quartzite test specimens (Richey 2018)

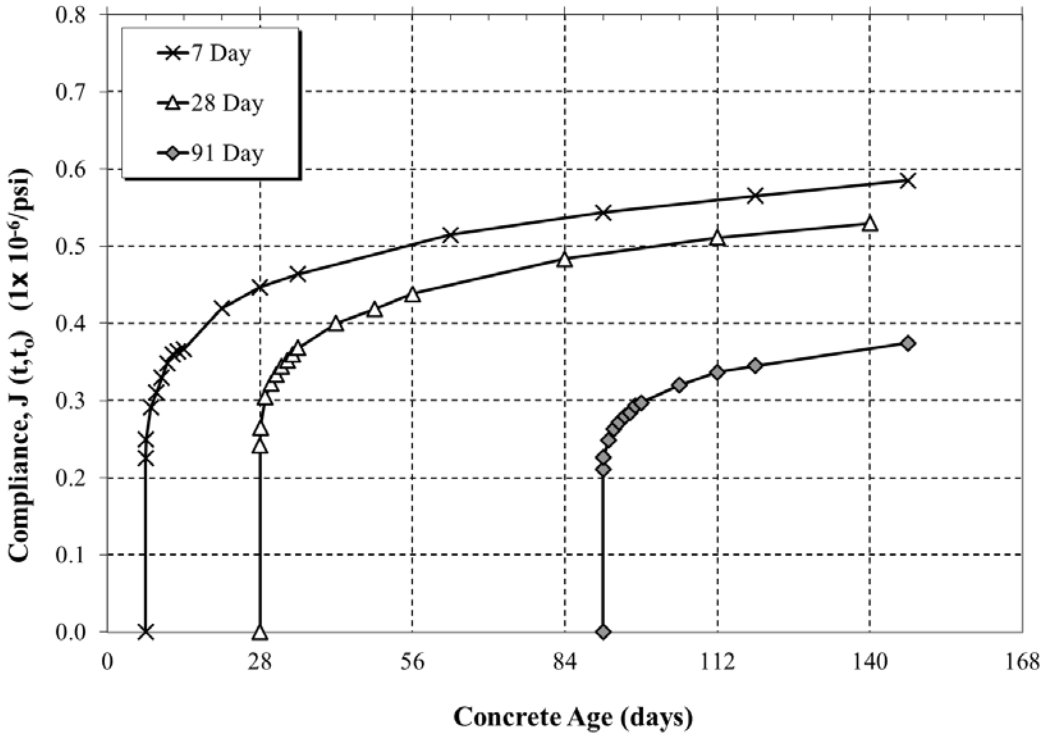

Figure 2-16: Compliance values for all loading ages of limestone test specimens (Richey 2018)

Richey (2018) concluded that the measured compliance values for each loading age were very similar for the two aggregate types. It was also concluded that the drying shrinkage strains for were very similar as well for both the limestone and quartzite mixtures (Richey 2018). In addition to the measured values, Richey (2018) determined that the ACI 209 and the CEB MC 2010 Model preformed the best when predicting creep and compliance. The measured versus predicted creep strains for the limestone and quartzite aggregate types with the ACI 209 Model are presented in Figure 2-17 and Figure 2-18, respectively. It can be seen that the limestone mixtures are slightly under predicted using the ACI 209 Model. In concluding, Richey (2018) found that there was no significant impact on switching between quartzite and limestone coarse aggregates when it comes to creep and drying shrinkage; however, Richey (2018) recommended that testing should continue to further justify this trend.

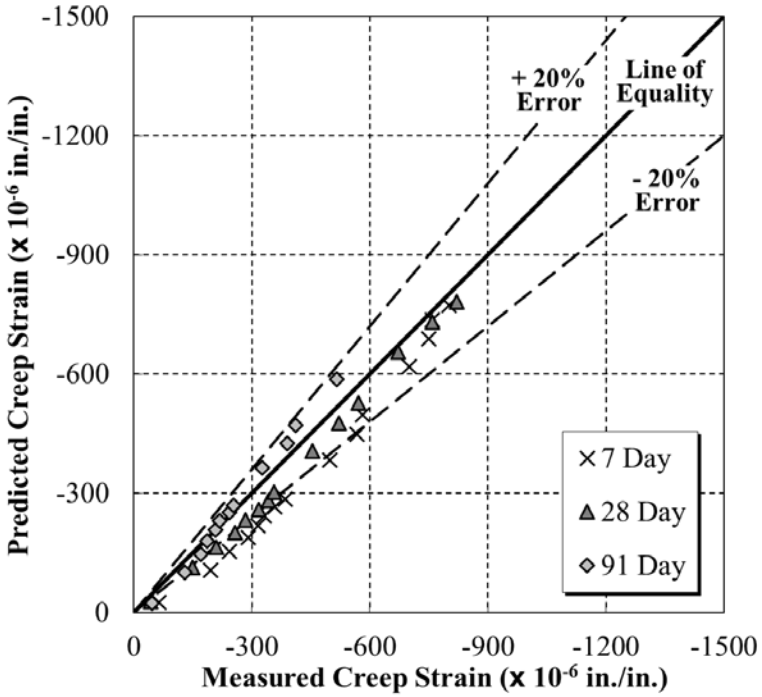

Figure 2-17: Measured versus predicted creep strains for quartzite mixtures using the ACI 209 Model (Richey 2018)

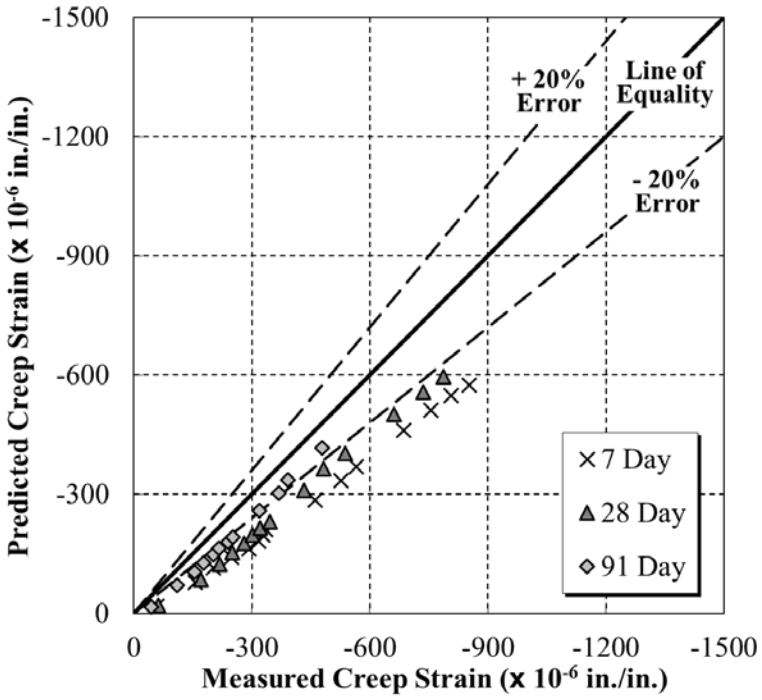

Figure 2-18: Measured versus predicted creep strains for limestone mixtures using the ACI 209 Model (Richey 2018)

2.5.2 Long-Term Prestress Losses of Box-Girder Bridges (Kamatchi et al. 2014)

According to Kamatchi et al. (2014), the evaluation of long-term prestress losses and camber, taking into account the effect of creep and shrinkage are essential for the sustainability of prestressed concrete bridges. In the study, an effort was made to compare field collected data on prestress losses and camber with respective estimations from creep and shrinkage models from ACI 209, CEB MC 1990, GL2000, and B3 (Kamatchi et al. 2014).

2.5.2.1 Field Measurements

The bridge used in this study, as shown in Figure 2-19, is an existing cast-in-place box-girder bridge span which is noted as the central span of a typical flyover bridge with an effective span length of 131 feet, concrete grade M45, prestressed from both ends with 21 cables of 19T13 (Kamatchi et al. 2014). Surface-mounted, strain gauges were installed at several key locations throughout the twin-cell box girder, as shown in Figure 2-20, with the goal of measuring long-term prestressed loses (Kamatchi et al. 2014).

Figure 2-19: Bridge used to analyze long-term prestress losses (Kamatchi et al. 2014)

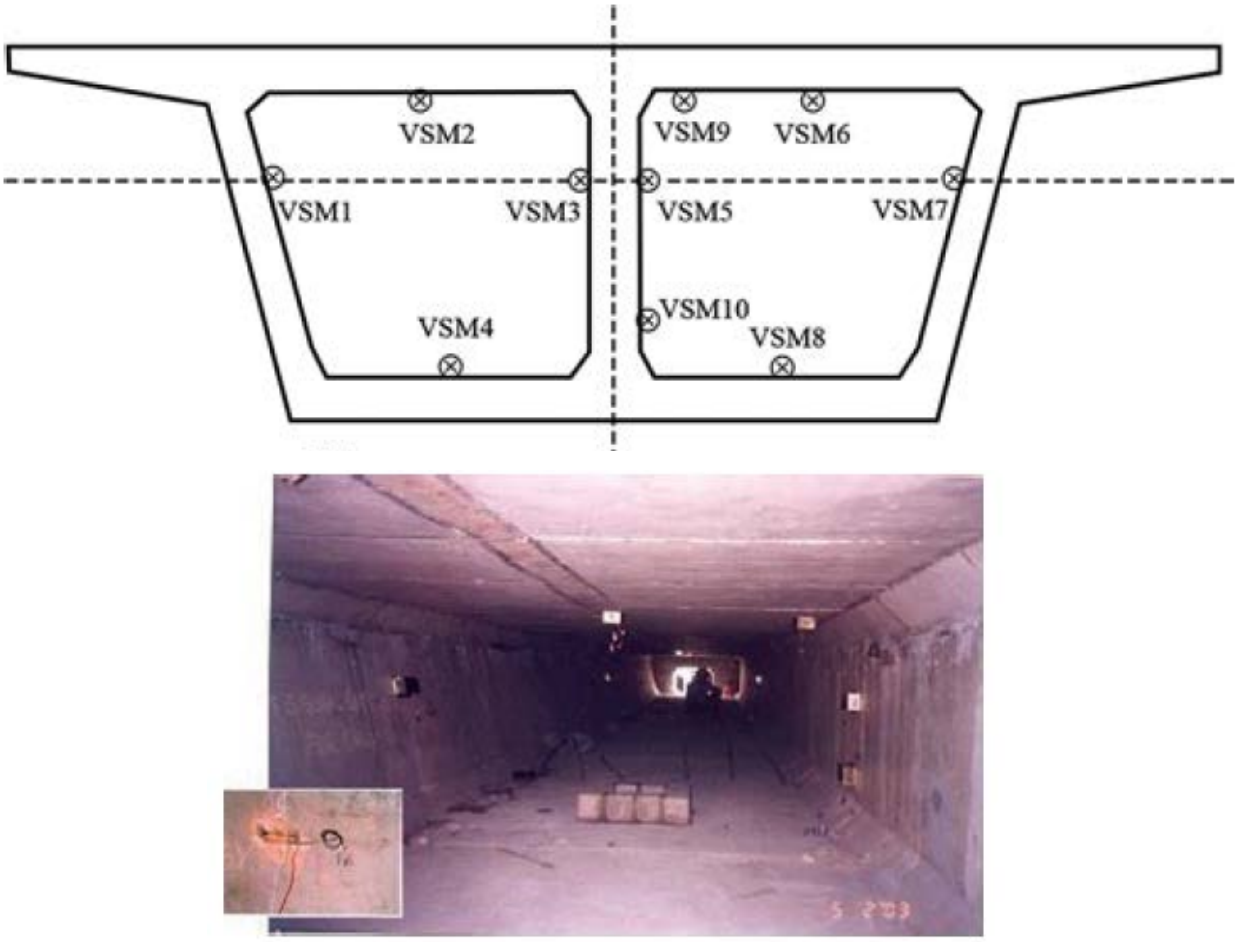

Figure 2-20: Locations of surface-mounted strain gauges (Kamatchi et al. 2014)

2.5.2.2 Results from study

The total long-term prestress loss due to creep and shrinkage compared to measured losses are shown in Figure 2-21. The comparison of long-term midspan camber with predictions from described models are shown in Figure 2-22. From the average values of percentage differences with respect to field measurements for the first five years after bridge construction, the ACI 209 and CEB MC 90 Model seem to underestimate the prestress losses by 27 percent and 11.5 percent and camber by 17.3 percent and 2.45 percent, respectively (Kamatchi et al. 2014). The GL 2000 and B3 models overestimate the prestress loses by 20.2 percent and 3.37 percent and camber by 33 percent and 13 percent, respectively (Kamatchi et al. 2014). Kamatchi et al. (2014) state however that the B3 and CEM MC 90 Models provide the better representation of long-term prestress losses due to creep and shrinkage. It is recommended that B3 Model is used for long-term prestressed loses and the CEB MC 90 Model for long-term camber (Kamatchi et al. 2014).

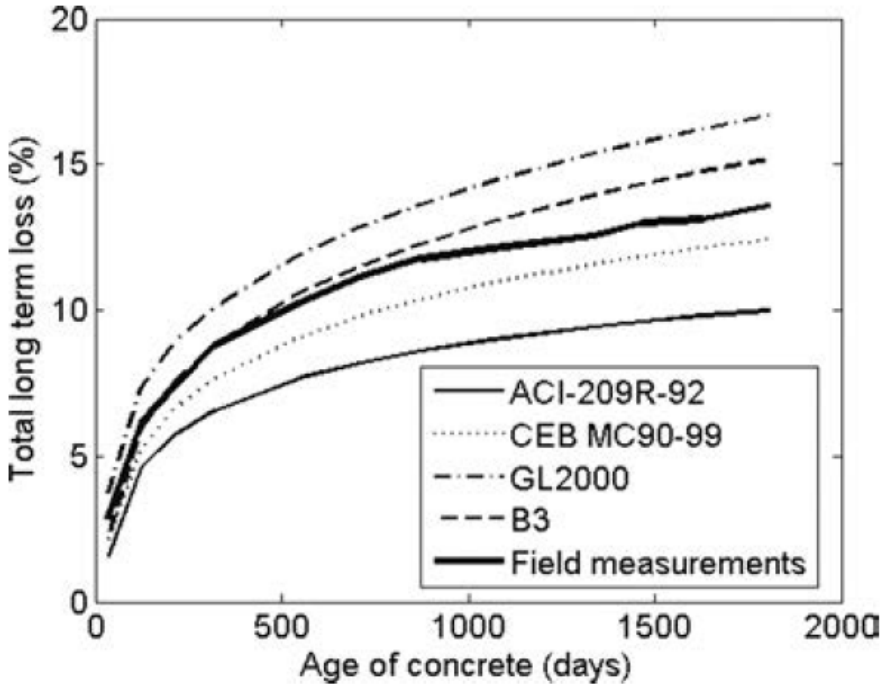

Figure 2-21: Comparison of long-term prestress loss in field measurements and predicted loses from listed models (Kamatchi et al. 2014)

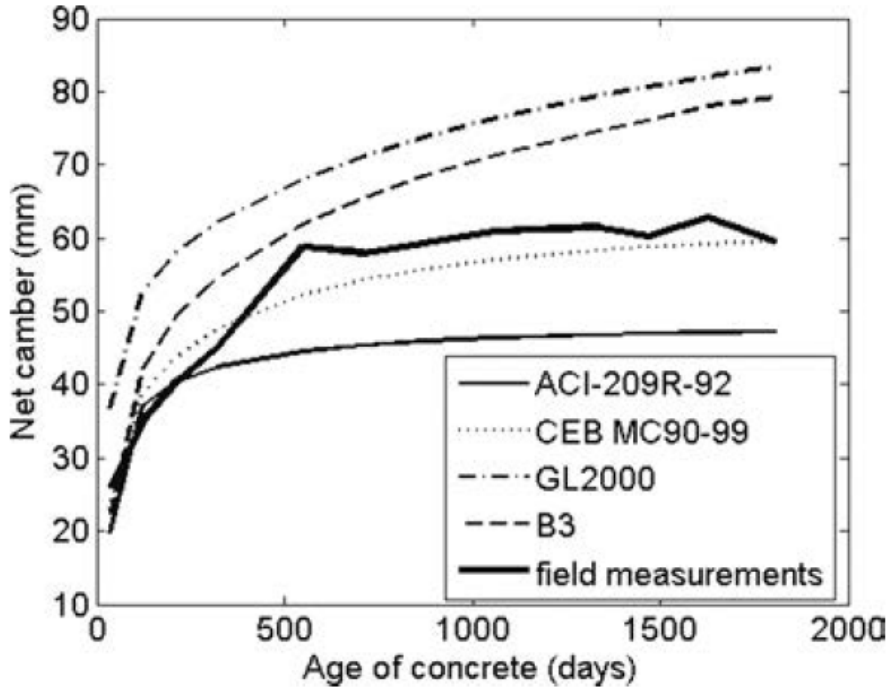

Figure 2-22: Comparison of long-term camber in field measurements and predicted camber from listed models (Kamatchi et al. 2014)

2.5.3 Creep Study of Chevire Bridge by Raphael et al. (2018)

The Chevire Bridge, located in France and shown in Figure 2-23, is a segmental bridge that is 1563 meters long composed of 22 spans with the central span being steel girders supported on two prestressed concrete cantilevers with a length of 242 meters and subsequent spans of shorter length away from midspan (Raphael et al. 2018). The entire superstructure of the bridge is constructed with segmental concrete units except for the central steel span.

Figure 2-23: Chevire Bridge located in France (Raphael et al. 2018)

The vertical displacement of the Chevire Bridge free-end cantilevers has been measured and monitored since 1994. The measured displacement was 3.94 in. (10 cm) nearly 4 years post completion and 7.17 in. (18.2 cm) in the year 2000, as compared to the predicted vertical displacement of 1.19 in. (3.01 cm) and 2.41 in. (6.13 cm) by the BPEL code (used in original bridge design) and Eurocode 2, respectively (Raphael et al. 2018).

2.5.3.1 Analysis of Results

Initially a database was created using data that had been collected by several research laboratories and institutions, which included the results from over 432 creep tests on specimens of different shapes and dimensions under various environmental and load conditions (Raphael et al. 2018). The database was used for comparison of predicted compliance values by the Eurocode 2 and BPEL code. Results of the predictions are plotted using residuals as shown in Figure 2-24 and Figure 2-25. It can be seen that the majority of data fall in the positive range for both models equating to the models under predicting compliance, where in some cases after further analysis long term-compliance is underestimated by 300 percent (Raphael et al. 2018).

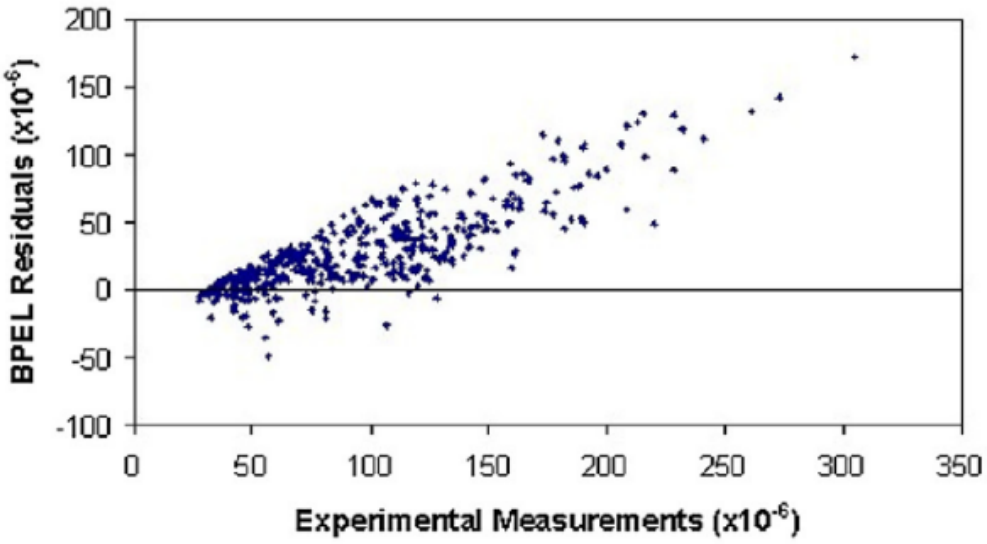

Figure 2-24: Compliance residuals (MPa^{-1}) for BPEL model (Raphael et al. 2018)

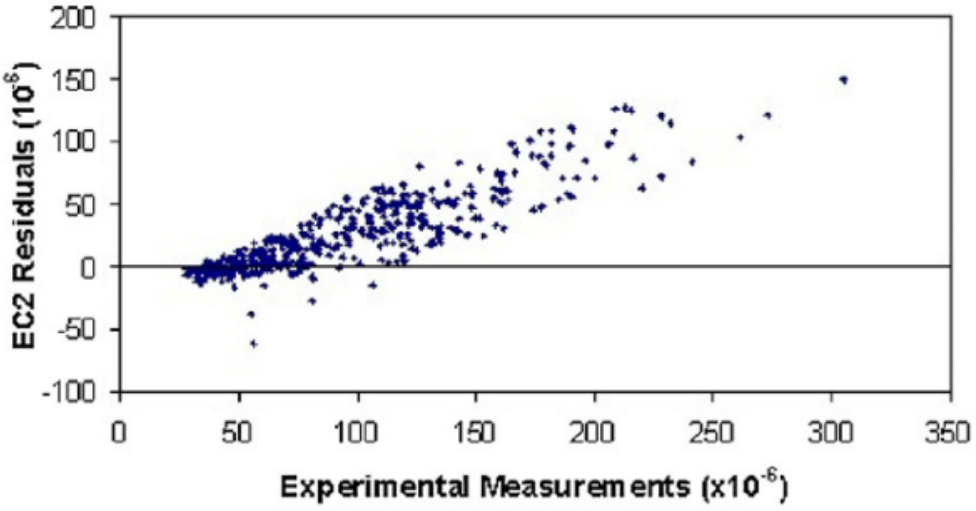

Figure 2-25: Compliance residuals (MPa^{-1}) for Eurocode 2 (Raphael et al. 2018)

Raphael et al. (2018) also created a mechanical-reliability model to evaluate the sensitivity of measures that effect the creep of concrete, where the Chevire Bridge was modeled and creep deformations were determined for random input variables. The software developed calculates the sensitivity measures and assesses the probability of failure based on long-term deflection limits. In concluding, Raphael et al. (2018) concluded that the Eurocode 2 was best used in a stable manner to account for creep deformations as compared to the BPEL code.

CHAPTER 3: METHODOLOGY

3.1 INTRODUCTION

The primary objective of this research effort is to accurately predict the creep and shrinkage of the concrete in the I-59/I-20 segmental bridge in Birmingham, Alabama. This chapter details the experimental plan and procedures that were used to assess the creep and shrinkage behavior of concrete used in the project.

3.2 EXPERIMENTAL PLAN

The Birmingham I-59/I-20 segmental bridge project was under construction for the duration of this research project. Instead of mixing concrete in a laboratory environment, samples were collected from concrete batched on the jobsite, cured alongside segments, and transported to the laboratory for testing. The experimental plan for this research project consists of two main stages: field specimen collection and laboratory testing. In the first stage of experimental work, specimens were collected while the segments were cast at the jobsite. Samples were returned to Auburn University for the second stage of experimental work. The second stage of experimental work included testing the specimens for hardened properties as well as creep and shrinkage in accordance with relevant ASTM standards. All testing for the laboratory stage occurred in controlled conditions. Upon data collection in the second stage of the project, modeling of the creep and shrinkage results commenced.

3.2.1 Specimen Types

For the purpose of creep testing ASTM C512 (2015) prescribes the procedure to follow for creep testing. As noted in Section 2.2, it was important to be able to monitor the total strain and shrinkage strain to determine creep. Specimens were cast in the form of 6 in. × 12 in. cylinders. Upon removing cylinders from the molds, it was important to grind the ends of the cylinders to create a smooth surface. In addition to the cylindrical specimens it was determined to be important to also monitor shrinkage using AASHTO T160 (2017), which requires standard 3 in. × 3 in. × 11.25 in.

rectangular prisms for shrinkage testing. In testing, all prismatic specimens were stored on wire shelves to prevent any induced stress while allowing full air contact with the surface.

3.2.2 Loading Ages

Due to the fact that creep has varying magnitudes with age of loading as discussed, it was determined that creep would be tested at four loading ages. In conjunction with previous research and considering the accelerated construction schedule of the Birmingham I-59/I-20 segmental bridge, it was decided that creep testing would be performed with loading ages of 7 days, 28 days, 91 days and 182 days. Shrinkage testing began 2 days after each visit to the project site for air-cured concrete prismatic specimens and 7 days for moist-cured concrete prismatic specimens.

3.2.3 Sample Sizing

Three additional cylinders for each loading age were required to determine the strength and modulus of elasticity of the concrete prior to creep testing. For each field visit three companion cylinders were cast to monitor shrinkage of the creep specimens. An additional cylinder was cast on site and fitted with a temperature sensor to monitor the internal temperature of concrete as it cured to allow the equivalent-age maturity of the samples to be determined. Six concrete prisms were cast with the intention of moist-curing three prisms and air-curing three. A summary of the total amount of samples required for each field visit can be seen in Table 3-1.

Table 3-1: Total amount of samples required for each field visit

<table>
<tr><th rowspan="2">Curing Method</th><th rowspan="2">Loading Age</th><th colspan="4">6 in. × 12 in. Cylinders</th><th rowspan="2">Drying Shrinkage Prisms</th></tr>
<tr><th>Creep Specimen</th><th>Shrinkage Specimen</th><th>Strength/ Elastic Modulus Specimens</th><th>Temperature Cylinder</th></tr>
<tr><td rowspan="4">Accelerated Curing</td><td>7 Days</td><td>2</td><td rowspan="4">3</td><td>3</td><td rowspan="4">1</td><td rowspan="4">6</td></tr>
<tr><td>28 Days</td><td>2</td><td>3</td></tr>
<tr><td>91 Days</td><td>2</td><td>3</td></tr>
<tr><td>182 Days</td><td>2</td><td>3</td></tr>
<tr><td colspan="2">Column Totals</td><td>8</td><td>3</td><td>12</td><td>1</td><td>6</td></tr>
<tr><td colspan="2">Specimen Total</td><td colspan="4">24</td><td>6</td></tr>
</table>

For the purpose of the research it was determined that the best strategy for monitoring creep and shrinkage would be to collect samples throughout the duration of concrete casting of the segmental bridge project. A summary can be seen in Figure 3-1 for when samples were collected in the field in addition to the segment casting dates (courtesy of Mr. Eric Johnson, Corven Engineering). ALDOT approved mixture portions changed four times throughout the duration of the project and these are also displayed on Figure 3-1. It is important to note the non-linearity of the casting progression where the segments produced per day increase from one per day initially to eight per day at the peak of the casting schedule.

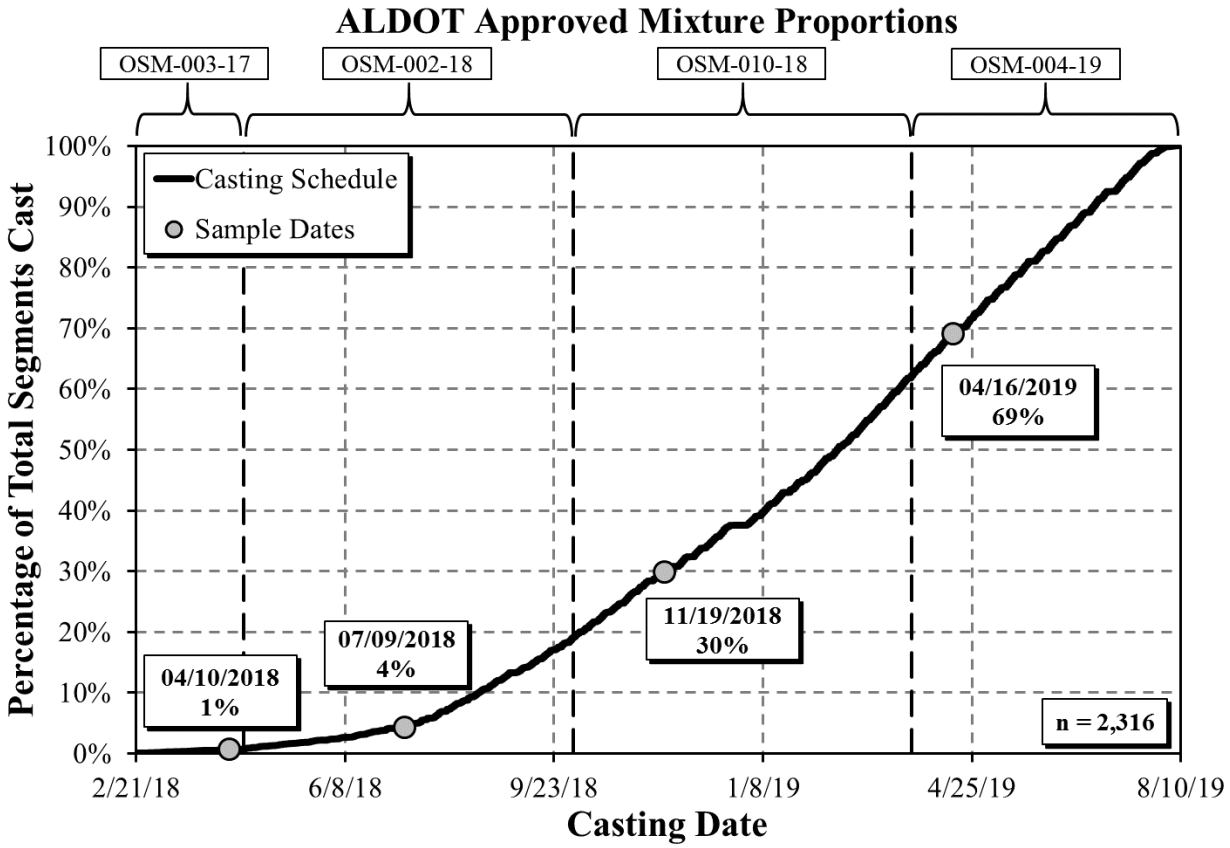

Figure 3-1: Segmental casting progression in conjuction with site visits and ALDOT approved mixture proportions

3.3 MIXTURE PROPORTIONS

ALDOT had several mixture design requirements, including strength, workability, and total air content. Per design specifications for the Birmingham I-29/I-20 segmental bridge, all concrete was required to adhere to the following compressive strength requirements: 2,500 psi prior to the removal of formwork, 4,000 psi prior to transverse post-tensioning, and a specified 28-day compressive strength of 6,500 psi. Concrete slump was required to range from 3 in. to 9 in. for all concrete cast in the Birmingham I-59/I-20 segmental bridge. All fresh concrete was required to have a total air content that ranges from 3 percent to 6 percent.

All specimens were to be prepared on-site using ALDOT approved mixture proportions. Concrete was collected from a ready-mixed concrete truck that is transported to the project site from a batch plant in close proximity to the casting beds. Concrete was collected from the trucks delivering concrete to the casting yard using wheelbarrows. As per ASTM protocol, it was intentional for the concrete to be collected from the middle of the truck to ensure thoroughly mixed concrete for testing. Over the course of the project, the Contractor made changes to the concrete proportions to increase the early-age and 28-day compressive strength of the concrete. Mixture proportions were also adjusted to accommodate changes in chemical admixture suppliers and cement due to changes in the availability of Type III cement during the project. Four approved ALDOT concrete mixture proportions were considered throughout the duration of the sample collection period. Each approved mixture proportion is shown in Table 3-2 with the sampling dates shown for each corresponding mixture proportion.

Table 3-2: ALDOT approved mixture proportions for each sampling date listed

Material (lb/yd^3)	**ALDOT Approved Mixture Proportions**			
	OSM-003-17	**OSM-002-18**	**OSM-010-18**	**OSM-004-19**
	04/10/2018	**07/09/2018**	**11/19/2018**	**04/16/2019**
Portland Cement	Type I/II	Type I/II	Type III	Type I/II
	682	682	782	800
Water	264	264	283	275
Class F Fly Ash	170	170	138	---
Coarse Aggregate* (#67 Quartzite)	1800	1800	1750	1750
Fine Aggregate* (#100 Concrete Sand)	878	978	955	1088
Chemical Admixtures (oz./yd^3)	BASF	W.R. Grace & Company		
Air Entrainer	MasterAir AE 200	Daravair 1000		
	2	3	4.6	0.6
Type A	MasterPozzolith 322	Zyla 610		
	30.1	51.4	---	---
Type F	MasterPolyheed 1025	ADVA 140M		
	68	---	82.8	112
Type D	MasterSet DELVO	Recover		
	34.1	34.3	36.8	16
Type C	MasterSet AC 534	Daraset 400		
	102.2	102.2	110.4	112

Note: *Aggregates in saturated-surface dry state.

3.4 TEST SPECIMEN IDENTIFICATION SYSTEM

Due to the volume of test specimens collected throughout the duration of this research effort, an identification system was necessary to keep samples separated. All concrete cylinders and prisms were labeled with respective casting dates as well as a few additional notes. The creep testing cylinders and shrinkage prisms were labeled according to Figure 3-2 and Figure 3-3, respectively.

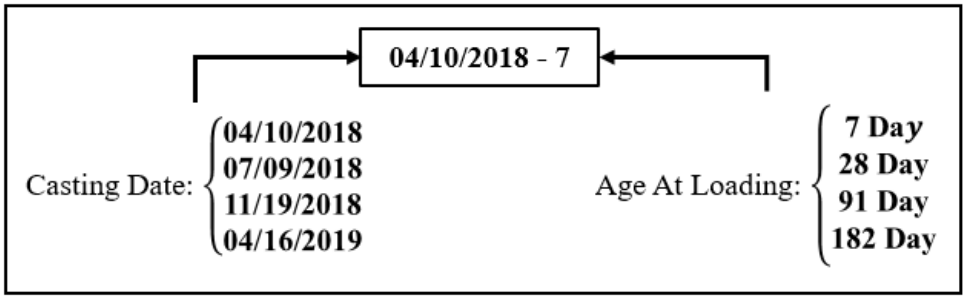

Figure 3-2: Identification system used for creep testing cylinders

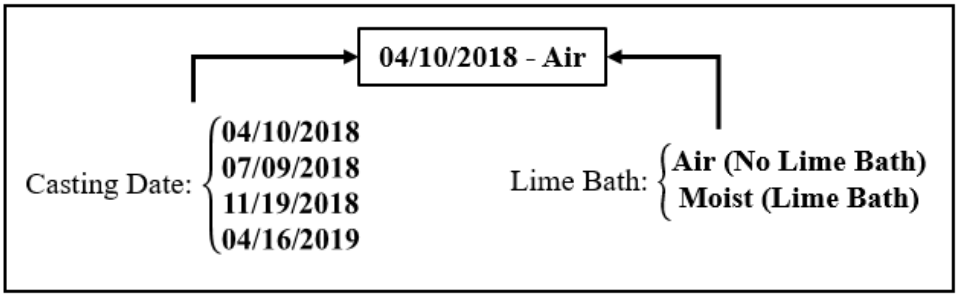

Figure 3-3: Identification system used for shrinkage prisms

3.5 TEST METHODS

This section outlines the various test methods used in the experiment. All testing methods were performed in the Concrete Materials Laboratory at Auburn University unless otherwise noted. All details related to casting, curing and testing the concrete specimens are explained in subsequent sections.

3.5.1 Methods for Testing Fresh Concrete Properties

All concrete collected at the jobsite was tested initially for slump, total air content, unit weight, and temperature. These tests were performed by the contractor to ensure the ALDOT specifications were met for the concrete delivered to the site.

3.5.1.1 Slump

The slump of a concrete mixture is a reference to how workable the concrete will be during placement. For all concrete collected in the field the contractor used AASHTO T119 (2018) to test for slump. ALDOT required the slump of all concrete placed into the bridge segments to range from 3 in. to 9 in. If proper slump was not met the, concrete producer may add water up to the maximum allowable by the ALDOT specification. If again concrete was not able to reach required slump, the concrete was discarded.

3.5.1.2 Air Content and Unit Weight

Air content and unit weight was determined for each concrete sample by the contractor at the jobsite. All testing was completed in accordance with AASHTO T121 (2019). All concrete delivered to the site was required to have a total air content ranging from 3 percent to 6 percent. If the concrete did not meet the required air content, the concrete was rejected and disposed of.

3.5.1.3 Concrete Temperature

Fresh concrete temperature was taken for each sampling of concrete. Testing of temperature occurred in accordance with AASHTO T309 (2015). The fresh concrete was required to have a minimum temperature of 50°F and was not to exceed a temperature 95°F according to ALDOT 501 (2018). If the fresh concrete temperature did not meet requirements, the concrete was rejected.

3.5.2 Collecting Test Specimens

Specimens were collected on the I-59/I-20 segmental bridge casting yard in Birmingham, Alabama, which was in parallel with the casting of bridge segments. All cylindrical and prismatic concrete specimens were prepared on the jobsite using the requirements prescribed by AASHTO T23 (2018) and AASHTO T160 (2017), respectively. As shown in Table 3-1, for each sampling date 24 cylindrical (6 in. × 12 in.) specimens and six prismatic specimens (3 in. × 3 in. × 11.25 in.) were prepared. One of the cylinders on each collection date was fitted with a temperature sensor that was embedded in the concrete to record curing temperature for the first 24 to 36 hours after being prepared. Cylindrical and prismatic specimens being prepared at time of sample collection can be seen in Figure 3-4 and Figure 3-5, respecively.

Figure 3-4: Concrete cylinders being prepared at the jobsite

Figure 3-5: Concrete prisms being prepared at the jobsite

3.5.3 Curing and Storing Test Specimens

Two types of curing were used for test specimens collected for the research project. Specimens were cured on-site as well as in the laboratory at Auburn University. Curing of the concrete specimens occurred following the requirements of AASHTO T23 (2018).

3.5.3.1 Field Curing

It was important for the purpose of this research project that the concrete specimens be cured using the same process as the bridge segments. Concrete cylinders were sealed with tight-fitting, plastic caps to prevent moisture loss during curing. All concrete prisms were covered with moistened burlap and wrapped in plastic. The contractor allowed the specimens to be stored inside the corresponding bridge segment to mimic the same curing practice. As the contractor completed finishing of the segment, the specimens were placed carefully into the formwork as shown in Figure 3-6.

Figure 3-6: Specimens being placed in formwork for on-site curing

After placing concrete specimens inside of the formwork the entire form was encapsulated using blankets to allow the contractor to provide heat curing, if needed. As curing began, heat was not added to the system until initial set of the concrete occurred. Upon initial set, heaters were

placed inside of the blankets to allow for accelerated curing, if deemed necessary by the contractor. Temperatures inside the formwork were not to exceed 150°F. The rate of heating was limited to not exceed 40°F per hour for the duration of initial curing. An example of the temperature profile for the initial curing of the concrete specimens that was recorded for the April 16, 2019 sampling date is presented in Figure 3-7. Note that in this example the enclosure temperature never exceeded 115°F and the internal concrete temperature never exceeded 130°F.

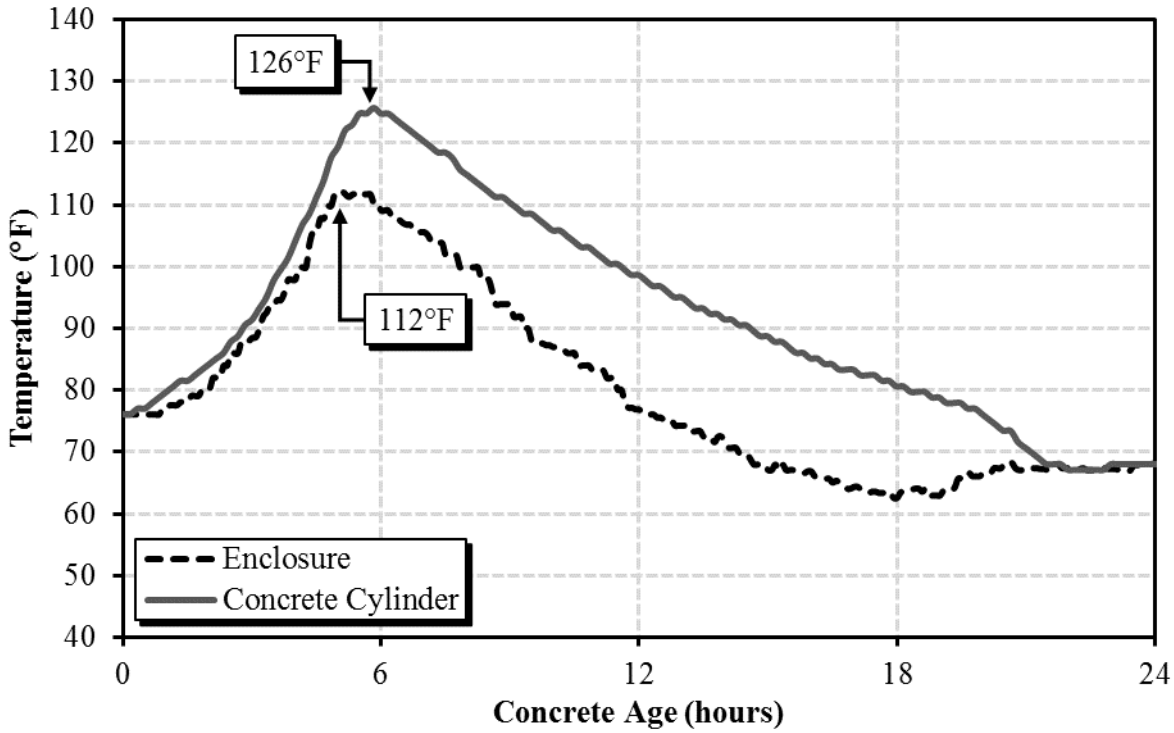

Figure 3-7: Example of concrete and enclosure temperatures from the April 16, 2019 sampling date

3.5.3.2 Laboratory Curing

Upon completing initial curing on the jobsite, the concrete specimens were transported to the laboratory at Auburn University. Since no additional curing was provided for the bridge segments, the concrete cylinders were demolded and placed into the creep-testing room. For each visit three prisms were stored on wire shelves and instantaneously exposed to drying shrinkage. Three of the concrete prisms were additionally cured in a lime-saturated water tank for a duration of seven days before being exposed to drying. ASTM C512 (2015) requires that the environment of the creep-testing facility must be kept between temperatures of 73.5°F ± 1.5°F and a relative humidity of 50% ± 4% for the duration of testing. The creep-testing room was monitored for temperature and

relative humidity throughout the project duration. The creep-testing room was equipped with a data logger to record temperature and relative humidity for the duration of the project.

3.5.4 Methods for Testing Hardened Concrete

The following sections outline procedures used for testing compressive strength, modulus of elasticity, drying shrinkage, and creep.

3.5.4.1 Compressive Strength

In order for creep testing to occur at a stress level of 40 percent of the concrete strength, the compressive strength of the concrete must be known at time of loading. For each loading age, three concrete cylinders were tested for compressive strength in accordance with AASHTO T22 (2017). Concrete specimens were prepared for testing by using an end grinder to ensure a smooth and level surface on both ends of the cylinders. Each cylindrical specimen was tested using a 400 kip compression testing machine, where a target load rate of 1000 lbs/sec. was applied until failure, and the maximum load was recorded for each specimen.

3.5.4.2 Modulus of Elasticity

The modulus of elasticity was tested using a compressometer, shown in Figure 3-8, in accordance with ASTM C469 (2014). At the time of creep loading, one cylinder was tested for compression to determine the initial compressive strength. Once placed in the compressometer, the second cylinder was be loaded at 1000 lbs/sec. until a longitudinal strain of 50 microstrain was reached. At this point the load applied was recorded. Loading continued at a rate 1000 lbs/sec. until the stress in the concrete was equal to 40 percent of the compressive strength of the first cylinder, at which point the longitudinal strain was recorded with the compressometer. After each modulus of elasticity test was performed the cylinder was tested to determine the compressive strength of the concrete.

Figure 3-8: Compressometer used to test modulus of elasticity

3.5.4.3 Drying Shrinkage

Drying shrinkage of the concrete specimens was tested in accordance with AASHTO T160 (2017). Testing occurred for the 3 in. × 3 in. × 11.25 in. rectangular prisms collected on-site. Testing began for the air-cured specimens as soon as the molds are removed. Testing of the moist-cured specimens started seven days of curing in the lime-saturated water tank. Once testing began, the change in length of the specimen was recorded using the standard length comparator shown in Figure 3-9. As required by AASHTO T160 (2017), readings began as soon as drying commenced for each set of prisms followed by 2 to 6 hours after exposure, once a day for the first week, once a week for the first month, once a month for the first year, and every three months following the first year. Each set of drying shrinkage specimens contained three prisms from which the readings were averaged to obtain one shrinkage value at each measurement age.

Figure 3-9: Standard length comparator used to measure drying shrinkage

An important aspect of being able to determine creep is to be able to isolate the creep strain from shrinkage strain. In addition to the cylinders sampled for creep, compressive strength, and modulus of elasticity, three additional cylinder samples were cast for drying shrinkage testing. Demountable Mechanical (DEMEC) strain points were glued on three sides of all creep and drying shrinkage cylinders. An example cylinder with DEMEC points installed can be seen in Figure 3-10. The shrinkage readings were sampled at the same time as total strain readings in order to isolate the creep strain. The DEMEC strain gauge used for this project is shown in Figure 3-11.

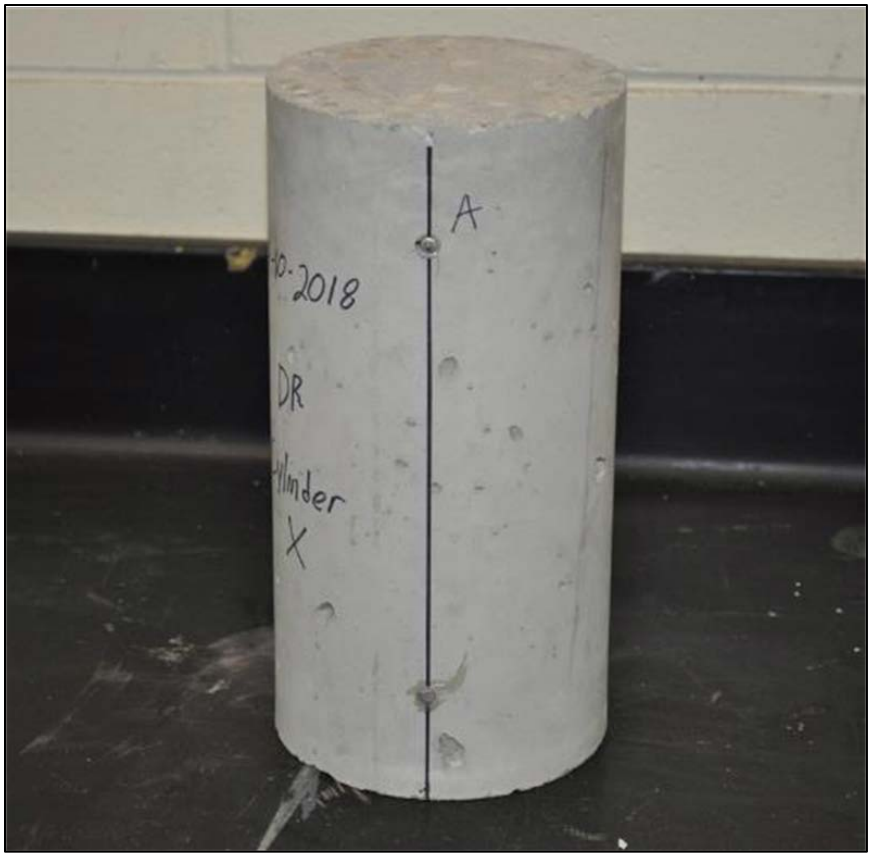

Figure 3-10: DEMEC points fixed to a concrete cylinder

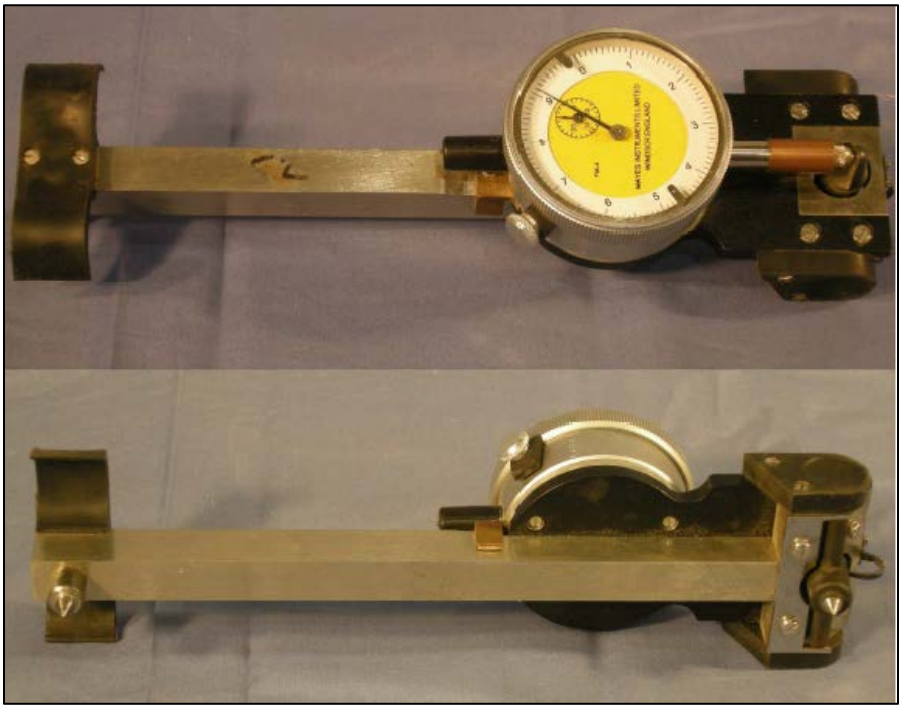

Figure 3-11: DEMEC strain gauge used during the project (Kavanaugh 2008)

3.5.4.4 Creep Testing

For the purpose of this research project, all creep testing followed the procedures and equipment required in ASTM C512 (2015). This section outlines the testing procedure as well as details of the equipment used for creep testing.

3.5.4.4.1 The Creep-Testing Room

All creep testing occurred in a controlled environment inside of the laboratory at Auburn University. Adhering to ASTM C512 (2015), the temperature and relative humidity of the creep testing room should remain between 73.5°F ± 1.5°F and 50% ± 4%, respectively. For the purpose of this research project these factors were recorded for the duration of testing. The creep-testing room can be seen in Figure 3-12 where specimens were tested.

Figure 3-12: Environmentally controlled creep-testing room

Wire storage racks are located along the wall inside the creep-testing room to hold additional testing specimens. All shrinkage test specimens for the project were stored in the creep-testing room. Any creep, drying shrinkage, and modulus of elasticity cylindrical specimens were stored upright in the creep-testing room until the appropriate loading age. The corresponding shrinkage and creep specimens for adequate access to record data can be seen in Figure 3-12.

3.5.4.4.2 Creep Testing Frames

This research project required 16 creep testing frames to monitor strain in concrete subjected to compression. Four creep testing frames were used for each of the four sample collection dates. ASTM C512 (2015) requires that frames must sustain ± 2 percent of the target load on the concrete specimens. A hydraulic ram and load cell were used to apply the desired load to each of the creep frames. The standard setup for the ram and load cell used for creep testing is shown in Figure 3-13. A creep frame used for testing throughout this research project can be seen in Figure 3-14 with additional schematics of the frame shown in Figure 3-15 and Figure 3-16.

Figure 3-13: Standard setup of hydraulic ram and load cell used to apply stress

Figure 3-14: Creep frame used for testing at Auburn University (Kavanaugh 2008)

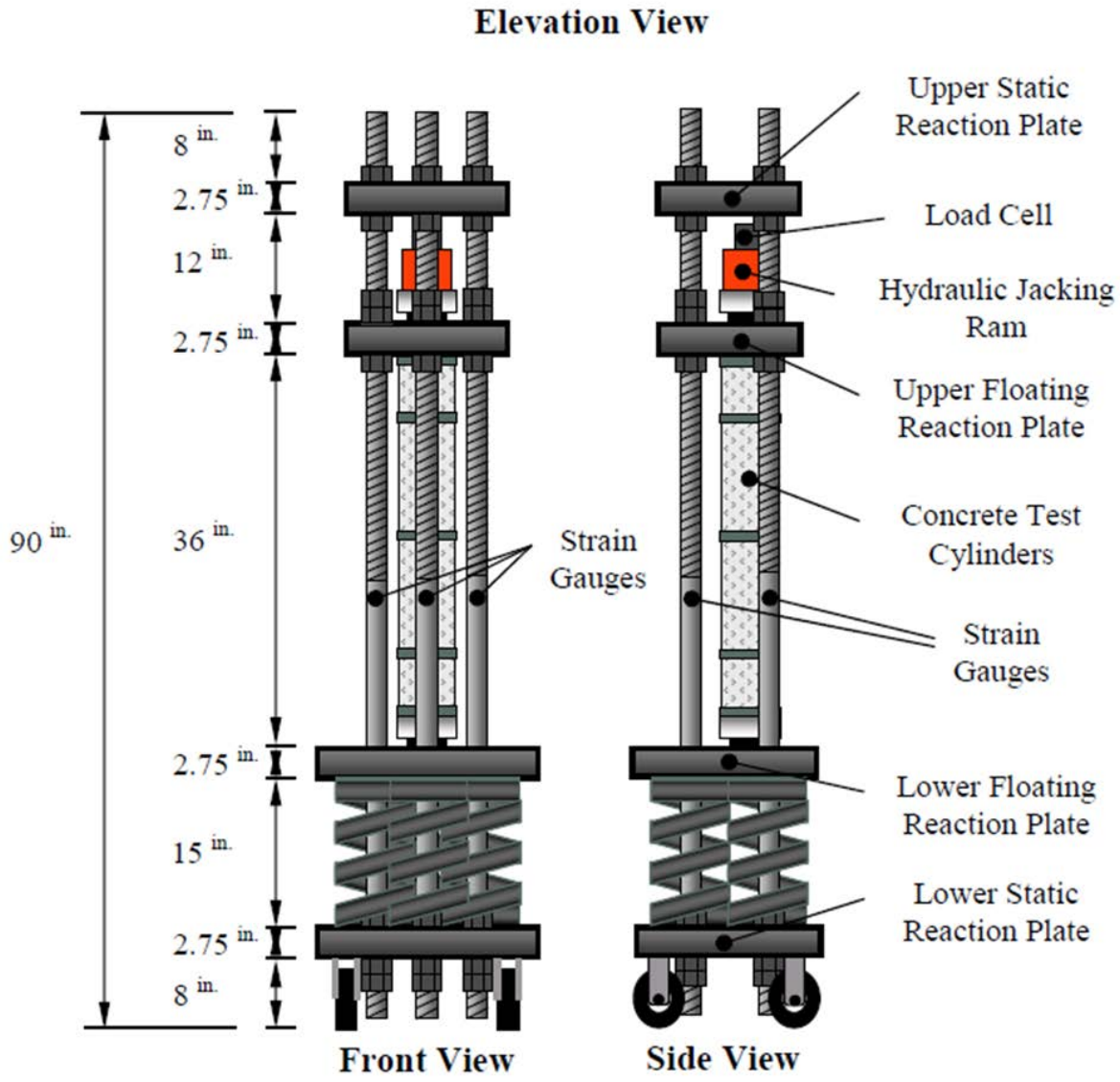

Figure 3-15: Creep Frame Schematic (Kavanaugh 2008)

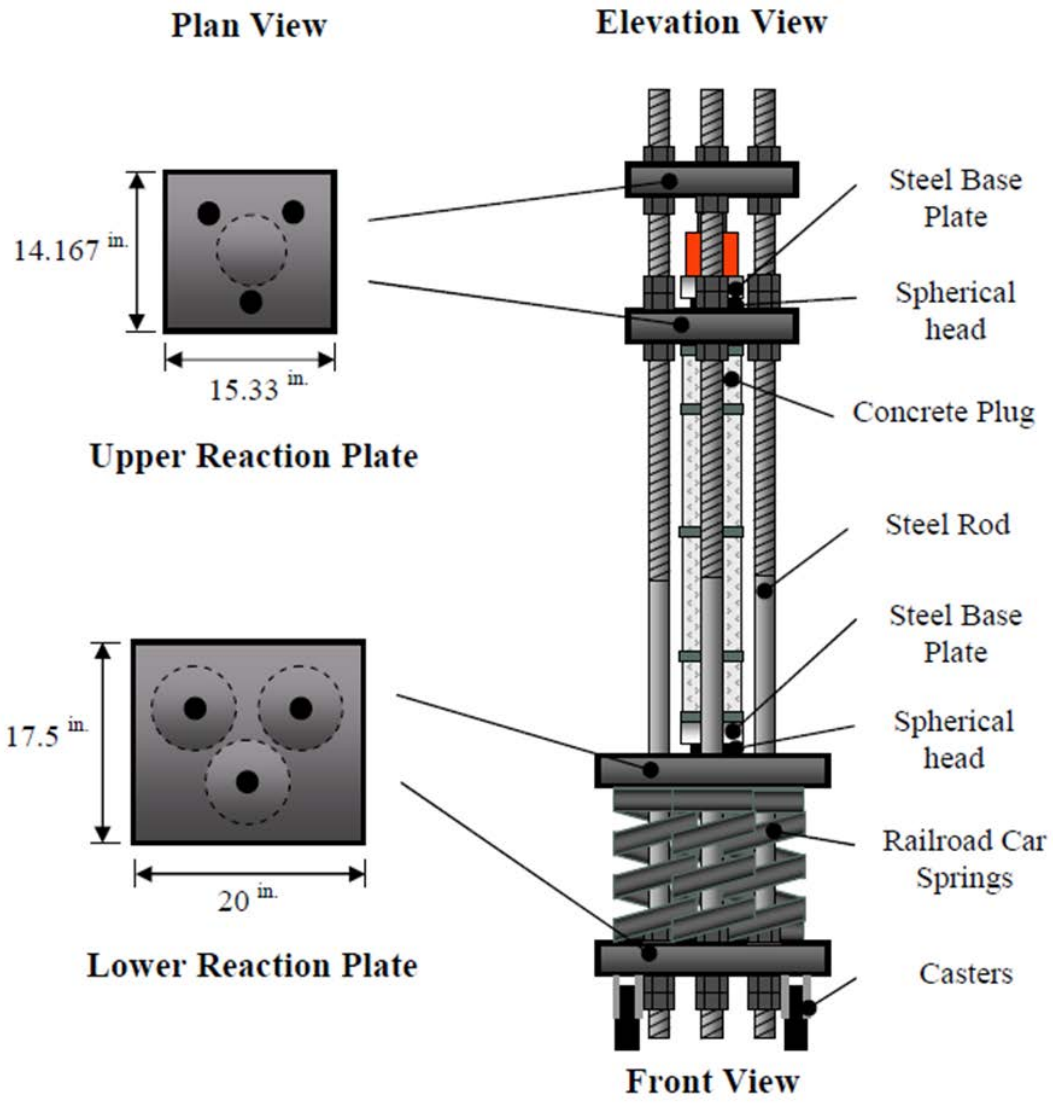

Figure 3-16: Creep Frame Schematic (Kavanaugh 2008)

The following description of the creep frames is based on a previous study performed by Kavanaugh (2008) at Auburn University. Each creep frame should be able to withstand the force required to load 6 in. × 12 in. concrete cylinders, having a compressive strength of 16,000 psi, to 40 percent of their ultimate strength. The plates were selected to be 2.75 inch thick Grade 50 steel. In the upper reaction plate, a six-inch diameter circle was etched to act as an alignment tool when loading concrete specimens shown in Figure 3-16. Each frame included four plates, where two of the plates would float as load was applied and the other two would act as the force to react against.

In addition to the reaction plates, each frame had three steel rods 90 in. long with threads on both ends shown in Figure 3-15. Each rod must be able to support 60 kips of force with minimal relaxation. 1.75 in. diameter rods were selected with a 65 ksi yield stress and 80 ksi ultimate stress. In order for the rods to withstand such stress, 1.75 in. Grade 8 heavy-duty hex nuts were threaded to ensure the floating plate would not move once secure. Six nuts were required for each frame made from C 1045 steel with a minimum Rockwell hardness of C24 and a minimum ultimate tensile stress of 150 ksi. From further testing by Kavanaugh (2008), it was determined that small imperfections in the nuts from fabrication resulted in a 2 percent loss in applied load to the specimens when the hydraulic ram was retracted. For this reason the target loading was at +4 percent of the desired 40 percent ultimate stress, as the target for creep testing is ±2 percent.

As the ram is extended the plates and rods concentrate the load into the railroad car springs. Each frame had three springs with a spring constant of 25,000 lbs/in. The springs were manufactured specifically for the creep frames in the laboratory at Auburn University. Duer/Carolina Coil, Inc. of Reidville, SC manufactured the springs. The springs are made of ASTM-A-304, Grade 220 steel, 15 in. tall with an outer diameter of 8.5 in. The creep testing frames used at Auburn University are designed specifically to withstand a decrease in load for long periods of time. As concrete begins to creep the springs keep the stress as constant as possible.

Each bar in the creep frame was equipped with DEMEC points on two locations 180 degrees apart from each other. These DEMEC points allow for the strains in each bar to be calculated to ensure proper load being applied to the specimens being tested. A DEMEC epoxied onto a steel bar is shown in Figure 3-17.

Figure 3-17: Epoxied DEMEC point on steel bar for load calculation

3.5.4.4.3 Creep Testing Procedure

ASTM C512 (2015) outlines all requirements pertaining to the creep-testing procedure. Upon returning with specimens from on-site curing, all concrete cylinders were demolded placed in the creep-testing room. All specimens were stored until the proper age of loading is reached for each set of samples. An outline of the standard procedure used for creep testing is shown below. Several steps were adopted from a procedure developed by Kavanaugh (2008) with modifications where necessary for this research experiment.

1. Obtain creep, shrinkage, and strength specimens.
2. End grind all specimens to achieve a level surface to prevent eccentrically loaded specimens.
3. Prepare creep and shrinkage specimens by attaching DEMEC points at 120-degree intervals around cylinder. Allow epoxy to reach strength before taking readings.
4. At time of loading, determine ultimate compressive strength and modulus of elasticity in accordance with AASHTO T22 (2017) and ASTM C469 (2014), respectively. Use one cylinder for ultimate strength and then perform modulus of elasticity testing on the two additional specimens before testing the compressive strength.
5. Place two creep specimens into the creep frame ensuring that the cylinders are positioned centered on each other.

6. Lower the top floating reaction plate to make contact with the top concrete plug, and ensure that all sides of the cylinders are level.
7. Record initial strain measurements for the creep specimens, drying shrinkage specimens, and steel bars.
8. Insert the hydraulic jack and load cell between the top two reaction plates. Ensure that the load cell rests flush with the top reaction plate.
9. Connect the load cell to the strain indicator.
10. Begin to apply load with the hydraulic jack until 104 percent of the target applied load is reached. (Note: As load is applied it is necessary to take intermediate readings of concrete strains to ensure no eccentricities have developed.)
11. After reaching desired target load tighten the nuts down to the top floating reaction plate by use of a pipe wrench. Lock nuts must be snug tight to the initial nuts.
12. Slowly retract the hydraulic jack, and take readings of the DEMEC points on the frames to ensure that the applied load remains within the 2 percent threshold. Reapply load if necessary.
13. Record concrete strain measurements immediately following the loading process.

Creep and shrinkage strain measurements were recorded following the intervals outlined in ASTM C512 (2015). After initial load, strains were recorded between two and six hours after loading, every day for the first week, weekly for the first month, monthly for the first year, and every three months after one year of testing has commenced. It was important to record the strain in each bar at each reading to ensure the required load tolerance is met. The strain in each bar was converted to the force in each bar, and the sum of the force in all three bars was the resulting force being applied to the specimens. If the applied load did not meet the desired target load, the hydraulic jack and load cell were used to reapply load to the system.

CHAPTER 4: CONSTRUCTION OVERVIEW OF THE BIRMINGHAM I-59/I-20 SEGMENTAL BRIDGE

4.1 INTRODUCTION

As mentioned in the previous chapter, all concrete samples were collected on-site at the Birmingham I-59/I-20 segmental bridge casting yard. Samples were collected from the same concrete mixtures that were used to cast the segmental bridge superstructure. This chapter provides an overview of the jobsite where all samples were collected as well as how the bridge was constructed.

4.2 PROJECT LOCATION

The I-59/I-20 segmental bridge project occurred at two major locations in Birmingham, Alabama. The bridge was assembled running through downtown Birmingham. With precast, segmental bridge construction it is important that the contractor have a large casting yard to store materials, equipment, and finished segments. For the Birmingham I-59/I-20 segmental bridge project all casting and storage of segments took place at an abandoned steel mill located at 1503 50th Street North Birmingham, Alabama 35212, adjacent to the Birmingham-Shuttlesworth International Airport. It was imperative to the contractor that all casting and storage would occur as close as possible to the erection site for the bridge. Portions of the abandoned steel mill were used for dry storage as well as to fabricate post-tension strand components.

4.3 CONSTRUCTION DURATION

Construction of the Birmingham I-59/I-20 segmental bridge superstructure occurred in two major phases: casting and erection of the segments. The first segment was cast on February 21, 2018, and the last segment was cast on August 9, 2019; a total casting duration of 534 days. At the peak of production eight segments were cast per day. The second major phase of the superstructure construction was the erection of segments at the bridge location on falsework. The first segment was erected on March 11, 2019, and the last segment was erected on October 14, 2019; a total

erection duration of 217 days. Segments were not erected in the same order as they were cast. The duration of the two major stages of the segmental superstructure construction is presented in Figure 4-1 (courtesy of Mr. Eric Johnson, Corven Engineering).

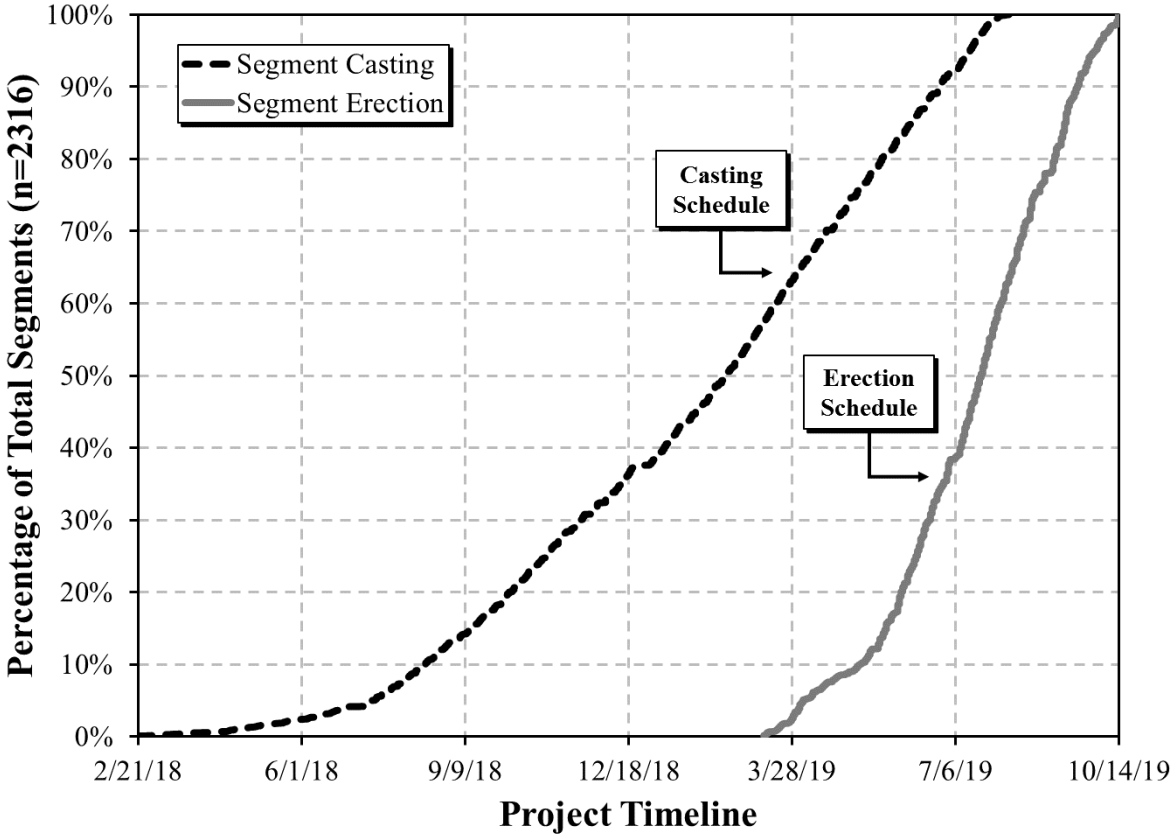

Figure 4-1: Birmingham I-59/I-20 segmental bridge superstructure construction duration

4.4 FORMWORK OF SEGMENTS

The contractor had eight primary segmental casting beds manufactured specifically for the project by a third-party contractor. Each form was equipped with adjustment points to allow for changes in grade. The formwork was also designed to have external vibrators installed on the walls to assist with proper consolidation. Typical formwork used to cast segments can be seen in Figure 4-2.

Figure 4-2: Formwork used to cast segments

After proper installation of each form, checks were made to ensure that the formwork met the desired specification. At the beginning of the casting stage all reinforcement was installed inside of the formwork. As the rate of production increased, a subsequent reinforcement fabrication box was developed to accelerate work associated with tying the reinforcement cage. The reinforcement box that matches the internal dimensions of the formwork is shown in Figure 4-3.

Figure 4-3: Reinforcement fabrication box for increased construction efficiency

4.5 CASTING OF SEGMENTS

This section outlines the standard procedure used in casting a typical bridge segment. This process was repeated for each segment with only minor differences throughout the casting stage of the project. During the peak of operation this process was repeated every day for eight casting beds.

4.5.1 Formwork Preparation

Before concrete could be placed, the formwork was prepared. The casting of each segment followed a match-casting method in which the face of one segment would be the back wall of the formwork for the next segment in a span. The formwork was then properly aligned with any minor change in orientation from the previous segment in the span. As shown in Figure 4-4, a rail system with hydraulic jacks allowed for the inside cell of the form to be removed.

Figure 4-4: System on rails used to remove internal cell of the formwork

After removing the previous segment and cleaning the formwork, a release agent approved by ALDOT was applied to all formwork surfaces. Reinforcement was then lifted from the previously mentioned box using a crane and placed into the formwork. Quality checks were completed to ensure the proper reinforcement layout and cover were achieved. Transverse post-tensioning ducts with tendons were also installed. With the use of the rail system, the internal cell of the formwork was installed. The match-cast segment can be seen with final reinforcement in the formwork in Figure 4-5.

Figure 4-5: Formwork for a segment ready for concrete placement

4.5.2 Concrete Production and Quality Assurance

Concrete placed in the segments had to meet the specific mixture proportions approved by ALDOT. With the size of the project the contractor found it beneficial to batch concrete on site. At the early stages of the project, the on-site batching plant was not operational, concrete was supplied and delivered to the segments from a third-party ready-mixed concrete producer. Once the on-site batching plant was running and approved by ALDOT, all raw materials were able to be stored locally, which allowed the delivery time to be reduced. The on-site batching plant can be seen in Figure 4-6. So long as the concrete met all ALDOT requirements, it could be placed into the formwork.

Figure 4-6: On-site batching plant for concrete production

As each batch of concrete arrived to the formwork a sample was taken for quality assurance testing. The on-site technician was responsible for testing each batch of concrete for the fresh properties required by ALDOT. Total air content, unit weight, slump, and concrete temperature was monitored and recorded. The total air content being measured on the jobsite can be seen in Figure 4-7. In addition to fresh properties, quality assurance cylinders were cast using concrete from the middle of each truck. These cylinders were used for compression testing to determine when formwork could be removed, when post-tensioning could be applied, and if the segment met the specified 28-day compressive strength.

Figure 4-7: Quality assurance testing prior to concrete placement

4.5.3 Concrete Placement

Concrete was placed from the top of each form for all typical segments, which did not allow a standard ready-mixed concrete truck to reach. Two methods were used during the project to move concrete from the truck to the top of each form. In early stages of the project a belt conveyor was used to raise concrete to the required height. The conveyor stayed in the same place and each ready-mixed concrete truck placed the batch of concrete onto the conveyor, which can be seen in Figure 4-8. As the segment was filled the arm of the conveyor belt was moved around at the top of the formwork to ensure the concrete was placed where needed.

Figure 4-8: Conveyor moving concrete to desired location at the top of the formwork

As the project progressed, it was determined that the conveyor system was inefficient and a second method of transport was implemented. The second method for moving concrete to the formwork was by using a concrete bucket and crane. The ready-mixed concrete truck discharged concrete into the bucket shown in Figure 4-9. Once filled, the bucket was lifted by a crane to the top of the formwork. Laborers quickly discharged the concrete into the form shown in Figure 4-10 and returned the bucket to be filled again. This placement method was much more efficient and was used for the remainder of the project.

Figure 4-9: Concrete bucket being filled by ready-mixed concrete truck

Figure 4-10: Concrete being placed into the formwork with a bucket

Proper consolidation was required for the concrete placed in the formwork. As discussed, each form was equipped with external vibrators attached to the walls; however, the energy from the external vibrators was often not adequate enough to consolidate the concrete properly throughout the formwork. Therefore, portable vibrators were used in addition to the external vibrators to focus consolidation at specific points in the formwork as shown in Figure 4-11.

Figure 4-11: Consolidation using a portable vibrator

4.5.4 Finishing Techniques

The last step in constructing a segment was to strike-off and float its top, which occurred after the formwork was filled and properly consolidated. All segments were finished using standard practices throughout the project duration. An aluminum or magnesium float was used to float the tops of each segment. The proper floating of a segment is shown in Figure 4-12.

Figure 4-12: Concrete being floated using a bull float

4.6 SEGMENT CURING, PROTECTION, AND STORAGE

After each segment was cast, curing techniques were implemented according to the contractor's quality control plan. As discussed previously all segments and quality assurance cylinders were cured using an elevated temperature curing method approved by ALDOT. Thermal blankets were wrapped around all formwork, and the temperature in the enclosure was elevated using electric heaters. Upon completing the initial elevated curing cycle, the concrete cylinders corresponding to each segment were tested in compression. Concrete cylinders were required to reach a minimum compressive strength of 2,500 psi for the formwork to be removed; therefore, if cylinders tested less than the required minimum compressive strength the segment would remain in the form until the required strength was achieved. Prior to stressing of the transverse post-tensioning, concrete cylinders were required to have a compressive strength of 4,000 psi. Once forms were removed, the segment was moved to become the next match-cast segment. In order to protect the formwork from excess heat and severe weather, a roll-away canopy was used for each form of a segment as shown in Figure 4-13.

Figure 4-13: Roll-away canopy to protect each form from severe weather

After a period of 28 days, additional quality assurance cylinders were tested to determine their compressive strength. The cylinders were required to have a compressive strength of 6,500 psi at 28 days. After being used to match cast the next segment in a span, segments were stored on-site until being transported to their final erection location. A rubber-tired gantry crane was used to move segments around in the casting yard, which can be seen in Figure 4-14. The design of the crane allowed easier access around the casting yard as well as lifting the segment with minimal stressing to the concrete.

Figure 4-14: Rubber-tired gantry crane used to transport segments around the casting yard

4.7 SEGMENTAL BRIDGE ERECTION PROCESS

Erection of the Birmingham I-59/I-20 segmental bridge occurred in spans, where a complete span was erected on falsework and then post-tensioned longitudinally. The remainder of this section convers the erection of a typical span in the bridge superstructure. Falsework shown in Figure 4-15 was used on the project to support the segments of each span prior to post-tensioning. The erection schedule allowed for subsequent spans to be erected so that falsework could be recycled every two spans in the system. This allowed for rapid construction of this segmental bridge.

Figure 4-15: Falsework used to erect each span

Each segment was transported from the casting yard to the bridge site on flatbed trucks. As each segment arrived, it was erected onto the falsework. Large cranes lifted segments into place. A segment being lifted using a crane on the bridge site is shown in Figure 4-16. As each segment was erected, laborers guided the segments into place next to the match-cast segment, which is shown in Figure 4-17.

Figure 4-16: Crane lifting a segment into place

Figure 4-17: Segment being guided into place on falsework

The face of one segment was covered with an ALDOT approved water-resistant epoxy before each segment was moved into position. Additional steel bars were used to apply the stress as required by the epoxy manufacturer (ALDOT 832 2018) to ensure proper bonding. All spans were completed with a narrow closure strip between the last typical segment and the column segment. This closure strip allowed for minor geometry adjustments to be made at these locations. With all segments in place, each span was longitudinally post-tensioned along the entire simple span. After two spans were completed in sequence, the closure strip shown in Figure 4-18 between the two spans was filled using concrete delivered on-site.

Figure 4-18: Closure strip between two spans to be filled with concrete

The additional top cover in segments allowed the surface to be leveled by grinding. For this reason ALDOT required quartzite aggregate as opposed to limestone aggregate, which may lead to polishing after grinding. Additionally, grinding provided grooves of approximately 1/32 in. to meet requirements of ALDOT Standard Specifications Section 455 (2018).

CHAPTER 5: TEST RESULTS

5.1 INTRODUCTION

This chapter presents all concrete testing results collected for this project. The results of fresh concrete testing are presented in Section 5.2, and the results of hardened concrete testing, excluding creep and shrinkage, are described in Section 5.3. A summary of all testing conditions is presented in Section 5.4. Shrinkage and creep test results are covered in Section 5.5 and Section 5.6, respectively. This research study consists of data collected from April 10, 2018 through September 25, 2020. A summary of lessons learned through testing is outlined in Section 5.7, with an overview of all test results for the duration of this research effort presented in Section 5.8. All recorded data for creep and shrinkage testing are provided in Appendix A.

5.2 FRESH CONCRETE PROPERTIES

In this section, all fresh properties of each concrete mixture used during the duration of this research project are presented. As presented in Table 3-2, each sampling date had different ALDOT approved mixture proportions resulting in different batch proportions for each concrete collected on these sampling dates. A summary of all fresh property testing of the concrete used in this research effort is presented in Table 5-1. Discussion of each fresh concrete property important to this study is found in subsequent sections including slump, total air content, and unit weight.

Table 5-1: Summary of all fresh concrete properties for all sampling dates

Fresh Concrete Property	Sampling Date			
	04/10/2018	**07/09/2018**	**11/19/2018**	**04/16/2019**
Slump (in.)	5.5	6.25	6	6
Total Air Content (%)	4.4	4.2	3.4	3.8
Unit Weight (lb/ft^3)	144	141	146	145
Concrete Temperature (°F)	76	87	76	76

5.2.1 Slump

All concrete mixtures were required to meet slump prescribed by ALDOT specifications for all segments that were cast. All measured values were between the required 3 to 9 inches. Slump of all concrete mixtures remained consistent throughout all sampling dates with a typical slump of approximately 6 inches.

5.2.2 Total Air Content

The ALDOT specification for total air content in fresh concrete is from 3 to 6 percent. All of the measured total air contents ranged from 3.4 to 4.4 percent, which meet ALDOT requirements. The lowest total air content was recorded for the 11/19/2018 sampling date, which correlates to the Type III cement ALDOT approved mixture proportions.

5.2.3 Concrete Unit Weight

Although ALDOT did not have a specification for unit weight of fresh concrete mixtures, the unit weight was recorded for all concrete samples. The average unit weight for all concrete mixtures was 144 lbs/ft^3, which is the same as the theoretical value calculated from the ALDOT approved mixture proportions presented in Table 3-2. A unit weight of 141 lbs/ft^3 was recorded for the 07/09/2018 sampling date; however, the slight decrease did not affect any further testing results.

5.3 HARDENED CONCRETE PROPERTIES

This section provides results of hardened concrete properties including compressive strength, modulus of elasticity, and maturity calculations. All testing for hardened concrete properties occurred in laboratory conditions at Auburn University. Key components of each property are discussed for later comparison of creep and shrinkage prediction methods.

5.3.1 Compressive Strength

The compressive strength results of the concrete sampled are presented in Table 5-2.

Table 5-2: Compressive strength testing results

Concrete Age (days)	Compressive Strength (psi)			
	04/10/2018	**07/09/2018**	**11/19/2018**	**04/16/2019**
7	5,100	5,600	6,400	7,300
28	6,100	6,700	7,200	8,000
91	6,000	7,100	7,500	8,300
182	6,400	7,100	7,400	8,100

The lowest concrete compressive strength of 5,100 psi was recorded at 7 days for the 04/10/2018 sampling date. In contrast, the highest concrete compressive strength of 8,300 psi was recorded at 91 days for the 04/16/2019 sampling date. The average 28-day concrete compressive strength of all concrete sampling dates was 7,000 psi. The development of concrete strength relative to time is illustrated in Figure 5-1. It can be seen that the concrete strength systematically increased from the first to last sampling date. It is also clear that the 28-day concrete strength was lower than the required 28-day strength of 6,500 psi for the first sampling date on 04/10/2018.

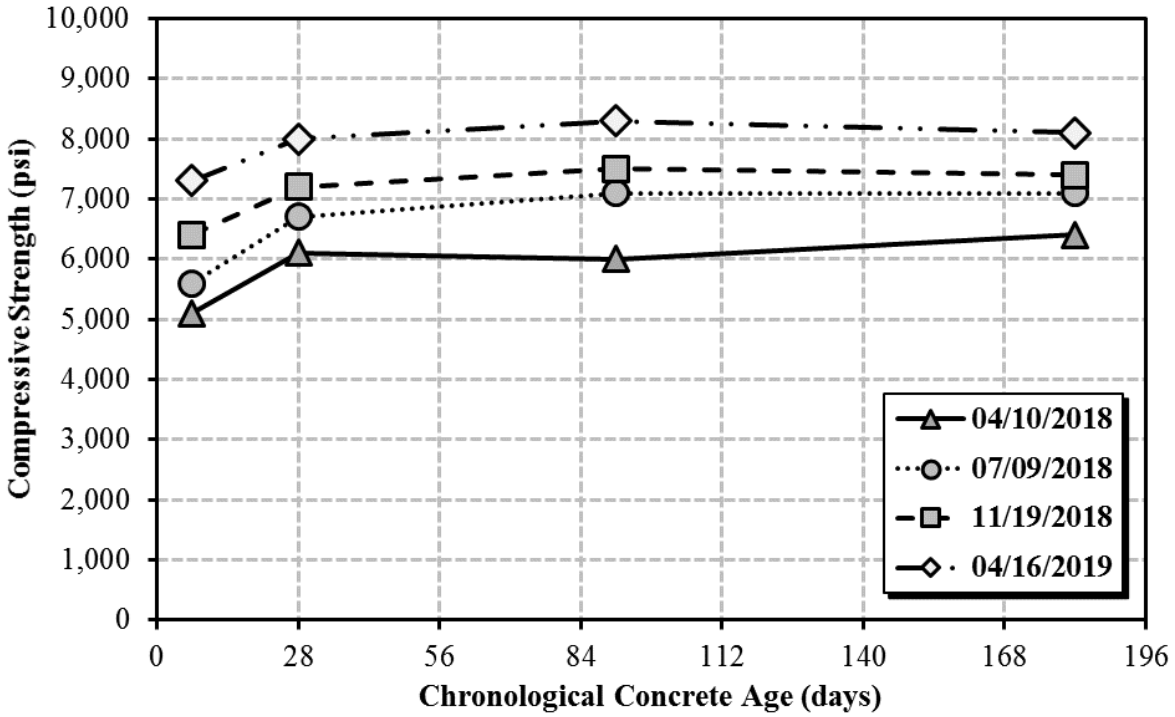

Figure 5-1: Compressive strength development

5.3.2 Modulus of Elasticity

The modulus of elasticity was tested just prior to determining the compressive strength for each creep loading age. The results from modulus of elasticity testing of concrete samples at each loading age are presented in Table 5-3.

Table 5-3: Modulus of elasticity testing results

Concrete Age (Days)	Modulus of Elasticity (ksi)			
	04/10/2018	07/09/2018	11/19/2018	04/16/2019
7	3,800	4,250	4,400	5,100
28	4,050	4,250	4,600	5,300
91	3,850	4,200	4,600	5,400
182	4,150	4,300	4,500	5,400

Similarly to compressive strength, the lowest modulus of elasticity of 3,800 ksi was recorded for the 7-day test of the 04/10/2018 sampling date. The average 28-day modulus of elasticity for all concrete sampling dates was 4,550 ksi. The modulus of elasticity development of all concrete samples with time is illustrated in Figure 5-2. There was little increase in modulus of elasticity after 28 days.

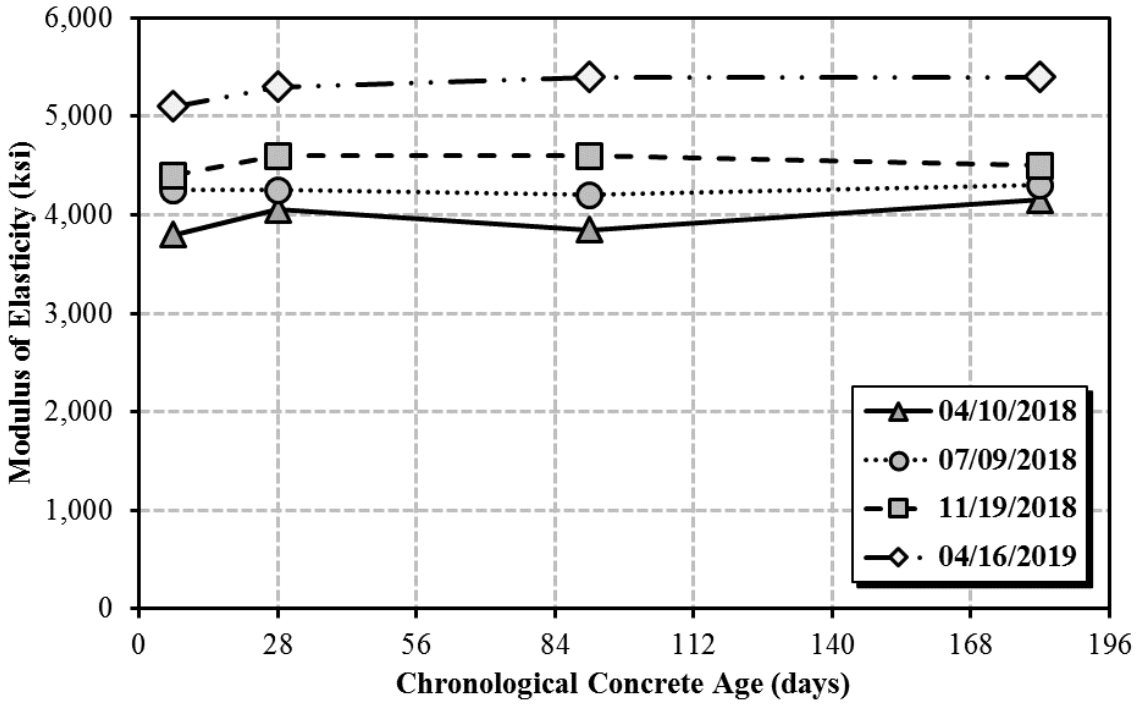

Figure 5-2: Modulus of elasticity development

5.3.3 Maturity

The creep behavior of concrete is impacted by the concrete maturity at the time of loading. Maturity of concrete is directly related to the temperatures at which the concrete is exposed to throughout the curing cycle. Concretes cured at higher temperatures result in an equivalent age larger than the chronological age, which correlates to increased strength and stiffness at early ages. As mentioned in Section 3.5.3.1, a temperature sensor was placed in a concrete cylinder to record the curing temperatures with age for each sampling date. A summary of recorded temperatures for the first 24 hours after concrete placement is presented in Table 5-4.

Table 5-4: Summary of temperatures recorded for the first 24 hours after concrete placement

Type of Temperature		24-Hour Curing Temperatures (°F)			
		04/10/2018	07/09/2018	11/19/2018	04/16/2019
Concrete	Maximum	121	113	108	126
	Minimum	74	70	53	67
	Average	99	95	81	90
Enclosure	Maximum	132	109	88	112
	Minimum	69	71	49	63
	Average	98	91	71	80

The maximum concrete temperature, 126°F, was recorded for the 04/16/2019 sampling date. No temperature exceeded the maximum curing environment temperature 150°F specified by ALDOT. The recorded temperatures for the 24-hour curing cycle are plotted in Figure 5-3 through Figure 5-6 for each sampling date.

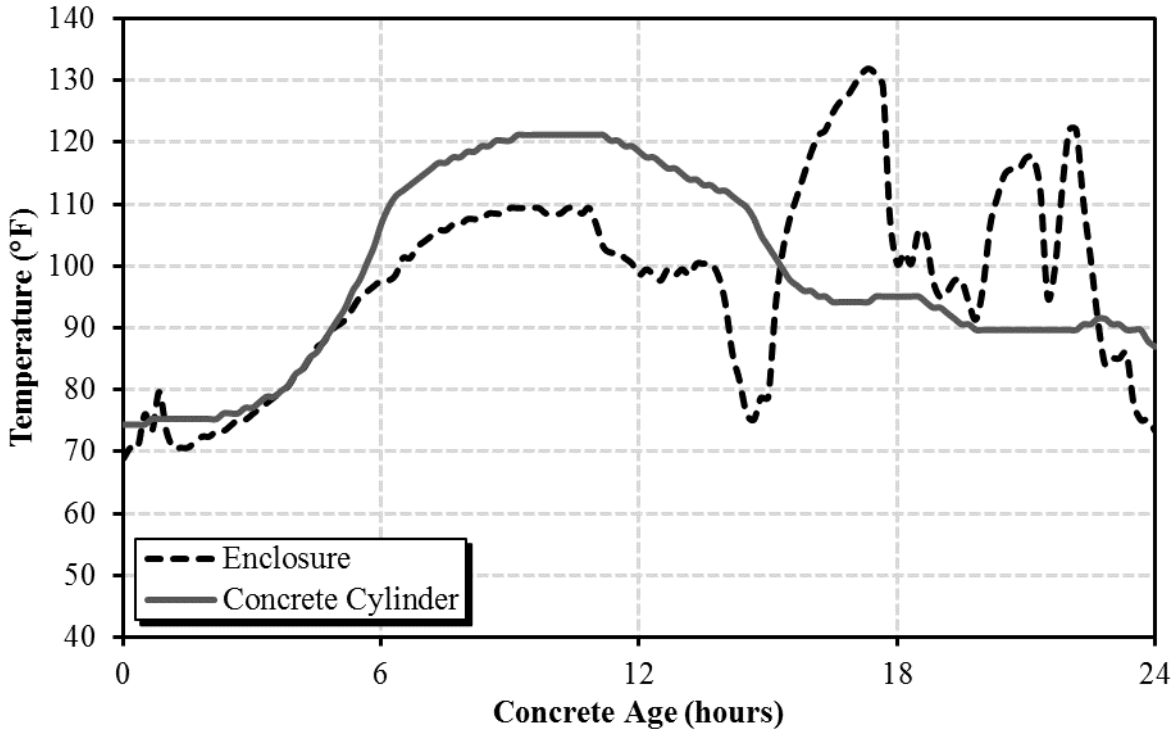

Figure 5-3: Temperature profile for the 04/10/2018 sampling date

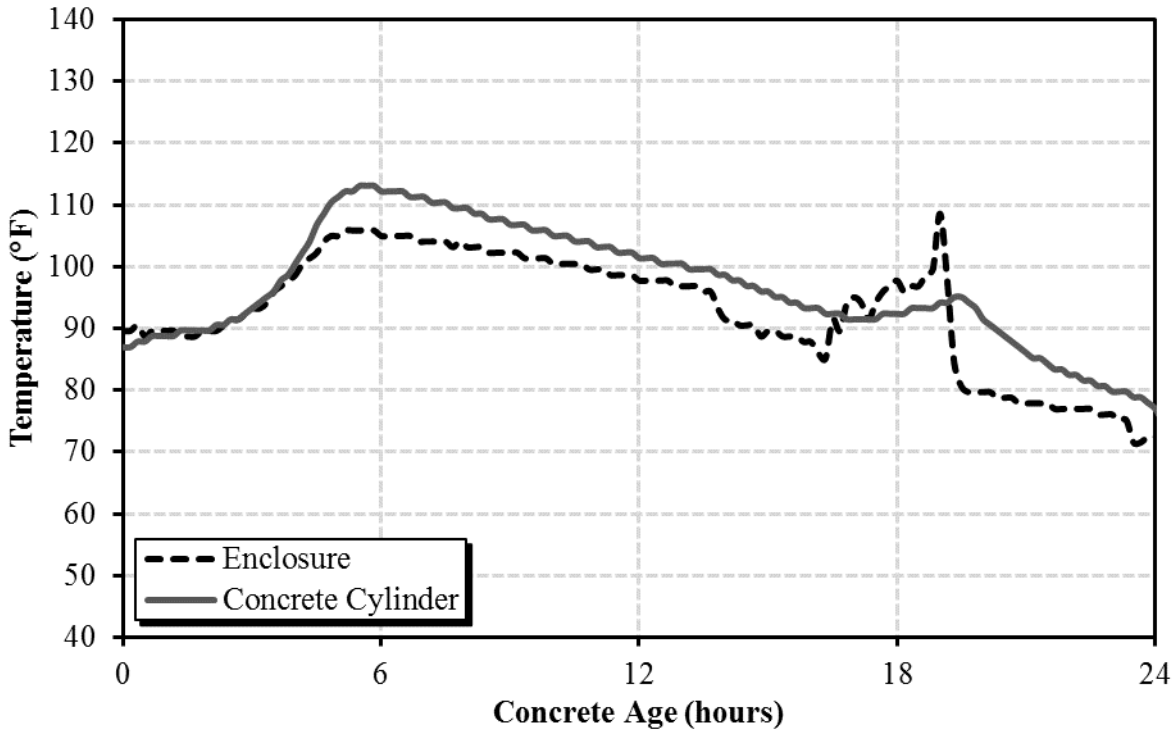

Figure 5-4: Temperature profile for the 07/09/2018 sampling date

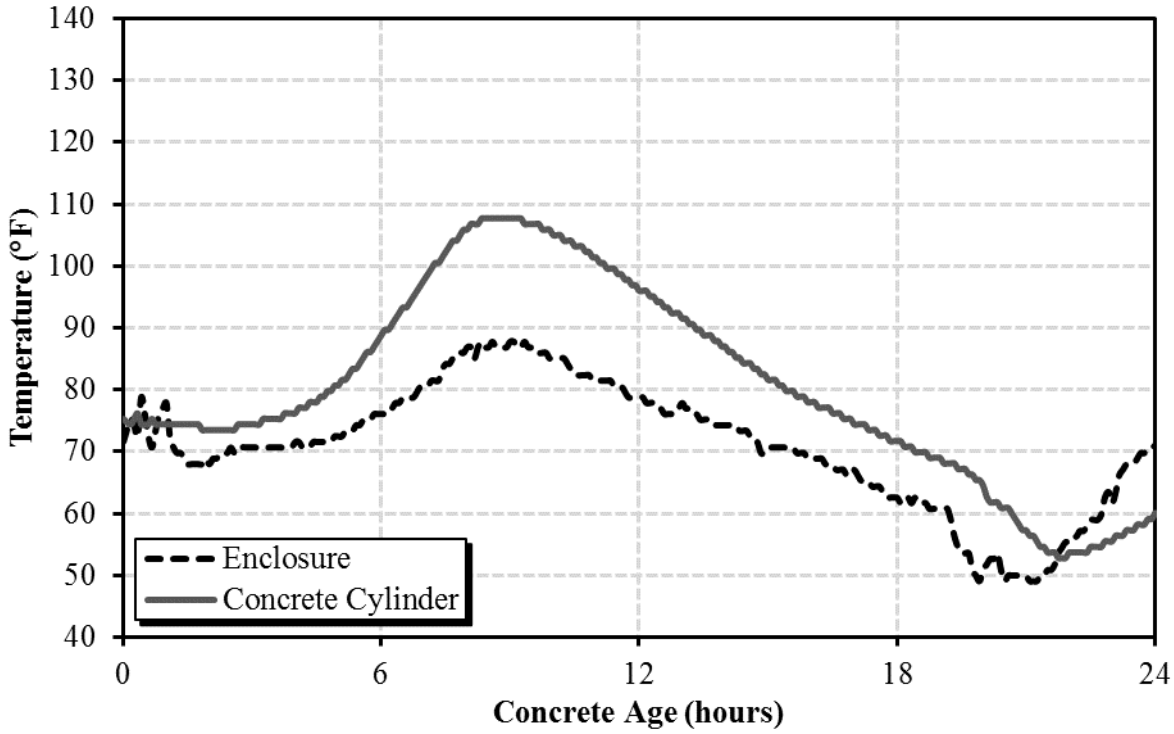

Figure 5-5: Temperature profile for the 11/19/2018 sampling date

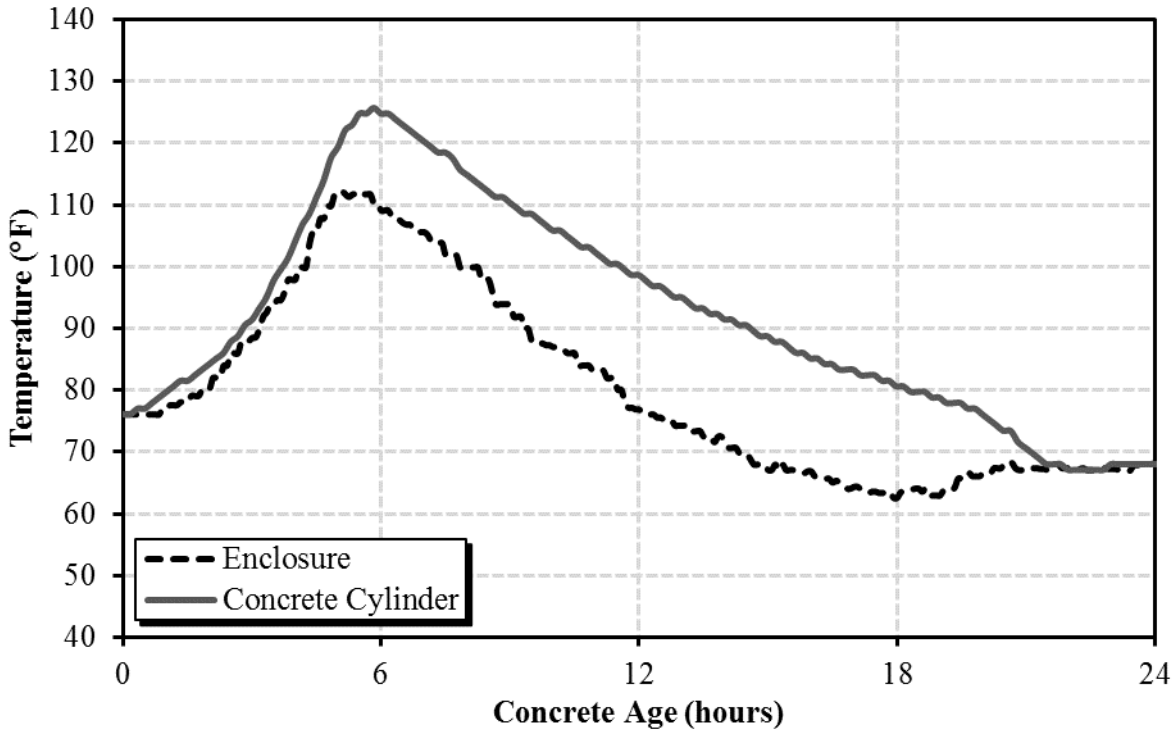

Figure 5-6: Temperature profile for the 04/16/2019 sampling date

In Section 2.4 it was discussed that the GL 2000, B3, CEB MC 1990, and CEB MC 2010 methods for predicting creep and shrinkage all incorporate the equivalent age of the concrete specimens. After determining the prescribed maturity function for each model and by using the measured concrete temperatures, the equivalent-age maturity of each concrete specimen was determined. The equivalent age at loading for each concrete creep specimen is presented in Table 5-5. The equivalent age when drying began for all concrete specimens is presented in Table 5-6.

Table 5-5: Equivalent age at loading for all creep testing specimens

Equivalent Age at Loading, t_0 (days)							
Sampling Date		**04/10/2018**			**07/09/2018**		
Maturity Method		CEB MC	GL 2000	B3	CEB MC	GL 2000	B3
Loading Age	**7 Days**	9.2	8.8	10.1	9.0	8.4	9.8
	28 Days	33.4	30.1	35.4	33.2	29.8	35.1
	91 Days	105.8	94.1	111.3	105.6	93.8	111.0
	182 Days	210.3	186.5	220.8	210.1	186.2	220.5
Sampling Date		**11/19/2018**			**04/16/2019**		
Maturity Method		CEB MC	GL 2000	B3	CEB MC	GL 2000	B3
Loading Age	**7 Days**	8.4	7.6	8.9	8.9	8.3	9.7
	28 Days	32.5	28.9	34.2	33.1	29.6	35.0
	91 Days	104.9	92.9	110.1	105.4	93.7	110.8
	182 Days	209.5	185.4	219.6	210.0	186.1	220.4

Table 5-6: Equivalent age when drying began for all shrinkage testing specimens

Equivalent Age when Drying Began, t_c (days)							
Curing Method		**Air-Cured**			**Moist-Cured**		
Maturity Method		CEB MC	GL 2000	B3	CEB MC	GL 2000	B3
Sampling Date	**04/10/2018**	2.3	2.7	2.9	9.2	8.8	10.1
	07/09/2018	2.2	2.3	2.6	9.0	8.4	9.8
	11/19/2018	1.5	1.5	1.7	8.4	7.6	8.9
	04/16/2019	2.0	2.2	2.5	8.9	8.3	9.7

5.4 TESTING CONDITIONS

This section focuses on all testing conditions for creep and shrinkage testing. The loading, temperature, and relative humidity data are presented in the subsequent sections, respectively.

5.4.1 Loading Data

ASTM C512 (2015) requires the applied load for creep testing be maintained within ±2 percent of the target load for the duration of the test. Auburn creep testing frames are equipped with flexible springs that apply load to test specimens, where a large amount of displacement is permitted before the creep specimen falls below the 2 percent margin of error in applied load. The applied load was calculated for each frame reading, and as an example the error in load for 04/10/2018 specimens loaded at 7 days is illustrated in Figure 5-7.

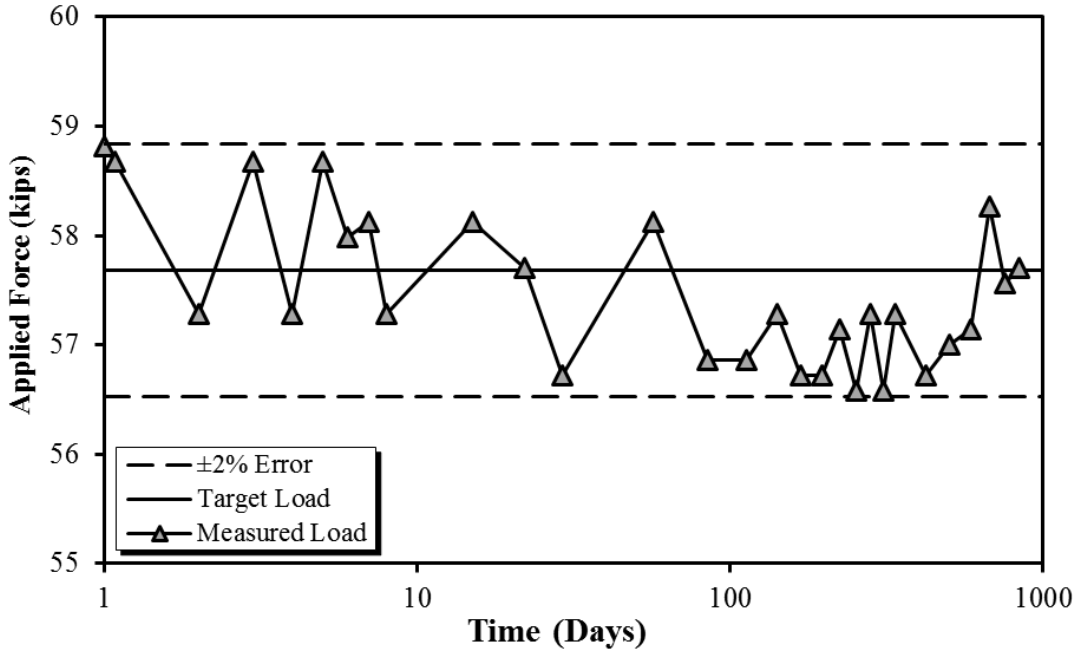

Figure 5-7: Applied load for 04/10/2018 creep specimen loaded at 7 days

The majority of variance of the applied load in all creep specimens resulted from the precision of strain measurements; however, load was maintained between the 2 percent margin of error for the duration of all creep testing. Readjustments in load were most often needed at

early stages of testing when creep development is rapid. The maximum positive and negative percent error in applied load for all creep testing specimens is tabulated in Table 5-7.

Table 5-7: Percent error in applied load summary

Mixture ID	Maximum Negative Error in Applied Load, (%)	Maximum Positive Error in Applied Load, (%)
04/10/2018-7	-1.90	1.98
04/10/2018-28	-1.98	1.87
04/10/2018-91	-1.85	1.24
04/10/2018-182	-1.88	1.99
07/09/2018-7	-1.85	1.90
07/09/2018-28	-1.84	1.85
07/09/2018-91	-1.62	1.87
07/09/2018-182	-1.37	1.94
11/19/2018-7	-1.62	1.82
11/19/2018-28	-1.88	1.90
11/19/2018-91	-1.91	1.39
11/19/2018-182	-1.97	1.71
04/16/2019-7	-1.74	1.98
04/16/2019-28	-1.41	1.99
04/16/2019-91	-1.89	1.84
04/16/2019-182	-1.89	1.93

5.4.2 Temperature of the Creep-Testing Room

Temperature in the creep-testing room was recorded with a data logger for the duration of testing. The average temperature in the creep-testing room for the duration of testing was 73.4°F. The minimum and maximum temperatures for the duration of testing were 69.7°F and 76.4°F, respectively. The distribution of temperature data for the entire duration of creep testing is presented in Figure 5-8.

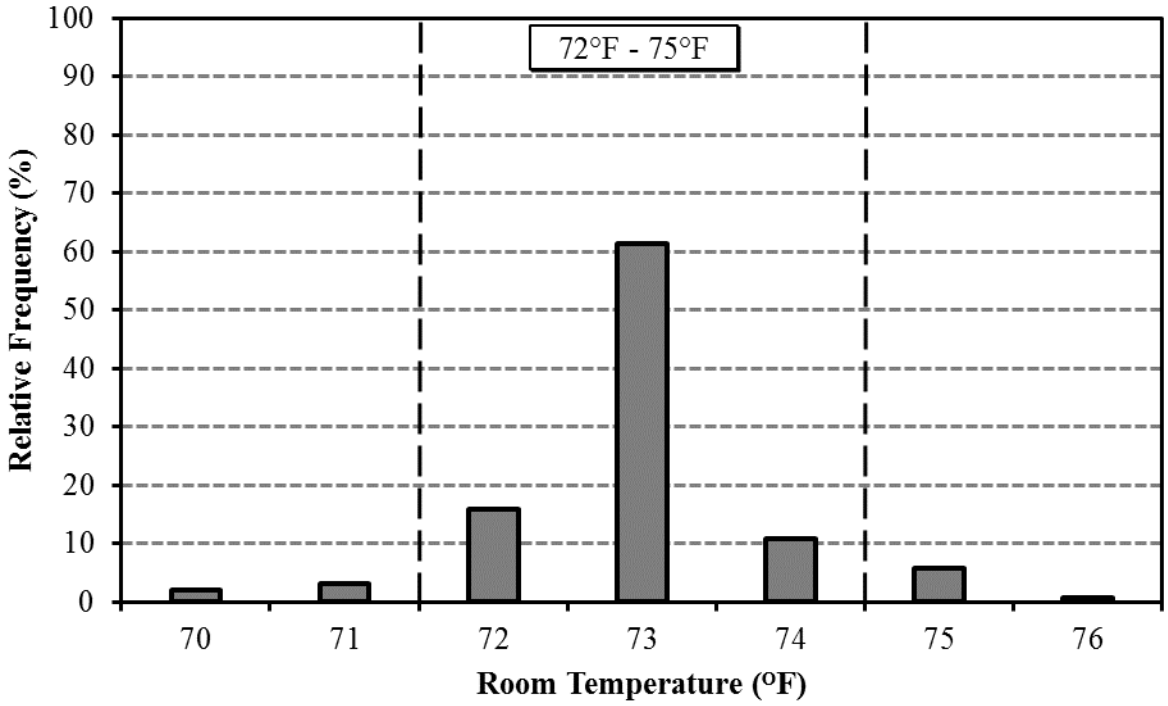

Figure 5-8: Creep-testing room temperature histogram

Temperature was maintained very well as required by ASTM C512 (2008). Data points that fall outside of the required range can be attributed to the sensor used to collect data. The sensor for the data logger was very close to the entry point of the controlled creep-testing room, and its reading might have been influenced by the door to this room being opened and closed.

5.4.3 Relative Humidity of the Creep-Testing Room

The relative humidity of the ambient environment of the creep-testing room was monitored with the same instrument that was used for temperature data. The average relative humidity for the duration of testing was 48.7 percent. The maximum and minimum relative humidity for the duration of testing were 59.4 and 38.8 percent, respectively. The relative humidity histogram is illustrated in Figure 5-9.

Although data seems to be more widely spread, the majority of data falls between the values of 46 to 54 percent required by ASTM C512 (2008). Reasons for data out of tolerance range include the dehumidifier or humidifier being temporarily out-of-service for repairs, the creep-testing room being occupied for measurements and loading, and the humidistat and data collection system being calibrated slightly different from each other. Often the relative humidity recorded by

the data logger was 44 percent; however, the humidistat reading was 47 percent. It is assumed that the slight variation in humidity had no significant impact on creep and shrinkage testing.

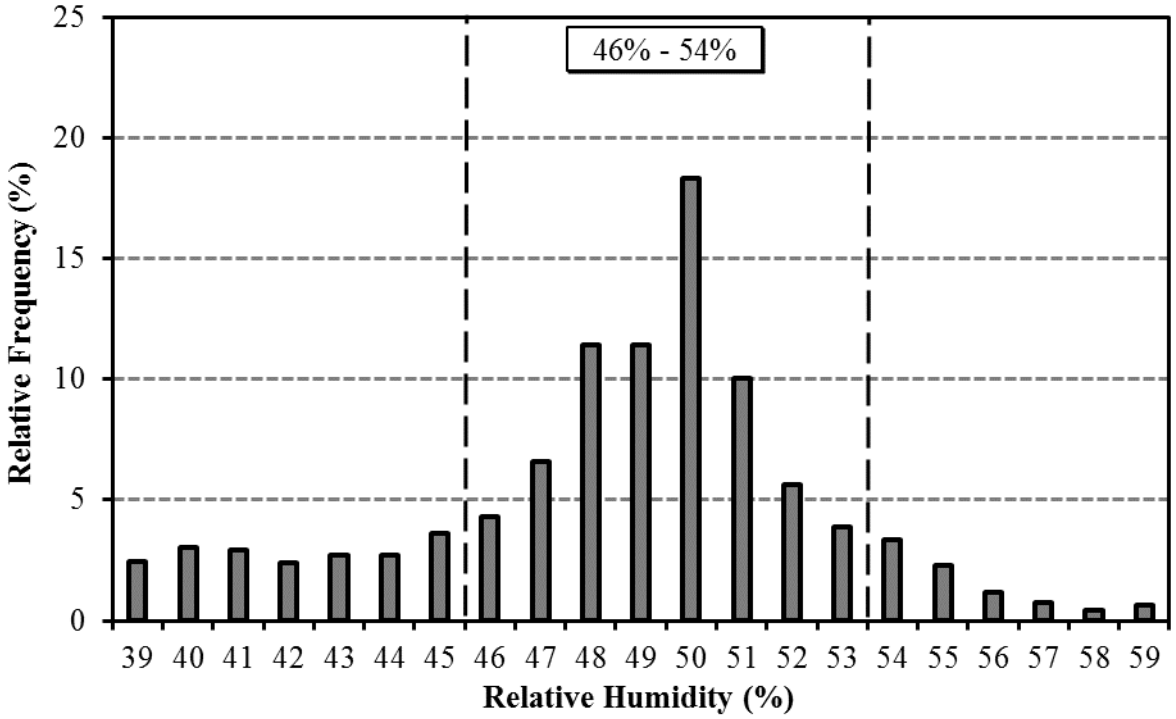

Figure 5-9: Creep-testing room relative humidity histogram

5.5 SHRINKAGE RESULTS

This section outlines all shrinkage testing results for all concrete specimens. Shrinkage was tested on concrete creep companion cylinders and concrete prisms. As described in Section 3.5.3.2, two curing regimes were used for concrete prisms including air- and moist-curing. All shrinkage data can be found in Appendix A. The shrinkage results for all testing specimens are tabulated in Table 5-8. For comparison purposes only the average 18-month shrinkage results are tabulated; however, shrinkage testing continues along with creep testing.

Table 5-8: Average 18-month shrinkage strains for all testing specimens

Average 18-Month Shrinkage Strains ($\times 10^{-6}$ in./in.)			
Sampling Date	**Cylindrical Specimens**	**Air-Cure Prismatic Specimens**	**Moist-Cure Prismatic Specimens**
04/10/2018	-563	-727	-807
07/09/2018	-520	-687	-700
11/19/2018	-481	-620	-670
04/16/2019	-435	-538	-550

The specimens corresponding to the 04/10/2018 sampling date experienced the greatest average 18-month shrinkage strains. As discussed in Section 2.3.1.2, as the strength of the concrete decreases the magnitude of drying shrinkage increases and vice versa. As presented in Table 5-2, the 04/10/2018 and 04/16/2019 sampling dates exhibited the least and greatest concrete strength, respectively. The specimens corresponding to the 04/16/2019 sampling date experienced the least average 18-month shrinkage strains. For all concrete shrinkage testing specimens, results were consistent with respect to the aforementioned strength relationship. Shrinkage testing results specific to the creep companion cylinders and prismatic specimens are presented in Section 5.5.1 and 5.5.2, respectively.

5.5.1 Creep Companion Cylinders

For cylindrical specimens, as presented in Table 5-8, the largest average 18-month shrinkage strain was experienced in the 04/10/2018 sampling date. The 04/16/2019 sampling date exhibited the smallest average 18-month shrinkage strain in cylindrical specimens. The development of shrinkage strains in cylindrical specimens with respect to time for all data collected for this project is illustrated in Figure 5-10.

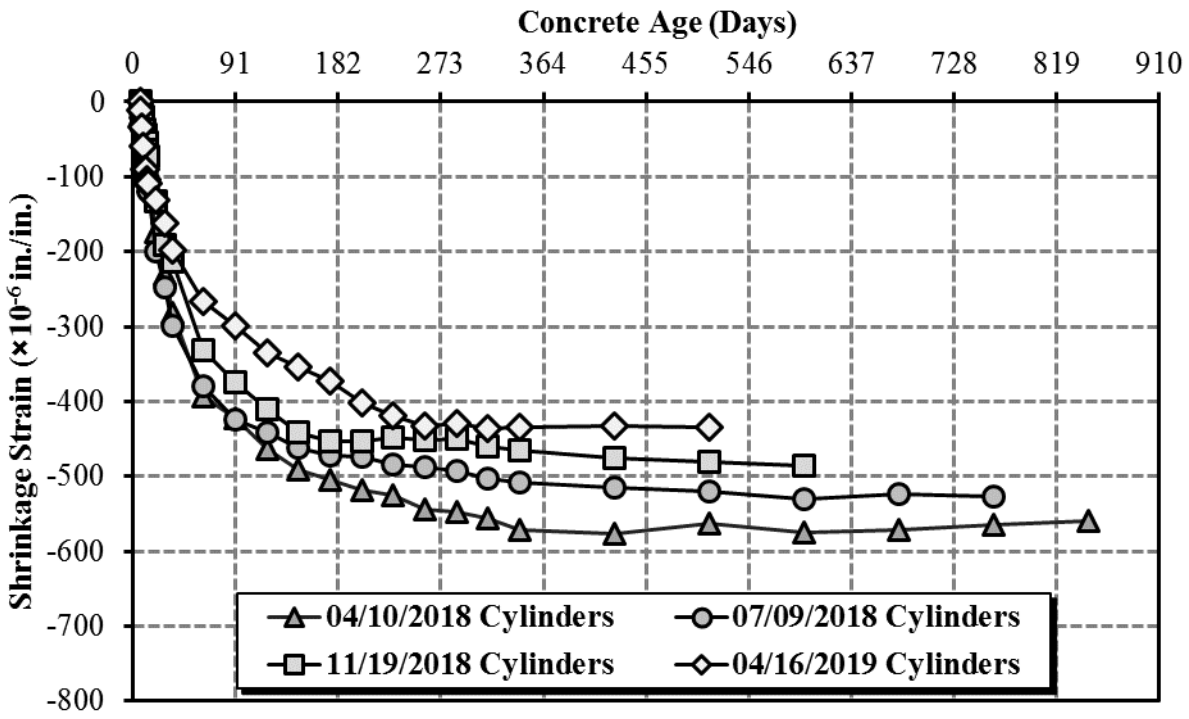

Figure 5-10: Development of shrinkage strains for 6"× 12" creep companion cylinders

The 04/10/2018 and 04/16/2019 sampling dates developed the greatest and least shrinkage strains, respectively. This difference in drying shrinkage corresponds with the difference in concrete strength as mentioned in Section 2.3.1.2. From visual observation of Figure 5-10, the vast majority of shrinkage was developed within the first year of drying, which is consistent with the historical observations discussed in Section 2.3.1.1.

5.5.2 Concrete Prisms

As presented in Table 5-8, the largest average 18-month shrinkage strain was recorded for the moist-cure specimens from the 04/10/2018 sampling date. The smallest average 18-month shrinkage strain was recorded for the air-cure specimens from the 04/16/2019 sampling date. The development of shrinkage strains in air- and moist-cure specimens for all data collected for this project is presented in Figure 5-11 and Figure 5-12, respectively.

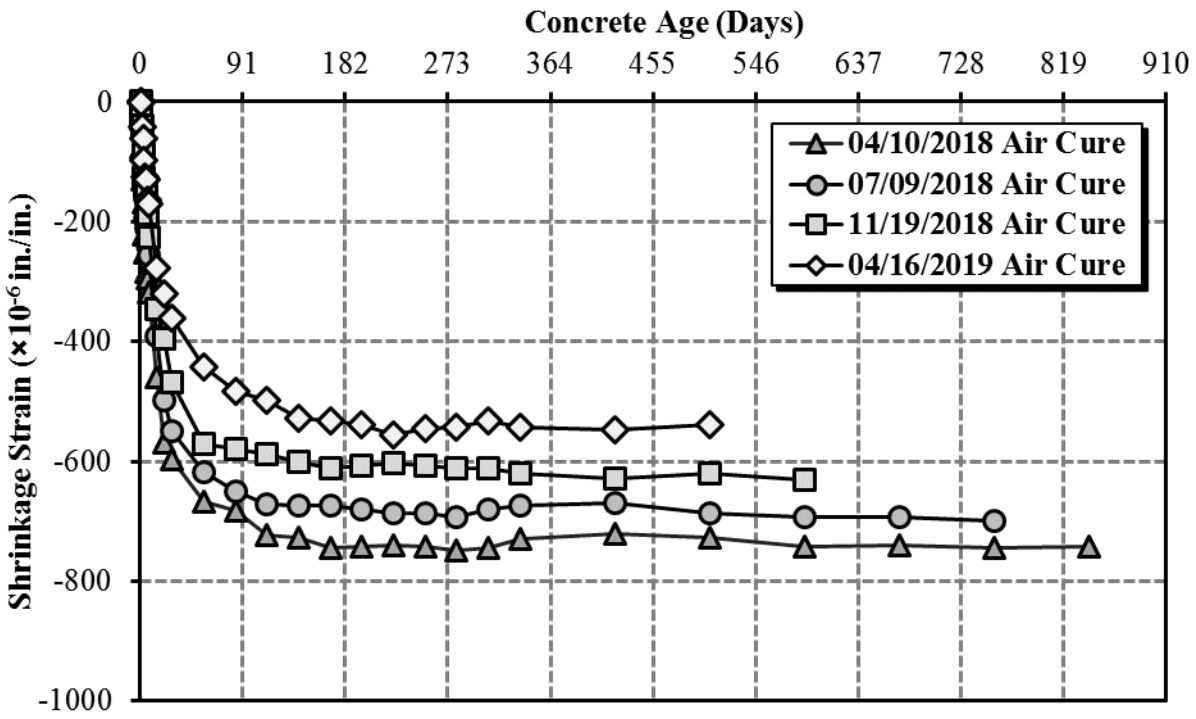

Figure 5-11: Development of shrinkage strains for air-cure concrete prisms

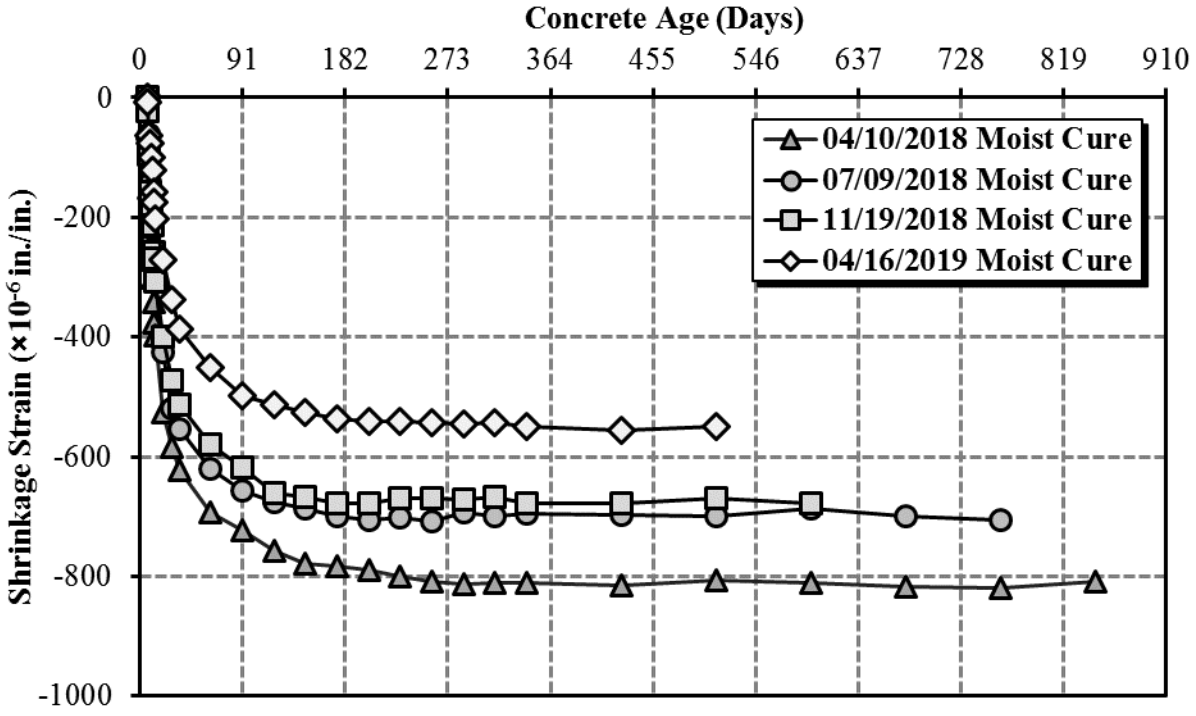

Figure 5-12: Development of shrinkage strains for moist-cure concrete prisms

All sampling dates developed greater shrinkage strains for the moist-cured specimens compared to the air-cured specimens, which was related to the increase in absorbed water in the moist-cured concrete specimens as discussed in Section 2.3.1; however, the difference between the two curing regimes was small relative to the magnitude of the average 18-month shrinkage strains. Similarly to the cylindrical specimens and strength relationship, the 04/10/2018 and 04/16/2019 sampling dates developed the greatest and least shrinkage strains, respectively. The overwhelming majority of shrinkage was developed within the first 91 days for the smaller—volume-to-surface area ratio—prism specimens compared to the cylindrical specimens.

5.6 CREEP AND COMPLIANCE RESULTS

Creep strains and compliance values from creep testing are presented in Sections 5.6.1 and 5.6.2, respectively. The most recent data for creep testing were recorded 12 months after loading, which satisfies the ASTM C512 (2015) requirement that defines the duration of creep testing to be at a minimum of one year.

5.6.1 Creep Strain Results

As discussed in Section 2.3.3.3, creep is related to concrete strength as well as the concrete mixture proportions. As presented in Table 3-2, each sampling date contained different ALDOT approved mixture proportions resulting in different strength and creep strain development. Development of creep strains is presented in Figure 5-13, Figure 5-14, Figure 5-15, and Figure 5-16 for the 04/10/2018, 07/09/2018, 11/19/2018, and 04/16/2019 sampling dates, respectively.

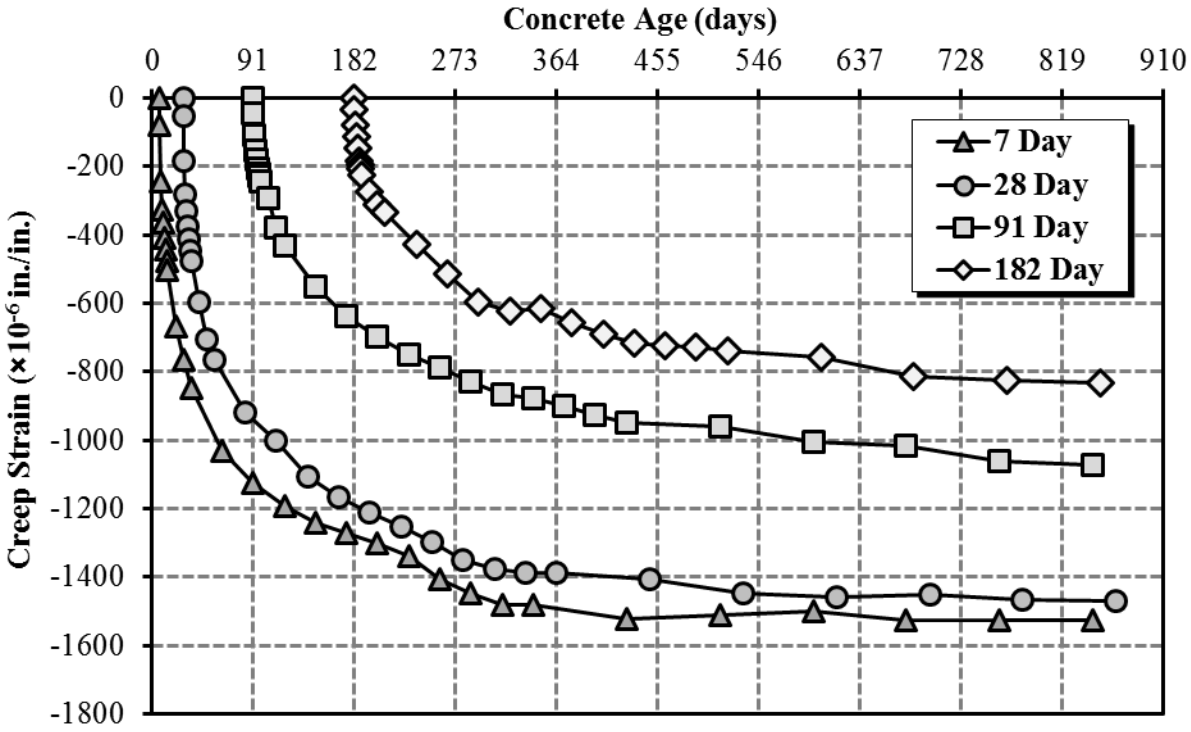

Figure 5-13: Creep strain development for the 04/10/2018 sampling date

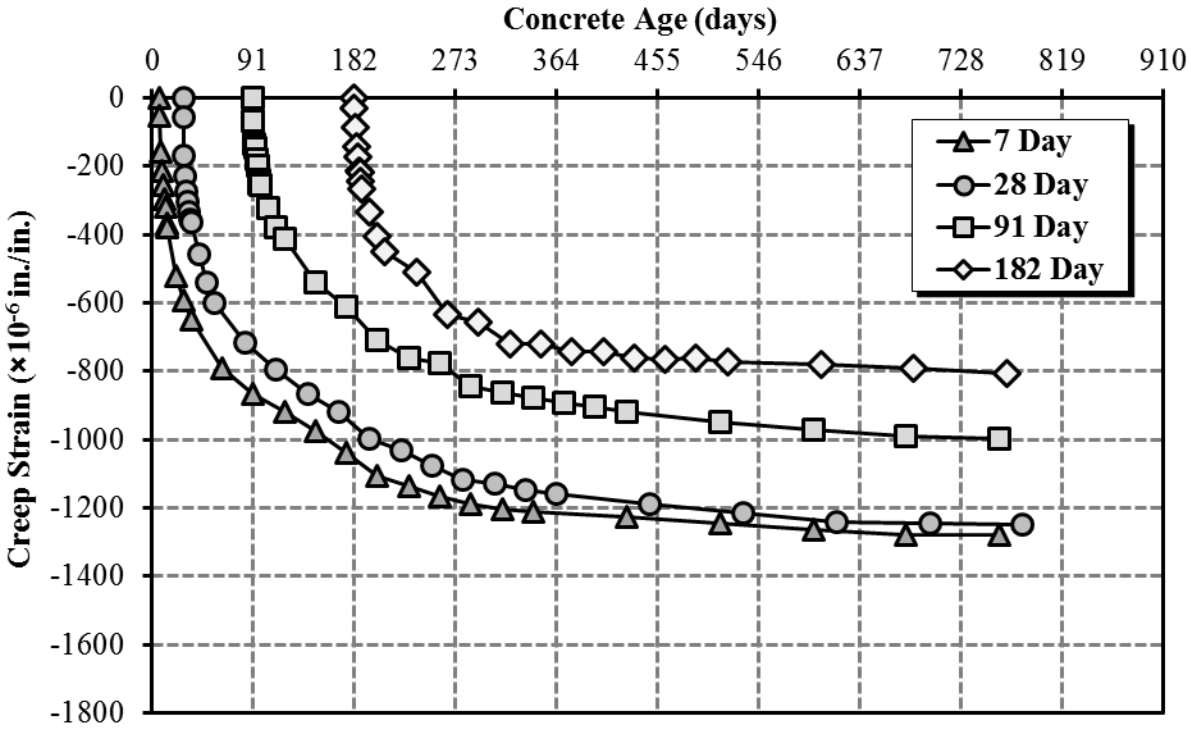

Figure 5-14: Creep strain development for the 07/09/2018 sampling date

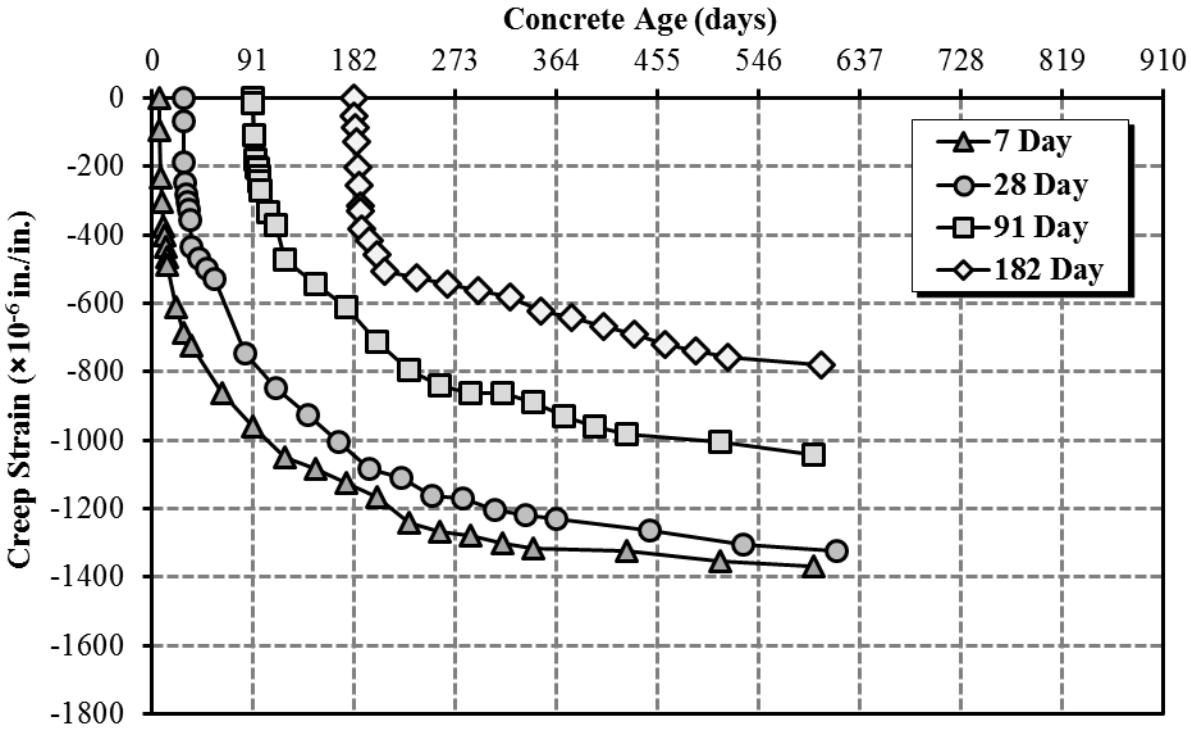

Figure 5-15: Creep strain development for the 11/19/2018 sampling date

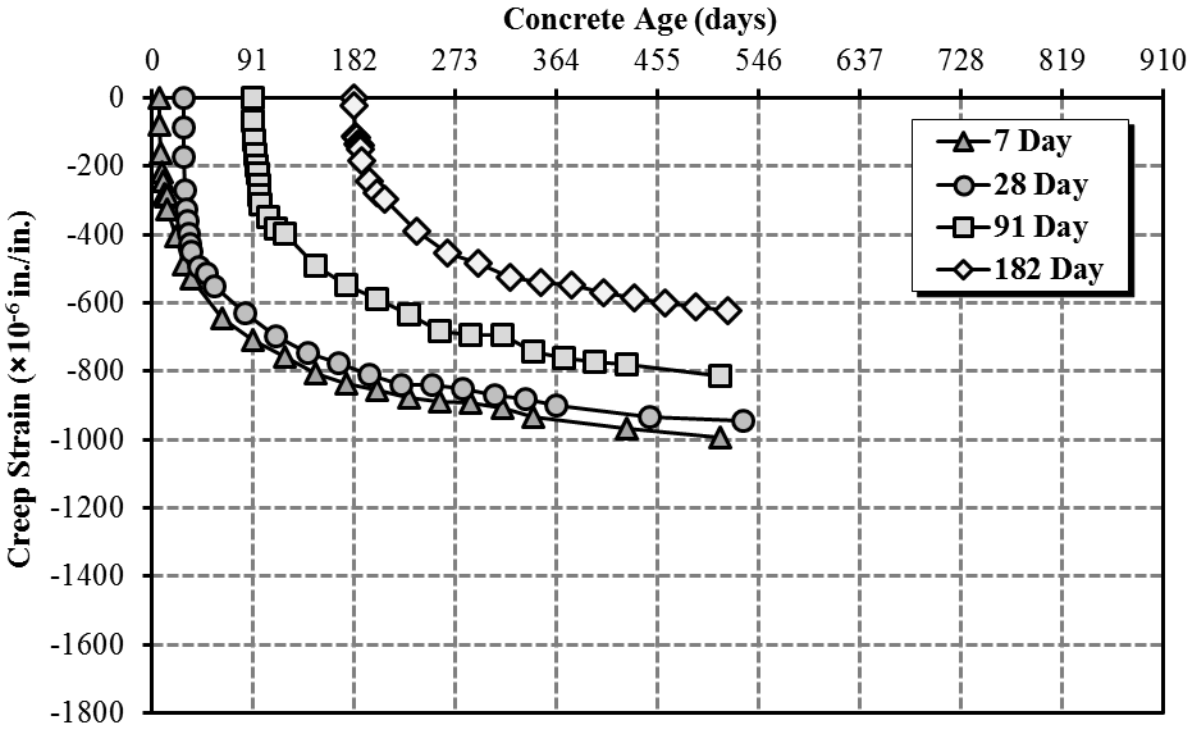

Figure 5-16: Creep strain development for the 04/16/2019 sampling date

5.6.2 Compliance Results

In Section 2.3.3 it was discussed that compliance allows for a more accurate comparison of creep strains by normalizing creep strains based on the applied stress. Compliance was calculated using Equation 2.1. The 12-month compliance results are presented in Table 5-9 for all specimens collected in this study.

Table 5-9: Compliance results for specified loading ages after 12 months under load

12-Month Compliance Results ($\times 10^{-6}$/psi)				
Sampling Date	**Loading Age**			
	7 Day	**28 Day**	**91 Day**	**182 Day**
04/10/2018	1.028	0.905	0.683	0.590
07/09/2018	0.815	0.697	0.594	0.544
11/19/2018	0.775	0.670	0.564	0.483
04/16/2019	0.538	0.476	0.449	0.408

The 04/10/2018 and 04/16/2019 sampling dates exhibited the greatest and least 12-month compliance results for each loading age, respectively. This correlates to least and greatest concrete strengths for each respective sampling date. At the earliest loading ages, the compliance varied between the 04/10/2018 and the 04/16/2019 sampling dates. The main difference between compliance results was attributed to the respective concrete strength of each sample date, with the strongest concrete having the lowest compliance and vice versa. Development of compliance is presented in Figure 5-17, Figure 5-18, Figure 5-19, and Figure 5-20 for the 04/10/2018, 07/09/2018, 11/19/2018, and 04/16/2019 sampling dates, respectively.

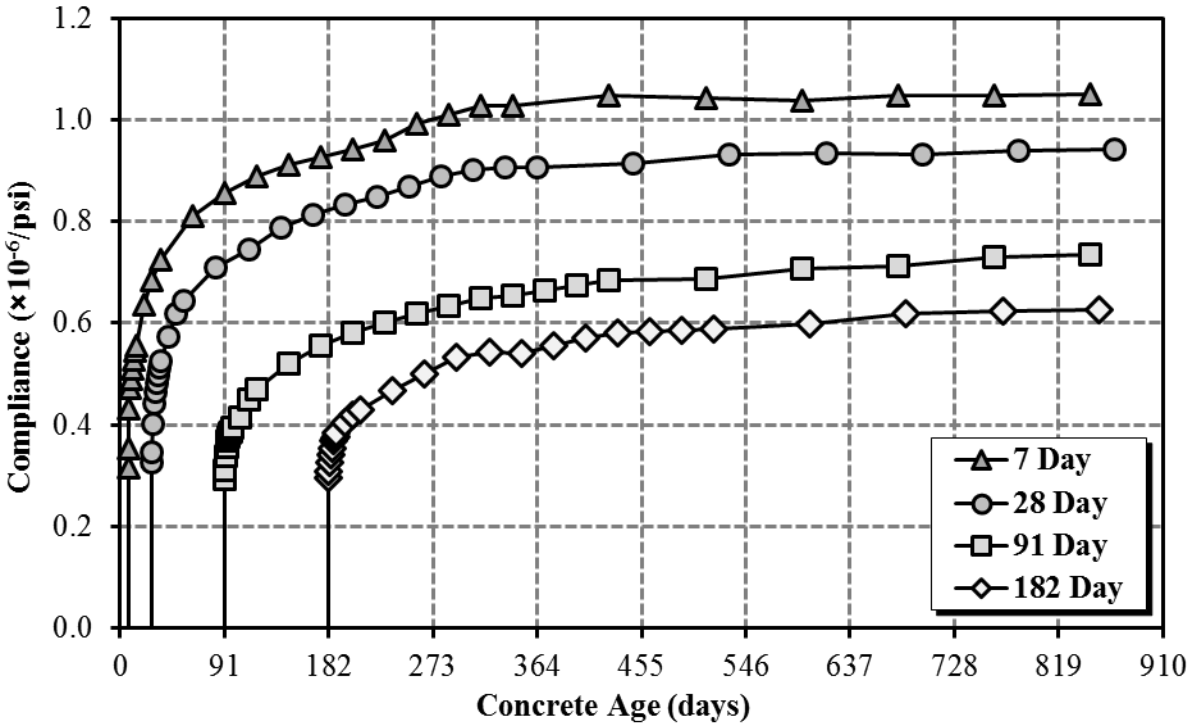

Figure 5-17: Compliance development for the 04/10/2018 sampling date

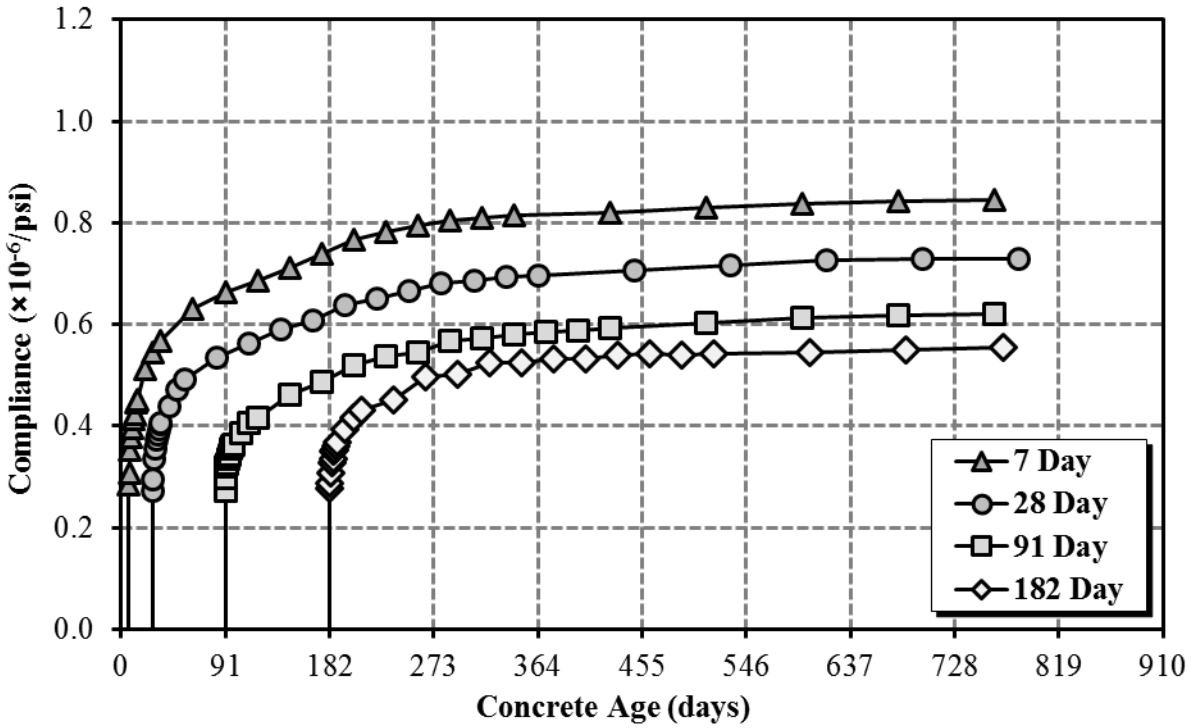

Figure 5-18: Compliance development for the 07/09/2018 sampling date

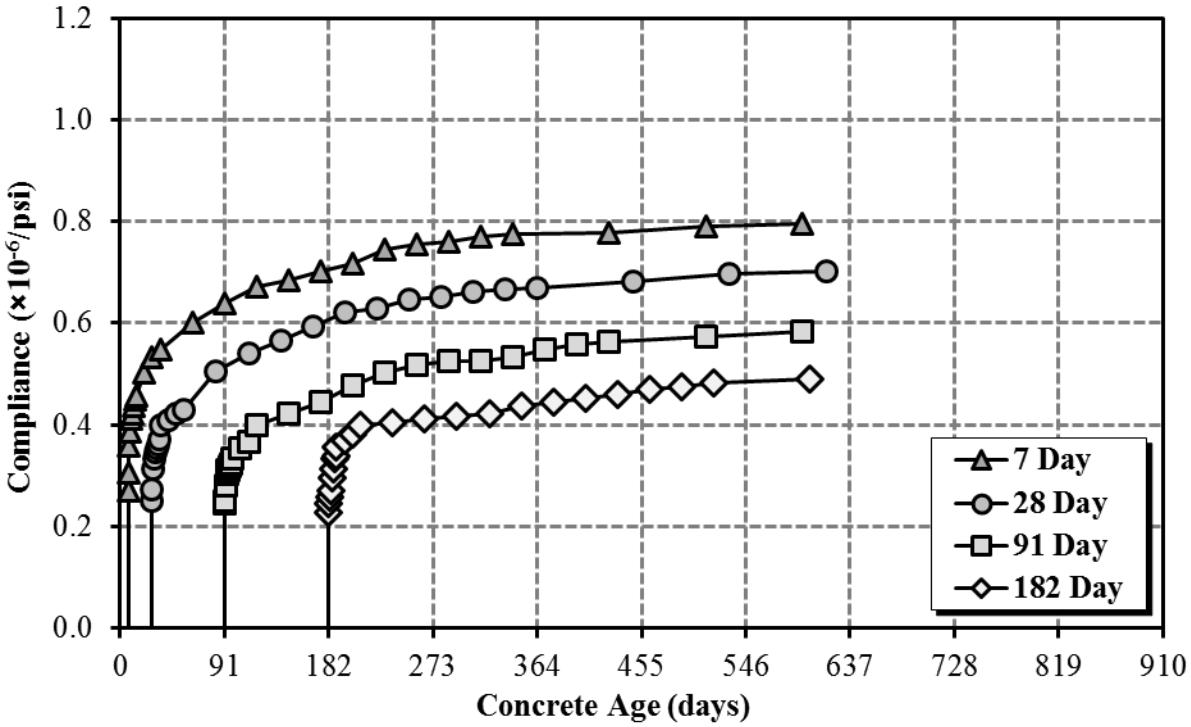

Figure 5-19: Compliance development for the 11/19/2018 sampling date

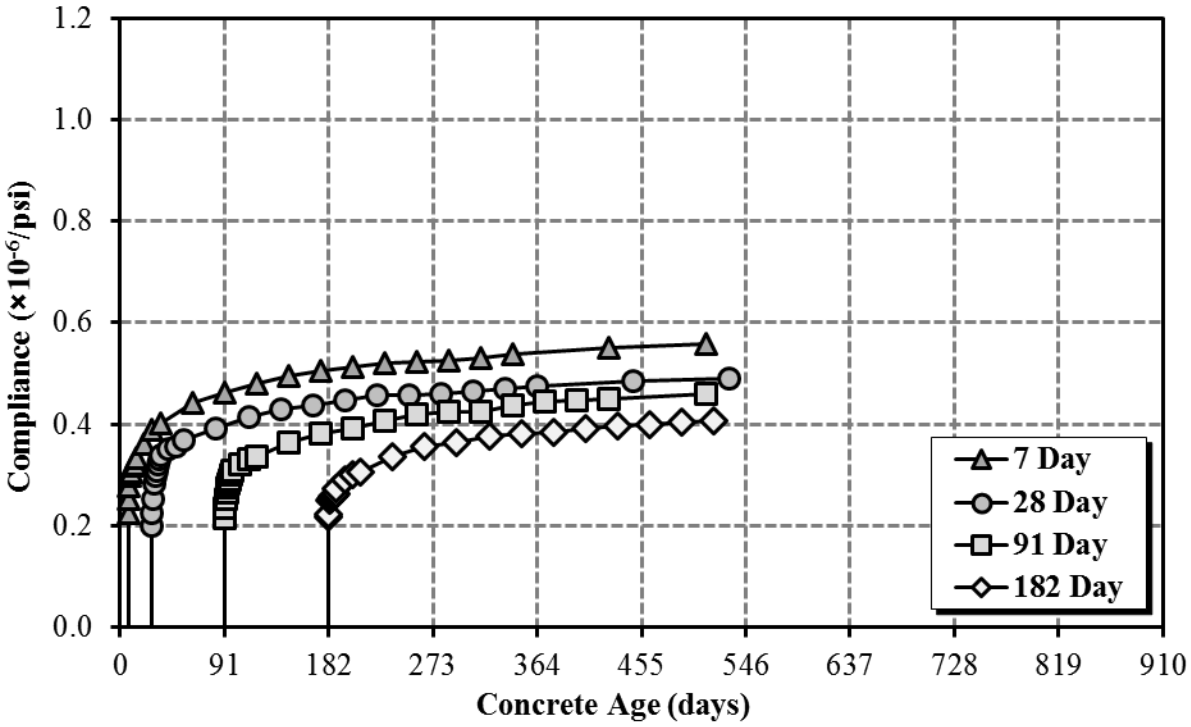

Figure 5-20: Compliance development for the 04/16/2019 sampling date

5.7 LESSONS LEARNED THROUGH TESTING

This section details important lessons learned through testing for the duration of this research project are presented. The key areas are focused on creep testing and shrinkage testing.

5.7.1 Creep Testing

In early stages of creep testing for any loading age, many individual data points are recorded, as an example: for one creep measurement there are 42 individual displacement readings across the frame, creep cylinders, and shrinkage cylinders. These readings are the most important portion of testing because if the initial displacements are incorrect, all future measurements may be impacted. A data collection template proved beneficial to keep track of all data when many measurements need to be recorded.

The next lesson pertains to loading specimens with proper alignment before applying any significant load. If any eccentricities occur upon loading, significant errors in strain measurements develop that become worse with time under load. It was found useful to use a level on three sides of the cylinders to have cylinders as close to perfectly plumb as possible. It is advised to apply an initial load of 10 percent of the required total load to the specimens, and then check the strains on the sides of both concrete specimens to ensure that the strains were similar before loading to the full target load. If any initial eccentricities are discovered, the load should be removed and the specimens realigned.

5.7.2 Shrinkage Testing

For the duration of the project only one major lesson was learned. Similarly to the creep testing, the best way to produce accurate results is to get an accurate initial strain measurement. All procedures from AASHTO T160 (2017) were followed.

5.8 SUMMARY OF RESULTS

5.8.1 Fresh Concrete Properties

After analysis of results from fresh concrete testing the following conclusions are made:

- The unit weight and temperature of fresh concrete for all sampling dates were very similar, and the unit weights were similar to the unit weight calculated from the ALDOT approved mixture proportions.

- The slump of all fresh concrete mixtures was within the required 3 to 9 inches as prescribed by ALDOT specifications for all segments that were cast.
- Total air contents ranged from 3.4 to 4.4 percent, which satisfied the ALDOT specification for total air content in fresh concrete from 3 to 6 percent.

5.8.2 Hardened Concrete Properties

After analysis of results from hardened concrete testing, excluding creep and shrinkage, the following conclusions are made:

- The 04/16/2019 and 04/10/2018 sampling dates developed the greatest and least compressive strengths over time, respectively.
- Similarly to compressive strength, the 04/16/2019 and 04/10/2018 sampling dates developed the greatest and least modulus of elasticity over time, respectively.

5.8.3 Creep and Shrinkage Testing Results

After review of creep and shrinkage testing results for all sampling dates, several conclusions are made:

- The 04/10/2018 and 04/16/2019 sampling dates exhibited the greatest and least magnitude of shrinkage across all specimen types and curing regimes, respectively, which corresponds to the difference in concrete strength as previously discussed.
- Almost all shrinkage developed within the first year for the cylindrical specimens and first three months for the prismatic specimens, and the difference in development between specimen types is attributed to the relative size of the shrinkage specimens.
- When comparing the 28-day loading age, the 04/10/2018 and 04/16/2019 sampling dates experienced the greatest and least creep, respectively.
- The 04/10/2018 and 04/16/2019 sampling dates exhibited the greatest and least 12-month compliance results for each loading age, respectively.
- Concrete compressive strength systematically increased throughout the duration of the project, which is believed to be the main contributing factor for decreased creep and shrinkage deformations observed through testing.

CHAPTER 6: PREDICTING CREEP AND SHRINKAGE IN THE CONCRETE OF THE I-59/I-20 BIRMINGHAM ALABAMA SEGMENTAL BRIDGE

6.1 INTRODUCTION

One of the primary objectives of this research effort is to compare volumetric changes in concrete mixtures collected from the Birmingham I-59/I-20 segmental bridge project to predicted values from methods outlined in Section 2.4 that included:

- ACI 209 (2008),
- AASHTO LRFD 2017,
- GL 2000 (Gardner and Lockman 2001),
- B3 (Bazant and Baweja 2000),
- CEB MC 1990 (CEB 1990), and
- CEB MC 2010 (fib 2012).

This chapter presents results from predicting creep and shrinkage strains in concrete by providing comparisons between data collected during this research effort and the predicted values from the before mentioned methods. Gardner and Lockman (2001) state for model comparison, "shrinkage within 15 percent would be excellent, and a prediction within 20 percent would be adequate." Based on this statement, any model that predicts results within 20 percent of the measured data was deemed excellent. In order to graphically visualize measured and predicted results, error bands are displayed on all comparison figures at ±20 percent. Any value that falls above the line of equality corresponds to an over prediction of the measured value, and vice versa.

In Section 2.4 it was presented that compliance values are used for representing both initial elastic and creep strains to reduce the imperfections in test data; however, the predicted modulus of elasticity is required for calculation of predicted compliance. A summary of all modulus of elasticity predictions is presented in Section 6.2.

Creep and shrinkage prediction results using the six methods mentioned are presented in Sections 6.3 through 6.8. Each section defines the input parameters as well as provides a graphical

comparison of predicted compliance and shrinkage results to measured results from creep and shrinkage testing. Although shrinkage was predicted for both cylindrical and prism specimens, this chapter focuses on the cylindrical specimens, which had a more representative volume-to-surface area ratio of segments cast for the Birmingham I-59/I-20 segmental bridge.

Results for predicting shrinkage in the prism specimens are presented in Appendix B. Compliance results for all models are broken down for each sampling date and loading age in Appendix B. A detailed statistical analysis of each prediction model, to determine which model is most accurate in predicting creep and shrinkage, is presented in Chapter 7.

6.2 MODULUS OF ELASTICITY PREDICTIONS

The modulus of elasticity is predicted for each loading age of creep testing by all methods listed in Section 6.1. Descriptions of how each method predicts the modulus of elasticity at varying concrete ages are presented in Section 2.4. A summary of inputs for modulus of elasticity prediction is presented in Table 6-1. The predicted modulus of elasticity for all loading ages and methods is presented Table 6-2.

Table 6-1: Modulus of elasticity prediction methods summary of inputs

Defined	Method	Input		Formulation
Section 2.4.1	ACI 209	Compressive Strength	Table 5-2	Equation 2.15
		Unit Weight	Table 5-1	
Section 2.4.2	AASHTO LRFD 2017	Compressive Strength	Table 5-2	Equation 2.30
		Unit Weight	Table 5-1	
Section 2.4.3	GL 2000	Compressive Strength	Table 5-2	Equation 2.36
Section 2.4.4	B3	Compressive Strength	Table 5-2	Equation 2.63
		28-Day Elastic Modulus	Equation 2.49	
Section 2.4.5	CEB MC 1990 and CEB MC 2010	Compressive Strength	Table 5-2	Equation 2.84
		Cement Class Type I/II	Normal-Hardening	
		Cement Class Type III	Rapid-Hardening	
		Aggregate Type	Quartzite	

Table 6-2: Measured and Predicted modulus of elasticity for all loading ages and method

Modulus of Elasticity (ksi)							
Sampling Date	**Age (days)**	**Measured Value**	**ACI 209**	**AASHTO LRFD 2017**	**GL 2000**	**B3**	**CEB MC**
04/10/2018	**7**	3,800	4,070	4,260	4,210	3,990	4,590
	28	4,050	4,450	4,520	4,560	4,450	5,030
	91	3,850	4,420	4,490	4,530	4,730	5,350
	182	4,150	4,560	4,590	4,660	4,780	5,450
07/09/2018	**7**	4,250	4,130	4,210	4,390	4,170	4,720
	28	4,250	4,520	4,470	4,760	4,670	5,190
	91	4,200	4,660	4,560	4,880	4,960	5,520
	182	4,300	4,660	4,560	4,880	5,010	5,620
11/19/2018	**7**	4,400	4,660	4,720	4,660	4,250	5,090
	28	4,600	4,940	4,910	4,910	4,840	5,320
	91	4,600	5,040	4,970	5,000	5,140	5,590
	182	4,500	5,010	4,950	4,970	5,190	5,670
04/16/2019	**7**	5,100	4,920	4,860	4,940	4,540	5,000
	28	5,300	5,150	5,010	5,150	5,100	5,510
	91	5,400	5,250	5,070	5,240	5,420	5,850
	182	5,400	5,190	5,030	5,180	5,470	5,960

6.3 ACI 209 MODEL CREEP AND SHRINKAGE PREDICTIONS

All creep and shrinkage predictions with the ACI 209 Model are defined in Section 2.4.1. The ACI 209 creep and shrinkage prediction method does not clearly define whether cement content is only portland cement used in mixture proportions or total cementitious material content, which includes SCMs. From previous studies of creep and shrinkage in concrete corresponding to the Birmingham I-59/I-20 segmental bridge (Richey 2018), it was decided that cement content should be taken as the sum of all cementing materials for each mixture proportion. The ACI 209 Model does not specify directly when it addresses slump; however, since most of the workability is from the use of chemical admixtures a pre-admixture slump of zero inches is used. A summary of key input parameters and justification is presented in Table 6-3.

Table 6-3: ACI 209 creep and shrinkage prediction method summary of inputs

Creep and Shrinkage Model Input Parameters		
Input		***Justification***
Relative humidity	48.7%	Average measured value
Volume-to-surface area ratio of cylinders	1.5 in.	Excluding cylinder ends not exposed to atmosphere
Volume-to-surface area ratio of prisms	0.66 in.	All six sides exposed to atmosphere
Slump	0 in.	Assumed pre-admixture slump
Cement content	Varies	Used total cementitious material content
Air content	Table 5-1	Determined with fresh concrete testing
Predicted elastic modulus for each loading age	Table 6-2	Determined with Equation 2.15

A comparison of the measured and predicted compliance for all loading ages across all sample dates is provided in Figure 6-1. The majority of compliance values are well outside the ±20 percent error bands. The 04/10/2018 sampling date is by far the most under predicted in comparison to the later sampling dates. In general the ACI 209 Model substantially underestimates compliance when compared to testing results.

The measured versus predicted shrinkage strains for all cylindrical specimens is presented in Figure 6-2. Similar to compliance, the 04/10/2018 sampling date is most under predicted where the majority of shrinkage strains fall on or below the negative error band; however, the 04/16/2019 sampling date is over predicted at larger strain values. Unlike compliance, the ACI 209 Model predicts a large portion shrinkage strains within the error bands.

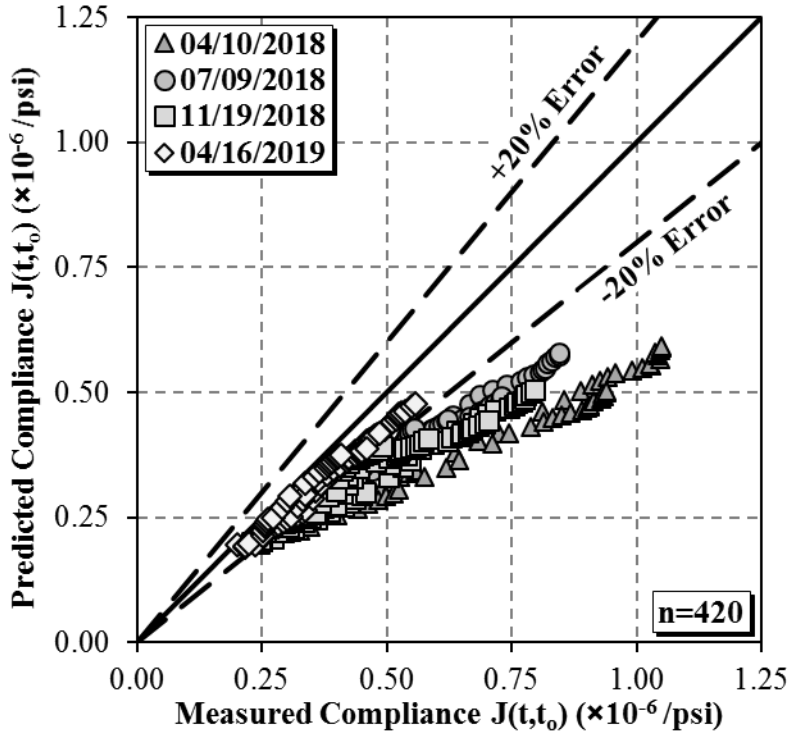

Figure 6-1: Measured versus predicted compliance using the ACI 209 Model

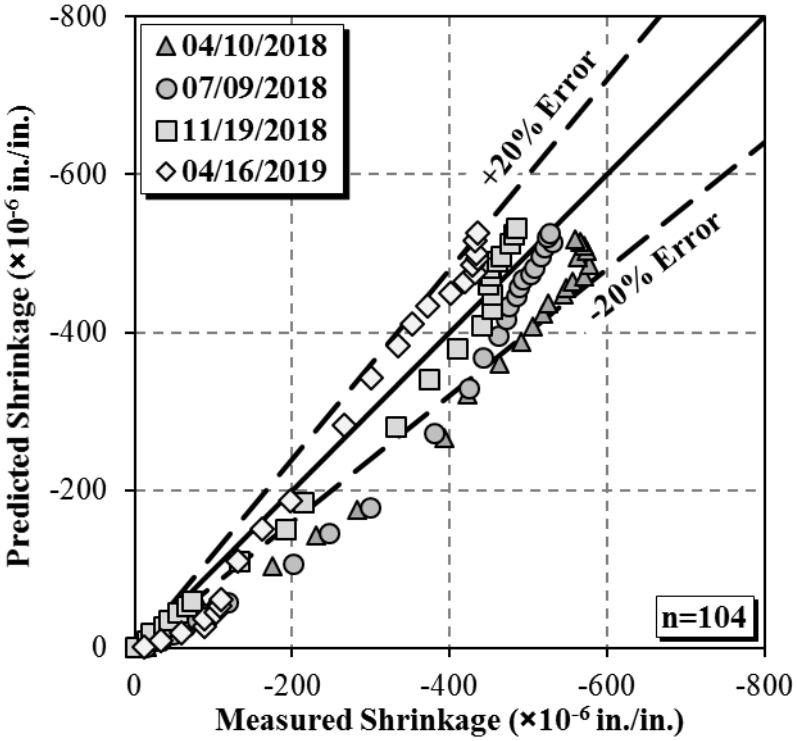

Figure 6-2: Measured versus predicted shrinkage strains for cylinders using the ACI 209 Model

6.4 AASHTO LRFD 2017 MODEL CREEP AND SHRINKAGE PREDICTIONS

All creep and shrinkage predictions with the AASHTO LRFD 2017 Model are defined in Section 2.4.2. No assumptions for input parameters are made for creep and shrinkage predictions, unlike the ACI 209 Model. Key input parameters and justification for the AASHTO LRFD Model are presented in Table 6-4.

Table 6-4: AASHTO LRFD 2017 creep and shrinkage prediction method summary of inputs

Creep and Shrinkage Model Input Parameters		
Input		***Justification***
Relative humidity	48.7%	Average measured value
Volume-to-surface area ratio of cylinders	1.5 in.	Excluding cylinder ends not exposed to atmosphere
Volume-to-surface area ratio of prisms	0.66 in.	All six sides exposed to atmosphere
Chronological age at application of loading	Varies	7, 28, 91, 182 days
Compressive strength at loading	Table 5-2	Determined with hardened concrete testing
Predicted elastic modulus at loading	Table 6-2	Determined with Equation 2.30
Specimens exposed to drying before 5 days of curing	+20% shrinkage strains	Based on AASHTO LRFD 2017 provisions

A comparison between the measured and predicted compliance values for all specimens using the AASHTO LRFD 2017 Model is presented in Figure 6-3. The vast majority of compliance is underestimated across all sampling dates. The compliance results for the 04/10/2018 sampling date are well below the negative error band. In general the AASHTO LRFD 2017 Model is very poor at estimating compliance.

Shrinkage comparisons using the AASHTO LRFD 2017 Model are presented in Figure 6-4. Unlike compliance, the vast majority of shrinkage strains are within the error bands. Even for the greatest shrinkage strains, the AASHTO LRFD 2017 Model predicts shrinkage strains within ±20 percent of the measured results.

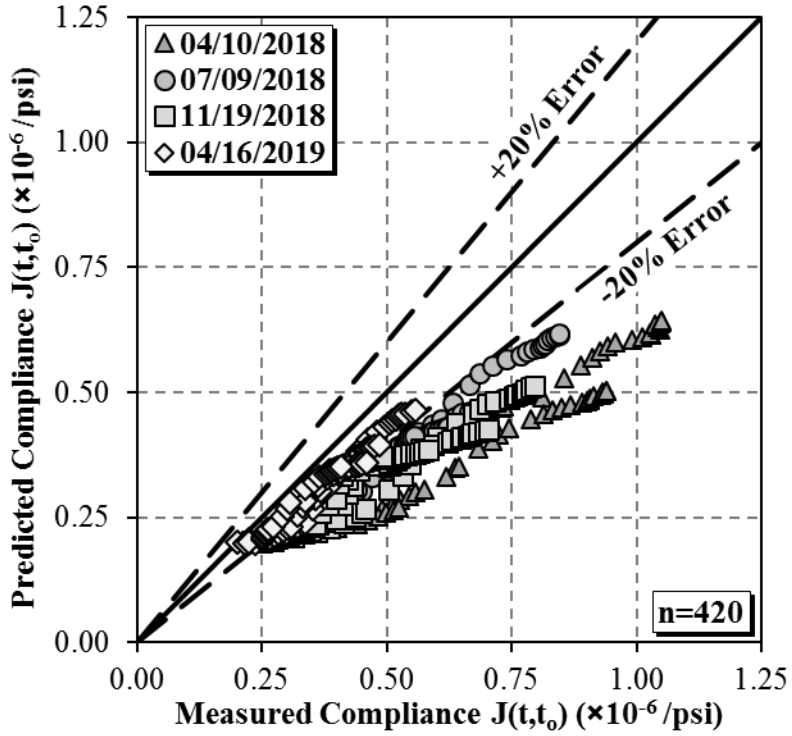

Figure 6-3: Measured versus predicted compliance using the AASHTO LRFD 2017 Model

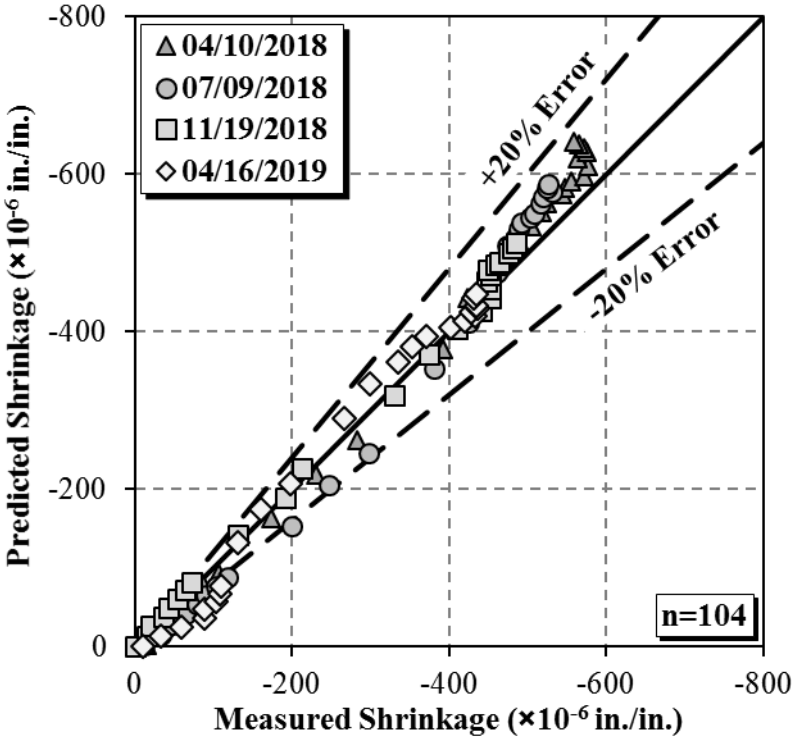

Figure 6-4: Measured versus predicted shrinkage strains for cylinders using the AASHTO LRFD 2017 Model

6.5 GL 2000 MODEL CREEP AND SHRINKAGE PREDICTIONS

All predictions of creep and shrinkage use the methods outlined in Section 2.4.3 for the GL 2000 Model. Based on the inputs required for the GL 2000 Model, no assumptions are needed. It is important to remember that the GL 2000 Model uses the adjusted equivalent-age maturity of the concrete at loading. Input parameters for the GL 2000 Model are summarized in Table 6-5 with justification where necessary.

Table 6-5: GL 2000 creep and shrinkage prediction method summary of inputs

Creep and Shrinkage Model Input Parameters		
Input		***Justification***
Relative humidity	48.7%	Average measured value
Volume-to-surface area ratio of cylinders	1.5 in.	Excluding cylinder ends not exposed to atmosphere
Volume-to-surface area ratio of prisms	0.66 in.	All six sides exposed to atmosphere
28-day measured compressive strength	Table 5-2	Determined with hardened concrete testing
Predicted elastic modulus at loading age	Table 6-2	Determined with Equation 2.36
Equivalent age at loading	Table 5-5	Based on GL 2000 maturity index and measured concrete temperatures
Equivalent age when drying began	Table 5-6	Based on GL 2000 maturity index and measured concrete temperatures

Compliance values predicted with the GL 2000 Model are compared to measured compliance values in Figure 6-5. It can be seen that the majority of compliance values are within the ±20 percent error bands. Some of the 04/10/2018 data are slightly outside of the -20 percent band, and the 04/16/2019 specimens appear to be over predicted. The 07/09/2018 and 11/19/2018 sampling dates are predicted very close to the line of equality.

The measured versus predicted shrinkage strains in cylindrical specimens using the GL 2000 Model are presented in Figure 6-6. The GL 2000 Model seems to underestimate shrinkage values at early ages with most data below the negative error band; however, the ultimate shrinkage strains appear to be estimated reasonably well for all sampling dates.

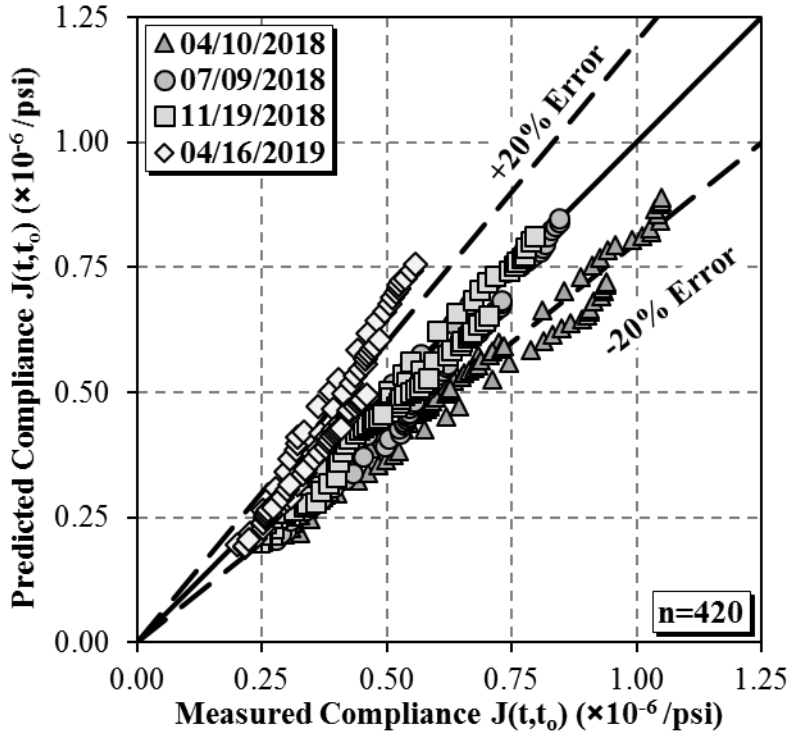

Figure 6-5: Measured versus predicted compliance using the GL 2000 Model

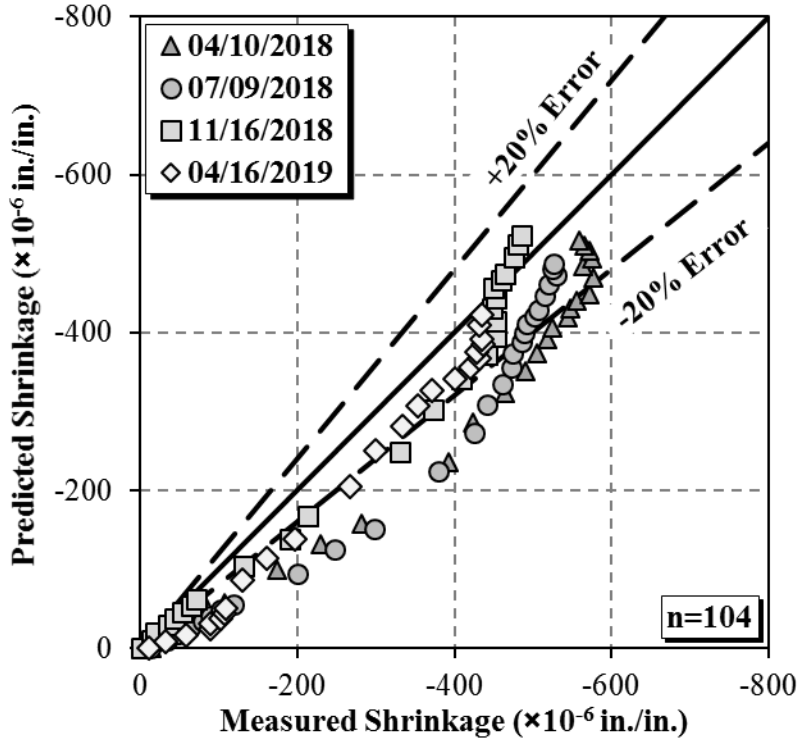

Figure 6-6: Measured versus predicted shrinkage strains for cylinders using the GL 2000 Model

6.6 B3 MODEL CREEP AND SHRINKAGE PREDICTIONS

Creep and shrinkage prediction with the B3 Model follows the formulation described in Section 2.4.4 with only one assumption. Similar to the ACI 209 Model, the cement content is assumed as the total cementitious materials content which includes any SCMs in the mixture proportions. Like the GL 2000 Model, the B3 Model uses equivalent-age maturity of the concrete to predict compliance and shrinkage. The key input parameters of the B3 Model for creep and shrinkage are summarized in Table 6-6.

Table 6-6: B3 Model creep and shrinkage prediction method summary of inputs

Creep and Shrinkage Model Input Parameters		
Input		***Justification***
Relative humidity	48.7%	Average measured value.
Volume-to-surface area ratio of cylinders	1.5 in.	Excluding cylinder ends not exposed to atmosphere
Volume-to-surface area ratio of prisms	0.66 in.	All six sides exposed to atmosphere
28-day measured compressive strength	Table 5-2	Determined with hardened concrete testing
28-day predicted modulus of elasticity	Table 6-2	Determined with Equation 2.63
Equivalent age at loading	Table 5-5	Based on B3 maturity index and measured concrete temperatures
Equivalent age when drying began	Table 5-6	Based on B3 maturity index and measured concrete temperatures
Cement content	Varies	Used total cementitious material content

The summary of compliance results using the B3 Model compared to measured values are presented in Figure 6-7. Based on visual assessment, it appears that the majority of early-age compliance is below the negative error band. In addition, the majority of the compliance values corresponding to the 04/10/2018 sampling date are underestimated. The opposite is true for the 04/16/2019 sampling date where the B3 Model overestimates compliance.

B3 Model predicted shrinkage strains are presented in Figure 6-8 where all measured shrinkage strains are severely underestimated. Although the development appears to be linear for the B3 Model shrinkage predictions, the overall predictions are very poor.

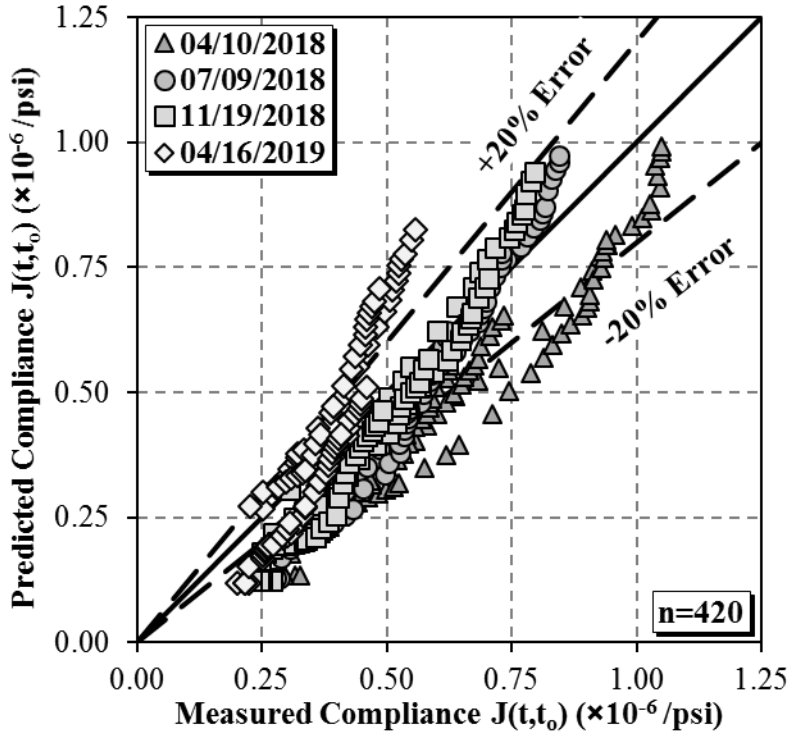

Figure 6-7: Measured versus predicted compliance using the B3 Model

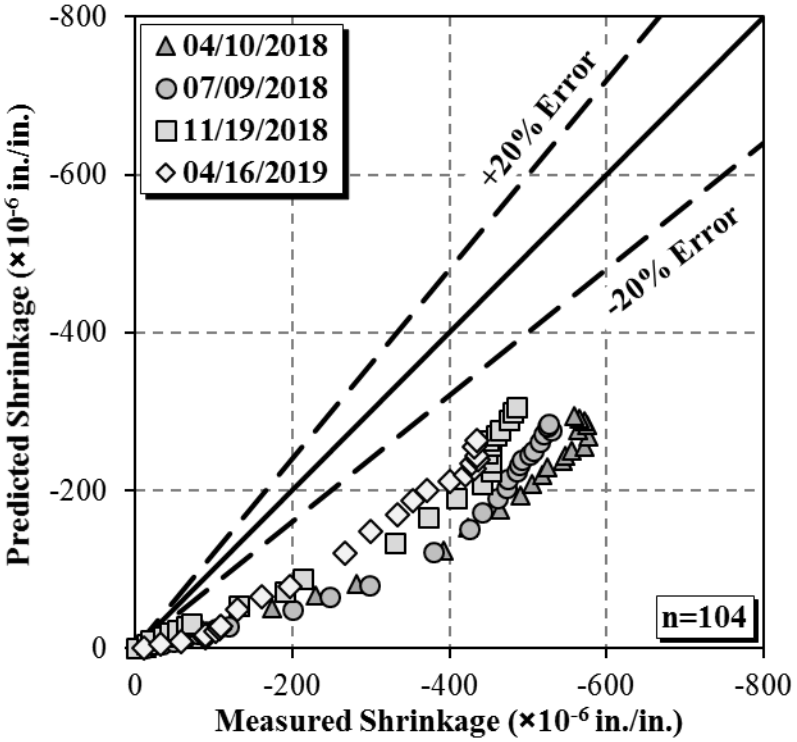

Figure 6-8: Measured versus predicted shrinkage strains for cylinders using the B3 Model

6.7 CEB MC 1990 MODEL CREEP AND SHRINKAGE PREDICTIONS

The predictions of creep and shrinkage using the CEB MC 1990 follow the methods outlined in Section 2.4.5. Again no direct assumptions had to be made for the inputs for compliance and shrinkage predictions. As discussed in Section 2.4.6, there are only minor changes between the CEB MC 1990 and CEB MC 2010 Models, so the input parameters that apply to either model are presented in Table 6-7. Inputs for the CEB MC Models are in SI units; however, predicted values are presented in USCS units for comparison purposes.

Table 6-7: CEB MC 1990 creep and shrinkage prediction method summary of inputs

Creep and Shrinkage Model Input Parameters		
Input		***Justification***
Relative humidity	48.7%	Average measured value
Notional member size of cylinders	76.2 mm	Based on CEB MC provisions
Notional member size of prisms	38.1 mm	Based on CEB MC provisions
28-day measured compressive strength	Table 5-2	Determined with hardened concrete testing
Predicted elastic modulus at loading age	Table 6-2	Determined with Equation 2.84
Equivalent age at loading	Table 5-5	Based on CEB MC maturity index and measured concrete temperatures
Cement class, Type I/II	42.5 N	Normal-hardening cement
Cement class, Type III	42.5 R	Rapid-hardening cement
Equivalent age when drying began	Table 5-6	Based on CEB MC maturity index and measured concrete temperatures

A summary for compliance predicted using the CEB MC 1990 Model versus the measured results are presented in Figure 6-9. Similarly to the GL 2000 Model, compliance for the most part is predicted within the error bands. Results from the 04/10/2018 and 04/16/2019 sampling dates appear to be slightly underestimated and overestimated, respectively.

Measured versus predicted shrinkage strains using the CEB MC 1990 Model are presented in Figure 6-10. The development of shrinkage appears linear; however, all shrinkage strains fall below the negative error band corresponding to an underestimate of ultimate shrinkage strains.

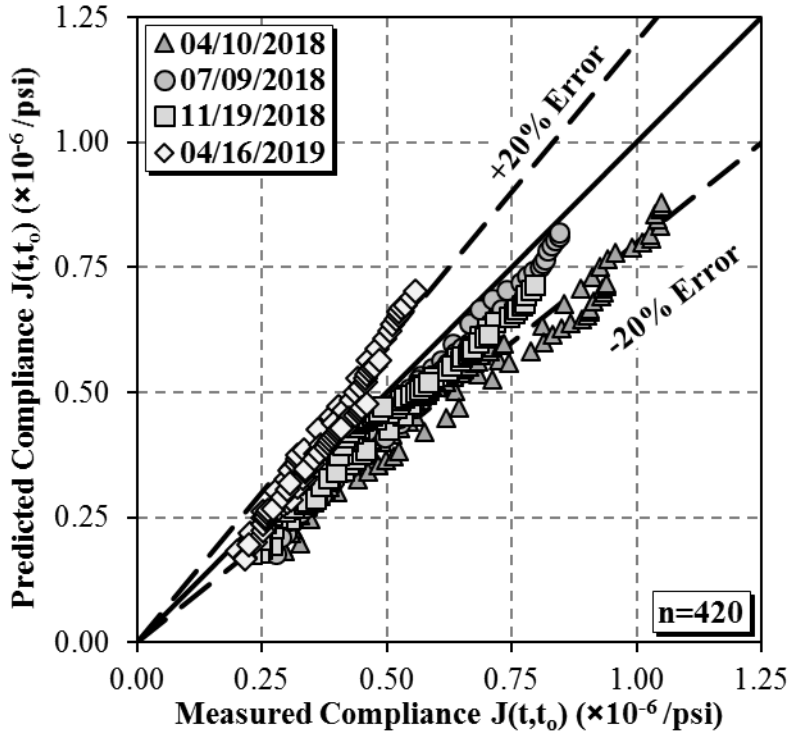

Figure 6-9: Measured versus predicted compliance using the CEB MC 1990 Model

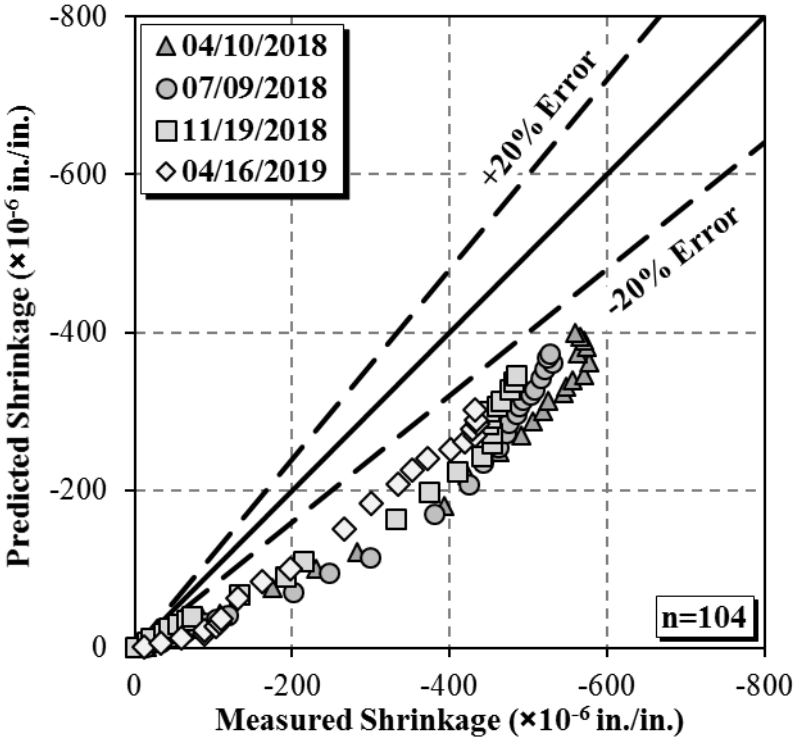

Figure 6-10: Measured versus predicted shrinkage strains for cylinders using the CEB MC 1990 Model

6.8 CEB MC 2010 MODEL CREEP AND SHRINKAGE PREDICTIONS

As stated in the previous section all input parameters are the same between the CEB MC 1990 and CEB MC 2010 Models as presented in Table 6-7. The CEB MC 2010 Models creep and shrinkage predictions is as defined in Section 2.4.6. Measured versus predicted compliance using the CEB MC 2010 Model are presented in Figure 6-11.

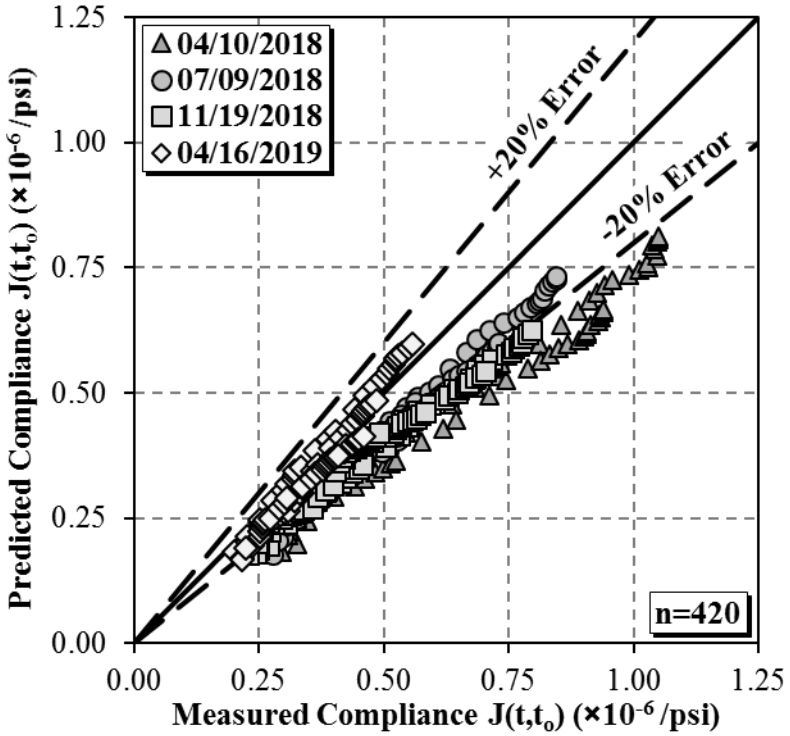

Figure 6-11: Measured versus predicted compliance using the CEB MC 2010 Model

Unlike its predecessor, CEB MC 1990, the majority of compliance is underestimated using the CEB MC 2010 Model. Most of the compliance values for the 04/16/2019 sampling date are within the error bands; however, the majority of compliance values for the remaining sampling dates are below the line of equality. In general, the CEB MC 1990 Model underestimates compliance when compared to the measured results.

Shrinkage strains, presented in Figure 6-12, are predicted somewhat closer to the measured strains using the CEB MC 2010 Model than using the CEB MC 1990 Model. In general the CEB MC 2010 Model underestimates shrinkage strains for the concrete collected for this project, where the majority of shrinkage strains are below the -20 percent error band.

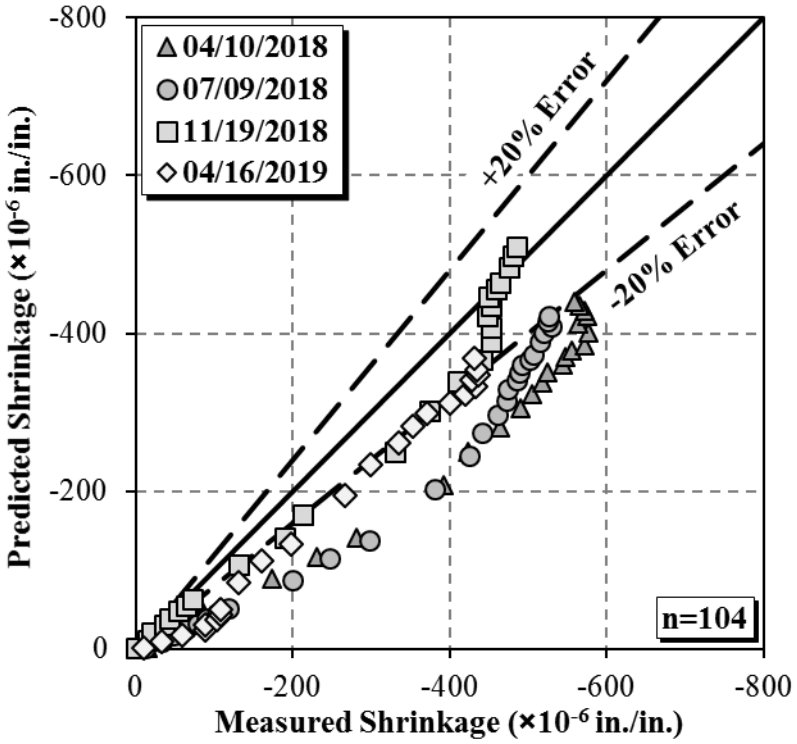

Figure 6-12: Measured versus predicted shrinkage strains for cylinders using the CEB MC 2010 Model

CHAPTER 7: STATISTICAL ANALYSIS AND MODEL CALIBRATION

7.1 INTRODUCTION

This chapter focuses on statistical analysis of the creep and shrinkage prediction methods selected for this research effort to determine the most accurate model for predicting both creep and shrinkage. In order to complete one of the most important objectives of this research project, the most accurate model was calibrated specifically for the creep and shrinkage characteristics of the concrete in the Birmingham I-59/I-20 segmental bridge.

The statistical comparison techniques used in this chapter are covered in Section 7.2. Results from statistical analysis are presented in Section 7.3. Model selection based on the statistical analysis is presented in Section 7.4. The calibration of the model selected as most accurate for predicting both creep and shrinkage is discussed in Section 7.5. As a secondary objective of this research effort, the CEB MC 1990 Model was calibrated for potential use in bridge analysis software and is presented in Section 7.6. A summary of the statistical analysis and model calibration is covered in Section 7.7.

7.2 STATISTICAL COMPARISON TECHNIQUES

Several statistical measures are used for comparing accuracy between models. Percent error, calculated using Equation 7.1, is a simple method for comparison between known values (ACI 209.2R 2008). Any negative percent error presented in this statistical analysis corresponds to the under prediction of a measured value, and any positive percent error corresponds to the over prediction of a measured value.

$$\%\text{Error} = \left(\frac{\hat{X} - \bar{X}}{\bar{X}}\right) \times 100 \qquad \text{Equation 7.1}$$

Where,

$\hat{X}$ = predicted value and

$\bar{X}$ = measured value.

The next measure of model accuracy used in this statistical analysis is the unbiased estimate of the standard deviation of the error. McCuen (1985) defines the unbiased estimate of the standard deviation of the error, Sj, according to Equation 7.2. Sj values are similar to sample standard deviation; however, instead of comparing values in a data set to the mean value, respective differences between measured and predicted values are compared. A model that predicts with 100 percent accuracy will have a Sj value of zero. Sj values have the same units as the data being compared.

$$S_j = \sqrt{\frac{1}{n-1}\sum_{i}^{n} {\Delta_i}^2} \qquad \text{Equation 7.2}$$

Where,

S_j = unbiased estimate of the standard deviation of the error,

n = the number of data points, and

Δ_i = the difference between measured and predicted values.

For graphical analysis of model accuracy, two additional statistical techniques are used. The sample variance quantifies the variation between similar values, and when plotted against the mean value, a low variance indicates that the values are very close to one another. Variance is defined in Equation 7.3 (ACI 209.2R 2008). The final graphical measure used in visualizing model accuracy is a plot of residual values. A residual value is simply the measured value subtracted from the predicted value, where a negative residual correlates to under prediction of measured value.

$$S^2 = \frac{\sum(y_i - \mu)^2}{n-1} \qquad \text{Equation 7.3}$$

Where,

S^2 = sample variance,

y_i = the value of one data point,

μ = mean of all data points, and

n = number of data points.

7.3 STATISTICAL ANALYSIS RESULTS

In order to quantify how accurately each model predicts compliance and shrinkage a rating system is developed based on the unbiased estimate of the standard deviation of the error as mentioned in the previous section. A rating index between 0.00 and 1.00 is given to each data set. A rating index of 1.00 is given to the lowest Sj and a value of 0.00 is given to the highest Sj, representing the most accurate and least accurate value, respectively. For all other Sj values, a rating index is obtained by linearly interpolating between the minimum and maximum Sj values.

A mean rating index is computed for each model which quantifies each model's accuracy to predict the measured values as compared to all other models. In addition to the mean rating index for each model, a model ranking is assigned based strictly on the mean rating index. Model ranking is assigned with a value of 1 through 6, where the model with the highest mean rating index receives a 1 indicating that is it the most accurate model, and the model with the lowest mean rating index receives a 6 indicating that it is the least accurate model.

7.3.1 Accuracy of Compliance Prediction Models

All measured and predicted compliance values for each loading age are combined to obtain one Sj value for a specific sampling date. The mean rating indices for compliance obtained when using the above mentioned method are presented in Table 7-1.

Table 7-1: Mean Rating Indices for all models to predict compliance

Sampling Date	Index	Compliance Prediction Model					
		ACI 209	**AASHTO LRFD 2017**	**GL 2000**	**B3**	**CEB MC 1990**	**CEB MC 2010**
04/10/2018	S_j ($\times 10^{-6}$/psi)	0.274	0.265	0.140	0.155	0.142	0.173
	Rating Index	0.00	0.041	0.54	0.48	0.54	0.41
07/09/2018	S_j ($\times 10^{-6}$/psi)	0.157	0.154	0.058	0.092	0.057	0.096
	Rating Index	0.48	0.49	0.88	0.74	0.88	0.72
11/19/2018	S_j ($\times 10^{-6}$/psi)	0.158	0.165	0.036	0.078	0.057	0.100
	Rating Index	0.47	0.44	0.97	0.80	0.88	0.71
04/16/2019	S_j ($\times 10^{-6}$/psi)	0.052	0.065	0.082	0.107	0.056	0.029
	Rating Index	0.91	0.85	0.78	0.68	0.89	1.00
Mean Rating Index		**0.46**	**0.45**	**0.79**	**0.68**	**0.80**	**0.71**
Model Ranking		**5**	**6**	**2**	**4**	**1**	**3**

Rating Index: 1 = most accurate prediction of compliance and 0 = least accurate prediction of compliance; linearly interpolated to obtain intermediate values.
Model Ranking: 1 = most accurate model and 6 = least accurate model; based on Mean Rating Index.

Items of interest for comparison between all models prediction of compliance values for data collected throughout this research effort include:

- The most accurate model for a single sampling date is the CEB MC 2010 Model prediction of the 04/16/2019 specimens.
- The least accurate model for a single sampling date is the ACI 209 Model prediction of the 04/10/2018 specimens.
- The CEB MC 1990 and GL 2000 Models are the most accurate for predicting compliance across all data collected during the project. The CEB MC 1990 Model merited a slightly better mean rating index (0.80) than the CEB MC 1990 Model (0.79).
- The AASHTO LRFD 2017 and ACI 209 Models are the least accurate for predicting compliance for the concrete tested in this project; however, the ACI 209 Model merited a slightly better mean rating index (0.46) than the AASHTO LRFD 2017 Model (0.45).

7.3.2 Accuracy of Shrinkage Prediction Models

Comparison for shrinkage prediction models is divided in two parts: creep companion cylinders and concrete prisms. The mean rating indices for the prediction of shrinkage of the cylinders are presented in Table 7-2. Concrete prismatic specimens are compared separately depending on curing regime, and their results are presented in Table 7-3.

Table 7-2: Mean rating indices for all models to predict shrinkage in cylindrical specimens

Sampling Date	Index	Shrinkage Prediction Model					
		ACI 209	**AASHTO LRFD 2017**	**GL 2000**	**B3**	**CEB MC 1990**	**CEB MC 2010**
04/10/2018	S_j ($\times 10^{-6}$ in./in.)	77.5	34.6	96.2	235	168	139
	Rating Index	0.72	0.91	0.63	0.00	0.31	0.44
07/09/2018	S_j ($\times 10^{-6}$ in./in.)	56.8	37.2	89.8	210	154	121
	Rating Index	0.81	0.90	0.66	0.11	0.37	0.52
11/19/2018	S_j ($\times 10^{-6}$ in./in.)	27.2	15.1	37.5	156	129	37.7
	Rating Index	0.95	1.00	0.90	0.36	0.48	0.90
04/16/2019	S_j ($\times 10^{-6}$ in./in.)	50.8	25.6	51.0	142	112	68.6
	Rating Index	0.84	0.95	0.84	0.42	0.56	0.76
Mean Rating Index		**0.83**	**0.94**	**0.76**	**0.22**	**0.43**	**0.65**
Model Ranking		**2**	**1**	**3**	**6**	**5**	**4**

Rating Index: 1 = most accurate prediction of shrinkage and 0 = least accurate prediction of shrinkage; linearly interpolated to obtain intermediate values.
Model Ranking: 1 = most accurate model and 6 = least accurate model; based on Mean Rating Index.

Table 7-3: Mean rating indices for all models to predict shrinkage in prismatic specimens

Sampling Date		Index	Shrinkage Prediction Model					
			ACI 209	**AASHTO LRFD 2017**	**GL 2000**	**B3**	**CEB MC 1990**	**CEB MC 2010**
Air Cured	04/10/2018	S_j ($\times 10^{-6}$ in./in.)	212	128	69.1	309	205	146
		Rating Index	0.38	0.70	0.93	0.00	0.40	0.63
	07/09/2018	S_j ($\times 10^{-6}$ in./in.)	162	97.1	52.1	267	175	108
		Rating Index	0.57	0.82	1.00	0.16	0.52	0.78
	11/19/2018	S_j ($\times 10^{-6}$ in./in.)	109	78.4	88.6	173	138	71.9
		Rating Index	0.78	0.90	0.86	0.53	0.67	0.92
	04/16/2019	S_j ($\times 10^{-6}$ in./in.)	89.6	51.6	61.0	139	90.8	70.9
		Rating Index	0.85	1.00	0.97	0.66	0.85	0.93
	Mean Rating Index		**0.65**	**0.86**	**0.94**	**0.34**	**0.61**	**0.82**
	Model Ranking		**4**	**2**	**1**	**6**	**5**	**3**
Moist Cured	04/10/2018	S_j ($\times 10^{-6}$ in./in.)	289	222	121	266	259	197
		Rating Index	0.00	0.26	0.65	0.09	0.11	0.35
	07/09/2018	S_j ($\times 10^{-6}$ in./in.)	199	162	59.4	182	189	119
		Rating Index	0.35	0.49	0.88	0.41	0.38	0.65
	11/19/2018	S_j ($\times 10^{-6}$ in./in.)	172	184	29.7	116	191	28.1
		Rating Index	0.45	0.40	0.99	0.66	0.38	1.00
	04/16/2019	S_j ($\times 10^{-6}$ in./in.)	62.6	103	51.1	52.6	95.4	37.4
		Rating Index	0.87	0.71	0.91	0.91	0.74	0.96
	Mean Rating Index		**0.42**	**0.47**	**0.86**	**0.52**	**0.40**	**0.74**
	Model Ranking		**5**	**4**	**1**	**3**	**6**	**2**

Rating Index: 1 = most accurate prediction of shrinkage and 0 = least accurate prediction of shrinkage; linearly interpolated to obtain intermediate values.
Model Ranking: 1 = most accurate model and 6 = least accurate model; based on the Mean Rating Index.

A few key findings are evident from the statistical analysis of the predicted shrinkage strains in both specimen types:

- The AASHTO LRFD 2017 Model, having a mean rating index of 0.94, predicts shrinkage strains in the cylindrical specimens by far the most accurately for all sampling dates.

- The ACI 209 Model, with a mean rating index of 0.83, ranked as the second best model to predict shrinkage for all cylindrical specimens.
- The B3 Model by far, having a mean rating index of 0.22, is the least accurate of all models considered for predicting shrinkage of the cylindrical specimens.
- In general, shrinkage of the air-cured prismatic specimens is predicted more accurately than the moist-cured prismatic specimens.
- The GL 2000 model proves to be most accurate in predicting shrinkage in the prismatic specimens using both curing regimes with a mean rating index of 0.94 and 0.86 for air- and moist-cured specimens, respectively.
- The AASHTO LRFD 2017 and CEB MC 2010 Models for predicting shrinkage in prismatic specimens are the second best models for air- and moist-cured prisms, respectively.
- The B3 Model is the least accurate to predict the shrinkage of the air-cure prisms, and the CEB MC 1990 model is the least accurate to predict shrinkage of the moist-cured prisms.

7.4 SELECTION OF THE MOST ACCURATE MODEL

An objective of this research effort is to identify the most accurate model to predict creep and shrinkage, followed by calibrating the selected model for ALDOT representing the most accurate prediction of the creep and shrinkage in the Birmingham I-59/I-20 segmental bridge. The model needs to be selected based on how accurately it can predict both compliance and shrinkage in cylindrical specimens. As for the model's use in the prediction of shrinkage of the Birmingham I-59/I-20 bridge, it is determined that predicting shrinkage with a larger volume-to-surface area ratio similar to the segments is the best strategy. Therefore, the ability of the models to predict the drying shrinkage of the prisms is not used in this section.

7.4.1 Graphical Analysis

In order to identify the best model to predict compliance and drying shrinkage, both graphical and quantitative analyses were performed. To visually determine what models perform the best, the previously mentioned mean rating indices for compliance and shrinkage were plotted with each respective variance. The mean rating indices versus variance for both compliance and cylinder shrinkage for all prediction models are presented in Figure 7-1 and Figure 7-2, respectively.

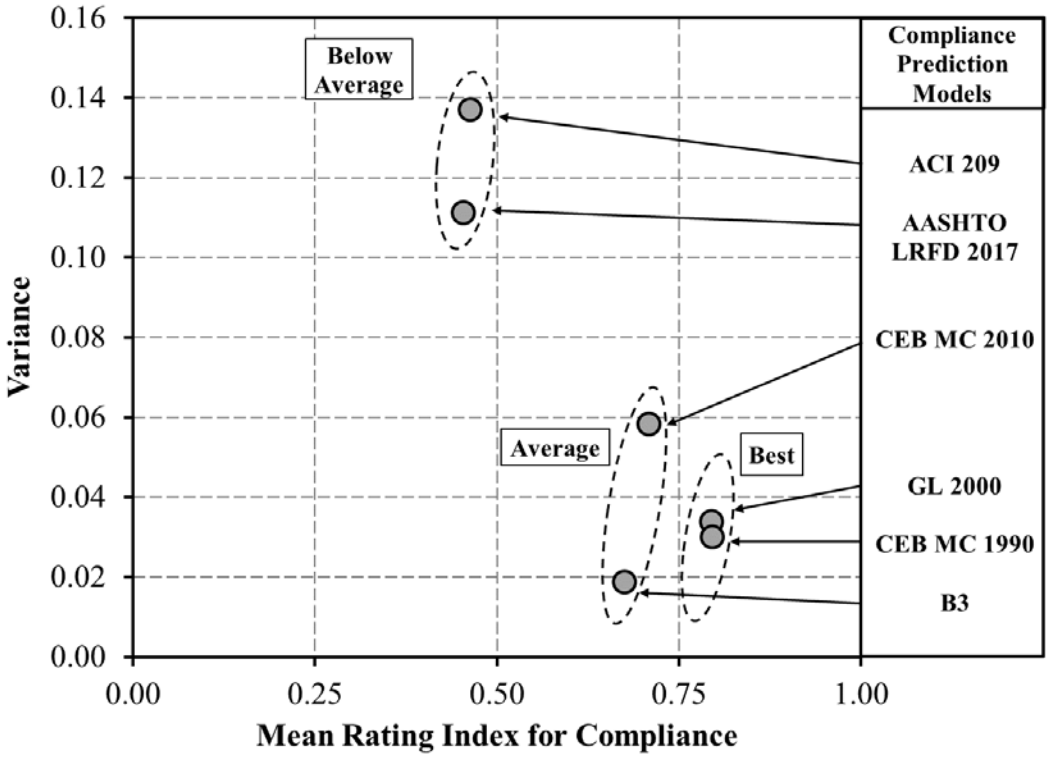

Figure 7-1: Mean rating indices versus variance for compliance

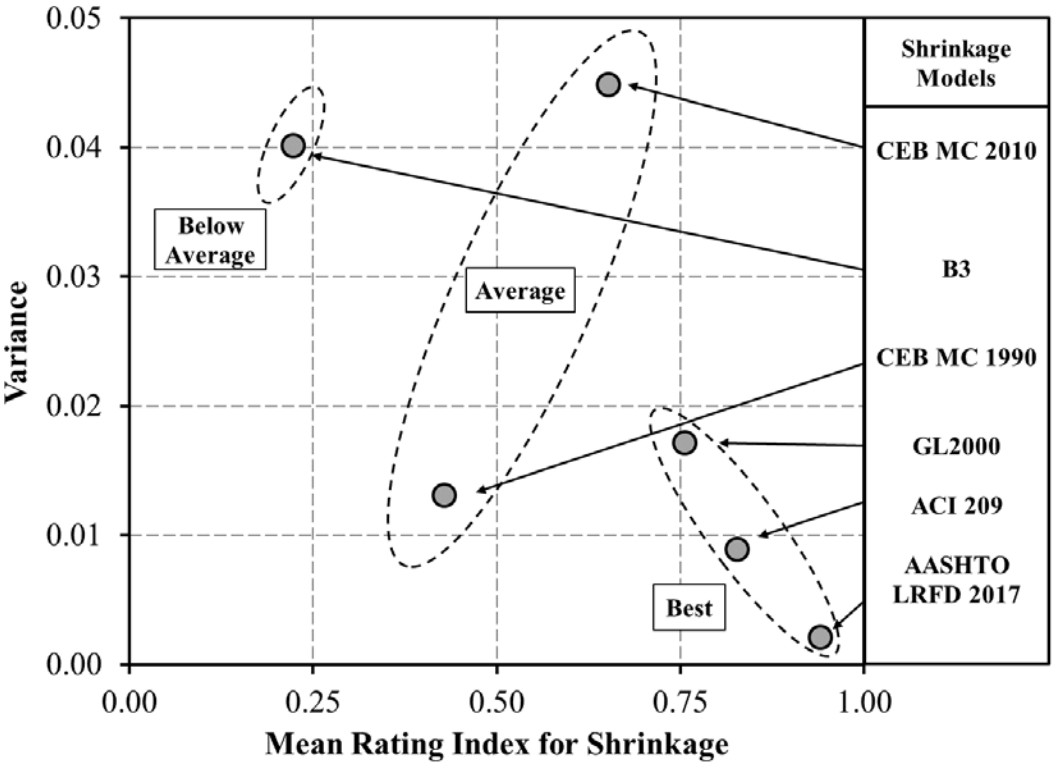

Figure 7-2: Mean rating indices versus variance for cylinder shrinkage

7.4.2 Quantitative Analysis

For quantitative analysis, the rating indices for each sampling date are used for their respective models. It was decided that for best correlation to the Birmingham I-59/I-20 segmental bridge, the rating index from each model for each sampling date should be weighted with the respective ratio of segments that were cast with the same ALDOT approved mixture proportions. The respective weights assigned to each sampling date, based on the number of segments cast with corresponding concrete mixture, are presented in Table 7-4.

Table 7-4: Rating index weights based on number of segments cast for the Birmingham I-59/I-20 bridge

Sampling Date	Rating Index Weights
04/10/2018	0.006
07/09/2018	0.183
11/19/2018	0.428
04/16/2019	0.383
Total	1.000

It should be noted that less than one percent of the total segments were cast with concrete mixture proportions corresponding to the 04/10/2018 sampling date. The majority of segments (nearly 43 percent) were cast using concrete with the same mixture proportions of concrete sampled on 11/19/2018. The weighted model performance for compliance and shrinkage is presented in Table 7-5 and Table 7-6, respectively.

Table 7-5: Weighted performance of compliance model predictions

Sampling Date	Index	Compliance Prediction Model					
		ACI 209	**AASHTO LRFD 2017**	**GL 2000**	**B3**	**CEB MC 1990**	**CEB MC 2010**
04/10/2018	Weighted Compliance Rating Index	0.000	0.000	0.004	0.003	0.004	0.003
07/09/2018		0.09	0.09	0.16	0.14	0.16	0.13
11/19/2018		0.20	0.19	0.42	0.34	0.38	0.30
04/16/2019		0.35	0.33	0.30	0.26	0.34	0.38
Weighted Compliance Model Rating Index		**0.64**	**0.60**	**0.88**	**0.74**	**0.88**	**0.82**
Weighted Compliance Model Ranking		**5**	**6**	**1**	**4**	**1**	**3**

Weighted Index: based on rating index weights presented in Table 7-4.
Model Rating Index: sum of weighted rating indices for a specified prediction model.
Model Ranking: 1 = most accurate model and 6 = least accurate model; based on Model Rating Index.

Table 7-6: Weighted performance of shrinkage model predictions

Sampling Date	Index	Shrinkage Prediction Model					
		ACI 209	**AASHTO LRFD 2017**	**GL 2000**	**B3**	**CEB MC 1990**	**CEB MC 2010**
04/10/2018	Weighted Shrinkage Rating Index	0.005	0.006	0.004	0.000	0.002	0.003
07/09/2018		0.15	0.16	0.12	0.02	0.07	0.10
11/19/2018		0.40	0.43	0.38	0.15	0.21	0.38
04/16/2019		0.32	0.36	0.32	0.16	0.21	0.29
Weighted Shrinkage Model Rating Index		**0.88**	**0.96**	**0.83**	**0.34**	**0.49**	**0.77**
Weighted Shrinkage Model Ranking		**2**	**1**	**3**	**6**	**5**	**4**

Weighted Index: based on rating index weights presented in Table 7-4.
Model Rating Index: sum of weighted rating indices for a specified prediction model.
Model Ranking: 1 = most accurate model and 6 = least accurate model; based on Model Rating Index.

It can be seen that the GL 2000 Model and the CEB MC 1990 Model are ranked as most accurate in predicting compliance based on the weighted model performance; however, for shrinkage predictions the AASHTO LRFD 2017 Model and ACI 209 Model are ranked as most accurate, and second most accurate, respectively. In order to determine the most accurate model for predicting both creep and shrinkage, the weighted rating indices were combined to form a single index. Total model performance was based on an equal contribution of model accuracy in predicting both creep and shrinkage, where the combined rating index is the average between compliance and shrinkage weighted rating index. The combined weighted performance for creep and shrinkage model predictions are presented in Table 7-7.

Table 7-7: Combined weighted performance of creep and shrinkage model predictions

Sampling Date	**Index**	**Creep and Shrinkage Prediction Models**					
		ACI 209	**AASHTO LRFD 2017**	**GL 2000**	**B3**	**CEB MC 1990**	**CEB MC 2010**
04/10/2018	Combined Rating Index	0.002	0.003	0.004	0.002	0.003	0.003
07/09/2018		0.12	0.13	0.14	0.08	0.11	0.11
11/19/2018		0.30	0.31	0.40	0.25	0.29	0.34
04/16/2019		0.33	0.34	0.31	0.21	0.28	0.34
Combined Model Rating Index		**0.76**	**0.78**	**0.85**	**0.54**	**0.69**	**0.80**
Combined Model Ranking		**4**	**3**	**1**	**6**	**5**	**2**

Combined Index: Equal contribution of compliance and shrinkage Weighted Rating Indices.
Model Rating Index: sum of combined rating indices for a specified prediction model.
Model Ranking: 1 = most accurate model and 6 = least accurate model; based on the Combined Model Rating Index.

7.4.3 Final Model Selection

From the graphical analysis it can be seen that the GL 2000 and CEB MC 1990 Models are best in accurately predicting compliance with a high mean rating index and a low variance. The AASHTO LRFD 2017 and ACI 209 Models; however, are labeled as below average due to the respective low mean rating index and high variance. After review of the variance of the mean rating indices for shrinkage it can be seen that the AASHTO LRFD 2017, GL 2000, and ACI 209 Models are best at predicting shrinkage of the concrete cylinders. The AASHTO LRFD 2017 Model has by

far the highest mean rating index with a very low variance. The B3 Model is labeled as below average to accurately predict drying shrinkage in the concrete cylinders due its very low mean rating index and high variance.

After reviewing the quantitative analysis results of model accuracy in Table 7-7 it can be concluded that the GL 2000 Model has the highest combined model rating index for compliance and drying shrinkage predictions. With the relative weights associated with the rating index, the CEB MC 2010 Model is considered the second best model overall for predicting compliance and drying shrinkage. It should be noted that the B3 Model has the lowest model rating index which only means that it predicts with the least accuracy the data collected during this project.

Based on all analyses performed, the GL 2000 Model was selected as the most accurate model to predict creep and shrinkage in the Birmingham I-59/I-20 segmental bridge. To meet the main objective of this research effort, the GL 2000 Model was calibrated to more accurately predict compliance and shrinkage for the data collected for this project.

7.5 GL 2000 MODEL CALIBRATION

The last major objective of this research project was to calibrate the most accurate model for predicting creep and shrinkage in the Birmingham I-59/I-20 segmental bridge. As mentioned previously, the GL 2000 Model was selected as the most accurate model to predict creep and shrinkage in the bridge segments. A sensitivity analysis was performed to determine what empirical parameters will reduce error the most for creep and shrinkage predictions. Following the sensitivity analysis, the GL 2000 Model was calibrated to best represent the creep and shrinkage data collected for the bridge segments. The prediction accuracy of the calibrated model is also compared to the original version of the model to evaluate the improvements obtained from the calibration.

After initial analysis of the GL 2000 model, it was determined that the main factor influencing both compliance and shrinkage between different sampling dates is the concrete compressive strength at 28 days. The decision was made that each sampling date will be grouped in classes by the percent difference of measured 28-day compressive strength relative to the weighted average 28-day strength. To determine the weighted average 28-day strength, weights were assigned by the total amount of segments corresponding to each sampling date, as presented in Table 7-4. A summary of the group classifications are presented in Table 7-8 based on 28-day

compressive strengths, where the middle sampling dates (07/09/2018 and 11/19/2018) are grouped together. For corresponding bridge segments, see summary of segment groups shown in Table 7-9.

Table 7-8: Group classification for sampling dates

Sampling Date	Weight	28-Day Compressive Strength (psi)	Percent Difference Relative to Average 28-day Strength	I-59/I-20 Bridge Segment Group Classification
04/10/2018	0.006	6,100	-17.6%	**A**
07/09/2018	0.183	6,700	-9.5%	**B**
11/19/2018	0.428	7,200	-2.8%	
04/16/2019	0.383	8,000	8.0%	**C**

Table 7-9: Birmingham I-59/I-20 Bridge segment classification

I-59/I-20 Bridge Segment Group Classification	First Casting Date	Last Casting Date	ALDOT Mixture Proportions
A	02/21/2018	04/16/2018	OSM-003-17
B	04/17/2018	03/24/2019	OSM-002-18
			OSM-010-18
C	03/25/2019	08/09/2019	OSM-004-19

7.5.1 Sensitivity Analysis of GL 2000 Model

The first step in predicting compliance accurately in the GL 2000 Model is to have an accurate representation of the modulus of elasticity of the concrete at all loading ages. A summary of the average 28-day properties for each group are compared in Table 7-10.

Table 7-10: Comparison of average 28-day properties for the GL 2000 Model

I-59/I-20 Bridge Segment Group Classification	Compressive Strength (psi)	Measured Modulus of Elasticity (ksi)	GL 2000 Predicted Modulus of Elasticity (ksi)	Error (%)
A	6,100	4,050	4,560	13%
B	6,950	4,425	4,835	9%
C	8,000	5,300	5,150	-3%

Based on this comparison, it can be seen that the GL 2000 Model over predicts the modulus of elasticity for the lower-strength concretes and begins to under predict for concretes with higher strength. After evaluation of Equation 7.4, it was determined that a single parameter, tau "τ", shown in Equation 7.5, could be calibrated for a more accurate prediction of the modulus of elasticity. The effects of varying the parameter tau on the modulus of elasticity is illustrated in Figure 7-3. As tau increases and decreases, the modulus of elasticity increases and decreases, accordingly.

$$E_c = 500{,}000 + 52{,}000\sqrt{f_c} \qquad \text{Equation 7.4}$$

$$E_c = 500{,}000 + \tau\sqrt{f_c} \qquad \text{Equation 7.5}$$

Where,

τ = Empirical parameter being calibrated ($psi^{0.5}$)

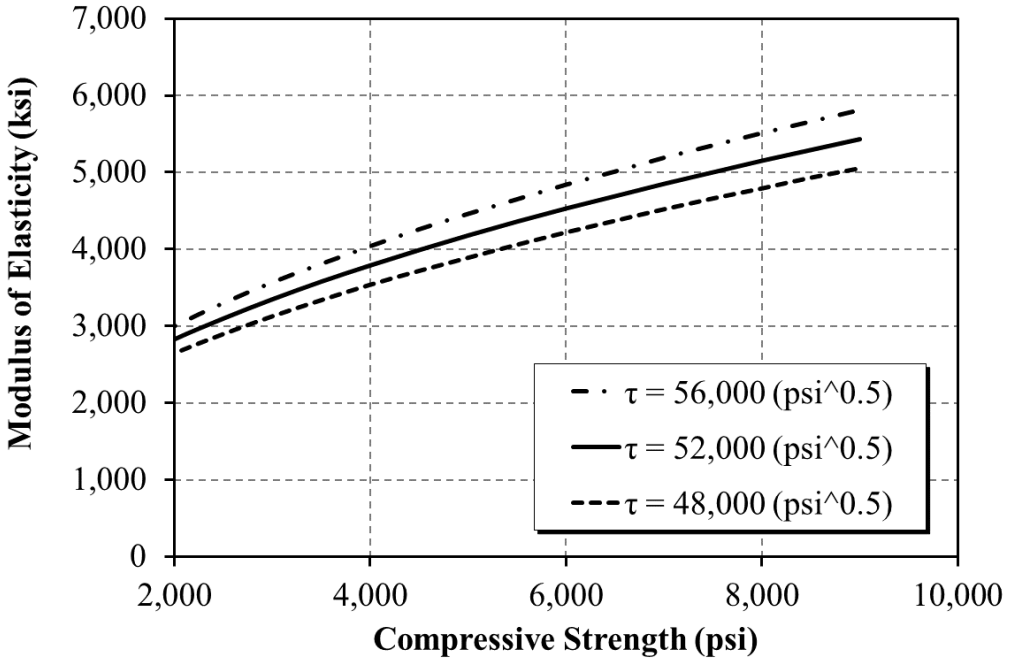

Figure 7-3: GL 2000 Model calculation of modulus of elasticity with varied τ

The next analysis was performed on the compliance predictions directly for the GL 2000 Model. A graphical analysis method was used to visualize how the predictions with the GL 2000 Model can be improved for the different group classifications. Compliance results are compared in Figure 7-4 for the 28-day loading age for Group A and Group C representing the lowest strength and greatest strength concrete groups, respectively.

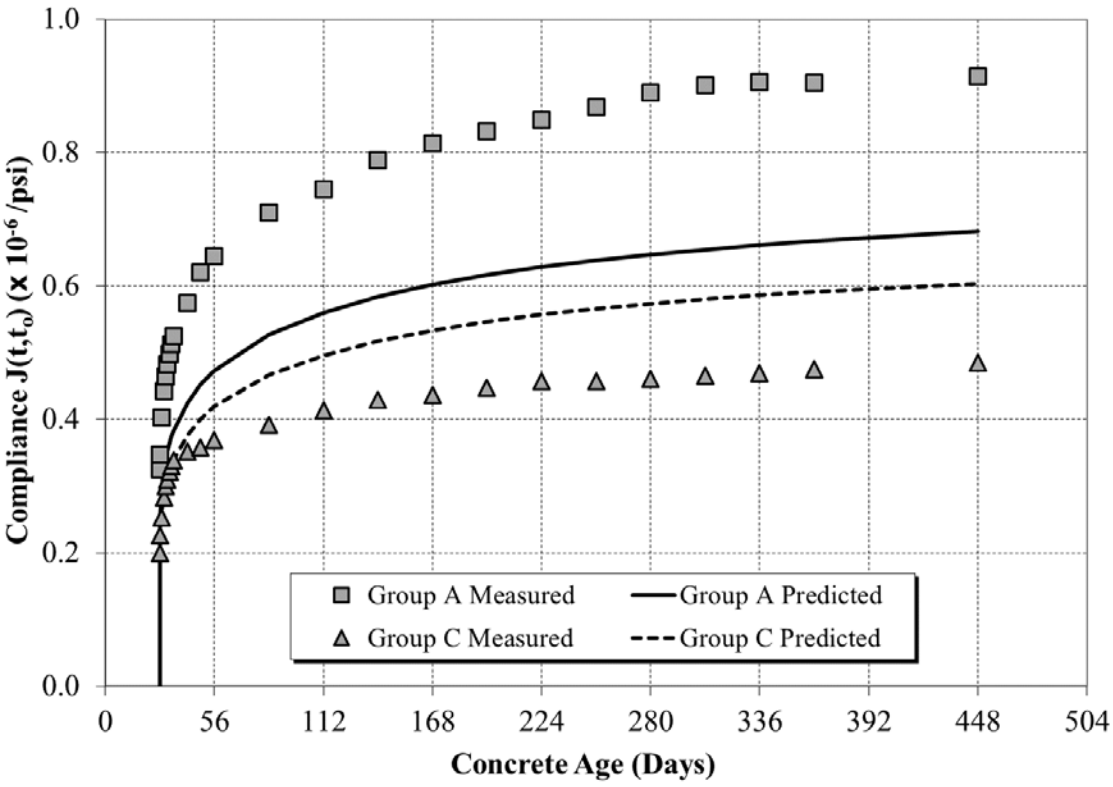

Figure 7-4: GL 2000 analysis of compliance for lowest and greatest strength concrete groups

It is apparent in the original compliance predictions that two major factors are affecting the accuracy of the GL 2000 Model: the ultimate compliance values and the rate at which compliance develops. It was concluded that calibration needed to occur in response to the 28-day creep coefficient presented in Equation 7.6. It is determined that the two empirical parameters λ and ω, shown in Equation 7.7, will best modify the compliance prediction of the GL 2000 Model.

$$\phi(t,t_0) = \phi(t_c)\left[2\left(\frac{(t-t_0)^{0.3}}{(t-t_0)^{0.3}+14}\right) + \left(\frac{7}{t_0}\right)^{0.5}\left(\frac{t-t_0}{t-t_0+7}\right)^{0.5} + 2.5(1-1.086h^2)\left(\frac{t-t_0}{t-t_0+77(v/s)^2}\right)^{0.5}\right] \quad \text{Equation 7.6}$$

$$\phi(t,t_0) = \phi(t_c)\left[2\left(\frac{(t-t_0)^{0.3}}{(t-t_0)^{0.3}+14}\right)\right.$$
$$+\left(\frac{7}{t_0}\right)^{0.5}\left(\frac{t-t_0}{t-t_0+7}\right)^{\lambda} \qquad \text{Equation 7.7}$$
$$\left.+\omega(1-1.086h^2)\left(\frac{t-t_0}{t-t_0+77(^{v}/_{s})^2}\right)^{0.5}\right]$$

Where,

λ = Empirical parameter being calibrated (unitless) and

ω = Empirical parameter being calibrated (unitless).

The effects of varying the empirical parameters λ and ω independently from each other on compliance are illustrated in Figure 7-5 and Figure 7-6, respectively. From these figures it can be concluded that λ predominately influences the rate of development for compliance, and modifying the second parameter, ω, influences the long-term compliance.

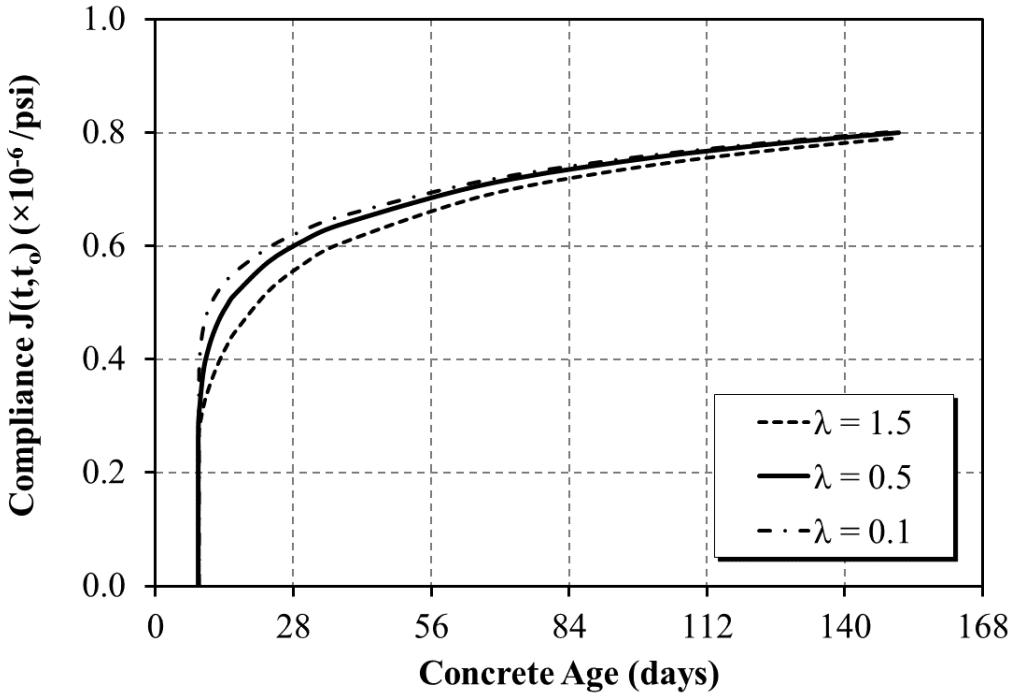

Figure 7-5: Effects of varying empirical parameter λ on GL 2000 calculated compliance

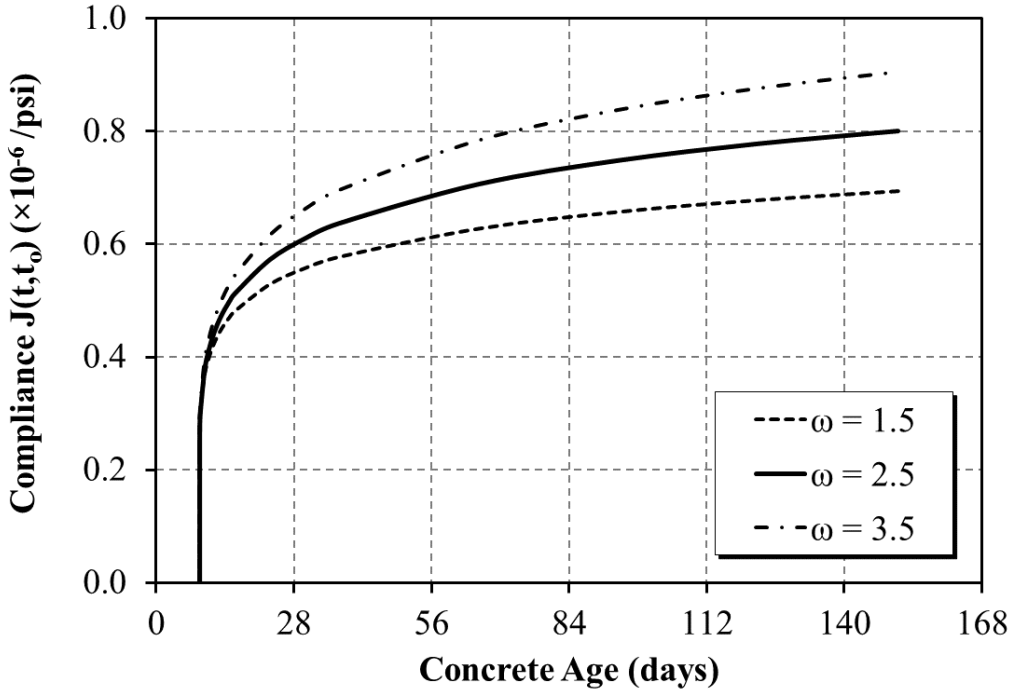

Figure 7-6: Effects of varying empirical parameter ω on GL 2000 calculated compliance

The last modification to the GL 2000 Model is to more accurately predict shrinkage in the concrete cylinders. Similar to compliance, a graphical analysis is performed to observe what can be improved for shrinkage predictions. The measured and predicted shrinkage strains are compared in Figure 7-7 for Group A and C classifications representing the lowest and greatest strength concrete groups, respectively.

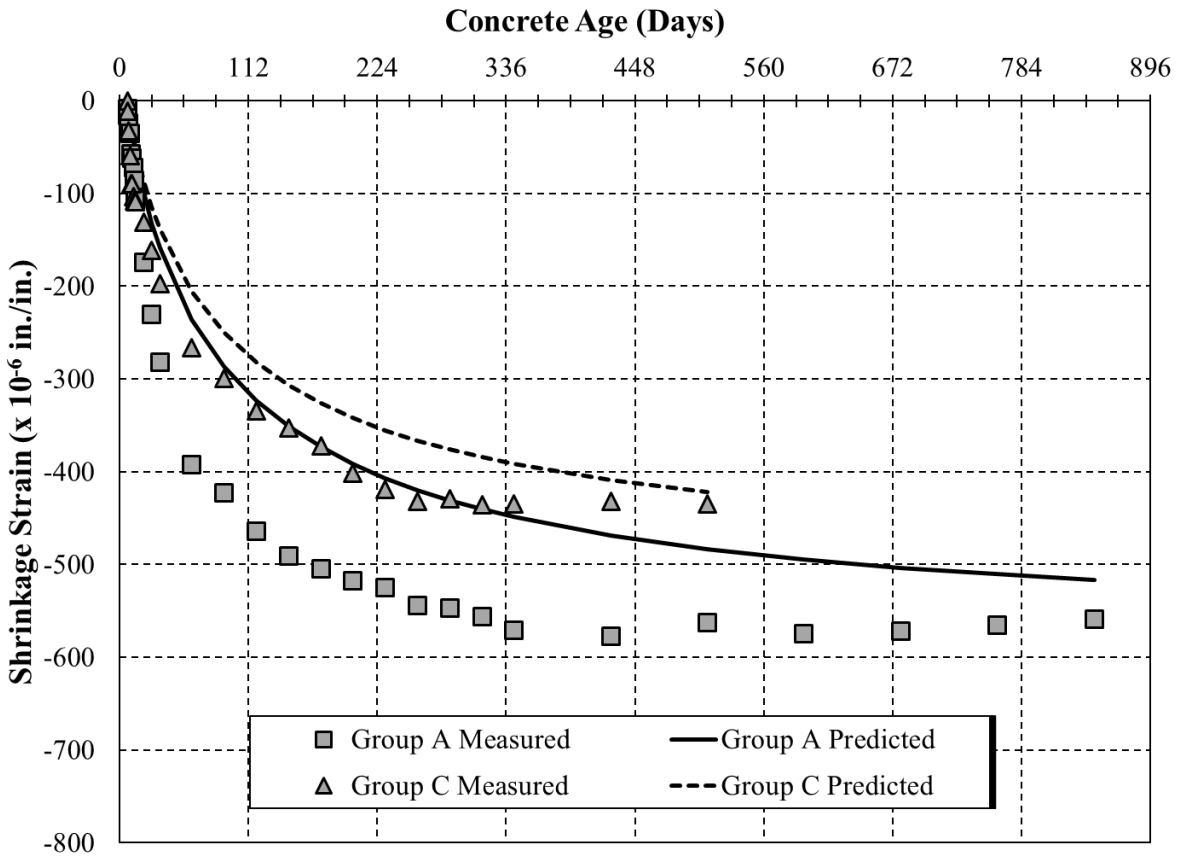

Figure 7-7: GL 2000 analysis of shrinkage for lowest and greatest strength concrete groups

After observing the trends in the original prediction, it was decided that modifying the ultimate shrinkage strain as well as the time-dependent rate of development will have the most effect on predicting shrinkage more accurately. The original formulation of the ultimate shrinkage strain for the GL 2000 Model is shown in Equation 7.8. For use in calibration, the empirical parameter θ is selected and is defined in Equation 7.9. The development of shrinkage when varying the empirical parameter θ is illustrated in Figure 7-8. As the empirical parameter is increased, the resulting ultimate shrinkage strain is increased.

$$\varepsilon_{shu} = 1000k\left(\frac{4350}{f_{cm28}}\right)^{0.5} \times 10^{-6} \qquad \text{Equation 7.8}$$

$$\varepsilon_{shu} = \theta k\left(\frac{4350}{f_{cm28}}\right)^{0.5} \times 10^{-6} \qquad \text{Equation 7.9}$$

Where,

θ = Empirical parameter being calibrated (in./in.)

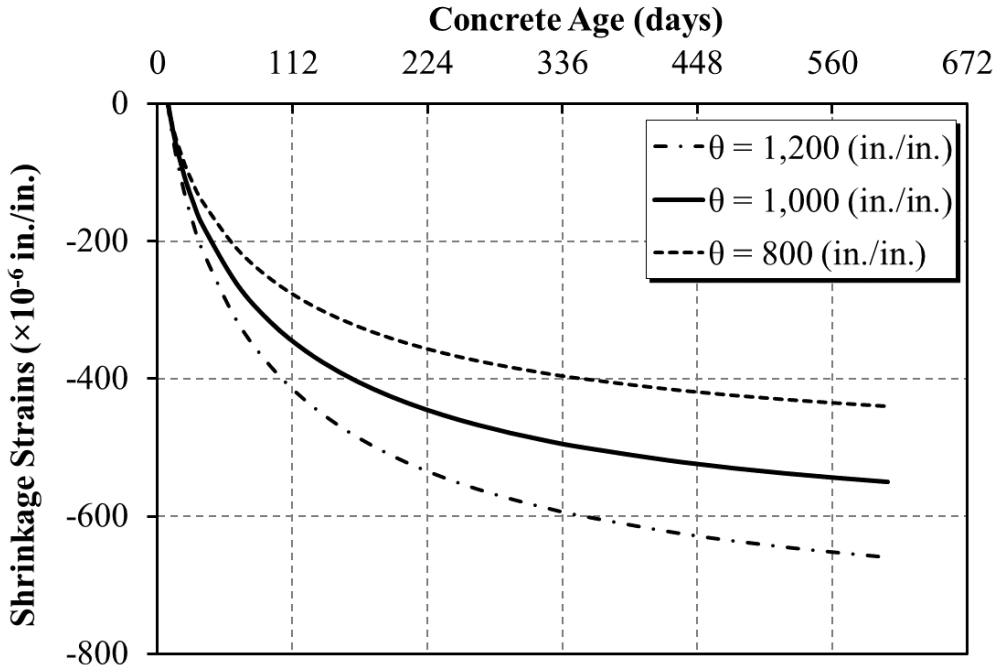

Figure 7-8: Effects of varying empirical parameter θ on the GL 2000 predicted drying shrinkage

The original formulation of the time-dependent factor for shrinkage in the GL 2000 Model is defined in Equation 7.10. For use in calibration, the empirical parameter ψ is selected and can be seen in Equation 7.11. The development of shrinkage when varying the empirical parameter ψ is illustrated in Figure 7-9. As the empirical parameter is decreased the rate of development is increased.

$$\beta(t - t_c) = \left[\frac{(t - t_c)}{(t - t_c) + 77(v/s)^2}\right]^{0.5} \quad \text{Equation 7.10}$$

$$\beta(t - t_c) = \left[\frac{(t - t_c)}{(t - t_c) + \psi(v/s)^2}\right]^{0.5} \quad \text{Equation 7.11}$$

Where,

ψ = empirical parameter being calibrated (day/in.^{2})

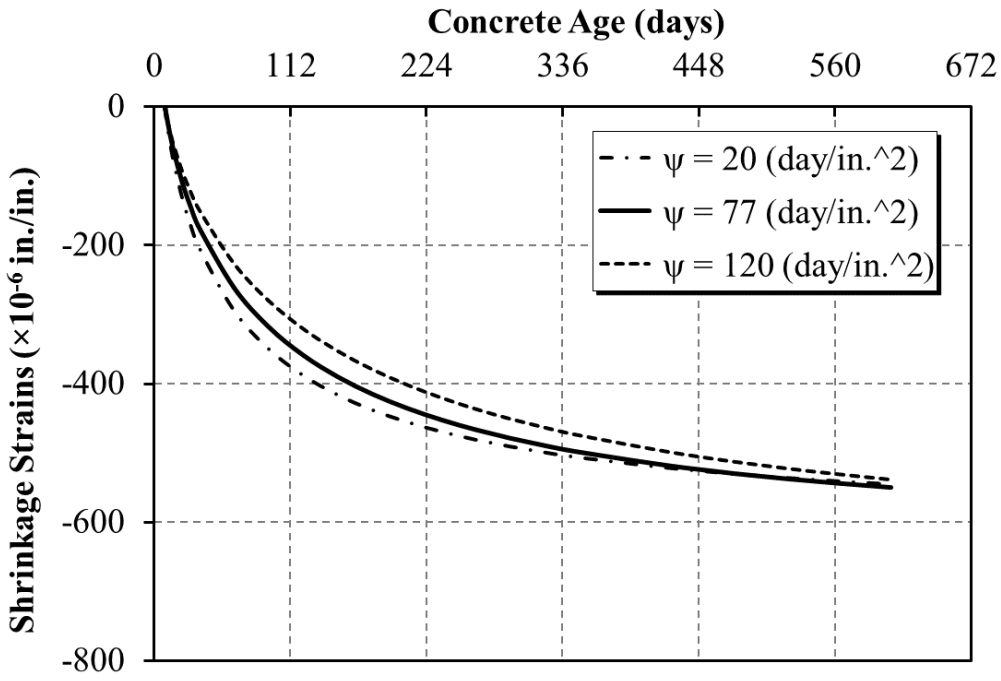

Figure 7-9: Effects of varying empirical parameter ψ on the GL 2000 predicted drying shrinkage

7.5.2 Results for Calibration of the GL 2000 Model

Each empirical parameter was calibrated by minimizing the sum of the square of the error for each segment group classification. For compliance predictions, τ was calibrated using the results from modulus of elasticity testing. Using the modified modulus of elasticity predictions, λ and ω were varied simultaneously during calibration. For shrinkage model calibration, θ and ψ were varied simultaneously. After each empirical parameter was calibrated, the prediction accuracy of the calibrated model is reviewed to evaluate the overall model performance. The calibrated empirical parameters for the GL 2000 Model are presented in Table 7-11.

Table 7-11: Original and calibrated empirical parameters for the GL 2000 Model

Empirical Parameter	Original GL 2000 Model	Modified GL 2000 Model		
		Group A	Group B	Group C
τ ($psi^{0.5}$)	52,000	45,000	47,000	54,000
λ (unitless)	0.50	0.30	0.65	0.65
ω (unitless)	2.5	3.3	2.3	1.5
θ (in./in.)	1,000	1,150	1,000	1,000
ψ ($day/in.^2$)	77	25	25	25

7.5.2.1 Modified GL 2000 Model: Modulus of Elasticity

The Modified GL 2000 Model is calibrated using all measured data for the project. The Modified GL 2000 Model prediction of modulus of elasticity for segment Groups A to C are defined in Equations 7.12 to 7.14, respectively.

Group A Segments:

$$E_{cmt} = 500{,}000 + 45{,}000\sqrt{f_{cmt}} \qquad \text{Equation 7.12}$$

Group B Segments:

$$E_{cmt} = 500{,}000 + 47{,}000\sqrt{f_{cmt}} \qquad \text{Equation 7.13}$$

Group C Segments:

$$E_{cmt} = 500{,}000 + 54{,}000\sqrt{f_{cmt}} \qquad \text{Equation 7.14}$$

A comparison of measured and predicted modulus of elasticity using the Modified GL 2000 Model is presented in Table 7-12. The maximum positive and negative percent error between the measured and predicted modulus of elasticity is 6% and -5%, respectively. The best prediction renders a percent error of nearly 0% for the 7-day and 91-day loading of the 04/16/2019 sampling date. As shown in Table 7-13, overall the Modified GL 2000 Model more accurately predicts the measured modulus of elasticity than the Original GL 2000 Model. In order to visualize the improvement, the measured and predicted modulus of elasticity for the Original and Modified GL 2000 Models are presented in Figure 7-10.

Table 7-12: Comparison of measured and predicted modulus of elasticity using the Modified GL 2000 Model

I-59/I-20 Bridge Segment Classification	Loading Age (Days)	Measured Modulus of Elasticity (ksi)	Modified GL 2000 Modulus of Elasticity (ksi)	Error (%)
Group A	**04/10/2018**			
	7	3,800	3,710	-2%
	28	4,050	4,010	-1%
	91	3,850	3,990	4%
	182	4,150	4,100	-1%
Group B	**07/09/2018**			
	7	4,250	4,020	-5%
	28	4,250	4,350	2%
	91	4,200	4,460	6%
	182	4,300	4,460	4%
Group B	**11/19/2018**			
	7	4,400	4,260	-3%
	28	4,600	4,490	-2%
	91	4,600	4,570	-1%
	182	4,500	4,540	1%
Group C	**04/16/2019**			
	7	5,100	5,110	0%
	28	5,300	5,330	1%
	91	5,400	5,420	0%
	182	5,400	5,360	-1%

Table 7-13: Mean percent error for Original and Modified GL 2000 Models

Model	Mean Percent Error
Original GL 2000 Model	7.3
Modified GL 2000 Model	0.1

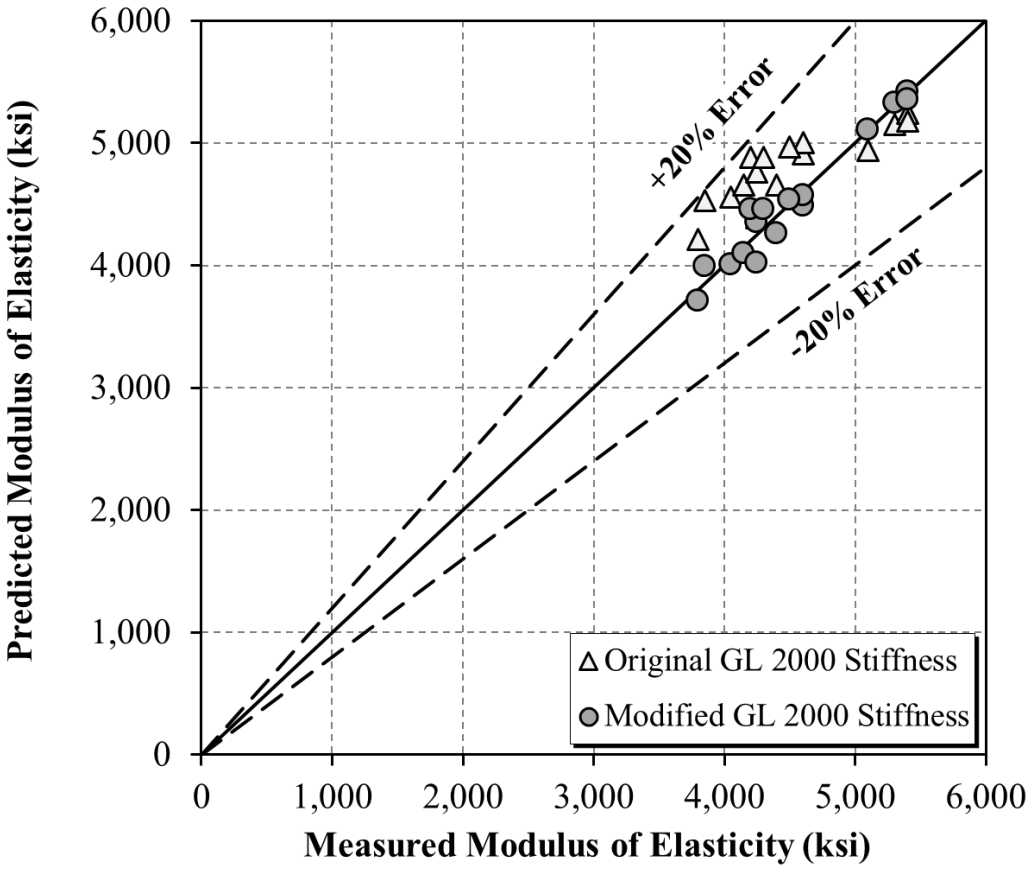

Figure 7-10: Measured versus predicted modulus of elasticity with the Original and Modified GL 2000 Models

7.5.2.2 Modified GL 2000 Model: Compliance

The 28-day creep coefficient formulation was calibrated using all collected data for the project and is shown in Equations 7.15 to 7.17, where both empirical parameters have been modified for segment groups A to C, respectively.

Group A Segments:

$$\phi(t,t_0) = \phi(t_c)\left[2\left(\frac{(t-t_0)^{0.3}}{(t-t_0)^{0.3}+14}\right) + \left(\frac{7}{t_0}\right)^{0.5}\left(\frac{t-t_0}{t-t_0+7}\right)^{0.30} + 3.3(1-1.086h^2)\left(\frac{t-t_0}{t-t_0+77(v/s)^2}\right)^{0.5}\right] \quad \text{Equation 7.15}$$

Group B Segments:

$$\phi(t,t_0) = \phi(t_c)\left[2\left(\frac{(t-t_0)^{0.3}}{(t-t_0)^{0.3}+14}\right) + \left(\frac{7}{t_0}\right)^{0.5}\left(\frac{t-t_0}{t-t_0+7}\right)^{0.65} + 2.3(1-1.086h^2)\left(\frac{t-t_0}{t-t_0+77(v/s)^2}\right)^{0.5}\right] \quad \text{Equation 7.16}$$

Group C Segments:

$$\phi(t,t_0) = \phi(t_c)\left[2\left(\frac{(t-t_0)^{0.3}}{(t-t_0)^{0.3}+14}\right) + \left(\frac{7}{t_0}\right)^{0.5}\left(\frac{t-t_0}{t-t_0+7}\right)^{0.65} + 1.5(1-1.086h^2)\left(\frac{t-t_0}{t-t_0+77(v/s)^2}\right)^{0.5}\right] \quad \text{Equation 7.17}$$

S_j values are calculated to assess the unbiased error for compliance for all sampling dates. The goal in calibration is to reduce the overall error between the measured compliance and the compliance prediction from the Modified GL 2000 Model. In addition to the total unbiased error for all data points, the error for each sampling date is recorded for comparison to the Original GL 2000 Model. A comparison of S_j values for the Original and Modified GL 2000 Models for compliance predictions are presented in Table 7-14. For all sampling dates the Modified GL 2000 Model provides much more accurate compliance predictions. The most improvement is obtained for the 04/10/2018 sampling date. The overall S_j for all data shows a 54% improvement between model versions. The residual values for compliance using the Original and Modified GL 2000 Model are plotted in Figure 7-11.

Table 7-14: Comparison of S_j values for predicted compliance for the Original and Modified GL 2000 Models

Sampling Date	**Original GL 2000 Model**	**Modified GL 2000 Model**	**Improvement**
	S_j ($\times 10^{-6}$/psi)	S_j ($\times 10^{-6}$/psi)	(%)
04/10/2018	0.140	0.043	69%
07/09/2018	0.058	0.041	29%
11/19/2018	0.036	0.029	20%
04/16/2019	0.082	0.040	51%
All Data	0.089	0.039	57%

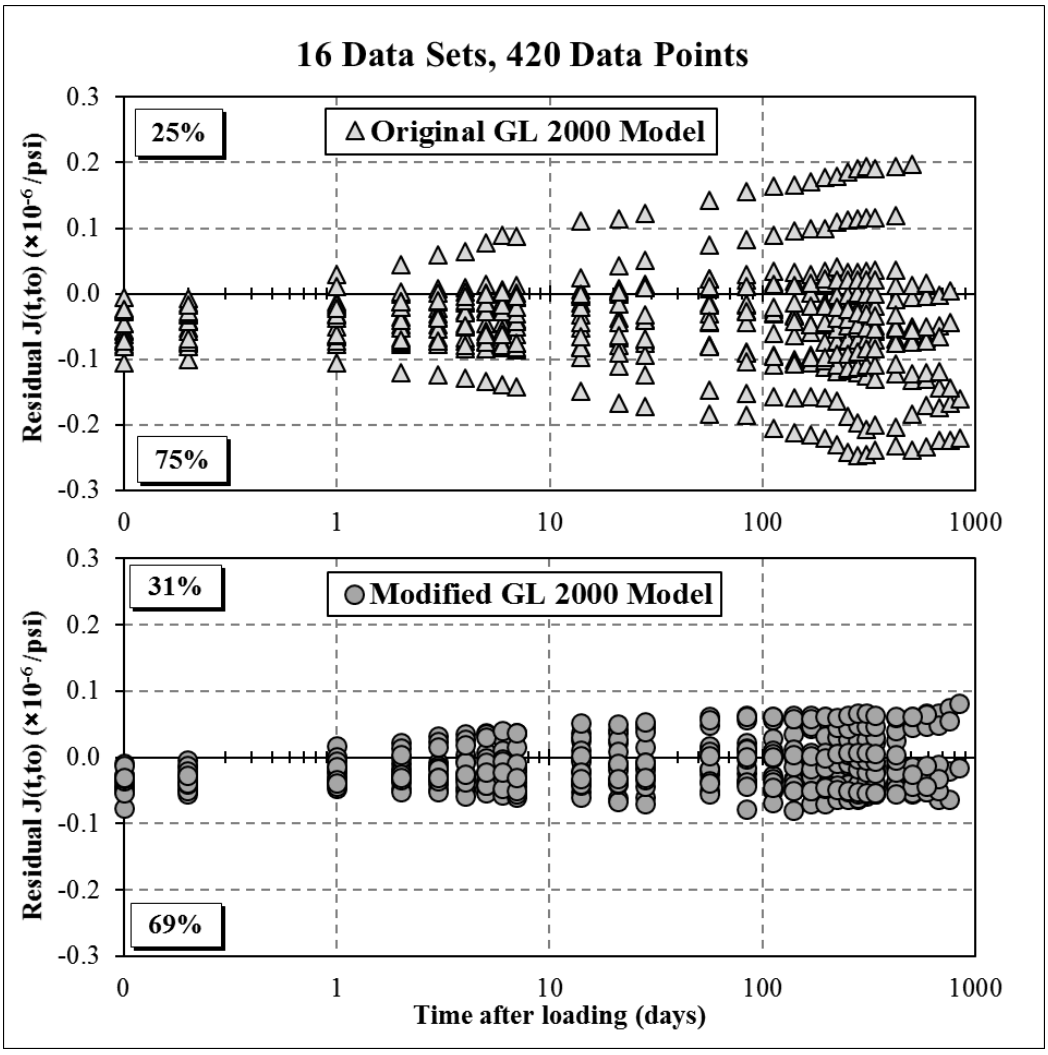

Figure 7-11: Residual compliance for Original and Modified GL 2000 Models

The measured versus predicted compliance using the Modified GL 2000 Model for all test results is presented in Figure 7-12. Almost all points fall within the ±20 percent error bands, which when compared to the Original GL 2000 Model, shown in Figure 6-5, is a significant improvement. The Modified GL 2000 Model is calibrated to return the most accurate predictions for all of the collected data. The measured versus predicted compliance using the Modified GL 2000 Model is separated by sampling date and loading age in Figure 7-13.

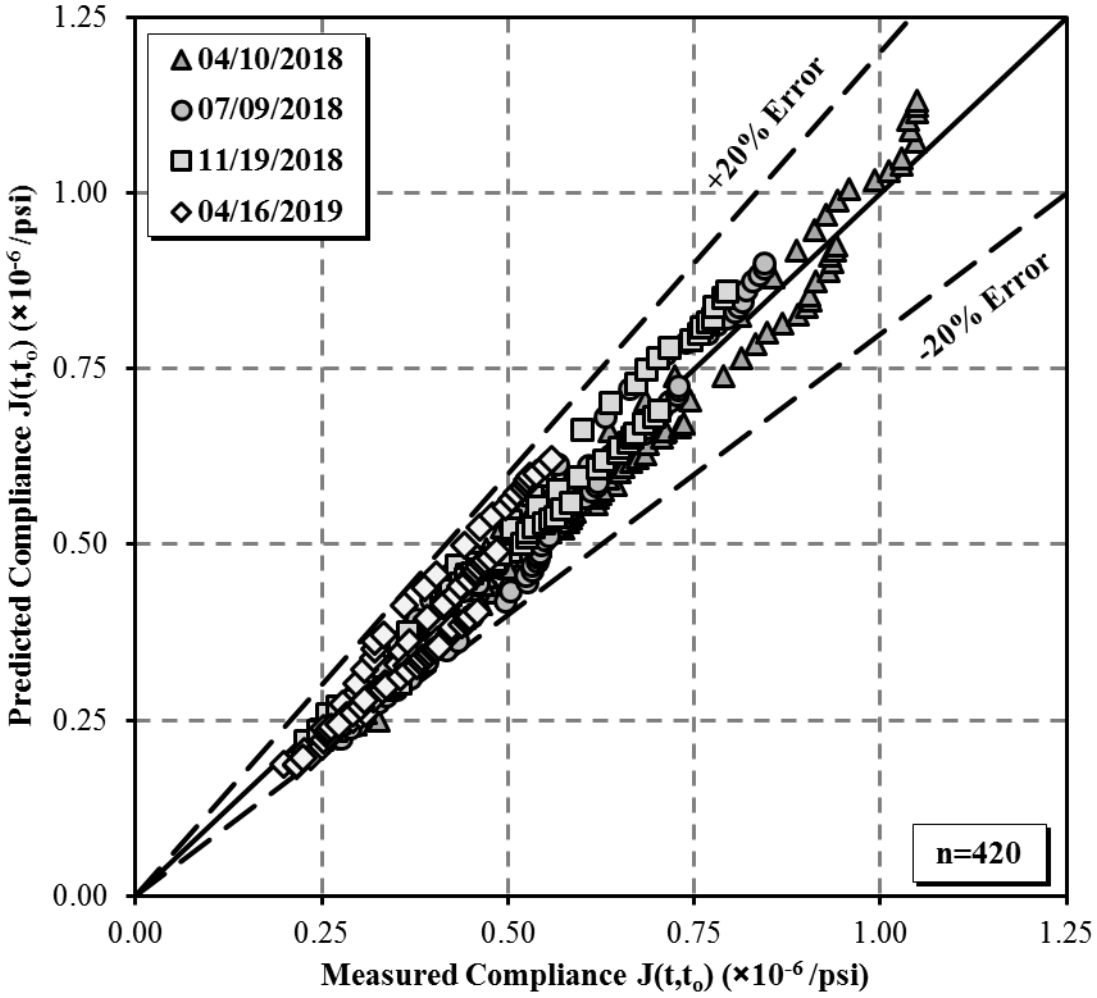

Figure 7-12: Measured versus predicted compliance using the Modified GL 2000 Model

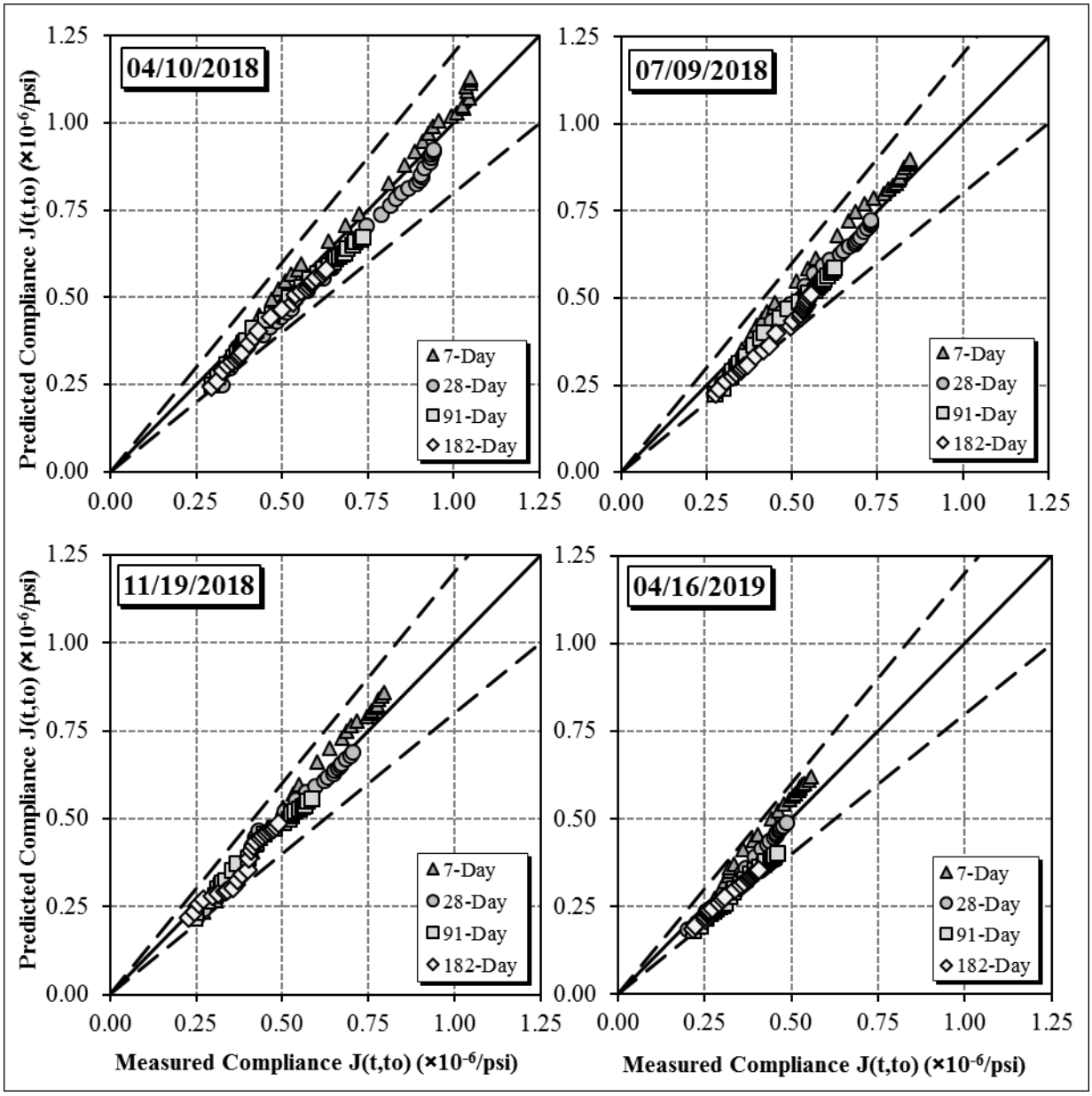

Figure 7-13: Measured versus predicted compliance using the Modified GL 2000 Model separated by sampling dates and loading ages

7.5.2.3 Modified GL 2000 Model: Shrinkage

The final modification to the GL 2000 Model is presented to more accurately predict the shrinkage values. The Modified GL 2000 Model for predicting ultimate shrinkage in Group A segments is defined in Equation 7.18. The Modified GL 2000 Model formulation for predicting ultimate shrinkage in Group B and C segments is presented in Equation 7.19. The shrinkage age factor for for all segment groups is presented in Equation 7.20 for the Modified GL 2000 Model.

Group A Segments:

$$\varepsilon_{shu} = 1150k\left(\frac{4350}{f_{cm28}}\right)^{0.5} \times 10^{-6} \qquad \text{Equation 7.18}$$

Group B and C Segments:

$$\varepsilon_{shu} = 1000k\left(\frac{4350}{f_{cm28}}\right)^{0.5} \times 10^{-6} \qquad \text{Equation 7.19}$$

All Segment Groups:

$$\beta(t - t_c) = \left[\frac{(t - t_c)}{(t - t_c) + 25(v/s)^2}\right]^{0.5} \qquad \text{Equation 7.20}$$

S_j values are used to determine the unbiased estimate of the error for predicting shrinkage of the cylindrical specimens. A comparison of S_j values for the Original and Modified GL 2000 Models is presented in Table 7-15. The overall S_j for all data is decreased by 60 percent. The least amount of improvement is for the 11/19/2018 sampling date at 11 percent; however, the greatest improvement is for the 04/10/2018 sampling dates, which is reduced by 87 percent. The residual shrinkage strains for the Original and Modified GL 2000 Models are shown in Figure 7-14.

Table 7-15: Comparison of S_j values for predicted shrinkage for the Original and Modified GL 2000 Models

Sampling Date	**Original GL 2000 Model**	**Modified GL 2000 Model**	**Improvement**
	S_j ($\times 10^{-6}$ in./in.)	S_j ($\times 10^{-6}$ in./in.)	(%)
04/10/2018	96.2	12.2	87%
07/09/2018	89.8	43.1	52%
11/19/2018	37.5	33.2	11%
04/16/2019	51.0	22.1	57%
All Data	73.3	29.6	60%

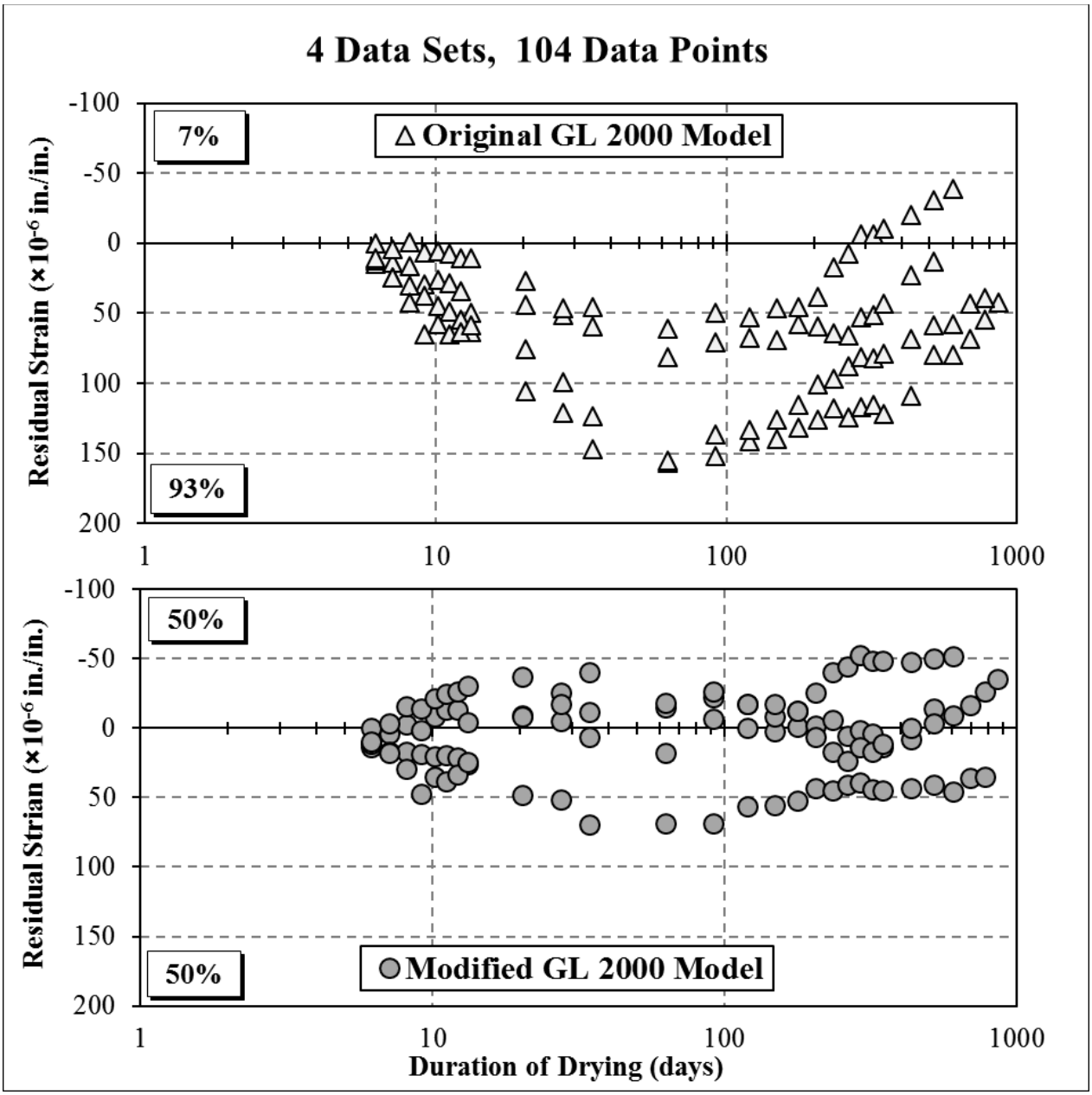

Figure 7-14: Shrinkage residuals for cylindrical shrinkage specimens using the Original and Modified GL 2000 Models

The measured versus predicted shrinkage strains using the Modified GL 2000 Model is presented in Figure 7-15. Similar to compliance, the majority of points fall within the ±20 percent error bands and are close to the line of equality, which when compared to the Original GL 2000 Model, shown in Figure 6-6, is a significant improvement. It can be concluded from Table 7-15 and Figures 7-14 and 7-15 that the Modified GL 2000 Model provides improved predictions of the shrinkage collected from the cylindrical specimens of the Birmingham I-59/I-20 segmental bridge.

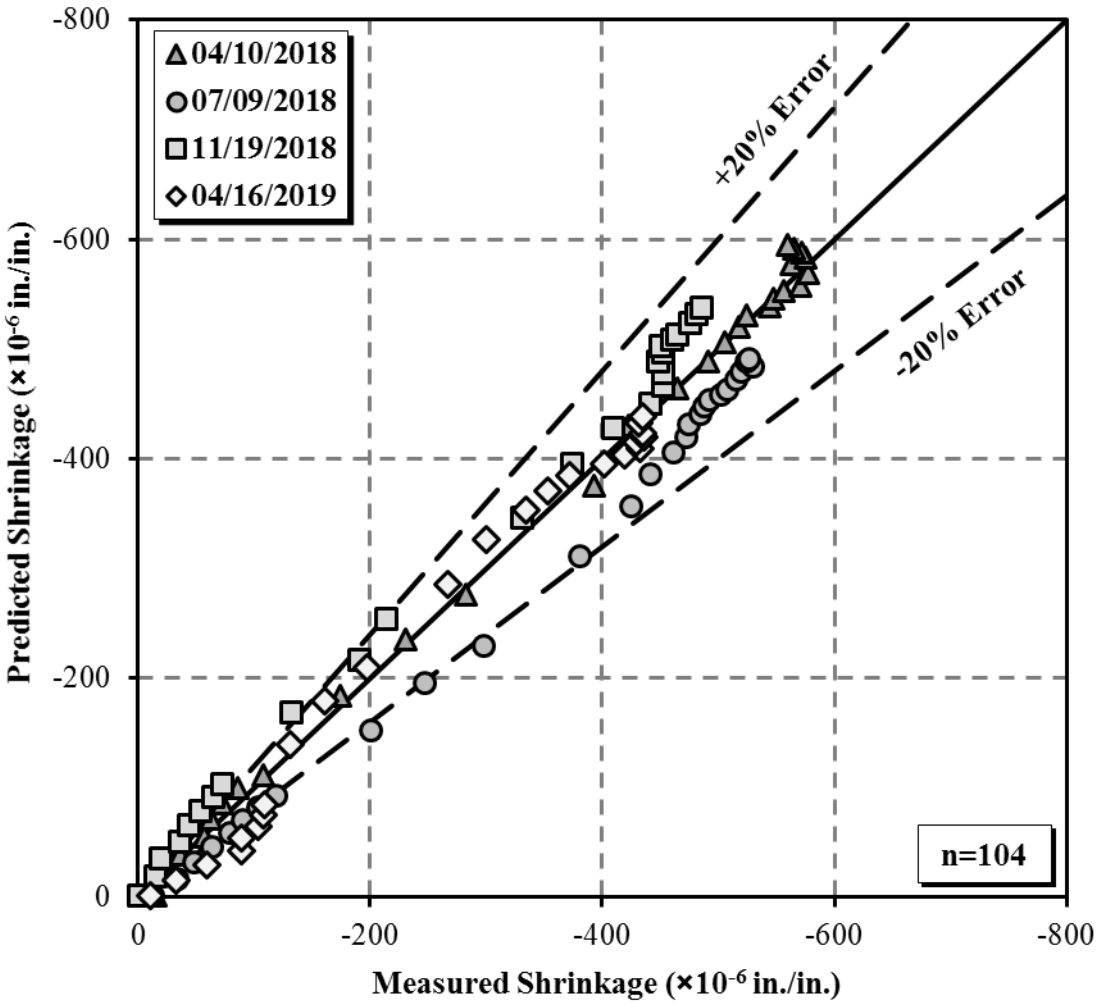

Figure 7-15: Measured versus predicted shrinkage using the Modified GL 2000 Model for cylindrical specimens

7.6 CEB MC 1990 MODEL CALIBRATION

As a secondary objective for this project, the CEB MC 1990 Model was calibrated as a recommendation that may be implemented into commonly used bridge design software (i.e. Bridge Designer 2) by the bridge designer to model creep and shrinkage in the Birmingham I-59/I-20 segmental bridge. Similar to the GL 2000 Model calibration, a sensitivity analysis was performed to determine what empirical parameters increase accuracy the most in results across all segment groups presented in Table 7-9. Following analysis, the CEB MC 1990 Model was calibrated to best represent the creep and shrinkage data collected for the bridge segments. The CEB MC 1990 Model uses SI units for all inputs; however, comparisons to test data are presented in USCS units for simplified comparisons. The prediction accuracy is additionally compared to the original version of the model to evaluate improvements.

7.6.1 Sensitivity Analysis for CEB MC 1990 Model

As discussed for the GL 2000 Model, modulus of elasticity at the time of loading has significant impact on the prediction of creep and shrinkage. The CEB MC 1990 Model predicts modulus of elasticity at loading ages other than 28 days by using the predicted 28-day modulus of elasticity. A comparison of the average 28-day properties for each segment group is presented in Table 7-16.

Table 7-16: Comparison of average 28-day properties for the CEB MC 1990 Model

I-59/I-20 Bridge Segment Group Classification	Compressive Strength (psi)	Measured Modulus of Elasticity (ksi)	CEB MC 1990 Predicted Modulus of Elasticity (ksi)	Error (%)
A	6,100	4,050	5,030	24%
B	6,950	4,425	5,260	19%
C	8,000	5,300	5,510	4%

Based on this comparison, it can be seen that the CEB MC 1990 Model over predicts the modulus of elasticity for all sample groups; however, as the compressive strength at 28 days increases the error decreases. After evaluation of Equation 7.21, it is determined that a single parameter, μ, shown in Equation 7.22, can be calibrated for a more accurate prediction of the modulus of elasticity at 28 days resulting in a more accurate prediction of the modulus of elasticity at time of loading. The effects of varying the parameter μ on the 28-day modulus of elasticity is

illustrated in Figure 7-16. As μ increases and decreases the modulus of elasticity at 28 days increases and decreases, accordingly.

$$E_{ci} = 21{,}500[f_{cm}/10]^{1/3} \quad \text{Equation 7.21}$$

$$E_{ci} = \mu[f_{cm}/10]^{1/3} \quad \text{Equation 7.22}$$

Where,

μ = Empirical parameter being calibrated (MPa).

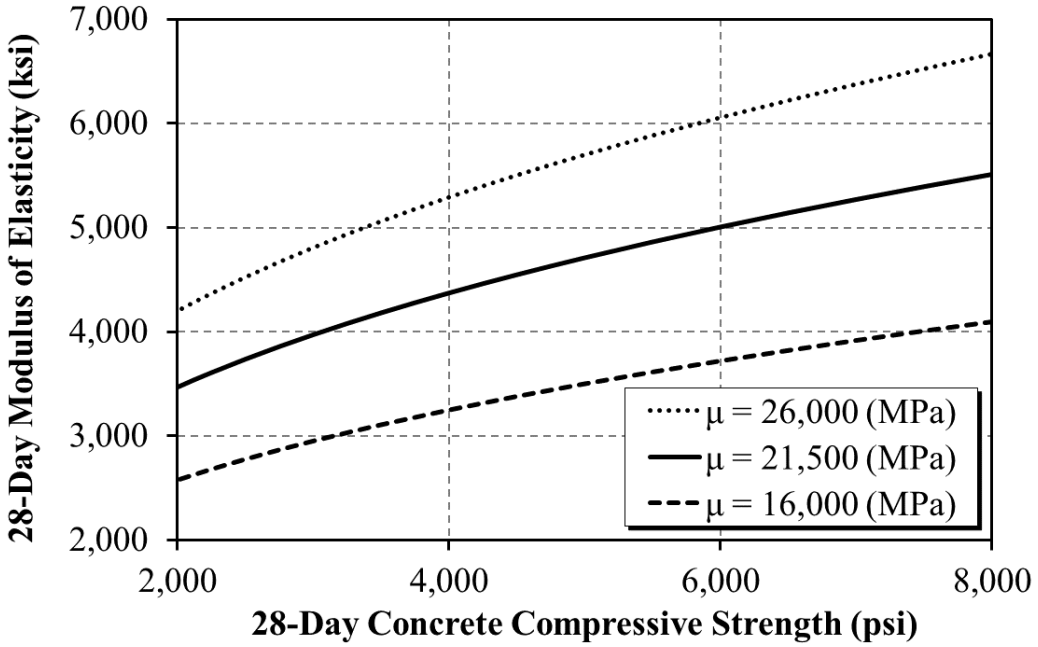

Figure 7-16: Effects of varying empirical parameter μ on CEB MC 1990 predicted modulus of elasticity at 28 days

The next analysis is performed on the compliance predictions for the CEB MC 1990 Model. A graphical analysis method is used to visualize how the predictions with the CEB MC 1990 Model can be improved for the different segment groups. Compliance results are compared in Figure 7-17 for the 28-day loading age for Group A and Group C segments representing the lowest strength and greatest strength concrete groups, respectively.

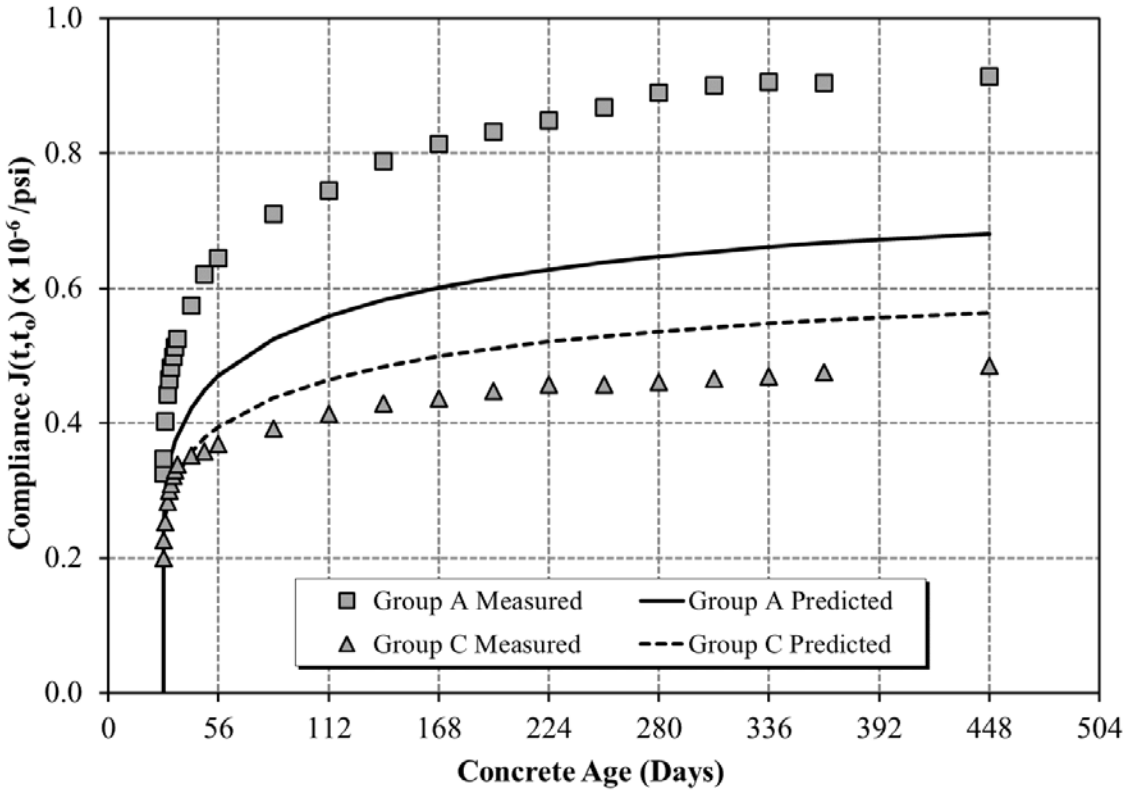

Figure 7-17: CEB MC 1990 Model graphical analysis of compliance for lowest and greatest strength concrete groups

The ultimate compliance values are predicted poorly for all segment groups. Calibration needs to occur in response to the notional creep coefficient shown in Equation 7.23. The empirical parameter, ρ, shown in Equation 7.24, will best modify the compliance predictions of the CEB MC 1990 Model.

$$\phi_o = \phi_{RH}\beta(f_{cm})\beta(t_0) \quad \text{Equation 7.23}$$

$$\phi_o = \rho[\phi_{RH}\beta(f_{cm})\beta(t_0)] \quad \text{Equation 7.24}$$

Where,

ρ = Empirical parameter being calibrated (unitless)

The effects of varying the empirical parameter ρ on compliance is illustrated in Figure 7-18. It can be concluded from the figure that ρ will increase and decrease the ultimate compliance value. As ρ increases and decreases the long-term compliance increases and decreases, accordingly. There is no evidence indicating that the rate of creep development should be modified.

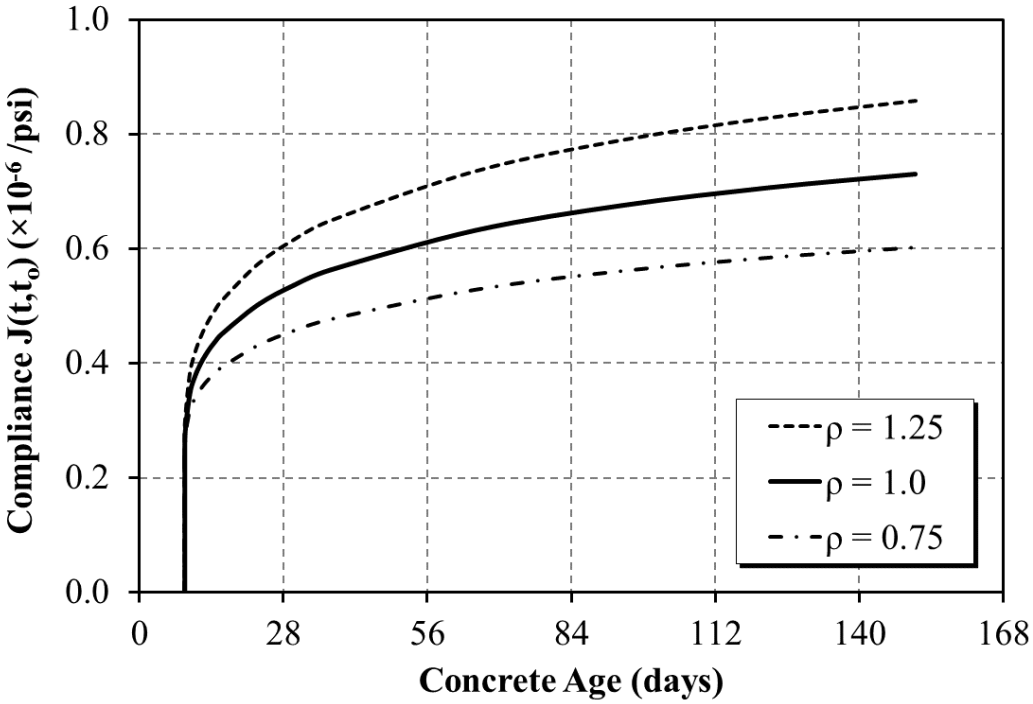

Figure 7-18: Effects of varying empirical parameter ρ on CEB MC 1990 calculated compliance

The last modification to the CEB MC 1990 Model is to more accurately predict shrinkage in the concrete cylinders. Similar to compliance, a graphical analysis is performed to observe what can be improved for shrinkage predictions. The measured and predicted shrinkage strains are compared in Figure 7-19 for Group A and C segment classifications representing the lowest and greatest concrete strengths, respectively.

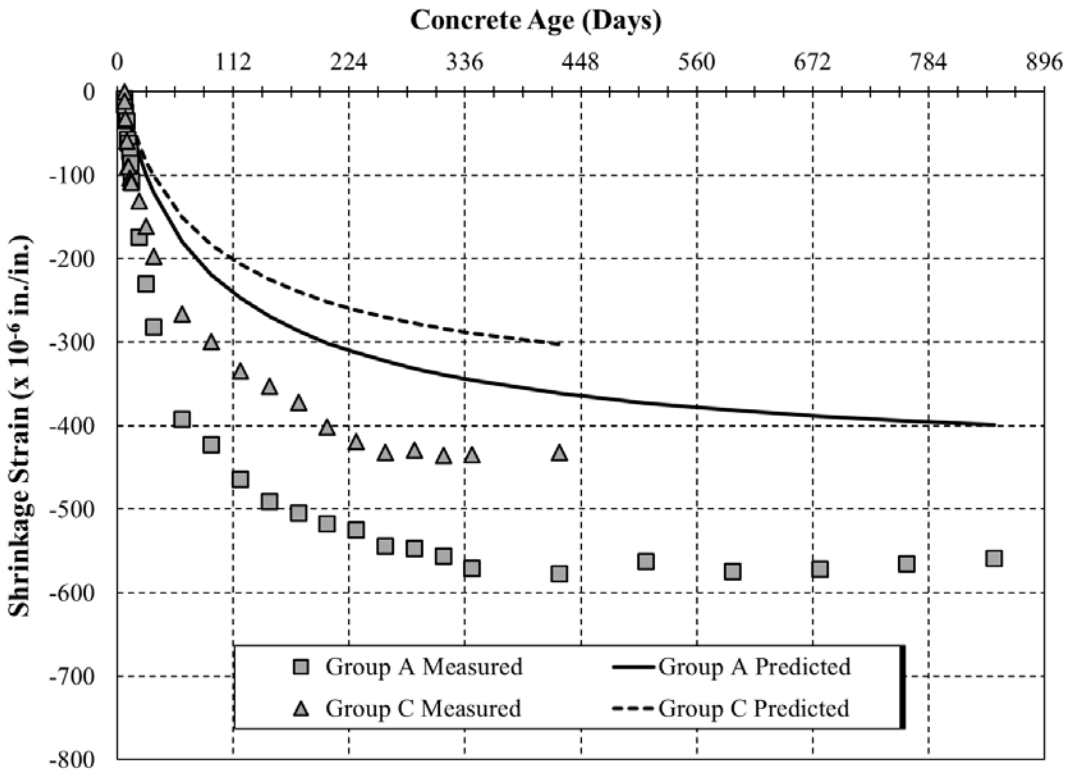

Figure 7-19: CEB MC 1990 Model graphical analysis of shrinkage for lowest and greatest strength concrete groups

After observing the trends in the original prediction, it was decided that modifying the notional shrinkage coefficient as well as the time-dependent rate of development will have the most effect on predicting shrinkage more accurately. The original formulation of the notional shrinkage coefficient for the CEB MC 90 Model is shown in Equation 7.25, prior to accounting for relative humidity. For use in calibration, the empirical parameter υ is selected and is defined in Equation 7.26. The development of shrinkage when varying the empirical parameter υ is illustrated in Figure 7-20. As the empirical parameter is increased, the resulting shrinkage strain is increased.

$$\varepsilon_s(f_{cm}) = [160 + 10\beta_{sc}(9 - f_{cm}/10)] \times 10^{-6} \qquad \text{Equation 7.25}$$

$$\varepsilon_s(f_{cm}) = [160 + \upsilon\beta_{sc}(9 - f_{cm}/10)] \times 10^{-6} \qquad \text{Equation 7.26}$$

Where,

υ = Empirical parameter being calibrated (MPa^{-1})

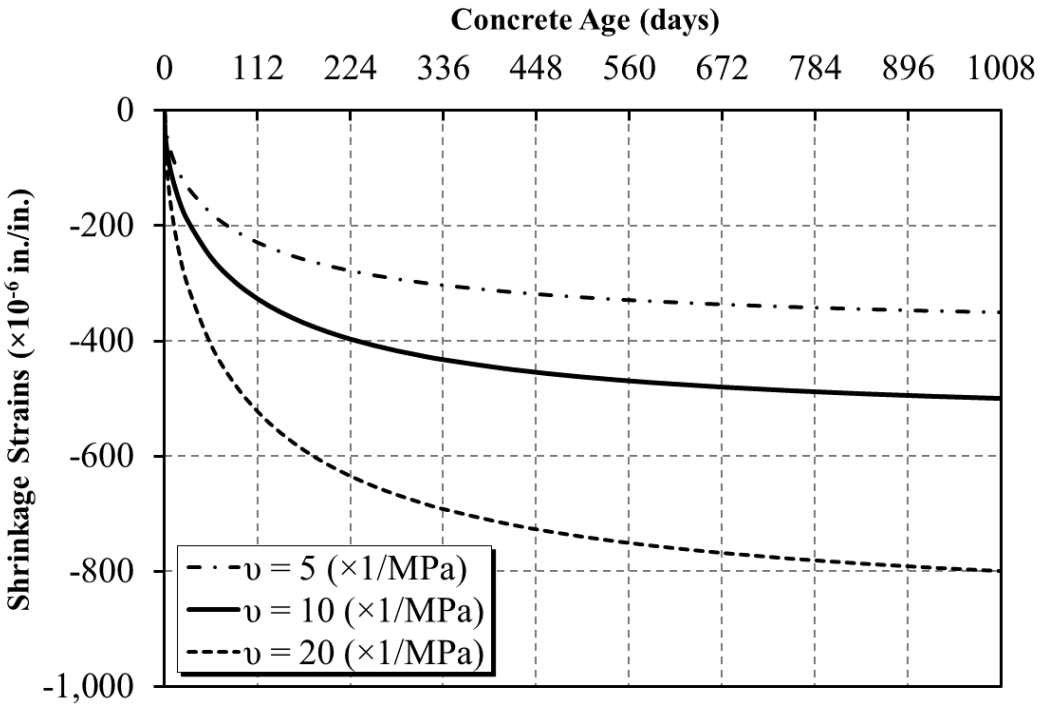

Figure 7-20: Effects of varying empirical parameter υ on the CEB MC 1990 predicted drying shrinkage

The original formulation of the time-dependent factor for shrinkage in the CEB MC 1990 Model is defined in Equation 7.27. For use in calibration the empirical parameter η is selected and can be seen in Equation 7.28. The development of shrinkage when varying the empirical parameter η is illustrated in Figure 7-21. As the empirical parameter decreases the rate of shrinkage development increases.

$$\beta_s(t-t_s) = \left[\frac{(t-t_s)}{350(h/100)^2 + (t-t_s)}\right]^{0.5} \quad \text{Equation 7.27}$$

$$\beta_s(t-t_s) = \left[\frac{(t-t_s)}{\eta(h/100)^2 + (t-t_s)}\right]^{0.5} \quad \text{Equation 7.28}$$

Where,

η = empirical parameter being calibrated (days/mm^2).

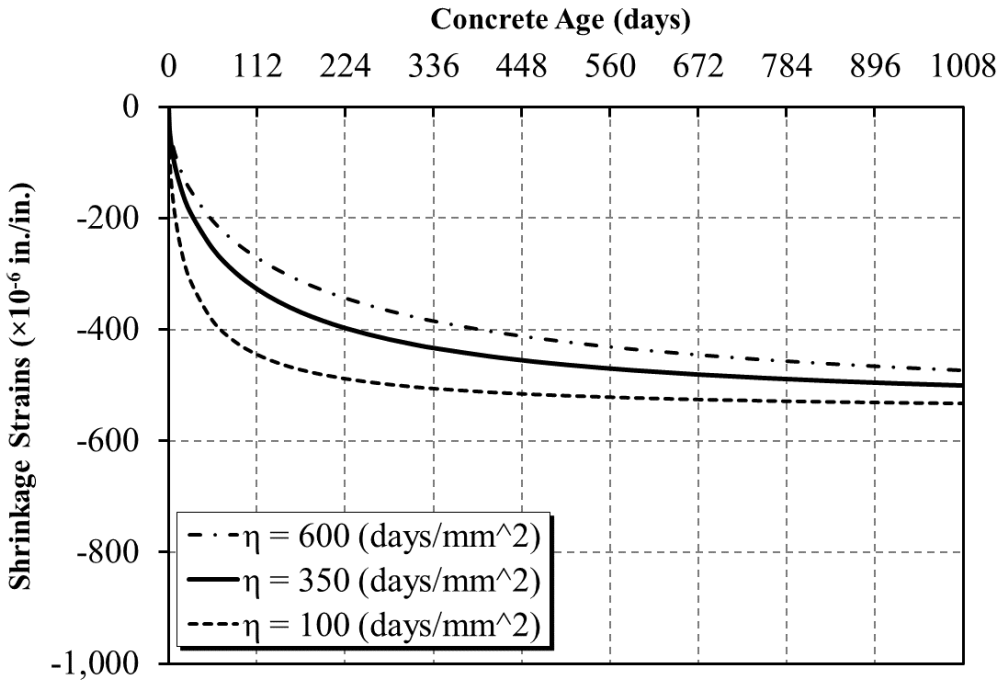

Figure 7-21: Effects of varying empirical parameter η on the CEB MC 1990 predicted drying shrinkage

7.6.2 Results for Calibration of the CEB MC 1990 Model

After each empirical parameter was calibrated, the prediction accuracy of the calibrated model was reviewed to evaluate the overall model performance. For compliance predictions, μ was calibrated using the modulus of elasticity testing results, and ρ was calibrated using the modified modulus of elasticity predictions. For shrinkage, υ and η were varied simultaneously during calibration. Similar to the GL 2000 Model, each empirical parameter was calibrated by minimizing the sum of the square error. The original and calibrated empirical parameters for the CEB MC 1990 Model are presented in Table 7-17.

Table 7-17: Original and calibrated empirical parameters for the CEB MC 1990 Model

Empirical Parameter	Original CEB MC 1990 Model	Modified CEB MC 1990 Model		
		Group A	Group B	Group C
μ (MPa)	21,500	16,500	17,500	20,500
ρ (unitless)	1.0	0.95	0.85	0.75
υ (MPa^{-1})	10	20	20	12.5
η ($days/mm^2$)	350	100	100	100

7.6.2.1 Modified CEB MC 1990 Model: Modulus of Elasticity

The Modified CEB MC 1990 Model was calibrated using all measured data for the project. The Modified CEB MC 1990 Model prediction of modulus of elasticity at 28 days for segment Groups A to C are defined in Equation 7.29 to 7.31, respectively.

Group A Segments:

$$E_{ci} = 16{,}500[f_{cm}/10]^{1/3} \qquad \text{Equation 7.29}$$

Group B Segments:

$$E_{ci} = 17{,}500[f_{cm}/10]^{1/3} \qquad \text{Equation 7.30}$$

Group C Segments:

$$E_{ci} = 20{,}500[f_{cm}/10]^{1/3} \qquad \text{Equation 7.31}$$

A comparison of measured and predicted modulus of elasticity using the Modified CEB MC 1990 Model is presented in Table 7-18. The maximum positive and negative percent error between the measured and predicted modulus of elasticity is 7% and -10%, respectively. The best prediction renders a percent error of nearly 0% for the 91-day loading age of the 11/19/2018 sampling date. As shown in Table 7-19, overall the Modified CEB MC 1990 Model more accurately predicts the measured modulus of elasticity than the Original CEB MC 1990 Model. In order to visualize the improvement, the measured and predicted modulus of elasticity for the Original and Modified CEB MC 1990 Models are presented in Figure 7-22.

Table 7-18: Comparison of measured and predicted modulus of elasticity using the Modified CEB MC 1990 Model

I-59/I-20 Bridge Segment Classification	Loading Age (Days)	Measured Modulus of Elasticity (ksi)	Modified CEB MC 1990 Modulus of Elasticity (ksi)	Error (%)
Group A	**04/10/2018**			
	7	3,800	3,521	-7%
	28	4,050	3,863	-5%
	91	3,850	4,105	7%
	182	4,150	4,182	1%
Group B	**07/09/2018**			
	7	4,250	3,844	-10%
	28	4,250	4,227	-1%
	91	4,200	4,491	7%
	182	4,300	4,576	6%
Group B	**11/19/2018**			
	7	4,400	4,098	-7%
	28	4,600	4,330	-5.9%
	91	4,600	4,604	0%
	182	4,500	4,689	4%
Group C	**04/16/2019**			
	7	5,100	4,770	-6%
	28	5,300	5,253	-1%
	91	5,400	5,582	3%
	182	5,400	5,687	5%

Table 7-19: Mean percent error for Original and Modified CEB MC 1990 Model

Model	Mean Percent Error
Original CEB MC 1990 Model	19.5
Modified CEB MC 1990 Model	-0.5

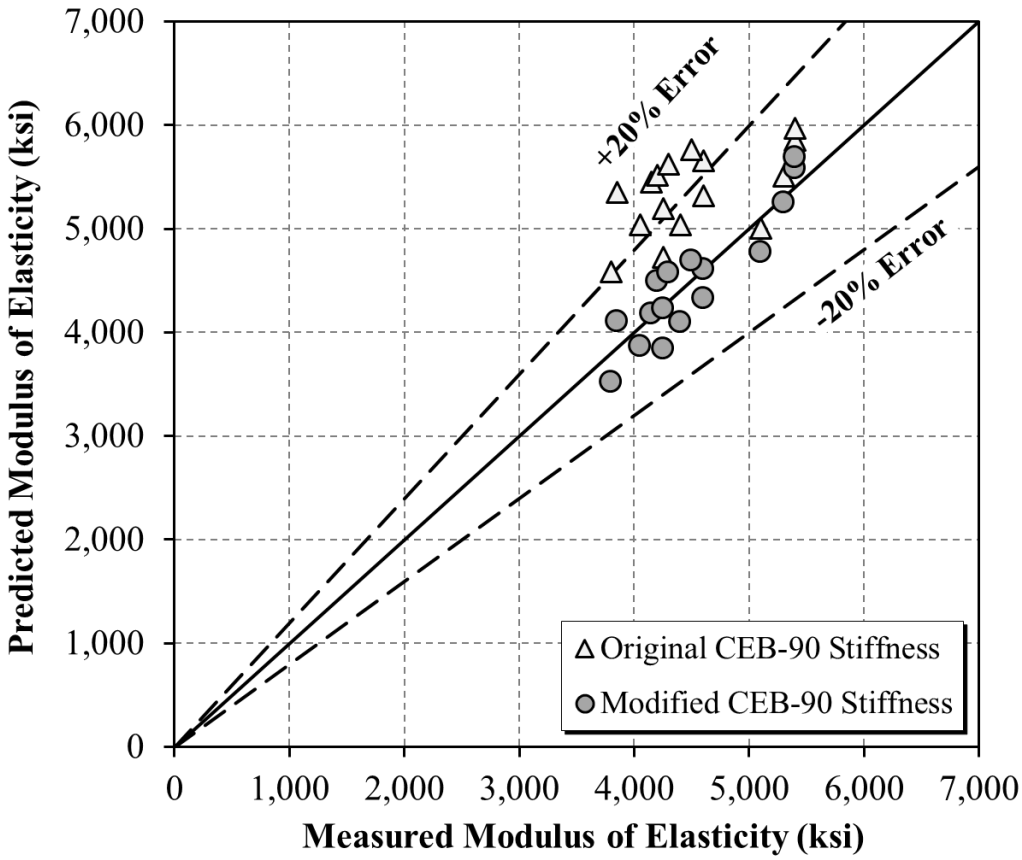

Figure 7-22: Measured versus predicted modulus of elasticity with the Original and Modified CEB MC 1990 Models

7.6.2.2 Modified CEB MC 1990 Model: Compliance

The notional creep coefficient formulation was calibrated using all collected data for the project and is shown in Equations 7.32 to 7.34 where the empirical parameter is modified for segment Groups A to C, respectively.

Group A Segments:

$$\phi_o = 0.95[\phi_{RH}\beta(f_{cm})\beta(t_0)] \quad \text{Equation 7.32}$$

Group B Segments:

$$\phi_o = 0.85[\phi_{RH}\beta(f_{cm})\beta(t_0)] \quad \text{Equation 7.33}$$

Group C Segments:

$$\phi_o = 0.75[\phi_{RH}\beta(f_{cm})\beta(t_0)] \quad \text{Equation 7.34}$$

S_j values were calculated to assess the unbiased error for compliance for all sampling dates. The goal in calibration is to reduce the overall error between the measured compliance and the compliance prediction from the Modified CEB MC 1990 Model. In addition to the total unbiased error for all data points, the error for each sampling date was recorded for comparison to the Original CEB MC 1990 Model. A comparison of S_j values for the Original and Modified CEB MC 1990 Models for compliance predictions are presented in Table 7-20. For all sampling dates the Modified CEB MC 1990 Model provides much more accurate compliance predictions. The most improvement is obtained for the 04/10/2018 sampling date. The overall S_j for all data shows a 68% improvement between model versions. The residual values for compliance using the Original and Modified CEB MC 1990 Models are plotted in Figure 7-23.

Table 7-20: Comparison of S_j values for predicted compliance for the Original and Modified CEB MC 1990 Models

Sampling Date	**Original CEB MC 1990 Model**	**Modified CEB MC 1990 Model**	**Improvement**
	S_j ($\times 10^{-6}$/psi)	S_j ($\times 10^{-6}$/psi)	(%)
04/10/2018	0.142	0.039	73%
07/09/2018	0.057	0.023	60%
11/19/2018	0.057	0.021	64%
04/16/2019	0.056	0.027	53%
All Data	0.088	0.028	68%

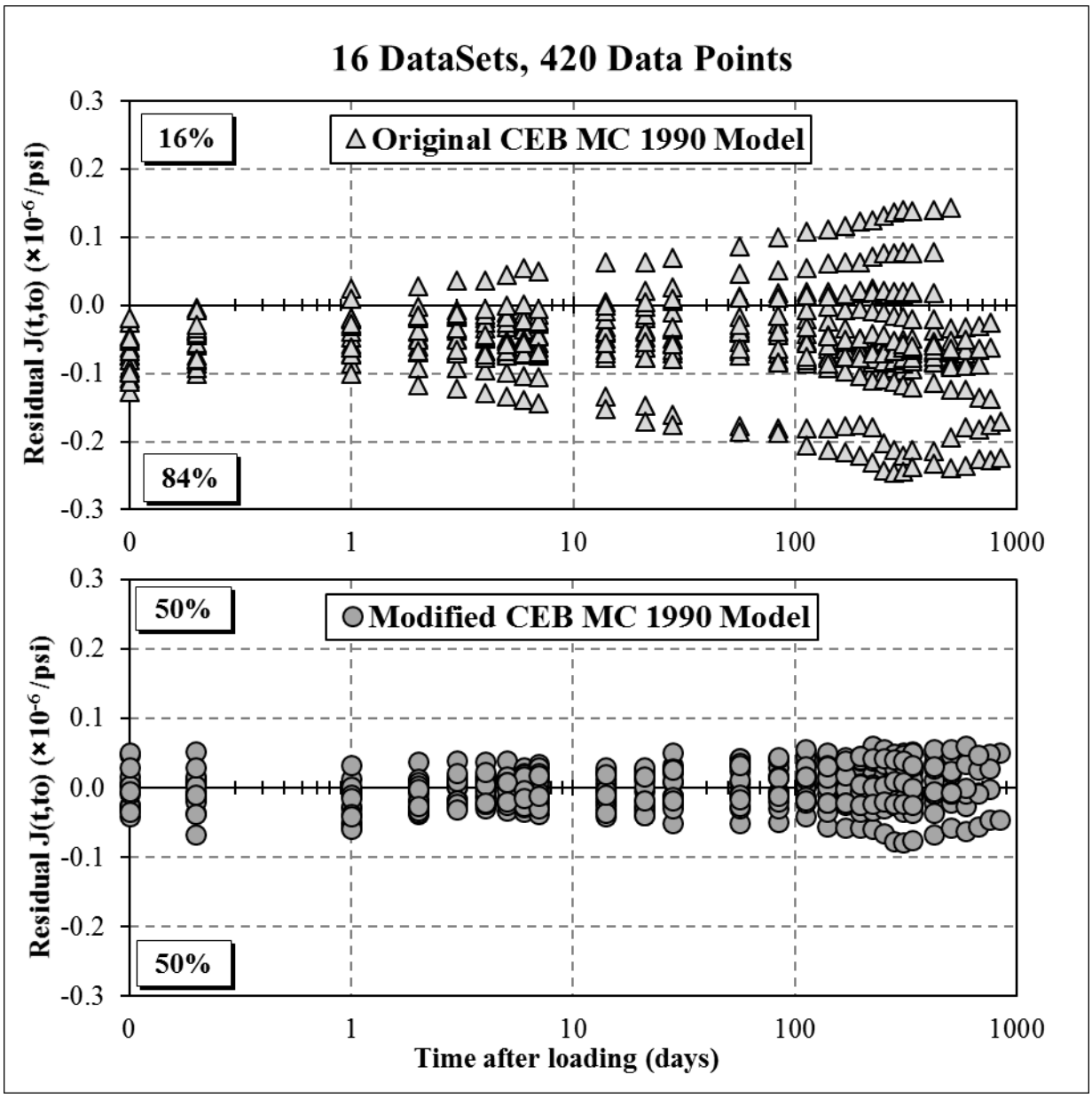

Figure 7-23: Residual compliance for Original and Modified CEB MC 1990 Models

The measured versus predicted compliance using the the Modified CEB MC 1990 Model for all test results is presented in Figure 7-24. Similar to the Modified GL 2000 Model, almost all points fall within the ±20 percent error bands, which when compared to the Original CEB MC 1990 Model, shown in Figure 6-9, is a very significant improvement. The measured versus predicted compliance, separated by sampling date and loading age, using the Modified CEB MC 1990 Model is presented in Figure 7-25.

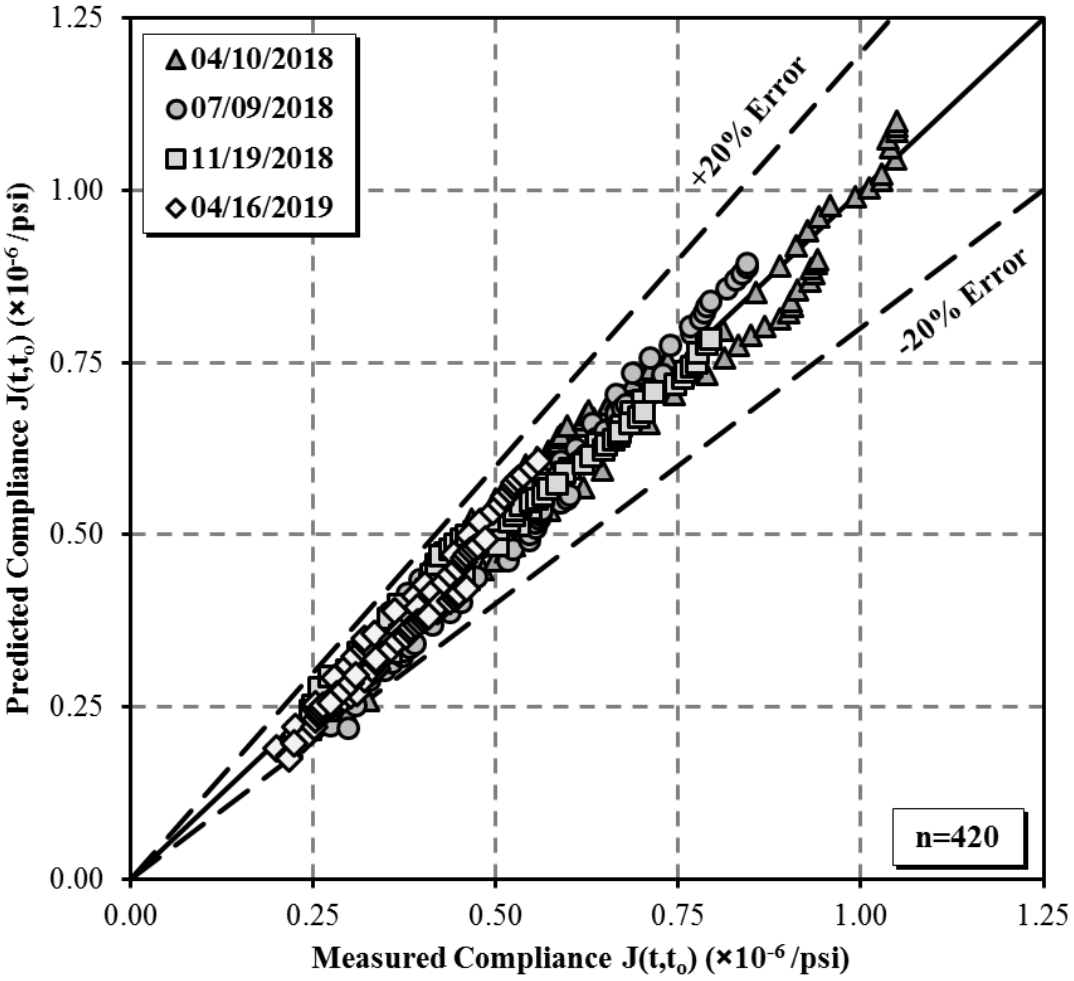

Figure 7-24: Measured versus predicted compliance using the Modified CEB MC 1990 Model

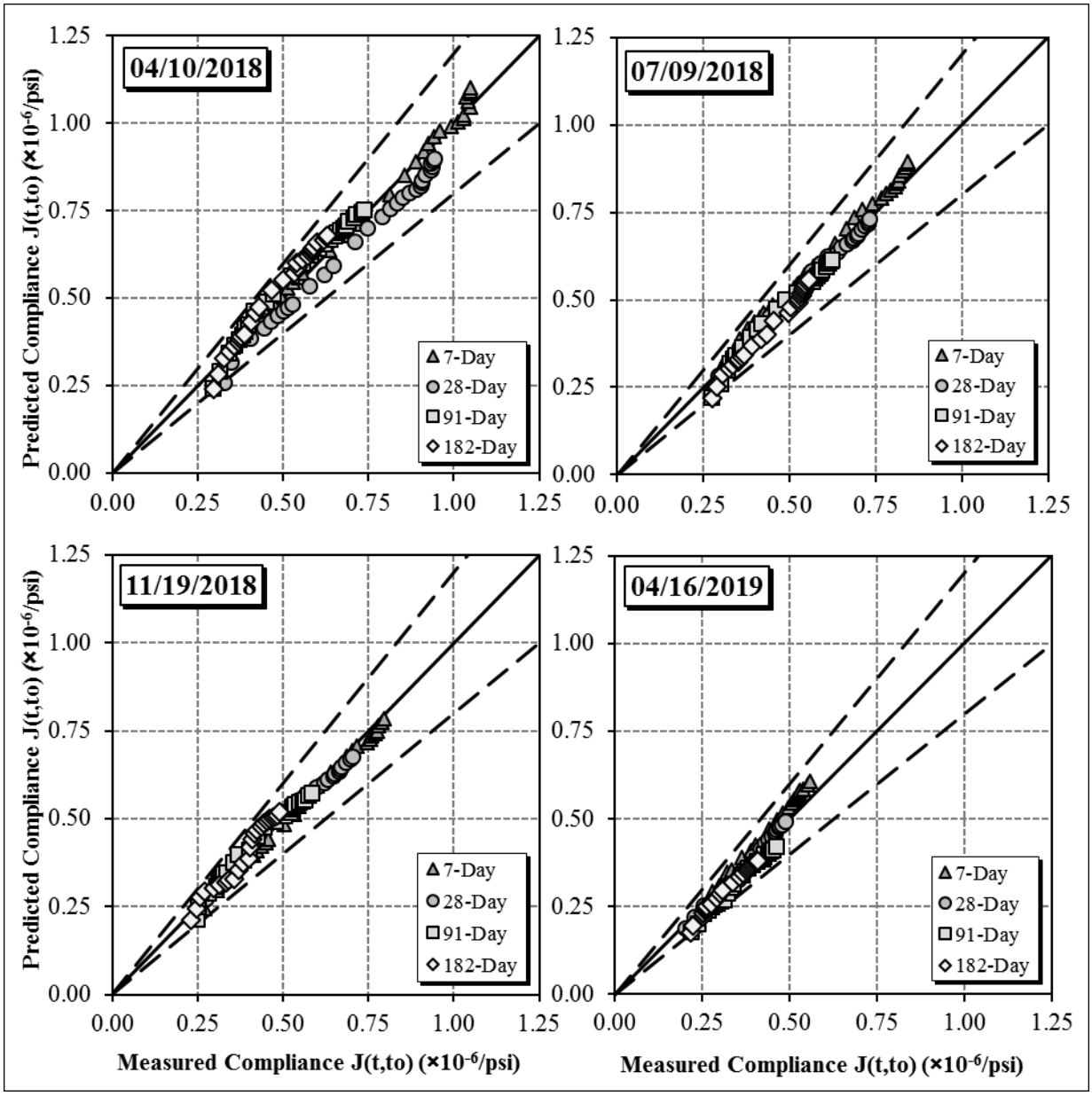

Figure 7-25: Measured versus predicted compliance using the Modified CEB MC 1990 Model separated by sampling dates and loading ages

7.6.2.3 Modified CEB MC 1990 Model: Shrinkage

The final modification to the CEB MC 1990 Model is presented to more accurately predict the shrinkage values in cylinders. The Modified CEB MC 1990 Model formulation to predict the notional shrinkage coefficient in Group A and B segments is defined in Equation 7.35. The Modified CEB MC 1990 Model formulation to predict the notional shrinkage coefficient in Group C segments is presented in Equation 7.36. The Modified CEB MC 1990 Model formulation for the shrinkage development factor with time is defined in Equation 7.37.

Group A and B Segments:

$$\varepsilon_s(f_{cm}) = [160 + 20\beta_{sc}(9 - f_{cm}/10)] \times 10^{-6} \qquad \text{Equation 7.35}$$

Group C Segments:

$$\varepsilon_s(f_{cm}) = [160 + 12.5\beta_{sc}(9 - f_{cm}/10)] \times 10^{-6} \qquad \text{Equation 7.36}$$

All Segment Groups:

$$\beta_s(t - t_s) = \left[\frac{(t - t_s)}{100(h/100)^2 + (t - t_s)}\right]^{0.5} \qquad \text{Equation 7.37}$$

S_j values are used to determine the unbiased estimate of the error in predicting shrinkage of the cylindrical specimens. A comparison of S_j values for the Original and Modified CEB MC 1990 Models is presented in Table 7-21. The total S_j for all data is decreased by 87 percent. The smallest improvement of 80 percent corresponds to the 04/16/2019 sampling date, and the largest improvement of 89 percent corresponds to the 04/10/2018 sampling date. The residual shrinkage strains for the Original and Modified CEB MC 1990 Models are presented in Figure 7-26.

Table 7-21: Comparison of S_j values for predicted shrinkage for the Original and Modified CEB MC 1990 Models

Sampling Date	**Original CEB MC 1990 Model**	**Modified CEB MC 1990 Model**	**Improvement**
	S_j ($\times 10^{-6}$ in./in.)	S_j ($\times 10^{-6}$ in./in.)	(%)
04/10/2018	168	18.1	89%
07/09/2018	154	19.4	87%
11/19/2018	129	15.7	88%
04/16/2019	112	22.7	80%
All Data	144	18.8	87%

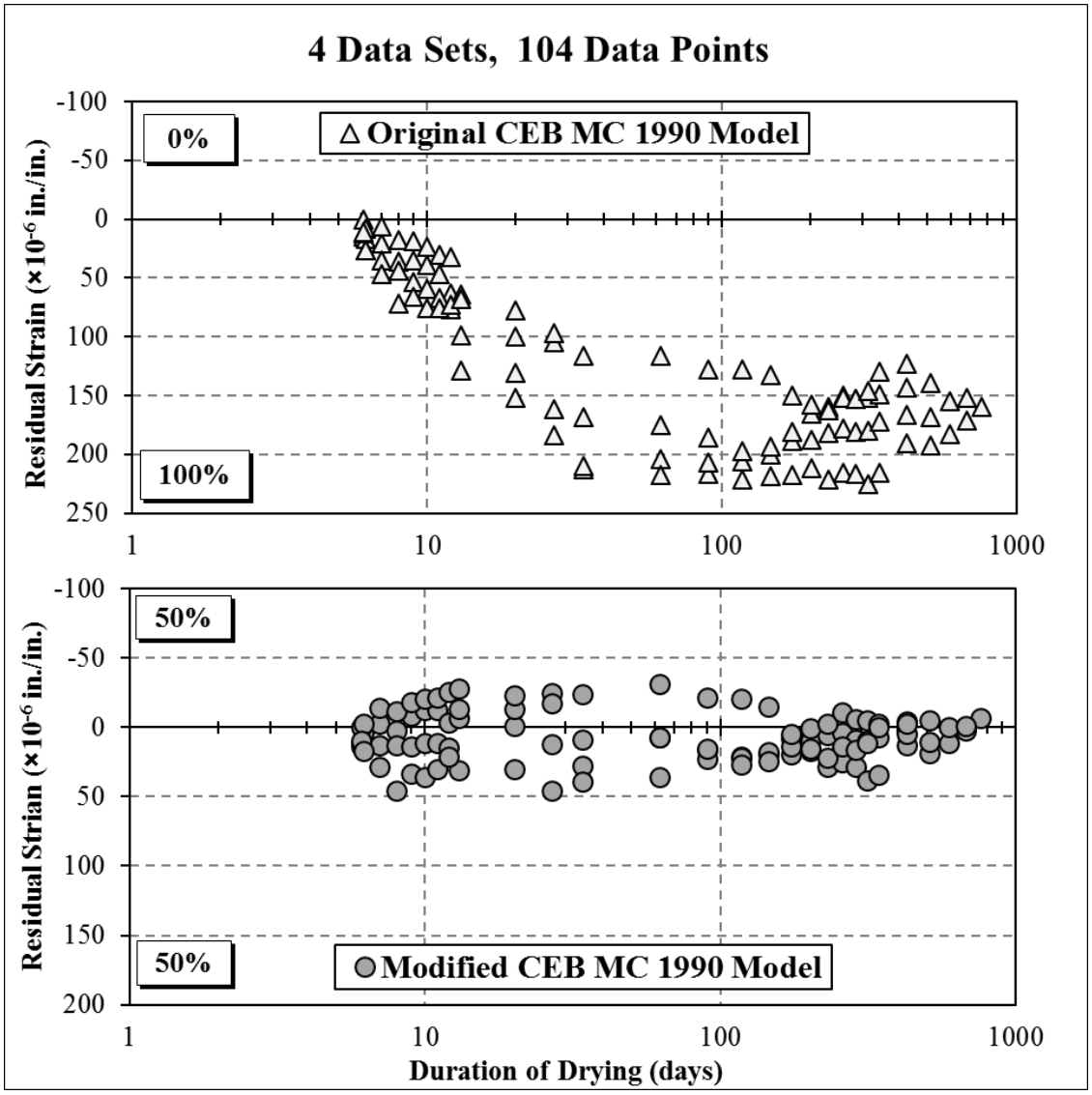

Figure 7-26: Shrinkage residuals for cylindrical shrinkage specimens using the Original and Modified CEB MC 1990 Models

The measured versus predicted shrinkage using the Modified CEB MC 1990 Model is presented in Figure 7-27. Similar to the Modified GL 2000 Model, the majority of points fall within the ±20 error margins, which when compared to the Original CEB MC 1990 Model, shown in Figure 6-10, is a significant improvement. It can be concluded from Figure 7-26, Figure 7-27, and Table 7-21 that the Modified CEB MC 1990 Model provides improved predicitons of the shrinkage collected from the cylindrical specimens of the Birmingham I-59/I-20 segmental bridge.

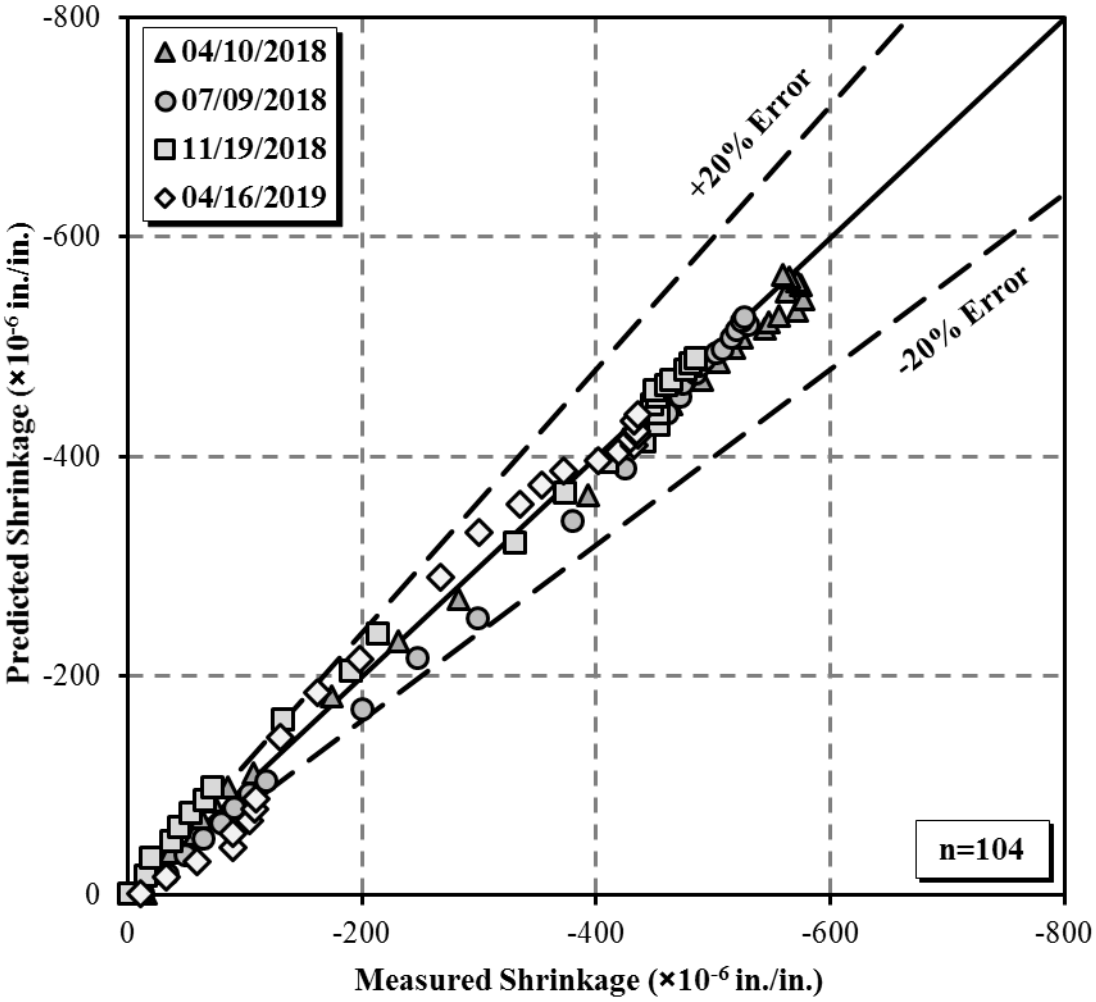

Figure 7-27: Measured versus predicted shrinkage using the Modified CEB MC 1990 Model

7.7 SUMMARY OF MODEL CALIBRATION

It is determined that the GL 2000 Model most accurately predicts the creep and shrinkage of concrete in the Birmingham I-59/I-20 segmental bridge. The Modified GL 2000 Model is calibrated to best represent the collected data for both creep and shrinkage. For the most accurate representation of the Birmingham I-59/I-20 segmental bridge, segments are grouped by casting date as shown in Table 7-9. As a secondary objective to this research effort the Modified CEB MC 1990 Model is calibrated to best represent creep and shrinkage in the same collected data. The following statements can be made in summary of model calibration:

- The GL 2000 Model was calibrated using 5 empirical parameters presented in Table 7-11 with one parameter for modulus of elasticity prediction, two for creep prediction, and two for shrinkage prediction.
- The Modified GL 2000 Model improves creep predictions most significantly in Group A segments with 69 percent improvement.
- Overall, the Modified GL 2000 Model improves creep predictions by 57 percent.
- Shrinkage predictions in Group A segments are improved most significantly at 87 percent with the Modified GL 2000 Model.
- Overall, the Modified GL 2000 Model improves shrinkage predictions by 60 percent.
- The CEB MC 1990 Model was calibrated using four empirical parameters presented in Table 7-17 with one for modulus of elasticity prediction, one for creep prediction, and two for shrinkage prediction.
- The Modified CEB MC 1990 Model improves the creep predictions in Group A segments most significantly at 73 percent.
- Overall improvement of creep predictions using the Modified CEB MC 1990 Model is 68 percent.
- Shrinkage predictions using the Modified CEB MC 1990 Model are improved nearly the same across all concrete groups at 87 percent.

CHAPTER 8: SUMMARY, CONCLUSIONS, AND RECOMMENDATIONS

8.1 SUMMARY OF WORK PERFORMED

The primary objective of this research effort was to accurately predict the creep and shrinkage of the concrete in the I-59/I-20 segmental bridge in Birmingham, Alabama. In the first stage of experimental work, specimens were collected while the bridge segments were cast at the jobsite. The second stage of experimental work included laboratory testing the specimens for the following hardened concrete properties: compressive strength, modulus of elasticity, creep, and shrinkage. In the second stage of the project, creep and shrinkage results were compared to predicted values from commonly used models.

8.1.1 Specimen Collection

For this study, 96 cylindrical (6"×12") and 24 prismatic (3"×3"×11.25") concrete specimens were collected across four sampling dates between April 10, 2018 and April 16, 2019. Over the course of the project, the Contractor made changes to the concrete proportions to increase the early-age and 28-day compressive strength of the concrete. Mixture proportions were also adjusted to accommodate changes in chemical admixture suppliers and cement due to changes in the availability of Type III cement during the project. These changes resulted in four different ALDOT approved mixture proportions. Each sampling date corresponded to a different ALDOT approved mixture, which was tested by quality control technicians to ensure concretes met the fresh properties specified by ALDOT. Specimens were cured alongside the bridge segments to ensure the same accelerated curing regime was followed. After initial curing, concrete samples were transported to the concrete materials testing laboratory at Auburn University where testing commenced.

8.1.2 Testing of Concrete Specimens

Shrinkage testing was performed according to AASHTO T160 (2017) for all concrete prisms collected for this research project. Prior to creep testing, concrete was tested for compressive

strength and modulus of elasticity in accordance with AASHTO T22 (2017) and ASTM C469 (2014), respectively. Creep testing was performed in accordance with ASTM C512 (2015) at four loading ages of 7, 28, 91, and 182 days. All creep specimens were loaded at 40 percent of their compressive strength at the corresponding loading age. The shrinkage strains in unloaded cylindrical specimens were also collected during creep testing to calculate the total load induced strain for creep specimens.

8.1.3 Modeling Compliance and Shrinkage

Compliance was modeled to represent the initial elastic and creep strains to obtain the most accurate comparison to measured results. Compliance allows for a more accurate comparison of creep results, because the results are normalized based on applied loading (ACI 209.2R 2008). The development of compliance and shrinkage was modeled for all concretes collected for the duration of this project using six commonly used prediction methods: ACI 209 (2008), AASHTO LRFD (2017), GL 2000 (Gardner and Lockman 2001), B3 Model (Bazant and Baweja 2000), CEB MC 1990 (CEB 1990), and CEB MC 2010 (fib 2012).

The results for each model were determined by using measured fresh and hardened concrete properties, which were different depending on the loading age as well as the concrete sampled during each jobsite visit. The predictions from the models were then compared to the measured test data to determine the most accurate prediction of compliance and shrinkage collected for the concrete placed in the Birmingham I-59/I-20 bridge segments. The most accurate model was determined to be the GL 2000 Model, which was calibrated to best represent the measured compliance and shrinkage of concrete in the Birmingham I-59/I-20 segmental bridge.

8.2 CONCLUSIONS

The subsequent sections focus on conclusions determined throughout this research project. The majority of which are concrete properties and the compliance and shrinkage prediction methods.

8.2.1 Concrete Properties

From this research effort, the following conclusions can be made in reference to the fresh and hardened properties collected for the concrete sampled from the Birmingham I-59/I-20 segmental bridge project:

- All concrete mixtures used in creep and shrinkage testing met fresh property requirements specified by ALDOT.
- Concrete compressive strength systematically increased throughout the duration of the project, which correlates not only to an increase in modulus of elasticity but also to a decrease in creep and shrinkage deformations, which was observed through testing.
- The measured compressive strength and modulus of elasticity are least and greatest in specimens collected on April 10, 2018 and April, 16, 2019, respectively.
- For creep testing, the April 10, 2018 and April 16, 2019 sampling dates exhibit the greatest and least amount of creep across all sampling dates, respectively, which matches the inverse of measured compressive strength trend.
- Similar to creep, cylindrical specimens collected on April 10, 2018 and April 16, 2019 exhibit the greatest and least magnitude of shrinkage across all sampling dates, respectively.
- In general shrinkage strains in concrete prismatic specimens are very similar between air- and moist-curing regimes, and the April 10, 2018 and April 16, 2019 sampling dates exhibit the greatest and least magnitude of shrinkage, respectively.

8.2.2 Compliance and Shrinkage Prediction Methods

The last major objective of this project was to calibrate the most accurate model to best represent the long-term volumetric changes that may occur in the Birmingham I-59/I-20 segmental bridge, and the following conclusions are based on statistical analysis and model calibration:

- The GL 2000 and CEB MC 1990 Models are most accurate in predicting compliance across all data collected for the project; the AASHTO LRFD 2017 Model is least accurate in predicting compliance.
- The AASHTO LRFD 2017 and B3 Models are most and least accurate in predicting shrinkage in cylindrical specimens across all measured data and models, respectively.
- Using a weighting system based on total number of segments cast with respect to each sampling date, the GL 2000 Model most accurately predicts the combined compliance and shrinkage in the concrete of the segments in the Birmingham I-59/I-20 segmental bridge.

- The Modified GL 2000 Model, developed during this project, significantly improves the accuracy of compliance and shrinkage predictions for concrete used in the Birmingham I-59/I-20 bridge segments.
- The calibrated CEB MC 1990 Model was developed for implementation in bridge design software that may be used for analysis of the Birmingham I-59/I-20 segmental bridge.

8.3 RECOMMENDATIONS FOR FUTURE WORK

The majority of recommendations for future work are in relation to improving the creep and shrinkage models specific to the Birmingham I-59/I-20 segmental bridge:

- Continue to monitor creep and shrinkage behavior of all specimens collected during the project.
- After 4 years of data collection, presumably around the January 1, 2022, evaluate all models with no prior bias and recalibrate the modified models, or calibrate a different model depending on the accuracy from updated statistics.

REFERENCES

AASHTO. 2017. *AASHTO LRFD Bridge Design Specifications: Customary U.S. Units*. 8th ed. Washington D.C.: American Association of State Highway and Transportation Officials (AASHTO).

AASHTO T22. 2017. Compressive Strength of Cylindrical Concrete Specimens. In *Standard Specifications for Transportation Materials and Methods of Sampling and Testing.* Washington, D.C: American Association of State Highway and Transportation Officials.

AASHTO T23. 2018. Making and Curing Concrete Test Specimens in the Field. *In Standard Specifications for Transportation Materials and Methods of Sampling and Testing.* Washington, D.C: American Association of State Highway and Transportation Officials.

AASHTO T119. 2018. Standard Method of Test for Slump of Hydraulic Cement Concrete. In *Standard Specifications for Transportation Materials and Methods of Sampling and Testing.* Washington, D.C: American Association of State Highway and Transportation Officials.

AASHTO T121. 2019. Method of Test for Density (Unit Weight), Yield, and Air Content (Gravimetric) of Concrete. In *Standard Specifications for Transportation Materials and Methods of Sampling and Testing*. Washington, D.C: American Association of State Highway and Transportation Officials.

AASHTO T160. 2017. Length Change of Hardened Hydraulic Cement Mortar and Concrete. In *Standard Specifications for Transportation Materials and Methods of Sampling and Testing.* Washington, D.C: American Association of State Highway and Transportation Officials.

AASHTO T309. 2015. Temperature of Freshly Mixed Portland Cement Concrete. In *Standard Specifications for Transportation Materials and Methods of Sampling and Testing*. Washington, D.C: American Association of State Highway and Transportation Officials.

ALDOT 455. 2018. Grinding Concrete Pavement Surfaces. *In Standard Specifications for Highway Construction*. Montgomery, AL. Alabama Department of Transportation.

ALDOT 501. 2018. Structural Portland Cement Concrete. *In Standard Specifications for Highway Construction*. Montgomery, AL. Alabama Department of Transportation.

ALDOT 832. 2018. Concrete Joint Fillers, Joint and Cracksealants, and Waterstop Materials. *In Standard Specifications for Highway Construction*. Montgomery, AL. Alabama Department of Transportation.

ASTM C157. 2008. Standard Test Method for Length Change of Hardened Hydraulic-Cement Mortar and Concrete. ASTM International. West Conshohocken, PA.

ASTM C469. 2014. Standard Test Method for Static Modulus of Elasticity and Poisson's Ratio of Concrete in Compression. *ASTM International*. West Conshohocken, Pennsylvania.

ASTM C512. 2015. Standard Test for Creep in Concrete. ASTM International. West Conshohocken, Pennsylvania.

ASTM C1074. 2018. Standard Practice for Estimating Concrete Strength by the Maturity Method. *ASTM International*. West Conshohocken, Pennsylvania.

ACI Committee 209. 1992. Prediction of Creep, Shrinkage, and Temperature Effects in Concrete Structures (ACI 209R). In *ACI Manual of Concrete Practice 2001: Part 1*. Farmington Hills, Michigan: American Concrete Institute, 209R-1-209R-47.

ACI Committee 209. 2008. Guide for Modeling and Calculating Shrinkage and Creep of Concrete (ACI 209.2R). Farmington Hills, MI: American Concrete Institute.

Bazant, Z. P. and Baweja, S. 2000. Description of Model B3 and Prediction Procedure. In *The Adam Neville Symposium: Creep and Shrinkage – Structural Design Effects*, ed. A. Al-Manaseer. Farmington Hills, Michigan: American Concrete Institute, 3-34.

Bazant, Z. P. 2001. Prediction of concrete creep and shrinkage: past, present and future. *Nuclear Engineering and Design* 203, no. 1: 27-38.

CEB. 1990. "Creep and Shrinkage." In *CEB-FIP Model Code 1990*. Lausanne, Switzerland: Comite Euro-International du Beton (CEB90), 53-65.

CEB. 1972. "Structural Effects of Time-Dependent Behavior of Concrete." Paris, France: Comite Europeen du Beton (CEB72).

CEB. 1970. "Concrete." In *International Recommendations for the Design and Construction of Concrete Structures*. London, Great Britain: Comite Europeen du Beton (CEB70), 25-30.

fib. 2012. "Creep and Shrinkage". In *fib Model Code 2012: Final Draft*. Lausanne, Switzerland: fédération internationale du béton (fib), 124-149.

Gallaway, T. M. 1975. "Precasting of Segmental Bridges." In *Journal Proceedings*, Vol. 72, no. 10: 566-572.

Gardner, N. J. and Lockman, M.J. 2001. Design Provisions for Drying Shrinkage and Creep of Normal-Strength Concrete. In *ACI Materials Journal* 98, no. 2: 159-167.

Goins. 2013. “Linn Cove ViaDuct.” Flicker. February 16, 2013. Accessed October 29, 2020. https://www.flickr.com/photos/jlgoins64/

Kavanaugh, B.P. 2008. Creep Behavior of Self-Consolidating Concrete. MS Thesis, Auburn, AL: Auburn University.

Kamatchi, P., Rao, K. B., Dhayalini, B., Saibabu, S., Parivallal, S., Ravisakar, K., and Iyer, N.R. 2014. "Long-Term Prestress Loss and Camber of Box-Girder Bridge." In *ACI Structural Journal* 110, no. 12: 1297-1306.

Libby, J. R. 1976. "Segmental Box Girder Bridge Superstructure Design." In *Journal Proceedings*, Vol. 73, no. 5: 279-290.

Neville, A. M. 2011. *Properties of Concrete*, 5th. New York, New York: John Wiley & Sons, Inc.

McCuen, R. H. 1985. *Statistical Methods for Engineers*. Lebanon, IN. Prentice Hall, Inc. pp. 439.

Mehta, P. K., and Monteiro, J.M. 2014. C*ONCRETE Microstructure, Properties and Materials*, 4th. New York, New York: McGraw-Hill Education.

Muller, J. M. 1969. "Long-span Precast Prestressed Concrete Bridges built in Cantilever." *Special Publication* 23: 705-740.

Podolny, W., and Muller, J. M. 1994. *Construction and Design of Prestressed Concrete Segmental Bridges*. New York, New York: John Wiley & Sons, Inc.

Raphael, W., Zgheib, E., and Chateauneuf, A. 2018. Experimental Investigations and Sensitivity Analysis to Explain the Large Creep of Concrete Deformations in the Bridge of Cheviré. *Case Studies in Construction Materials*, Vol. 9.

Richey, D. R. 2018. Creep and Shrinkage Behavior of Concrete in Segmental Bridge Construction. MS Thesis, Auburn, AL: Auburn University.

Rizkalla, S., Mirmiran, A., Zia P., Russell, H., and Mast, R. 2007. *Application of the LRFD Bridge Design Specifications to High-Strength Structural Concrete: Flexure and Compression Provisions*, NCHRP Report 595. Transportation Research Board, National Research Council, Washington, DC.

Rusch, H., Jungwirth, D., and Hilsdorf, H. K. 1983. *Creep and Shrinkage Their Effect on the Behavior of Concrete Structures*. New York, New York: Springer-Verlag.

Roberts, C. L., Breen, J. E., and Kreger, M. E. 1993. Measurement Based Revisions for Segmental Bridge Design and Construction Criteria. Center for Transportation Research, University of Texas at Austin.

Schindler, A.K., Barnes, R. W., Kamgang, J. K., and Kavanaugh, B. P. 2017. Compliance of Self Consolidating Concrete for Prestressed Applications. *ACI Materials Journal* 114, no. 2: 273-283.

Troxell, G. E., Raphael, J. M., and Davis, R. E. 1958, J. *ASTM Proc*., Vol. 58: 1101-1120.

Tadros, M. K., Al-Omaishi, N., Seguirant, S. P. and Gallt, J. G. 2003. *Prestress Losses in Pretensioned High-Strength Concrete Bridge Girders*, NCHRP Report 496. Transportation Research Board, National Research Council, Washington, DC.

Tazawa, E. 1999. *Autogenous Shrinkage of Concrete*. New York, New York: Routledge.

APPENDIX A: RAW TEST DATA

A.1 COLLECTED CREEP TESTING DATA

Tables A-1 through A-16 contain all creep testing data collected for the duration of this study. Each table contains the total strain, drying shrinkage strain, strain due to load, creep strains, and total force associated with the loading age indicated at the top. Each table also contains the compressive strength and modulus of elasticity that was measured prior to creep testing as well as the target applied load.

Table A-1: Raw data for 04/10/2018 specimens loaded at 7 days

Sampling Date				**04/10/2018**		
Loading Age				**7 Days**		
Compressive Strength (psi)				5,100		
Modulus of Elasticity (ksi)				3,800		
Target Applied Load (kips)				57.7		
Reading Interval		Total Strain (με)	Shrinkage Strain (με)	Total Strain due to Load (με)	Creep Strain (με)	Total Force (kips)
Day Zero	Pre-Load	---	---	---	---	---
	Post-Load	-664	-8	-656	0	58.8
	2 to 6 Hour	-752	-16	-736	-80	58.7
Week One	Day 1	-925	-24	-901	-245	57.3
	Day 2	-1016	-36	-980	-325	58.7
	Day 3	-1078	-57	-1021	-365	57.3
	Day 4	-1126	-62	-1063	-407	58.7
	Day 5	-1170	-72	-1097	-442	58.0
	Day 6	-1218	-86	-1133	-477	58.1
	Day 7	-1265	-107	-1158	-502	57.3
Month One	Week 2	-1497	-174	-1322	-667	58.1
	Week 3	-1652	-230	-1422	-766	57.7
	Week 4	-1787	-282	-1505	-849	56.7
Year One	Month 2	-2080	-393	-1687	-1031	58.1
	Month 3	-2204	-423	-1780	-1125	56.9
	Month 4	-2311	-464	-1847	-1191	56.9
	Month 5	-2387	-491	-1897	-1241	57.3
	Month 6	-2432	-505	-1926	-1271	56.7
	Month 7	-2476	-518	-1958	-1303	56.7
	Month 8	-2517	-525	-1992	-1337	57.1
	Month 9	-2607	-544	-2062	-1407	56.6
	Month 10	-2650	-547	-2102	-1447	57.3
	Month 11	-2694	-556	-2138	-1483	56.6
	Month 12	-2708	-571	-2137	-1482	57.3
After Year One	Month 15	-2757	-577	-2179	-1524	56.7
	Month 18	-2729	-563	-2165	-1510	57.0
	Month 21	-2731	-575	-2156	-1500	57.1
	Month 24	-2752	-572	-2180	-1525	58.3
	Month 27	-2746	-565	-2181	-1525	57.6
	Month 30	-2741	-559	-2182	-1527	57.7

Table A-2: Raw data for 04/10/2018 specimens loaded at 28 days

Sampling Date				**04/10/2018**		
Loading Age				**28 Days**		
Compressive Strength (psi)				6,100		
Modulus of Elasticity (ksi)				4,050		
Target Applied Load (kips)				69.0		
Reading Interval		Total Strain (με)	Shrinkage Strain (με)	Total Strain due to Load (με)	Creep Strain (με)	Total Force (kips)
Day Zero	Pre-Load	---	---	---	---	---
	Post-Load	-778	0	-778	0	67.6
	2 to 6 Hour	-839	-9	-830	-52	70.3
Week One	Day 1	-978	-16	-962	-183	69.6
	Day 2	-1076	-18	-1058	-279	68.9
	Day 3	-1125	-16	-1109	-330	69.9
	Day 4	-1187	-33	-1154	-376	69.4
	Day 5	-1235	-45	-1191	-412	68.5
	Day 6	-1277	-52	-1226	-447	69.7
	Day 7	-1320	-64	-1256	-477	67.9
Month One	Week 2	-1475	-103	-1373	-594	69.4
	Week 3	-1602	-120	-1482	-703	69.6
	Week 4	-1686	-144	-1542	-764	70.0
Year One	Month 2	-1891	-193	-1698	-919	69.9
	Month 3	-2054	-281	-1773	-994	70.3
	Month 4	-2196	-310	-1886	-1107	70.3
	Month 5	-2260	-314	-1945	-1167	70.1
	Month 6	-2303	-313	-1990	-1211	70.3
	Month 7	-2345	-316	-2029	-1251	70.3
	Month 8	-2417	-341	-2076	-1297	69.2
	Month 9	-2464	-337	-2127	-1348	68.9
	Month 10	-2500	-346	-2154	-1376	69.7
	Month 11	-2527	-361	-2165	-1387	70.0
	Month 12	-2537	-373	-2164	-1385	69.7
After Year One	Month 15	-2552	-367	-2185	-1406	70.3
	Month 18	-2595	-370	-2225	-1446	70.1
	Month 21	-2601	-365	-2236	-1457	70.3
	Month 24	-2606	-377	-2229	-1451	70.1
	Month 27	-2613	-369	-2245	-1466	69.7
	Month 30	-2630	-381	-2249	-1471	70.1

Table A-3: Raw data for 04/10/2018 specimens loaded at 91 days

Sampling Date		**04/10/2018**				
Loading Age		**91 Days**				
Compressive Strength (psi)		6,000				
Modulus of Elasticity (ksi)		3,850				
Target Applied Load (kips)		67.9				
Reading Interval		Total Strain (με)	Shrinkage Strain (με)	Total Strain due to Load (με)	Creep Strain (με)	Total Force (kips)
Day Zero	Pre-Load	---	---	---	---	---
	Post-Load	-714	0	-714	0	68.7
	2 to 6 Hour	-756	1	-758	-44	67.9
Week One	Day 1	-836	-13	-823	-109	68.4
	Day 2	-885	-18	-868	-154	68.0
	Day 3	-913	-18	-895	-181	66.6
	Day 4	-940	-22	-918	-204	66.6
	Day 5	-960	-23	-936	-223	66.9
	Day 6	-976	-34	-942	-228	67.3
	Day 7	-993	-34	-959	-245	67.2
Month One	Week 2	-1069	-62	-1007	-293	68.0
	Week 3	-1167	-74	-1093	-379	66.6
	Week 4	-1224	-82	-1143	-429	67.9
Year One	Month 2	-1370	-104	-1266	-552	68.4
	Month 3	-1447	-96	-1351	-638	67.4
	Month 4	-1506	-96	-1410	-697	66.7
	Month 5	-1564	-100	-1463	-750	66.9
	Month 6	-1622	-120	-1502	-789	67.2
	Month 7	-1665	-123	-1542	-829	68.4
	Month 8	-1711	-132	-1579	-866	68.6
	Month 9	-1739	-147	-1592	-879	67.7
	Month 10	-1774	-159	-1615	-901	66.9
	Month 11	-1791	-152	-1638	-925	66.7
	Month 12	-1814	-153	-1661	-947	66.6
After Year One	Month 15	-1826	-155	-1672	-958	67.0
	Month 18	-1868	-150	-1718	-1004	66.7
	Month 21	-1877	-147	-1730	-1017	66.9
	Month 24	-1915	-141	-1774	-1060	68.7
	Month 27	-1921	-135	-1787	-1073	67.4
	Month 30	---	---	---	---	---

Table A-4: Raw data for 04/10/2018 specimens loaded at 182 days

Sampling Date				**04/10/2018**		
Loading Age				**182 Days**		
Compressive Strength (psi)				6,400		
Modulus of Elasticity (ksi)				4,150		
Target Applied Load (kips)				72.4		
Reading Interval		Total Strain (με)	Shrinkage Strain (με)	Total Strain due to Load (με)	Creep Strain (με)	Total Force (kips)
Day Zero	Pre-Load	---	---	---	---	---
	Post-Load	-744	0	-743	0	71.0
	2 to 6 Hour	-777	1	-778	-35	73.8
Week One	Day 1	-823	-2	-821	-78	73.0
	Day 2	-855	2	-857	-114	73.4
	Day 3	-894	-4	-890	-147	73.1
	Day 4	-943	-17	-926	-182	73.3
	Day 5	-956	-18	-938	-195	73.8
	Day 6	-966	-18	-948	-205	73.7
	Day 7	-982	-15	-967	-223	73.8
Month One	Week 2	-1031	-14	-1017	-274	73.1
	Week 3	-1070	-14	-1056	-313	73.7
	Week 4	-1097	-18	-1078	-335	73.7
Year One	Month 2	-1210	-38	-1172	-429	73.8
	Month 3	-1296	-40	-1256	-513	72.6
	Month 4	-1382	-41	-1341	-598	73.8
	Month 5	-1418	-54	-1364	-621	73.5
	Month 6	-1422	-64	-1358	-614	72.0
	Month 7	-1464	-66	-1398	-655	73.8
	Month 8	-1505	-70	-1434	-691	73.5
	Month 9	-1529	-71	-1459	-715	73.4
	Month 10	-1535	-66	-1468	-725	73.1
	Month 11	-1543	-72	-1471	-728	73.3
	Month 12	-1547	-66	-1481	-738	73.8
After Year One	Month 15	-1568	-66	-1501	-758	73.5
	Month 18	-1619	-62	-1557	-813	73.7
	Month 21	-1630	-62	-1567	-824	71.6
	Month 24	-1634	-58	-1576	-833	72.6
	Month 27	---	---	---	---	---
	Month 30	---	---	---	---	---

Table A-5: Raw data for 07/09/2018 specimens loaded at 7 days

Sampling Date				**07/09/2018**		
Loading Age				**7 Days**		
Compressive Strength (psi)				5,600		
Modulus of Elasticity (ksi)				4,250		
Target Applied Load (kips)				63.3		
Reading Interval		Total Strain (με)	Shrinkage Strain (με)	Total Strain due to Load (με)	Creep Strain (με)	Total Force (kips)
Day Zero	Pre-Load	---	---	---	---	---
	Post-Load	-661	-8	-653	0	64.5
	2 to 6 Hour	-716	-13	-703	-51	64.4
Week One	Day 1	-845	-34	-811	-158	63.6
	Day 2	-915	-49	-866	-214	64.3
	Day 3	-972	-64	-908	-255	64.3
	Day 4	-1027	-79	-947	-294	64.3
	Day 5	-1063	-91	-972	-319	64.3
	Day 6	-1123	-103	-1019	-367	63.6
	Day 7	-1150	-119	-1031	-378	63.4
Month One	Week 2	-1373	-200	-1173	-520	62.6
	Week 3	-1493	-247	-1246	-593	63.3
	Week 4	-1598	-298	-1300	-647	62.9
Year One	Month 2	-1826	-380	-1445	-793	64.3
	Month 3	-1945	-425	-1521	-868	62.9
	Month 4	-2013	-441	-1572	-919	62.9
	Month 5	-2090	-461	-1629	-976	62.9
	Month 6	-2165	-472	-1693	-1040	62.7
	Month 7	-2232	-474	-1758	-1105	62.9
	Month 8	-2272	-485	-1788	-1135	64.1
	Month 9	-2305	-488	-1817	-1164	62.6
	Month 10	-2335	-492	-1842	-1190	73.1
	Month 11	-2357	-502	-1855	-1202	73.3
	Month 12	-2373	-507	-1865	-1213	62.2
After Year One	Month 15	-2393	-515	-1878	-1225	64.4
	Month 18	-2418	-520	-1898	-1245	62.4
	Month 21	-2446	-530	-1916	-1263	63.1
	Month 24	-2455	-524	-1931	-1278	62.9
	Month 27	-2458	-526	-1932	-1279	62.7
	Month 30	---	---	---	---	---

Table A-6: Raw data for 07/09/2018 specimens loaded at 28 days

Sampling Date				**07/09/2018**		
Loading Age				**28 Days**		
Compressive Strength (psi)				6,700		
Modulus of Elasticity (ksi)				4,250		
Target Applied Load (kips)				75.8		
Reading Interval		Total Strain (με)	Shrinkage Strain (με)	Total Strain due to Load (με)	Creep Strain (με)	Total Force (kips)
Day Zero	Pre-Load	---	---	---	---	---
	Post-Load	-749	-3	-746	0	77.3
	2 to 6 Hour	-810	-6	-804	-57	77.3
Week One	Day 1	-930	-15	-916	-169	76.6
	Day 2	-994	-20	-974	-228	77.0
	Day 3	-1045	-25	-1020	-274	76.8
	Day 4	-1078	-27	-1051	-305	77.2
	Day 5	-1111	-33	-1078	-332	77.0
	Day 6	-1140	-39	-1101	-355	77.2
	Day 7	-1162	-54	-1108	-362	77.0
Month One	Week 2	-1290	-88	-1202	-456	77.2
	Week 3	-1398	-111	-1287	-541	75.6
	Week 4	-1469	-124	-1345	-599	77.2
Year One	Month 2	-1612	-149	-1463	-716	77.2
	Month 3	-1733	-194	-1539	-793	76.3
	Month 4	-1829	-217	-1612	-866	76.1
	Month 5	-1884	-218	-1665	-919	76.1
	Month 6	-1974	-230	-1744	-998	77.0
	Month 7	-2017	-240	-1777	-1030	74.9
	Month 8	-2065	-244	-1821	-1075	75.5
	Month 9	-2113	-248	-1865	-1119	77.2
	Month 10	-2133	-258	-1875	-1129	73.1
	Month 11	-2158	-263	-1895	-1149	73.3
	Month 12	-2175	-269	-1907	-1160	75.4
After Year One	Month 15	-2210	-276	-1934	-1188	74.4
	Month 18	-2238	-276	-1962	-1216	74.4
	Month 21	-2267	-280	-1988	-1241	74.4
	Month 24	-2276	-283	-1993	-1246	62.9
	Month 27	-2279	-286	-1993	-1247	62.7
	Month 30	---	---	---	---	---

Table A-7: Raw data for 07/09/2018 specimens loaded at 91 days

Sampling Date		**07/09/2018**				
Loading Age		**91 Days**				
Compressive Strength (psi)		7,100				
Modulus of Elasticity (ksi)		4,200				
Target Applied Load (kips)		80.3				
Reading Interval		Total Strain (με)	Shrinkage Strain (με)	Total Strain due to Load (με)	Creep Strain (με)	Total Force (kips)
Day Zero	Pre-Load	---	---	---	---	---
	Post-Load	-784	0	-784	0	81.1
	2 to 6 Hour	-854	-1	-853	-69	81.1
Week One	Day 1	-920	-2	-918	-134	80.4
	Day 2	-931	-1	-930	-146	81.2
	Day 3	-967	-2	-965	-181	79.8
	Day 4	-989	-7	-982	-199	80.8
	Day 5	-1035	-12	-1022	-238	80.1
	Day 6	-1049	-13	-1036	-252	80.3
	Day 7	-1053	-13	-1040	-256	80.7
Month One	Week 2	-1116	-11	-1105	-322	81.0
	Week 3	-1176	-13	-1163	-379	80.4
	Week 4	-1213	-16	-1197	-413	81.0
Year One	Month 2	-1359	-36	-1323	-539	81.1
	Month 3	-1442	-47	-1395	-611	80.5
	Month 4	-1543	-49	-1494	-710	81.1
	Month 5	-1603	-60	-1543	-759	81.4
	Month 6	-1624	-63	-1561	-777	81.2
	Month 7	-1695	-67	-1627	-844	81.8
	Month 8	-1723	-78	-1645	-861	81.1
	Month 9	-1745	-82	-1662	-879	81.4
	Month 10	-1766	-88	-1677	-893	80.7
	Month 11	-1780	-93	-1687	-903	80.1
	Month 12	-1794	-91	-1703	-919	81.8
After Year One	Month 15	-1827	-95	-1732	-948	81.8
	Month 18	-1860	-105	-1755	-971	79.1
	Month 21	-1873	-99	-1774	-990	79.0
	Month 24	-1883	-101	-1782	-998	80.8
	Month 27	---	---	---	---	---
	Month 30	---	---	---	---	---

Table A-8: Raw data for 07/09/2018 specimens loaded at 182 days

Sampling Date				**07/09/2018**		
Loading Age				**182 Days**		
Compressive Strength (psi)				7,100		
Modulus of Elasticity (ksi)				4,300		
Target Applied Load (kips)				80.3		
Reading Interval		Total Strain (με)	Shrinkage Strain (με)	Total Strain due to Load (με)	Creep Strain (με)	Total Force (kips)
Day Zero	Pre-Load	---	---	---	---	---
	Post-Load	-804	0	-804	0	80.6
	2 to 6 Hour	-835	0	-835	-31	81.6
Week One	Day 1	-889	0	-889	-85	81.9
	Day 2	-949	-1	-948	-144	80.5
	Day 3	-977	-2	-975	-171	79.2
	Day 4	-1019	-2	-1017	-213	79.8
	Day 5	-1025	-4	-1021	-217	79.8
	Day 6	-1052	-4	-1048	-244	79.2
	Day 7	-1074	-4	-1070	-266	80.2
Month One	Week 2	-1145	-6	-1139	-335	81.7
	Week 3	-1220	-10	-1210	-406	81.7
	Week 4	-1268	-14	-1254	-450	81.9
Year One	Month 2	-1331	-18	-1313	-509	81.9
	Month 3	-1463	-24	-1438	-635	80.9
	Month 4	-1487	-28	-1459	-655	81.9
	Month 5	-1557	-33	-1524	-720	81.9
	Month 6	-1558	-36	-1522	-718	81.3
	Month 7	-1586	-39	-1547	-744	81.0
	Month 8	-1588	-40	-1547	-744	80.6
	Month 9	-1604	-41	-1563	-759	80.6
	Month 10	-1611	-41	-1570	-767	80.7
	Month 11	-1610	-44	-1566	-762	80.1
	Month 12	-1622	-45	-1576	-772	81.9
After Year One	Month 15	-1634	-52	-1582	-778	80.5
	Month 18	-1643	-49	-1594	-790	79.1
	Month 21	-1660	-52	-1608	-804	79.0
	Month 24	---	---	---	---	---
	Month 27	---	---	---	---	---
	Month 30	---	---	---	---	---

Table A-9: Raw data for 11/19/2018 specimens loaded at 7 days

Sampling Date				**11/19/2018**		
Loading Age				**7-Days**		
Compressive Strength (psi)				6,400		
Modulus of Elasticity (ksi)				4,400		
Target Applied Load (kips)				72.4		
Reading Interval		Total Strain (με)	Shrinkage Strain (με)	Total Strain due to Load (με)	Creep Strain (με)	Total Force (kips)
Day Zero	Pre-Load	---	---	---	---	---
	Post-Load	-703	0	-703	0	73.7
	2 to 6 Hour	-799	-1	-798	-95	73.1
Week One	Day 1	-951	-15	-936	-233	72.0
	Day 2	-1027	-20	-1008	-305	73.6
	Day 3	-1113	-37	-1077	-374	72.6
	Day 4	-1146	-44	-1103	-400	73.3
	Day 5	-1193	-54	-1139	-436	72.3
	Day 6	-1235	-65	-1169	-467	71.3
	Day 7	-1261	-72	-1189	-486	71.2
Month One	Week 2	-1445	-132	-1313	-610	73.0
	Week 3	-1579	-191	-1388	-685	71.5
	Week 4	-1640	-214	-1426	-723	71.0
Year One	Month 2	-1896	-331	-1565	-862	72.6
	Month 3	-2038	-374	-1664	-961	71.5
	Month 4	-2162	-410	-1752	-1049	72.4
	Month 5	-2228	-441	-1787	-1084	73.0
	Month 6	-2282	-453	-1829	-1126	71.2
	Month 7	-2323	-453	-1870	-1167	71.7
	Month 8	-2392	-448	-1944	-1241	72.4
	Month 9	-2423	-452	-1971	-1268	71.2
	Month 10	-2432	-450	-1982	-1279	80.7
	Month 11	-2464	-460	-2005	-1302	80.1
	Month 12	-2484	-465	-2020	-1317	71.0
After Year One	Month 15	-2503	-476	-2027	-1324	71.6
	Month 18	-2538	-481	-2057	-1354	71.2
	Month 21	-2557	-485	-2072	-1369	72.4
	Month 24	---	---	---	---	---
	Month 27	---	---	---	---	---
	Month 30	---	---	---	---	---

Table A-10: Raw data for 11/19/2018 specimens loaded at 28 days

Sampling Date				**11/19/2018**		
Loading Age				**28-Days**		
Compressive Strength (psi)				7,200		
Modulus of Elasticity (ksi)				4,600		
Target Applied Load (kips)				81.4		
Reading Interval		Total Strain (με)	Shrinkage Strain (με)	Total Strain due to Load (με)	Creep Strain (με)	Total Force (kips)
Day Zero	Pre-Load	---	---	---	---	---
	Post-Load	-730	0	-730	0	82.6
	2 to 6 Hour	-798	-1	-796	-66	82.7
Week One	Day 1	-918	-1	-916	-186	80.6
	Day 2	-982	-4	-978	-248	81.3
	Day 3	-1017	-5	-1012	-281	83.0
	Day 4	-1046	-12	-1034	-304	83.0
	Day 5	-1071	-15	-1056	-326	83.0
	Day 6	-1109	-22	-1086	-356	81.7
	Day 7	-1187	-23	-1164	-434	82.4
Month One	Week 2	-1235	-37	-1199	-468	81.9
	Week 3	-1287	-57	-1230	-500	82.8
	Week 4	-1398	-140	-1258	-527	79.9
Year One	Month 2	-1659	-183	-1476	-745	80.6
	Month 3	-1795	-219	-1576	-846	81.0
	Month 4	-1897	-240	-1656	-926	81.9
	Month 5	-1990	-253	-1737	-1006	81.6
	Month 6	-2069	-256	-1813	-1083	81.9
	Month 7	-2098	-257	-1841	-1110	80.2
	Month 8	-2153	-261	-1892	-1162	80.2
	Month 9	-2160	-259	-1901	-1171	81.3
	Month 10	-2202	-269	-1933	-1203	80.7
	Month 11	-2225	-275	-1950	-1220	80.1
	Month 12	-2237	-279	-1958	-1228	82.3
After Year One	Month 15	-2282	-286	-1996	-1265	81.7
	Month 18	-2325	-291	-2033	-1303	81.9
	Month 21	-2349	-294	-2054	-1324	82.4
	Month 24	---	---	---	---	---
	Month 27	---	---	---	---	---
	Month 30	---	---	---	---	---

Table A-11: Raw data for 11/19/2018 specimens loaded at 91 days

Sampling Date				**11/19/2018**		
Loading Age				**91-Days**		
Compressive Strength (psi)				7,500		
Modulus of Elasticity (ksi)				4,600		
Target Applied Load (kips)				84.8		
Reading Interval		Total Strain (με)	Shrinkage Strain (με)	Total Strain due to Load (με)	Creep Strain (με)	Total Force (kips)
Day Zero	Pre-Load	---	---	---	---	---
	Post-Load	-755	0	-755	0	83.8
	2 to 6 Hour	-770	-2	-768	-13	85.7
Week One	Day 1	-867	-1	-865	-110	84.9
	Day 2	-939	-3	-936	-181	84.7
	Day 3	-966	-8	-958	-203	86.0
	Day 4	-970	-9	-961	-206	85.7
	Day 5	-993	-11	-982	-227	84.6
	Day 6	-1021	-22	-999	-244	84.5
	Day 7	-1051	-25	-1026	-271	84.6
Month One	Week 2	-1121	-33	-1087	-332	84.7
	Week 3	-1162	-34	-1127	-372	84.6
	Week 4	-1264	-36	-1228	-473	84.7
Year One	Month 2	-1368	-67	-1300	-545	85.0
	Month 3	-1438	-79	-1359	-604	85.2
	Month 4	-1538	-79	-1459	-704	84.5
	Month 5	-1624	-74	-1550	-795	83.3
	Month 6	-1674	-78	-1595	-840	84.7
	Month 7	-1693	-76	-1616	-861	83.2
	Month 8	-1704	-86	-1618	-863	83.6
	Month 9	-1734	-91	-1643	-888	83.2
	Month 10	-1787	-102	-1685	-930	84.5
	Month 11	-1818	-104	-1714	-959	83.2
	Month 12	-1838	-103	-1736	-981	85.3
After Year One	Month 15	-1868	-107	-1761	-1006	85.7
	Month 18	-1909	-111	-1798	-1043	84.7
	Month 21	---	---	---	---	---
	Month 24	---	---	---	---	---
	Month 27	---	---	---	---	---
	Month 30	---	---	---	---	---

Table A-12: Raw data for 11/19/2018 specimens loaded at 182 days

Sampling Date				**11/19/2018**		
Loading Age				**182-Days**		
Compressive Strength (psi)				7,400		
Modulus of Elasticity (ksi)				4,500		
Target Applied Load (kips)				83.7		
Reading Interval		Total Strain (με)	Shrinkage Strain (με)	Total Strain due to Load (με)	Creep Strain (με)	Total Force (kips)
Day Zero	Pre-Load	---	---	---	---	---
	Post-Load	-681	0	-681	0	84.3
	2 to 6 Hour	-734	0	-734	-52	83.7
Week One	Day 1	-767	0	-767	-86	83.6
	Day 2	-809	-1	-808	-127	83.4
	Day 3	-883	-1	-883	-201	82.9
	Day 4	-942	-4	-938	-256	83.3
	Day 5	-999	-4	-995	-314	83.7
	Day 6	-1017	-7	-1010	-328	83.6
	Day 7	-1069	-7	-1063	-381	83.7
Month One	Week 2	-1116	-17	-1099	-417	83.4
	Week 3	-1160	-21	-1139	-457	84.1
	Week 4	-1222	-33	-1189	-508	83.9
Year One	Month 2	-1241	-36	-1206	-524	83.3
	Month 3	-1265	-40	-1224	-543	83.4
	Month 4	-1288	-43	-1245	-563	84.1
	Month 5	-1307	-46	-1261	-580	82.2
	Month 6	-1350	-47	-1303	-621	84.7
	Month 7	-1372	-49	-1323	-642	84.1
	Month 8	-1398	-49	-1349	-667	84.3
	Month 9	-1419	-49	-1370	-689	84.1
	Month 10	-1453	-51	-1402	-720	84.5
	Month 11	-1471	-51	-1420	-738	83.2
	Month 12	-1491	-52	-1438	-757	84.1
After Year One	Month 15	-1518	-56	-1462	-780	85.7
	Month 18	---	---	---	---	---
	Month 21	---	---	---	---	---
	Month 24	---	---	---	---	---
	Month 27	---	---	---	---	---
	Month 30	---	---	---	---	---

Table A-13: Raw data for 04/16/2019 specimens loaded at 7 days

Sampling Date				**04/16/2019**		
Loading Age				**7-Days**		
Compressive Strength (psi)				7,300		
Modulus of Elasticity (ksi)				5,100		
Target Applied Load (kips)				82.6		
Reading Interval		Total Strain (με)	Shrinkage Strain (με)	Total Strain due to Load (με)	Creep Strain (με)	Total Force (kips)
Day Zero	Pre-Load	---	---	---	---	---
	Post-Load	-670	0	-670	0	84.2
	2 to 6 Hour	-762	-11	-751	-80	82.1
Week One	Day 1	-863	-33	-830	-160	83.8
	Day 2	-946	-59	-887	-217	83.5
	Day 3	-1002	-89	-913	-243	83.8
	Day 4	-1039	-89	-949	-279	83.5
	Day 5	-1061	-103	-957	-287	83.5
	Day 6	-1064	-108	-956	-286	84.1
	Day 7	-1104	-109	-995	-325	83.1
Month One	Week 2	-1206	-131	-1076	-406	82.7
	Week 3	-1319	-161	-1158	-488	82.7
	Week 4	-1398	-198	-1200	-530	82.8
Year One	Month 2	-1583	-267	-1316	-646	82.5
	Month 3	-1678	-300	-1378	-708	83.1
	Month 4	-1762	-335	-1427	-757	84.6
	Month 5	-1830	-353	-1477	-807	81.8
	Month 6	-1879	-372	-1507	-837	83.2
	Month 7	-1925	-401	-1524	-854	83.2
	Month 8	-1968	-420	-1549	-879	83.9
	Month 9	-1992	-432	-1559	-889	81.4
	Month 10	-1993	-429	-1564	-894	84.1
	Month 11	-2014	-436	-1578	-907	81.7
	Month 12	-2037	-435	-1602	-932	84.1
After Year One	Month 15	-2070	-432	-1638	-968	82.8
	Month 18	-2097	-435	-1662	-992	82.8
	Month 21	---	---	---	---	---
	Month 24	---	---	---	---	---
	Month 27	---	---	---	---	---
	Month 30	---	---	---	---	---

Table A-14: Raw data for 04/16/2019 specimens loaded at 28 days

Sampling Date				**04/16/2019**		
Loading Age				**28-Days**		
Compressive Strength (psi)				8,000		
Modulus of Elasticity (ksi)				5,300		
Target Applied Load (kips)				90.5		
Reading Interval		Total Strain (με)	Shrinkage Strain (με)	Total Strain due to Load (με)	Creep Strain (με)	Total Force (kips)
Day Zero	Pre-Load	---	---	---	---	---
	Post-Load	-652	0	-652	0	92.3
	2 to 6 Hour	-740	-2	-738	-86	90.5
Week One	Day 1	-830	-7	-823	-171	90.7
	Day 2	-931	-8	-923	-271	90.5
	Day 3	-988	-10	-978	-326	89.9
	Day 4	-1026	-15	-1011	-359	89.9
	Day 5	-1069	-19	-1050	-398	90.0
	Day 6	-1104	-25	-1079	-427	90.2
	Day 7	-1142	-39	-1103	-451	90.2
Month One	Week 2	-1208	-60	-1148	-496	90.7
	Week 3	-1272	-105	-1167	-515	90.7
	Week 4	-1356	-153	-1202	-550	90.2
Year One	Month 2	-1472	-192	-1280	-628	92.3
	Month 3	-1578	-227	-1351	-699	89.3
	Month 4	-1669	-269	-1400	-748	89.2
	Month 5	-1737	-310	-1426	-774	90.2
	Month 6	-1782	-320	-1461	-809	89.6
	Month 7	-1827	-336	-1491	-839	89.3
	Month 8	-1840	-349	-1492	-840	89.8
	Month 9	-1850	-346	-1503	-851	91.6
	Month 10	-1869	-349	-1520	-868	89.3
	Month 11	-1884	-351	-1533	-881	81.4
	Month 12	-1904	-352	-1552	-900	90.2
After Year One	Month 15	-1932	-348	-1584	-932	91.4
	Month 18	-1948	-350	-1598	-946	91.6
	Month 21	---	---	---	---	---
	Month 24	---	---	---	---	---
	Month 27	---	---	---	---	---
	Month 30	---	---	---	---	---

Table A-15: Raw data for 04/16/2019 specimens loaded at 91 days

Sampling Date		**04/16/2019**				
Loading Age		**91-Days**				
Compressive Strength (psi)		8,300				
Modulus of Elasticity (ksi)		5,400				
Target Applied Load (kips)		93.9				
Reading Interval		Total Strain (με)	Shrinkage Strain (με)	Total Strain due to Load (με)	Creep Strain (με)	Total Force (kips)
Day Zero	Pre-Load	---	---	---	---	---
	Post-Load	-721	0	-721	0	94.3
	2 to 6 Hour	-787	0	-787	-66	95.3
Week One	Day 1	-855	-9	-846	-125	95.0
	Day 2	-899	-14	-885	-164	95.6
	Day 3	-935	-17	-918	-197	95.6
	Day 4	-962	-21	-942	-221	95.3
	Day 5	-999	-24	-975	-254	95.3
	Day 6	-1037	-29	-1008	-287	95.3
	Day 7	-1069	-36	-1034	-313	94.1
Month One	Week 2	-1122	-54	-1069	-348	92.9
	Week 3	-1173	-70	-1103	-383	95.0
	Week 4	-1206	-86	-1120	-399	95.5
Year One	Month 2	-1334	-120	-1214	-493	92.9
	Month 3	-1409	-139	-1270	-549	92.4
	Month 4	-1480	-169	-1311	-591	92.1
	Month 5	-1542	-187	-1355	-634	92.1
	Month 6	-1604	-200	-1404	-683	92.9
	Month 7	-1612	-196	-1416	-695	94.6
	Month 8	-1618	-203	-1415	-694	92.8
	Month 9	-1664	-202	-1462	-741	92.2
	Month 10	-1683	-200	-1483	-762	95.0
	Month 11	-1692	-199	-1493	-772	95.6
	Month 12	-1699	-199	-1499	-778	94.1
After Year One	Month 15	-1736	-202	-1534	-813	92.9
	Month 18	---	---	---	---	---
	Month 21	---	---	---	---	---
	Month 24	---	---	---	---	---
	Month 27	---	---	---	---	---
	Month 30	---	---	---	---	---

Table A-16: Raw data for 04/16/2019 specimens loaded at 182 days

Sampling Date				**04/16/2019**		
Loading Age				**182-Days**		
Compressive Strength (psi)				8,100		
Modulus of Elasticity (ksi)				5,400		
Target Applied Load (kips)				91.6		
Reading Interval		Total Strain (με)	Shrinkage Strain (με)	Total Strain due to Load (με)	Creep Strain (με)	Total Force (kips)
Day Zero	Pre-Load	---	---	---	---	---
	Post-Load	-710	0	-710	0	92.4
	2 to 6 Hour	-732	0	-732	-23	93.4
Week One	Day 1	-822	0	-822	-112	91.4
	Day 2	-827	-3	-824	-115	91.7
	Day 3	-850	-5	-845	-136	89.9
	Day 4	-849	-6	-844	-134	93.1
	Day 5	-854	-5	-849	-140	90.3
	Day 6	-861	-3	-858	-149	93.1
	Day 7	-897	-3	-894	-184	90.3
Month One	Week 2	-958	-5	-953	-244	92.5
	Week 3	-992	-6	-987	-277	93.4
	Week 4	-1012	-8	-1004	-295	93.2
Year One	Month 2	-1115	-16	-1099	-390	91.6
	Month 3	-1184	-22	-1162	-453	93.4
	Month 4	-1218	-25	-1193	-484	93.4
	Month 5	-1267	-32	-1235	-525	93.4
	Month 6	-1279	-28	-1251	-542	91.7
	Month 7	-1287	-31	-1256	-546	92.4
	Month 8	-1308	-28	-1280	-570	92.5
	Month 9	-1324	-31	-1293	-584	91.6
	Month 10	-1338	-28	-1309	-600	92.5
	Month 11	-1352	-30	-1322	-612	92.4
	Month 12	-1364	-31	-1333	-623	93.1
After Year One	Month 15	---	---	---	---	---
	Month 18	---	---	---	---	---
	Month 21	---	---	---	---	---
	Month 24	---	---	---	---	---
	Month 27	---	---	---	---	---
	Month 30	---	---	---	---	---

A.2 COLLECTED SHRINKAGE DATA

Tables A-17 and A-18 provide data for the shrinkage data collected for air- and moist-cured prismatic specimens respectively for the duration of this research project.

Table A-17: Raw data for air-cured prismatic shrinkage specimens for the project duration

Sampling Date		**04/10/2018 (Air)**	**07/09/2018 (Air)**	**11/19/2018 (Air)**	**04/16/2019 (Air)**
Reading Interval		Shrinkage Strain (με)	Shrinkage Strain (με)	Shrinkage Strain (με)	Shrinkage Strain (με)
Day Zero	0	---	---	---	---
	2 to 6 Hour	-77	-10	-30	-2
Week One	Day 1	-130	-55	-40	-42
	Day 2	-168	-112	-82	-62
	Day 3	-222	-143	-128	-97
	Day 4	-252	-195	-143	-125
	Day 5	-283	-212	-153	-130
	Day 6	-295	-238	-188	-163
	Day 7	-318	-255	-227	-170
Month One	Week 2	-460	-390	-345	-278
	Week 3	-568	-497	-395	-320
	Week 4	-597	-550	-467	-360
Year One	Month 2	-668	-618	-570	-443
	Month 3	-683	-650	-580	-482
	Month 4	-723	-672	-588	-497
	Month 5	-728	-673	-600	-527
	Month 6	-745	-673	-612	-532
	Month 7	-742	-680	-607	-539
	Month 8	-740	-687	-602	-555
	Month 9	-743	-687	-608	-545
	Month 10	-748	-692	-612	-543
	Month 11	-745	-680	-612	-532
	Month 12	-730	-673	-620	-543
After Year One	Month 15	-720	-670	-628	-548
	Month 18	-727	-687	-620	-538
	Month 21	-742	-692	-630	---
	Month 24	-741	-692	---	---
	Month 27	-745	-700	---	---
	Month 30	-743	---	---	---

Table A-18: Raw data for moist-cured prismatic shrinkage specimens for the project duration

Sampling Date		**04/10/2018 (Moist)**	**07/09/2018 (Moist)**	**11/19/2018 (Moist)**	**04/16/2019 (Moist)**
Reading Interval		Shrinkage Strain (με)	Shrinkage Strain (με)	Shrinkage Strain (με)	Shrinkage Strain (με)
Day Zero	0	---	---	---	---
	2 to 6 Hour	-53	-25	-22	-8
Week One	Day 1	-152	-62	-95	-63
	Day 2	-225	-142	-157	-75
	Day 3	-270	-175	-197	-100
	Day 4	-300	-220	-213	-122
	Day 5	-342	-258	-258	-158
	Day 6	-375	-278	-268	-175
	Day 7	-398	-302	-308	-202
Month One	Week 2	-525	-425	-400	-272
	Week 3	-583	-520	-472	-338
	Week 4	-622	-553	-513	-387
Year One	Month 2	-693	-620	-580	-450
	Month 3	-722	-657	-617	-497
	Month 4	-758	-675	-660	-513
	Month 5	-778	-687	-667	-526
	Month 6	-783	-700	-677	-537
	Month 7	-790	-705	-677	-540
	Month 8	-800	-702	-670	-540
	Month 9	-808	-707	-670	-542
	Month 10	-813	-693	-672	-545
	Month 11	-810	-700	-668	-542
	Month 12	-811	-695	-678	-550
After Year One	Month 15	-815	-698	-677	-555
	Month 18	-807	-700	-670	-550
	Month 21	-810	-687	-678	---
	Month 24	-818	-700	---	---
	Month 27	-820	-707	---	---
	Month 30	-808	---	---	---

APPENDIX B: DETAILED RESULTS FROM PREDICTION METHODS

This appendix provides detailed graphical illustrations for model results discussed in Chapters 6. Each section is broken down by method as well as compliance and shrinkage. For compliance each figure provides a comparison between measured and predicted compliance values for all loading ages corresponding to one sample date. For each model, shrinkage is divided between air-cured and moist-cured prismatic specimens. Measured shrinkage strains are compared to the predicted strains for each model. Appendix B is outlined according to the following:

B.1 ACI 209 Prediction Method
- Compliance: Figures B-1 through B-4
- Shrinkage: Figures B-5 and B-6

B.2 AASHTO LRFD Prediction Method
- Compliance: Figures B-7 through B-10
- Shrinkage: Figures B-11 and B-12

B.3 GL 2000 Prediction Method
- Compliance: Figures B-13 through B-16
- Shrinkage: Figures B-17 and B-18

B.4 B3 Prediction Method
- Compliance: Figures B-19 through B-22
- Shrinkage: Figures B-23 and B-24

B.5 CEB MC 1990 Prediction Method
- Compliance: Figures B-25 through B-28
- Shrinkage: Figures B-29 and B-30

B.6 CEB MC 2010 Prediction Method
- Compliance: Figures B-31 through B-34
- Shrinkage: Figures B-35 and B-36

B.1 ACI 209 PREDICTION METHOD

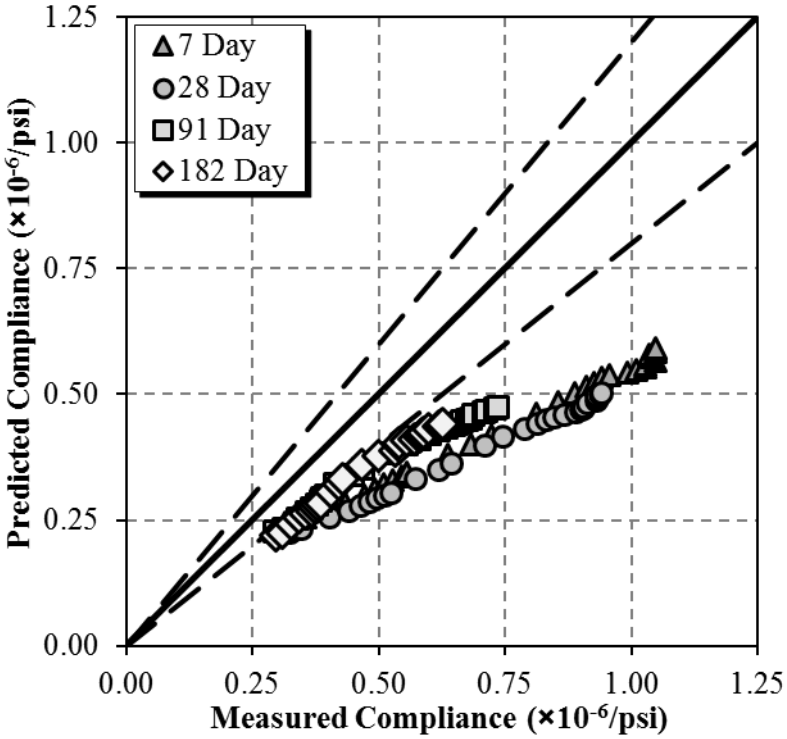

Figure B-1: Compliance comparison of 04/10/2018 specimens using the ACI 209 Model

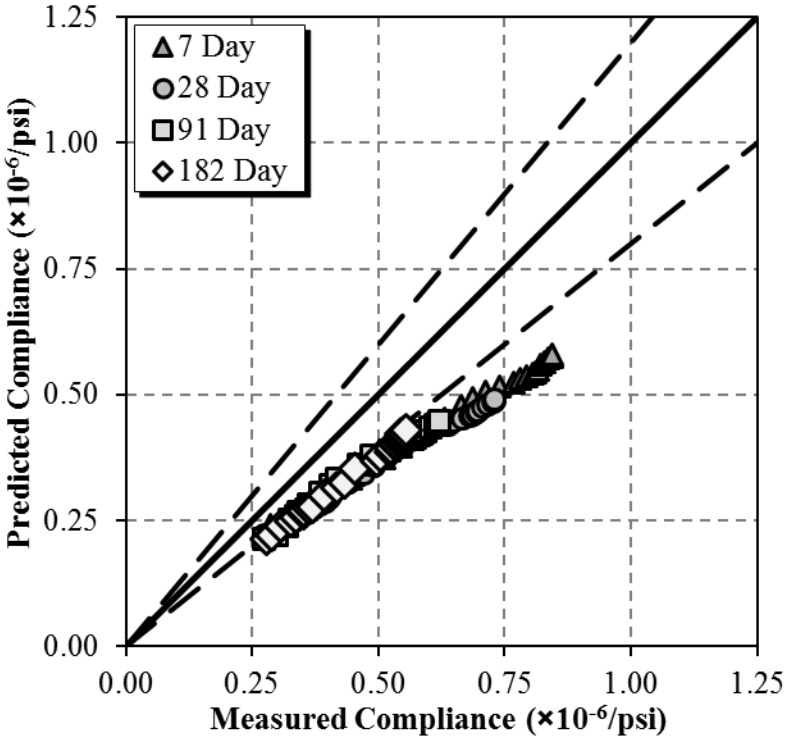

Figure B-2: Compliance comparison of 07/09/2018 specimens using the ACI 209 Model

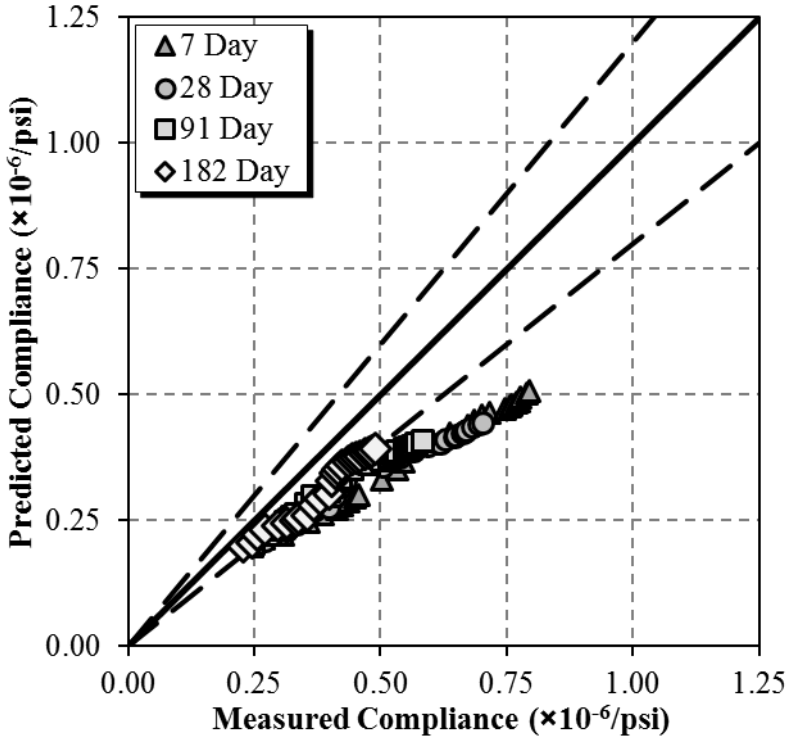

Figure B-3: Compliance comparison of 11/19/2018 specimens using ACI 209 Model

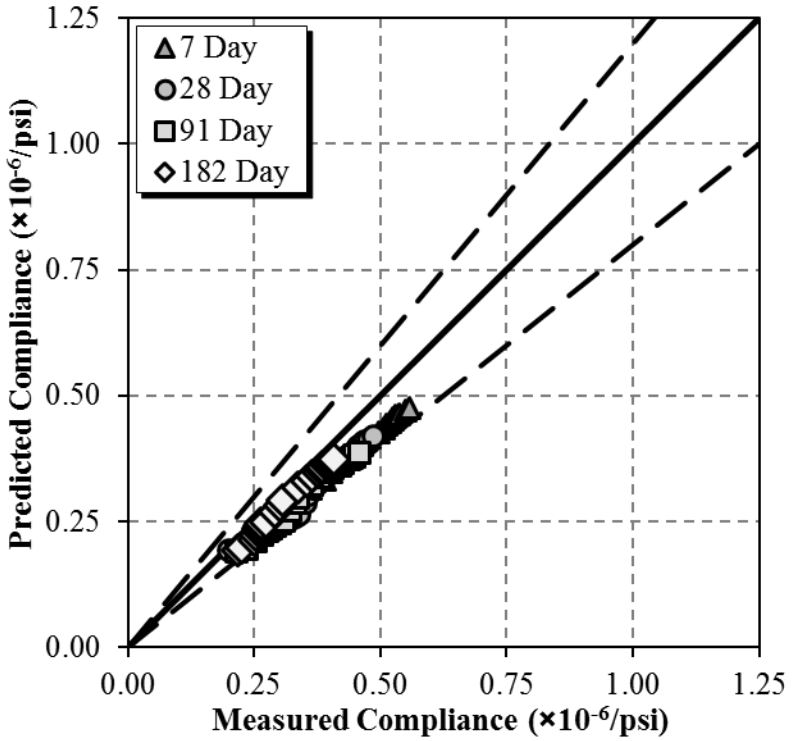

Figure B-4: Compliance comparison of 04/16/2019 specimens using the ACI 209 Model

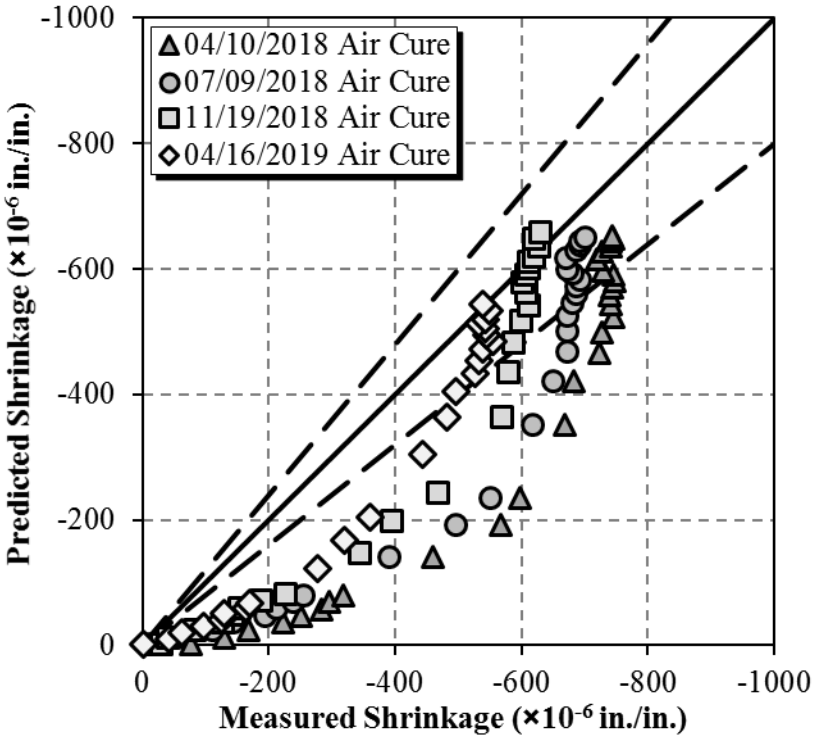

Figure B-5: Shrinkage comparison of air-cured prismatic specimens using the ACI 209 Model

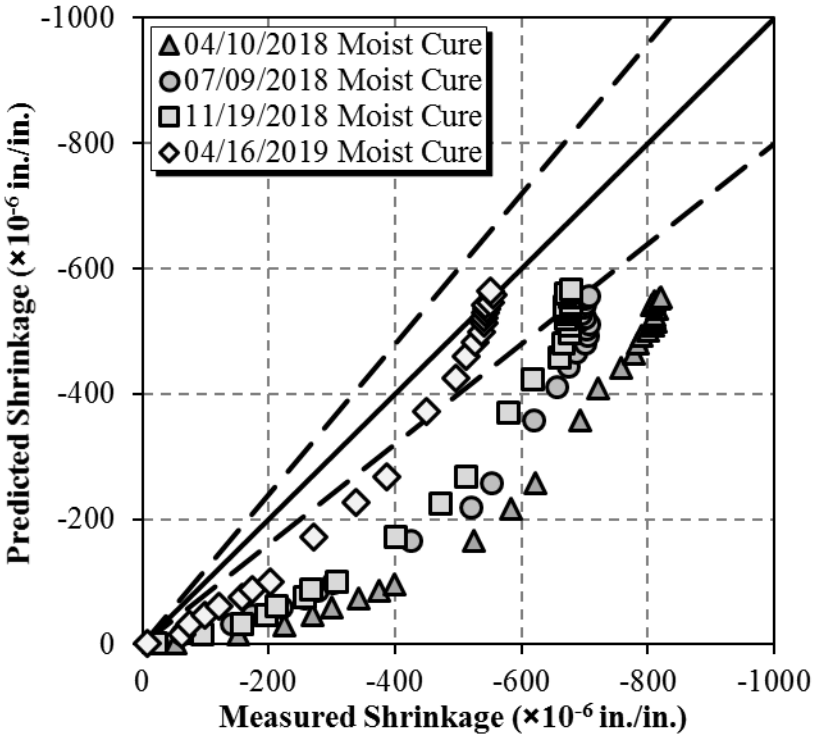

Figure B-6: Shrinkage comparison of moist-cured prismatic specimens using the ACI 209 Model

B.2 AASHTO LRFD 2017 MODEL

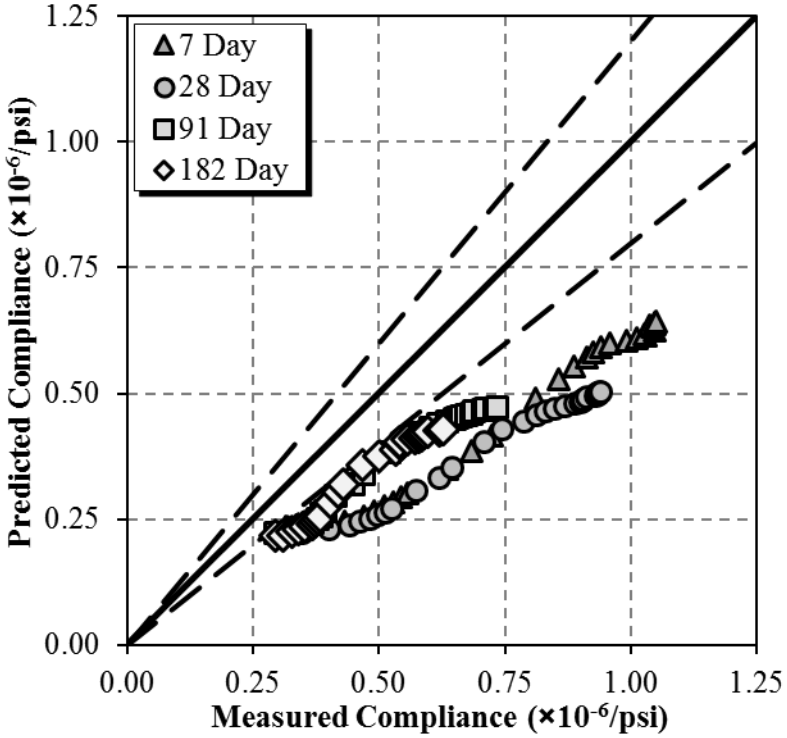

Figure B-7: Compliance comparison of 04/10/2018 specimens using the AASHTO LRFD 2017 Model

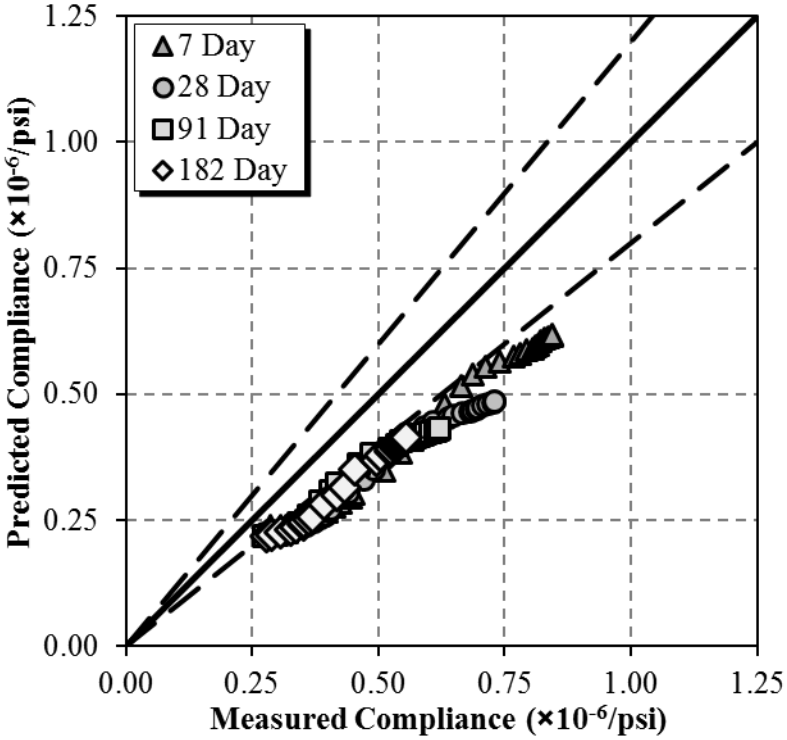

Figure B-8: Compliance comparison of 07/09/2018 specimens using the AASHTO LRFD 2017 Model

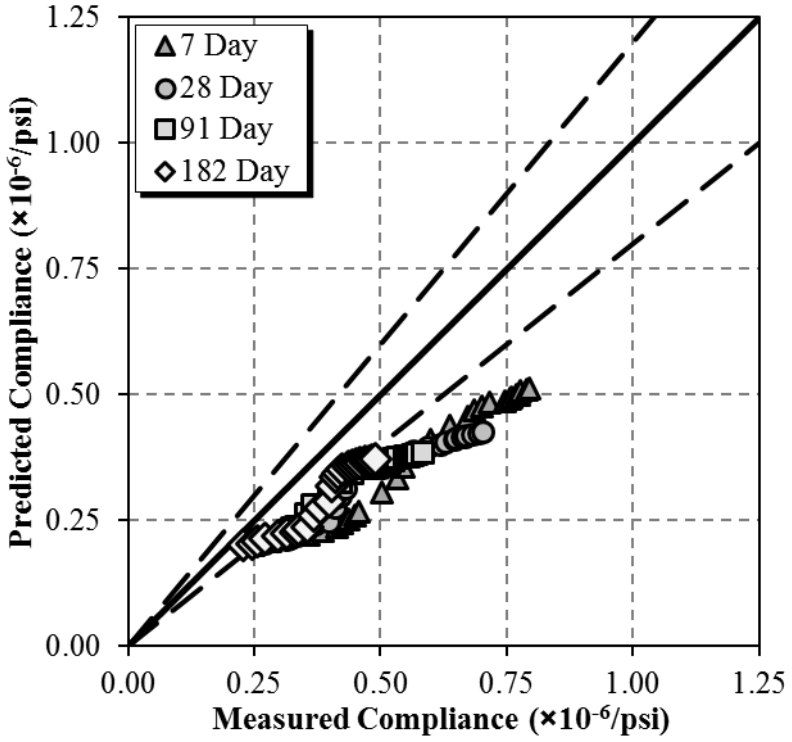

Figure B-9: Compliance comparison of 11/19/2018 specimens using the AASHTO LRFD 2017 Model

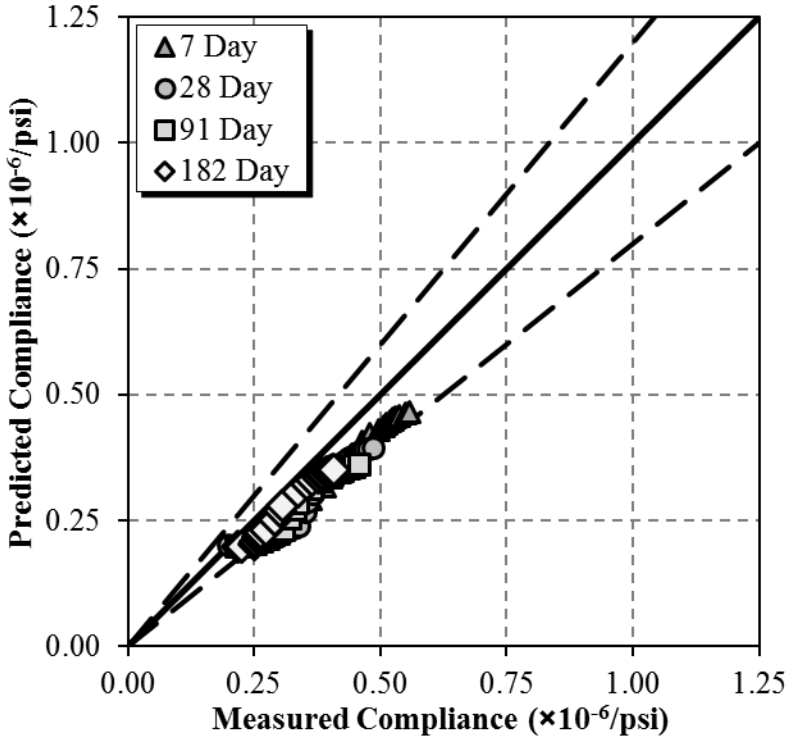

Figure B-10: Compliance comparison of 04/16/2019 specimens using the AASHTO LRFD 2017 Model

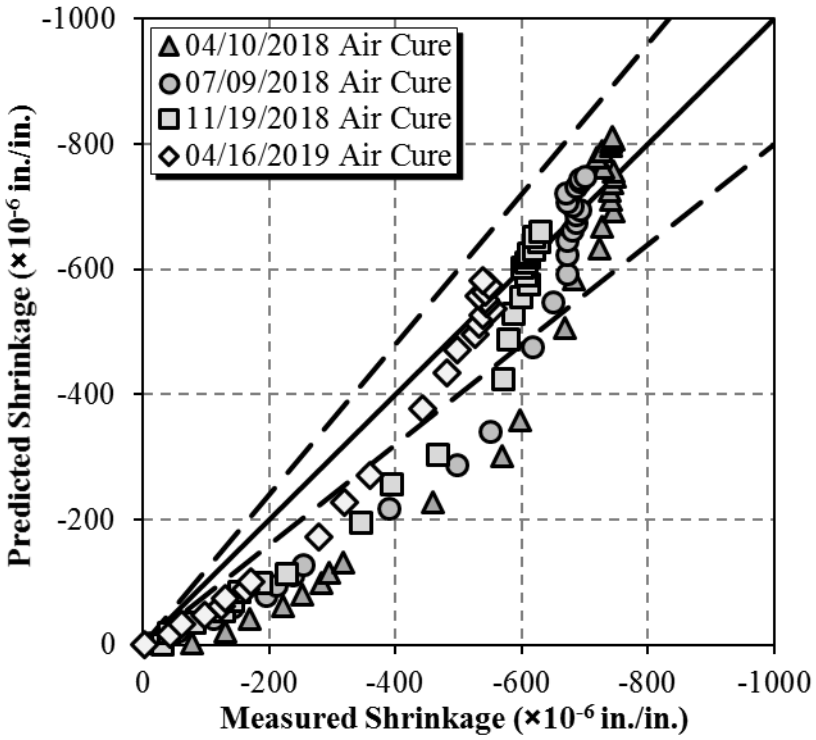

Figure B-11: Shrinkage comparison of air-cured prismatic specimens using the AASHTO LRFD 2017 Model

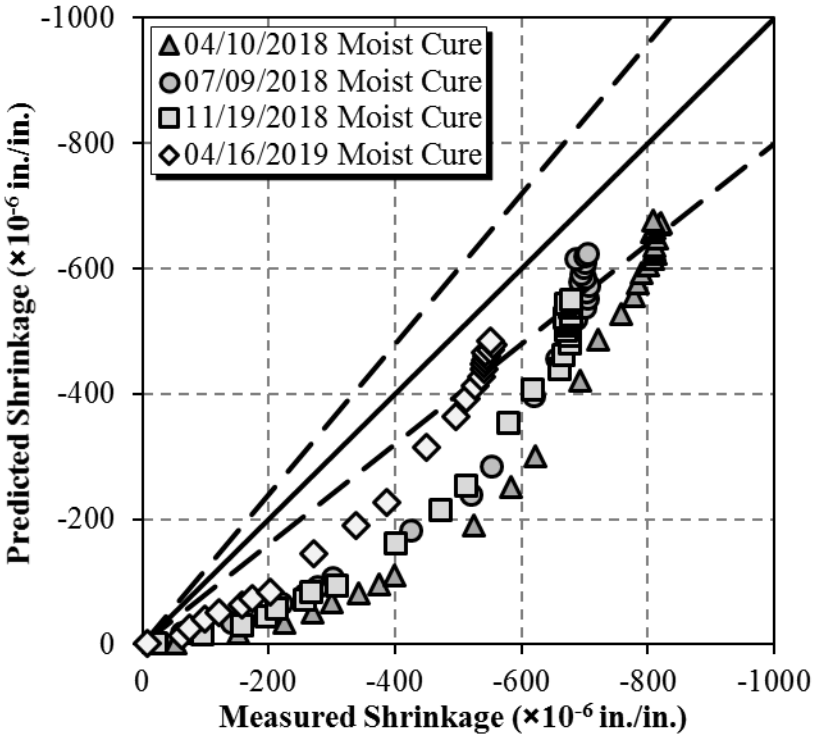

Figure B-12: Shrinkage comparison of moist-cured prismatic specimens using the AASHTO LRFD 2017 Model

B.3 GL 2000 PREDICTION METHOD

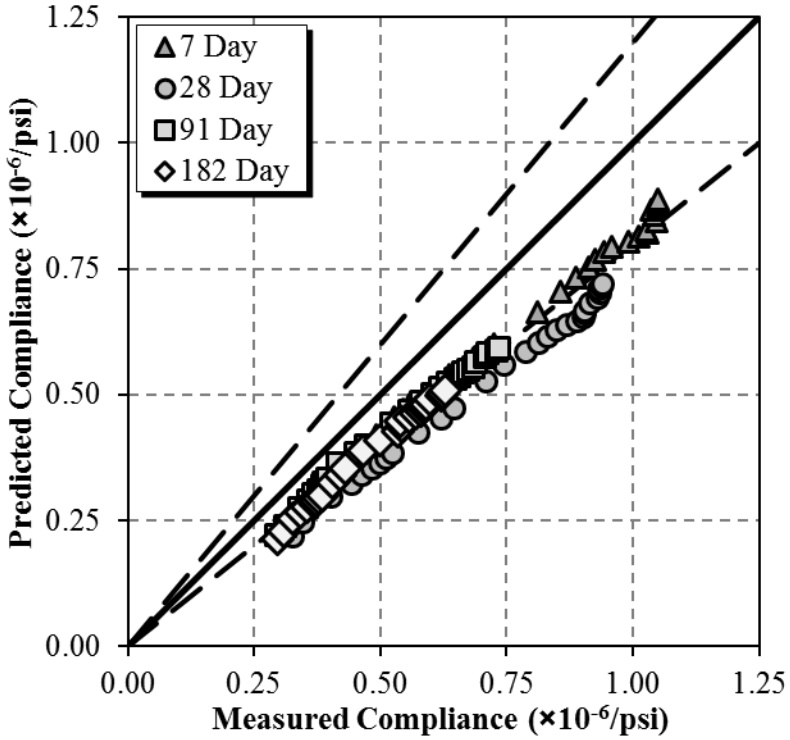

Figure B-13: Compliance comparison of 04/10/2018 using the GL 2000 Model

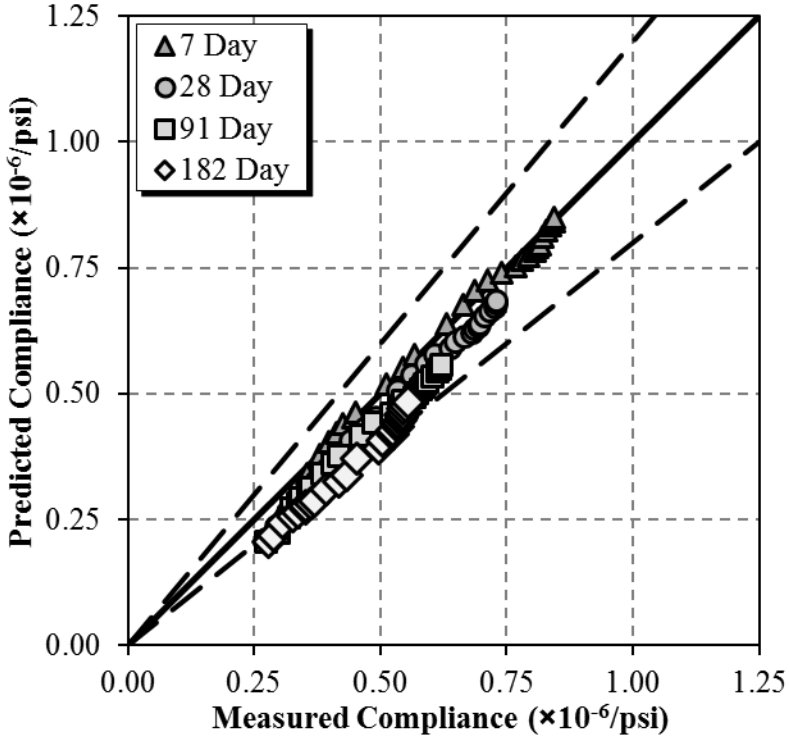

Figure B-14: Compliance comparison of 07/09/2018 specimens using the GL 2000 Model

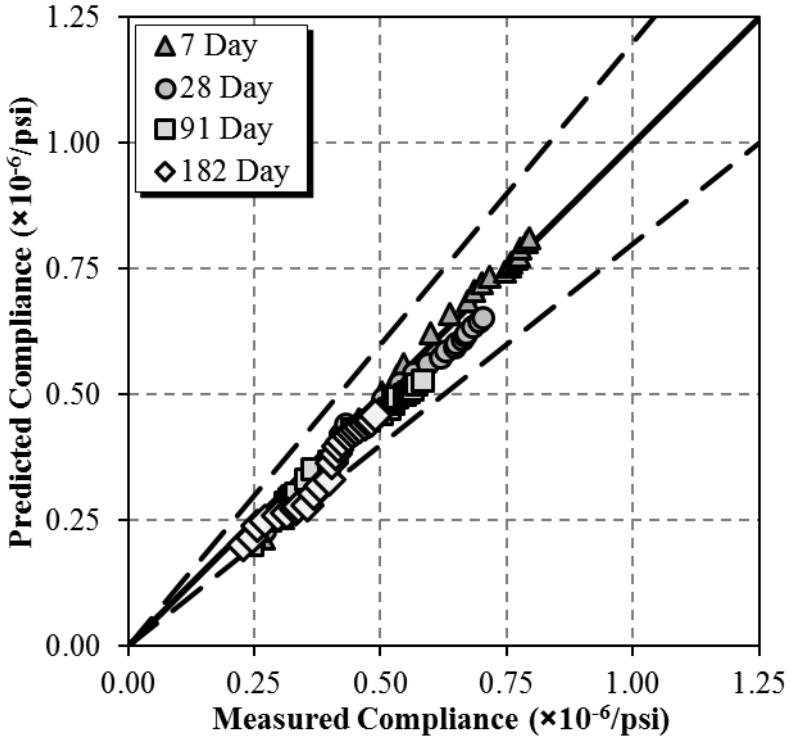

Figure B-15: Compliance comparison of 11/19/2018 specimens using the GL 2000 Model

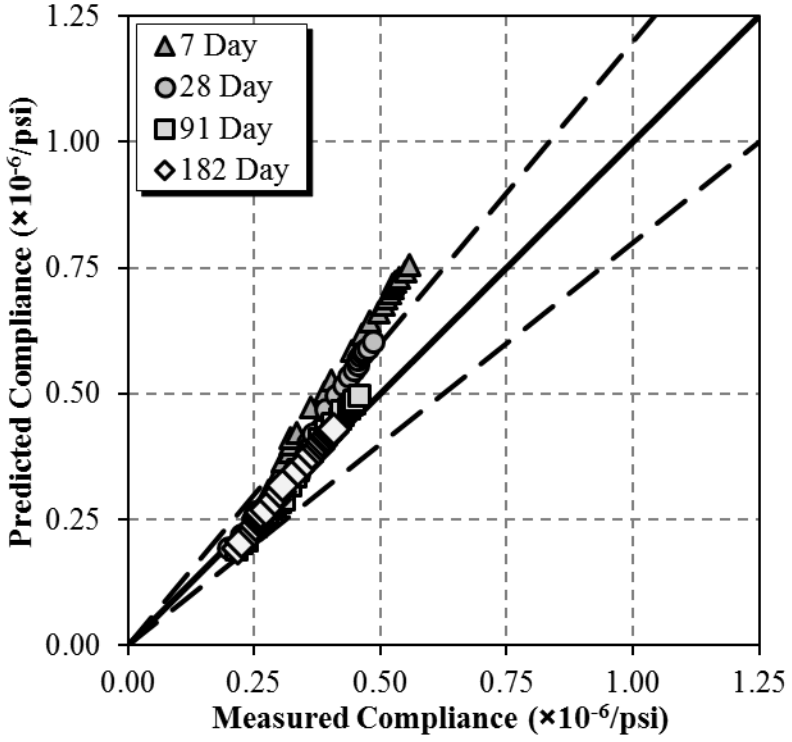

Figure B-16: Compliance comparison of 04/16/2019 specimens using the GL 2000 Model

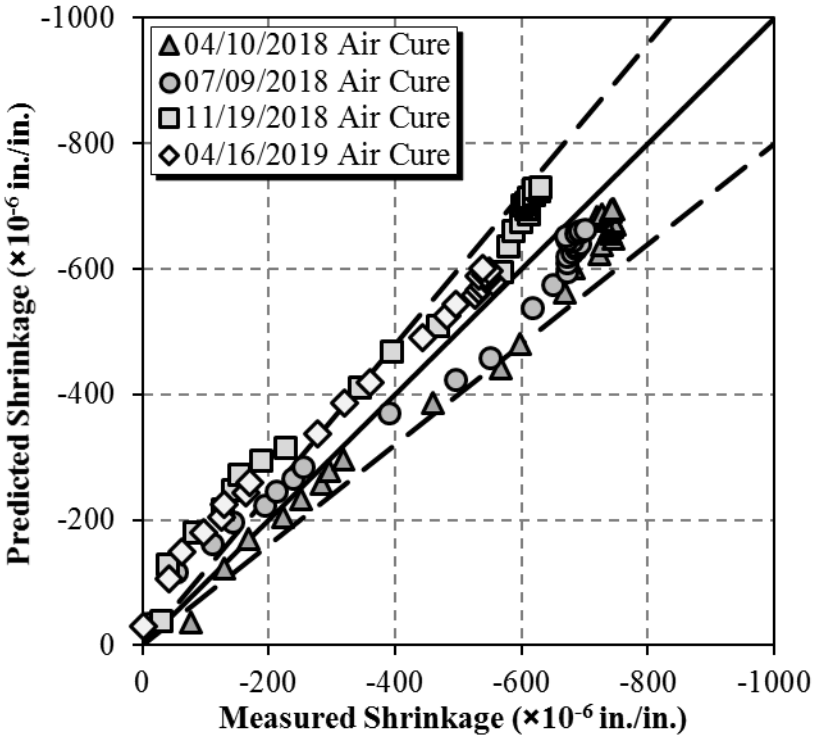

Figure B-17: Shrinkage comparison of air-cured prismatic specimens using the GL 2000 Model

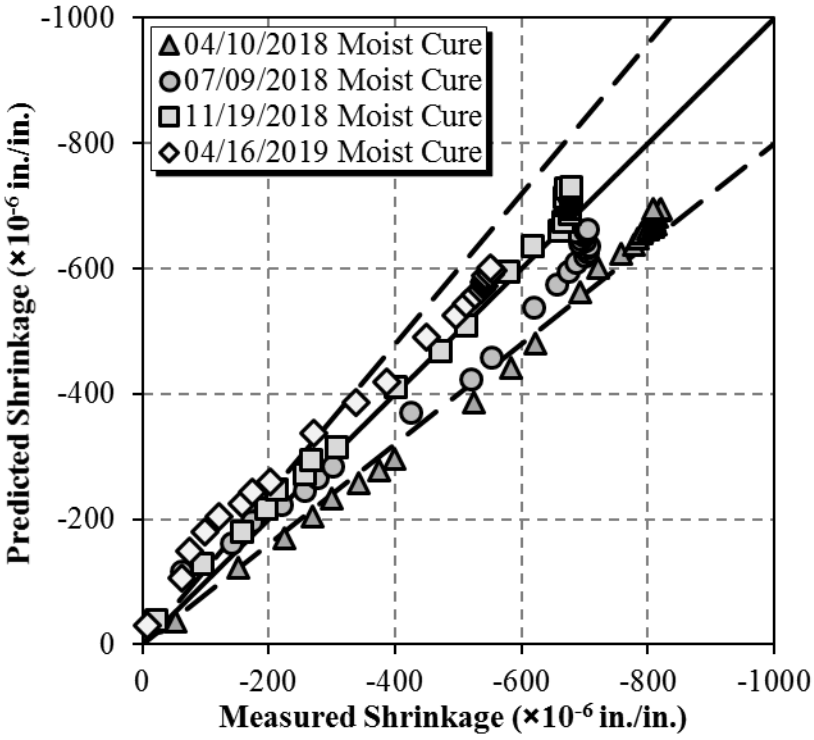

Figure B-18: Shrinkage comparison of moist-cured prismatic specimens using the GL 2000 Model

B.4 B3 PREDICTION METHOD

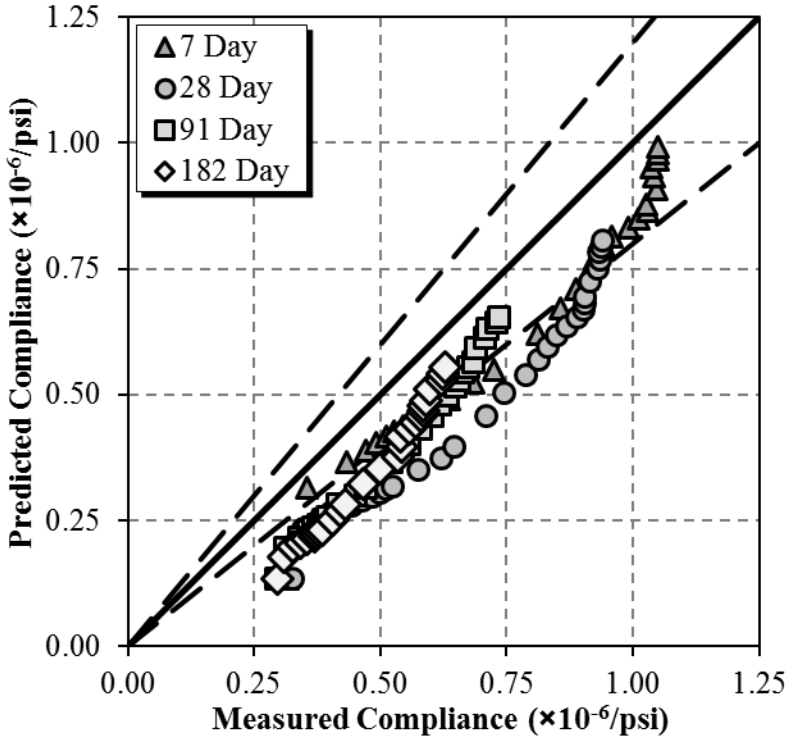

Figure B-19: Compliance comparison of 04/10/2018 specimens using the B3 Model

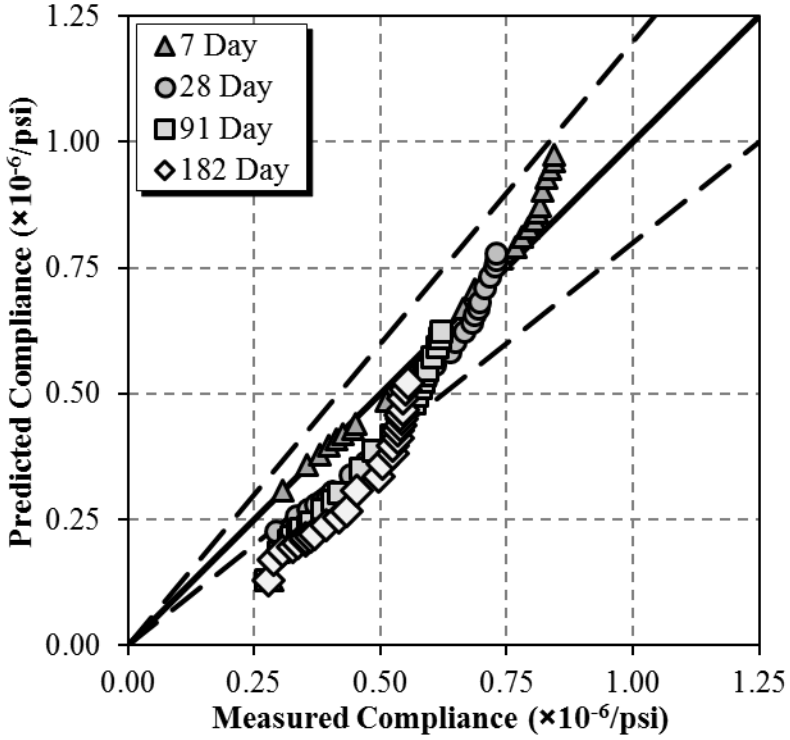

Figure B-20: Compliance comparison of 07/09/2018 specimens using the B3 Model

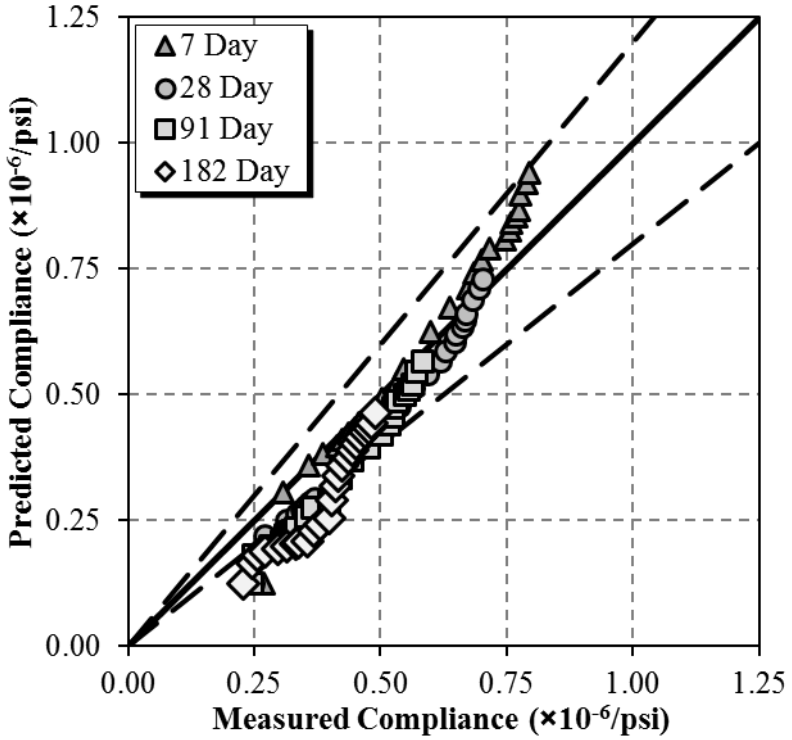

Figure B-21: Compliance comparison of 11/19/2018 specimens using the B3 Model

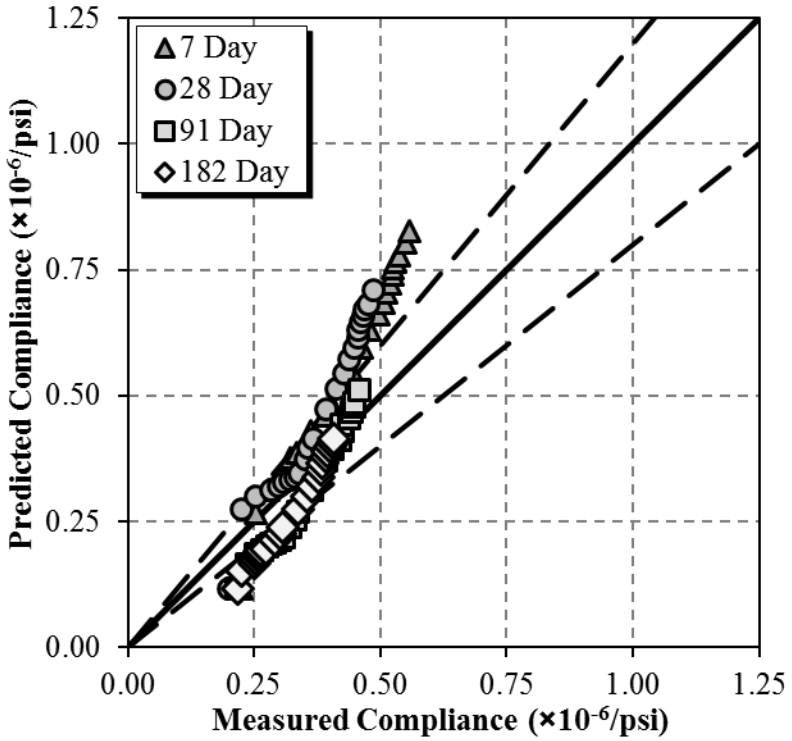

Figure B-22: Compliance comparison of 04/16/2019 specimens using the B3 Model

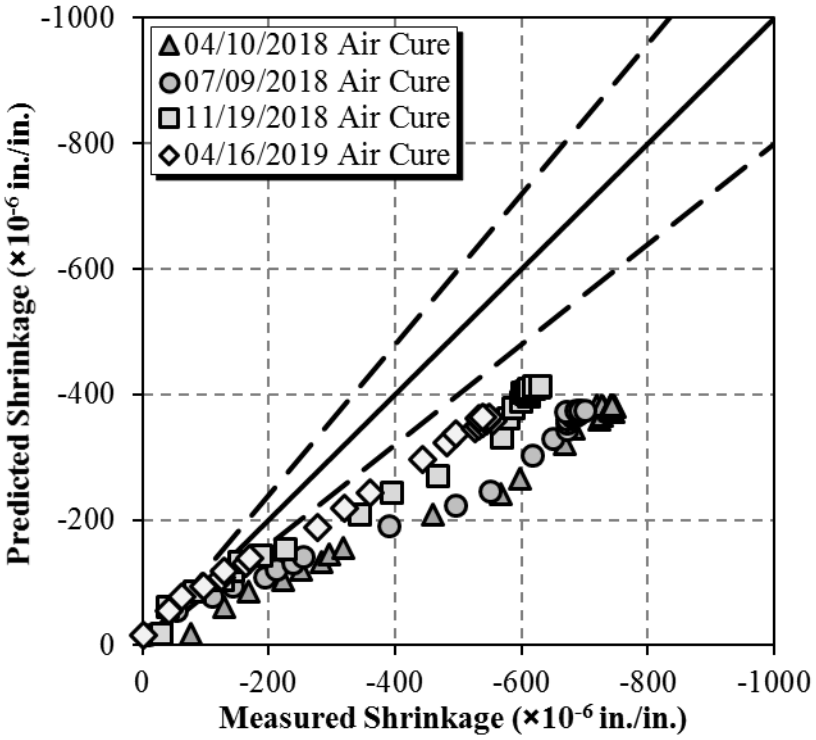

Figure B-23: Shrinkage comparison of air-cured prismatic specimens using the B3 Model

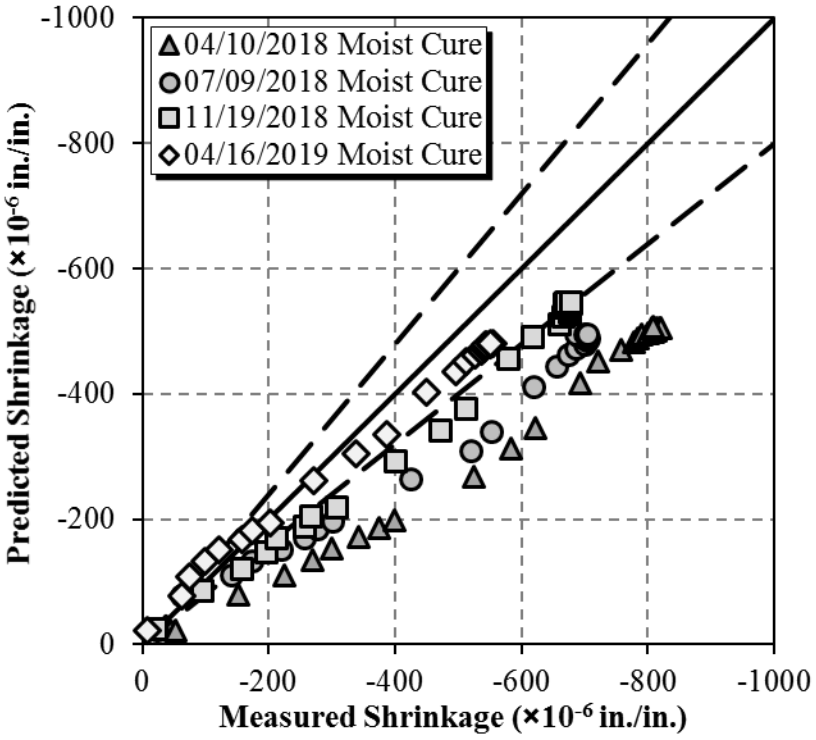

Figure B-24: Shrinkage comparison of moist-cured prismatic specimens using the B3 Model

B.5 CEB MC 1990 PREDICTION METHOD

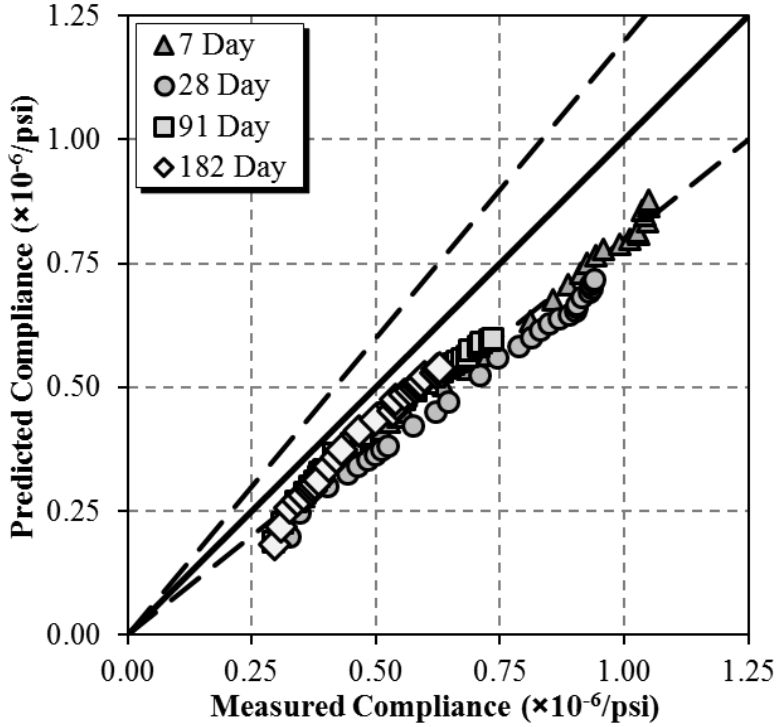

Figure B-25: Compliance comparison of 04/10/2018 specimens using the CEB MC 1990 Model

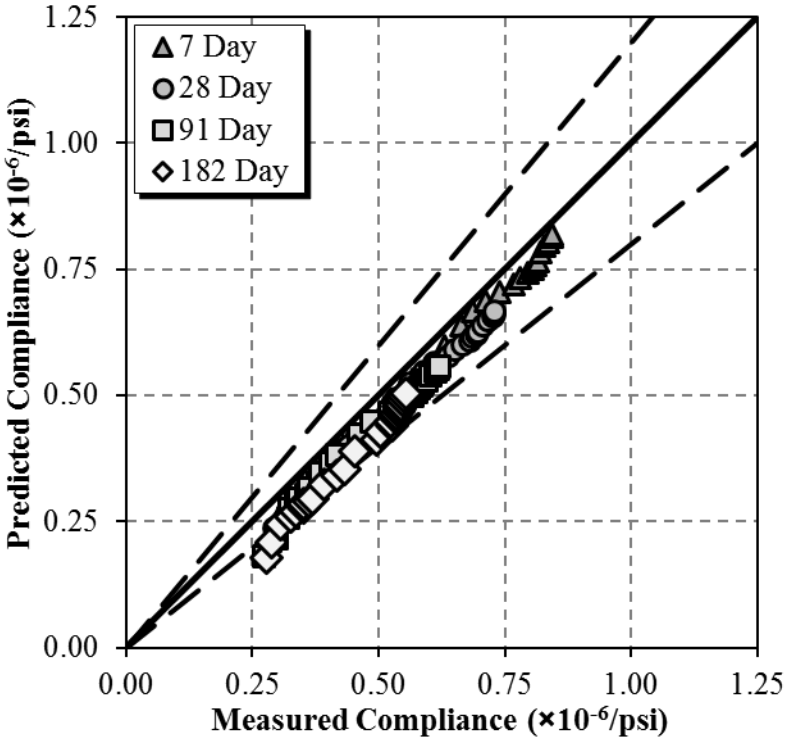

Figure B-26: Compliance comparison of 07/09/2018 specimens using the CEB MC 1990 Model

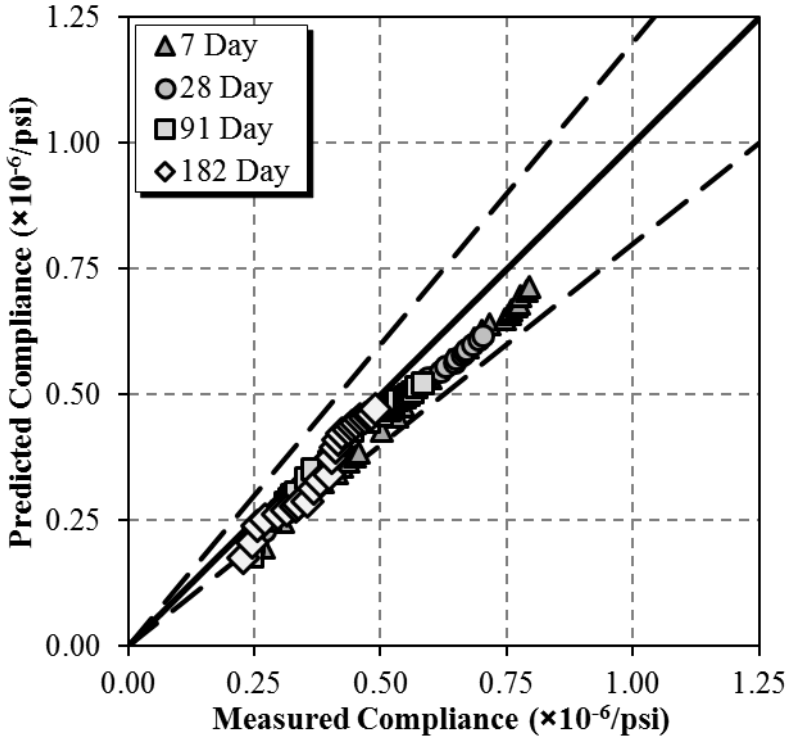

Figure B-27: Compliance comparison of 11/19/2018 specimens using the CEB MC 1990 Model

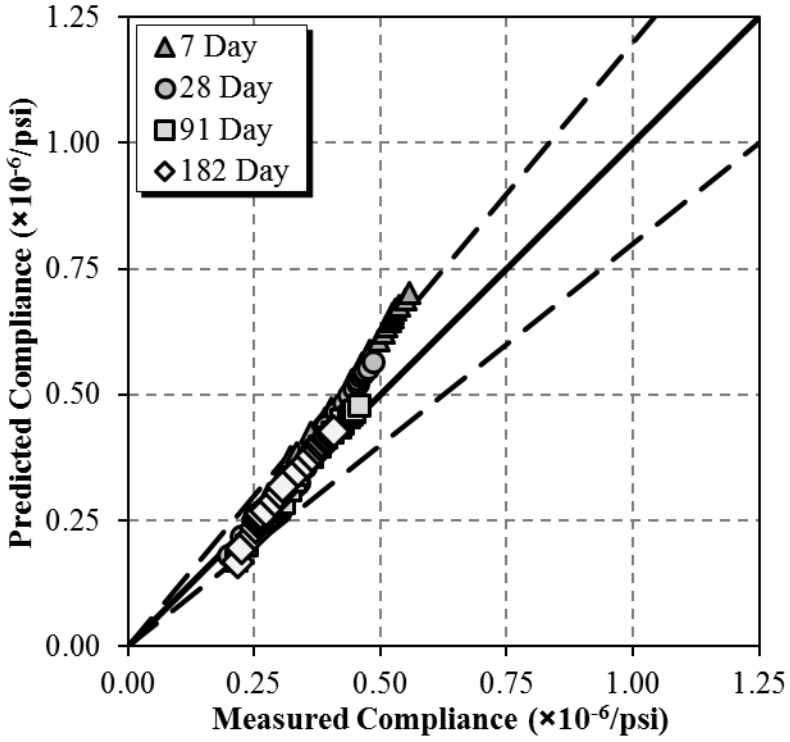

Figure B-28: Compliance comparison of 04/16/2019 specimens using the CEB MC 1990 Model

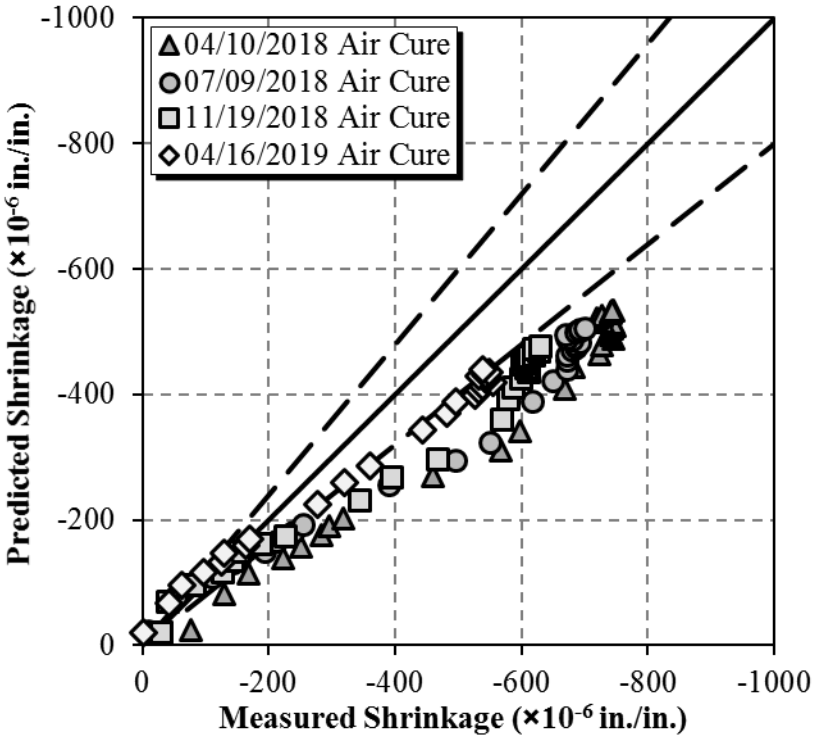

Figure B-29: Shrinkage comparison of air-cured prismatic specimens using CEB MC 1990 Model

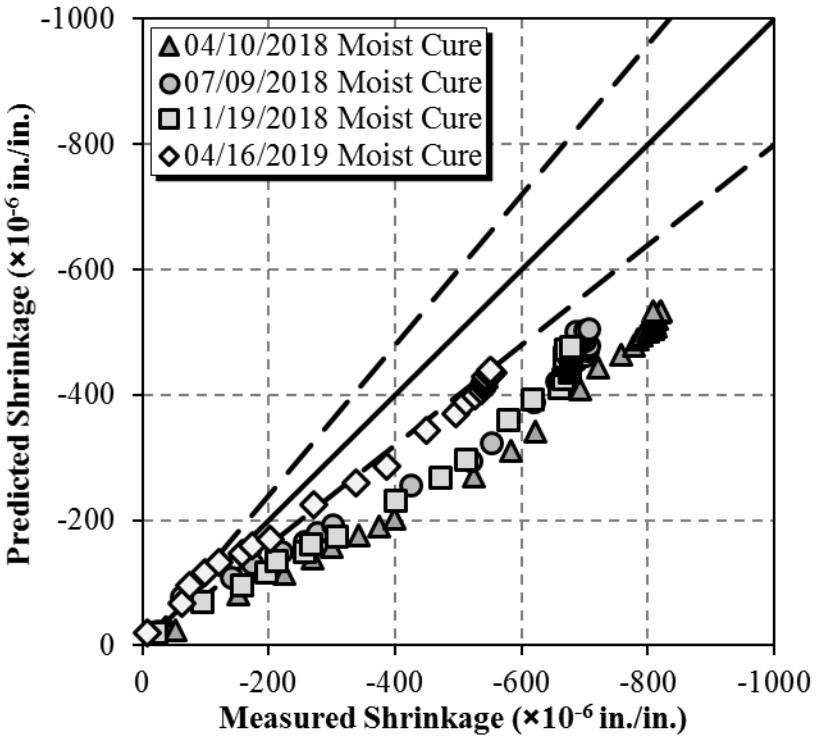

Figure B-30: Shrinkage comparison of moist-cured prismatic specimens using the CEB MC 1990 Model

B.6 CEB MC 2010 PREDICTION METHOD

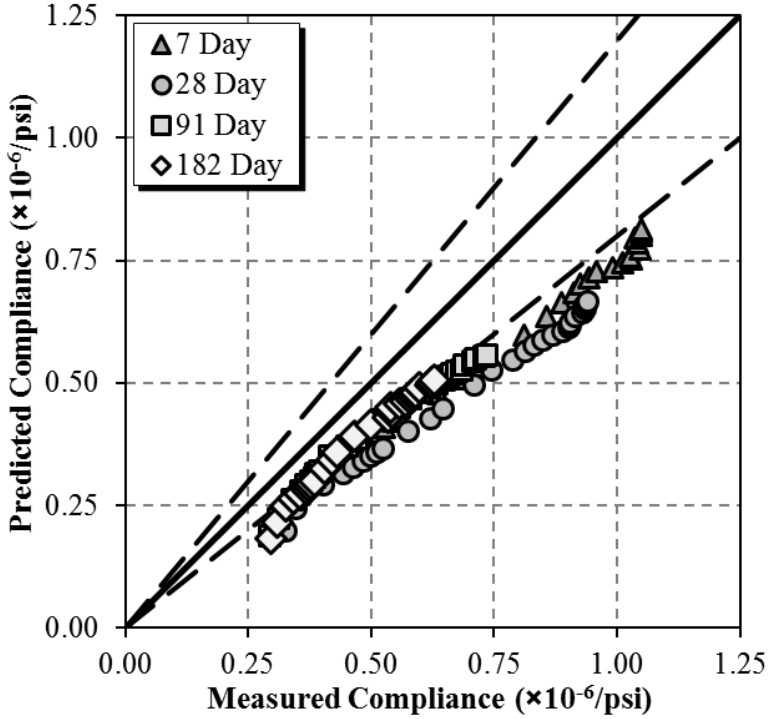

Figure B-31: Compliance comparison of 04/10/2018 specimens using the CEB MC 2010 Model

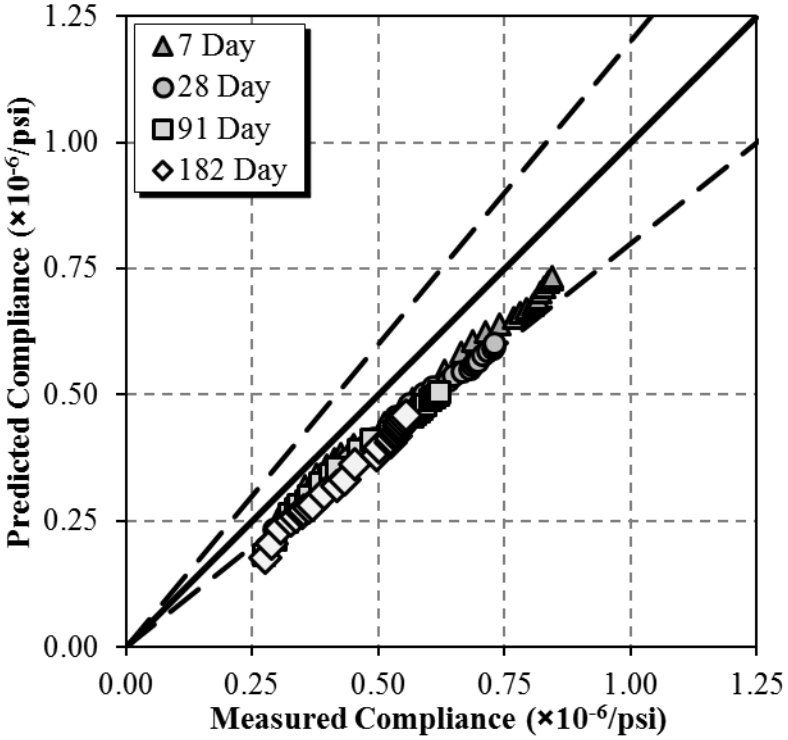

Figure B-32: Compliance comparison of 07/09/2018 specimens using the CEB MC 2010 Model

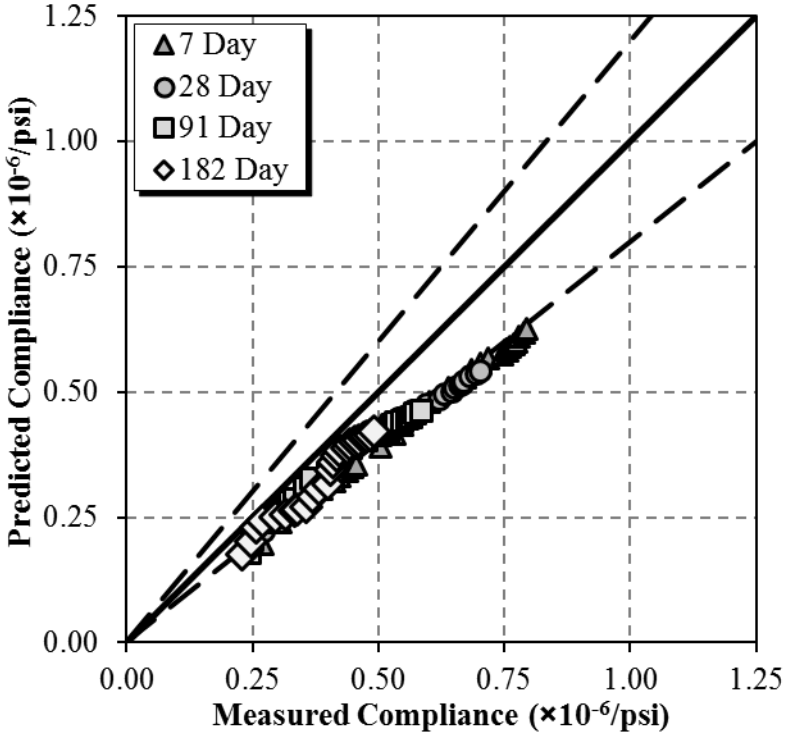

Figure B-33: Compliance comparison of 11/19/2018 specimens using the CEB MC 2010 Model

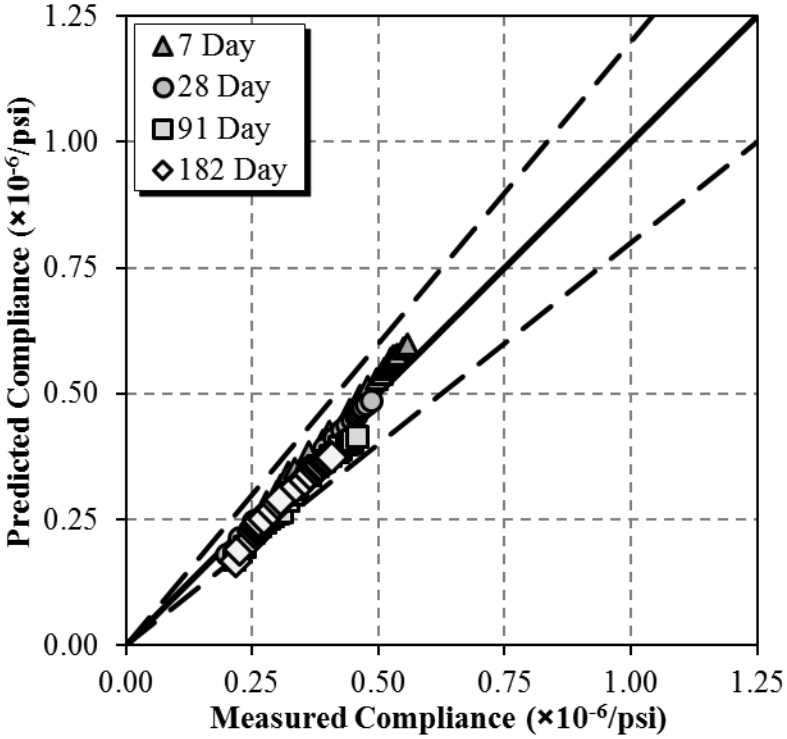

Figure B-34: Compliance comparison of 04/16/2019 specimens using the CEB MC 2010 Model

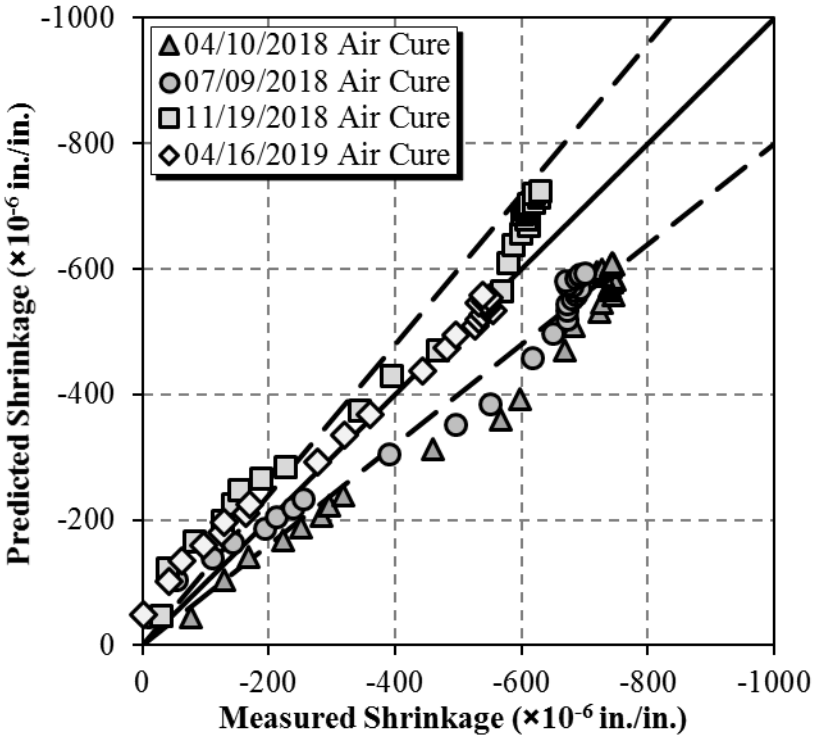

Figure B-35: Shrinkage comparison of air-cured prismatic specimens using the CEB MC 2010 Model

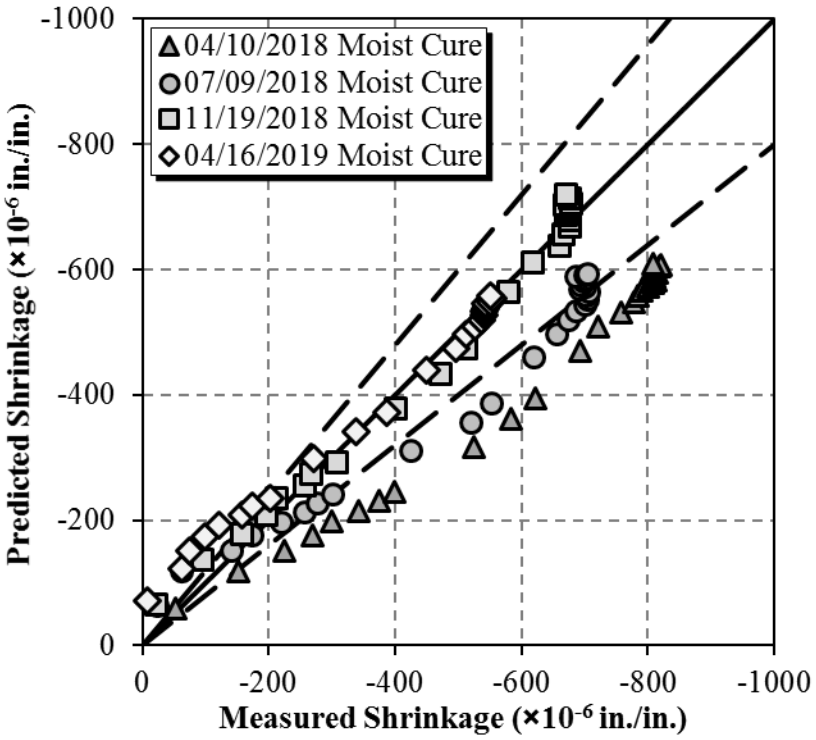

Figure B-36: Shrinkage comparison of moist-cured prismatic specimens using the CEB MC 2010 Model

APPENDIX C: BIRMINGHAM I-59/I-20 SEGMENTAL BRIDGE CASTING AND ERECTION DATA

All segment designations with corresponding casting and erection dates were provided by Corven Engineering who acted as lead bridge designer for the I-59/I-20 segmental bridge project in Birmingham, Alabama. Thanks to this data presented in Table C-1, each sample collection date was able to be grouped to corresponding bridge segments, which provided the ability to better define the modified prediction models.

Table C-1: Casting and Erection Data for I-59/I-20 Bridge Segments

Span	SEGMENT Label	CAST Date	ERECT Date	Span	SEGMENT Label	CAST Date	ERECT Date
WBL-1	WBL1-EU	01/11/19	06/26/19	EBL-1	EBL1-EU	01/22/19	06/12/19
	WBL1-T1	10/27/18	06/25/19		EBL1-T1	10/16/18	06/12/19
	WBL1-T2	10/29/18	06/25/19		EBL1-T2	10/18/18	06/12/19
	WBL1-D3	10/30/18	06/25/19		EBL1-D3	10/20/18	06/11/19
	WBL1-T4	10/31/18	06/25/19		EBL1-T4	10/23/18	06/11/19
	WBL1-T5	11/01/18	06/25/19		EBL1-T5	10/24/18	06/11/19
	WBL1-T6	11/02/18	06/25/19		EBL1-T6	10/26/18	06/11/19
	WBL1-D7	11/05/18	06/25/19		EBL1-T7	10/29/18	06/11/19
	WBL1-T8	11/06/18	06/25/19		EBL1-D8	10/30/18	06/11/19
	WBL1-T9	11/08/18	06/25/19		EBL1-T9	10/31/18	06/11/19
	WBL1-T10	11/10/18	06/25/19		EBL1-T10	11/01/18	06/11/19
	WBL2-PD	11/10/18	06/26/19		EBL1-T11	11/02/18	06/15/19
WBL-2	WBL2-PU	11/08/18	06/28/19		EBL2-PD	11/05/18	06/11/19
	WBL2-T1	11/10/18	07/01/19	EBL-2	EBL2-PU	10/31/18	06/03/19
	WBL2-T2	11/13/18	07/01/19		EBL2-T1	10/15/18	06/03/19
	WBL2-T3	11/15/18	07/01/19		EBL2-T2	10/17/18	06/03/19
	WBL2-D4	11/17/18	07/01/19		EBL2-T3	10/18/18	06/03/19
	WBL2-T5	11/19/18	07/01/19		EBL2-D4	10/20/18	06/02/19
	WBL2-T6	11/20/18	07/01/19		EBL2-T5	10/23/18	06/02/19
	WBL2-T7	11/21/18	06/30/19		EBL2-T6	10/24/18	06/02/19

	WBL2-D8	11/27/18	06/29/19		EBL2-T7	10/25/18	06/02/19
	WBL2-T9	11/28/18	06/28/19		EBL2-D8	10/29/18	06/02/19
	WBL2-T10	11/29/18	06/28/19		EBL2-T9	10/30/18	06/02/19
	WBL2-T11	12/04/18	06/28/19		EBL2-T10	10/31/18	06/02/19
	WBL3-PD	10/11/18	07/03/19		EBL2-T11	11/01/18	06/01/19
WBL-3	WBL3-PU	10/09/18	07/03/19		EBL3-PD	05/15/19	06/01/19
	WBL3-T1	01/04/19	07/11/19	EBL-3	EBL3-PU	05/13/19	05/25/19
	WBL3-T2	01/07/19	07/03/19		EBL3-T1	10/02/18	05/25/19
	WBL3-T3	01/08/19	07/03/19		EBL3-T2	10/04/18	05/25/19
	WBL3-D4	01/09/19	07/03/19		EBL3-T3	10/05/18	05/25/19
	WBL3-T5	01/10/19	07/02/19		EBL3-D4	10/09/18	05/25/19
	WBL3-T6	01/11/19	07/02/19		EBL3-T5	10/11/18	05/25/19
	WBL3-T7	01/12/19	07/02/19		EBL3-T6	10/12/18	05/25/19
	WBL3-D8	01/15/19	07/02/19		EBL3-T7	10/13/18	05/24/19
	WBL3-T9	01/16/19	07/02/19		EBL3-T8	10/15/18	05/24/19
	WBL3-T10	01/17/19	07/02/19		EBL3-D9	10/17/18	05/24/19
	WBL3-T11	01/18/19	07/02/19		EBL3-T10	10/18/18	05/24/19
	WBL4-PD	10/11/18	07/08/19		EBL3-T11	10/19/18	05/24/19
WBL-4	WBL4-PU	10/08/18	07/08/19		EBL4-ED	05/14/19	05/28/19
	WBL4-T1	09/06/18	08/05/19	EBL-4	EBL4-EU	04/10/19	07/16/19
	WBL4-T2	09/07/18	08/05/19		EBL4-T1	12/10/18	07/15/19
	WBL4-T3	09/10/18	08/05/19		EBL4-T2	12/12/18	07/15/19
	WBL4-D4	09/12/18	08/05/19		EBL4-D3	12/13/18	07/15/19
	WBL4-T5	09/13/18	08/05/19		EBL4-T4	12/14/18	07/15/19
	WBL4-T6	09/14/18	08/05/19		EBL4-T5	12/15/18	07/16/19
	WBL4-T7	09/17/18	08/05/19		EBL4-T6	12/17/18	07/16/19
	WBL4-T8	09/18/18	08/05/19		EBL4-D7	12/18/18	07/16/19
	WBL4-D9	09/19/18	08/05/19		EBL4-T8	12/19/18	07/16/19
	WBL4-T10	09/20/18	08/05/19		EBL4-T9	12/20/18	07/16/19
	WBL4-T11	09/21/18	08/05/19		EBL4-T10	12/21/18	07/16/19
	WBL5-ED	01/14/19	08/06/19		EBL5-PD	01/17/19	07/17/19
WBL-5	WBL5-EU	01/09/19	08/12/19	EBL-5	EBL5-PU	01/15/19	07/20/19
	WBL5-T1	01/31/19	08/08/19		EBL5-T1	02/19/19	07/25/19
	WBL5-T2	02/01/19	08/08/19		EBL5-T2	02/21/19	07/22/19
	WBL5-D3	02/02/19	08/08/19		EBL5-T3	02/22/19	07/22/19
	WBL5-T4	02/04/19	08/08/19		EBL5-D4	02/25/19	07/22/19
	WBL5-T5	02/05/19	08/08/19		EBL5-T5	02/26/19	07/21/19
	WBL5-D6	02/06/19	08/08/19		EBL5-D6	02/27/19	07/21/19
	WBL5-T7	02/08/19	08/08/19		EBL5-T7	02/28/19	07/21/19

	WBL5-T8	02/09/19	08/08/19		EBL5-T8	03/01/19	07/21/19
	WBL5-T9	02/11/19	08/08/19		EBL5-T9	03/02/19	07/21/19
	WBL6-PD	03/04/19	08/09/19		EBL6-PD	01/30/19	07/22/19
WBL-6	WBL6-PU	02/28/19	08/10/19	EBL-6	EBL6-PU	01/26/19	07/24/19
	WBL6-T1	01/15/19	08/14/19		EBL6-T1	02/15/19	07/27/19
	WBL6-T2	01/16/19	08/11/19		EBL6-T2	02/16/19	07/24/19
	WBL6-T3	01/17/19	08/11/19		EBL6-T3	02/18/19	07/24/19
	WBL6-D4	01/18/19	08/10/19		EBL6-D4	02/20/19	07/24/19
	WBL6-T5	01/22/19	08/10/19		EBL6-T5	02/21/19	07/24/19
	WBL6-T6	01/23/19	08/10/19		EBL6-T6	02/22/19	07/24/19
	WBL6-D7	01/24/19	08/10/19		EBL6-T7	02/23/19	07/24/19
	WBL6-T8	01/25/19	08/10/19		EBL6-T8	02/25/19	07/24/19
	WBL6-T9	01/26/19	08/10/19		EBL6-D9	02/26/19	07/24/19
	WBL6-T10	01/28/19	08/10/19		EBL6-T10	02/27/19	07/24/19
	WBL7-PD	03/12/19	08/11/19		EBL6-T11	02/28/19	07/24/19
WBL-7	WBL7-PU	03/09/19	08/14/19		EBL7-ED	04/26/19	07/25/19
	WBL7-T1	05/20/19	09/09/19	EBL-7	EBL7-EU	05/30/19	08/22/19
	WBL7-T2	05/21/19	09/09/19		EBL7-T1	04/08/19	08/21/19
	WBL7-T3	05/22/19	09/09/19		EBL7-T2	04/09/19	08/21/19
	WBL7-D4	05/23/19	09/09/19		EBL7-D3	04/10/19	08/21/19
	WBL7-T5	05/24/19	09/09/19		EBL7-T4	04/12/19	08/22/19
	WBL7-T6	05/28/19	09/09/19		EBL7-T5	04/13/19	08/22/19
	WBL7-T7	05/29/19	09/09/19		EBL7-T6	04/15/19	08/22/19
	WBL7-D8	05/30/19	09/09/19		EBL7-T7	04/16/19	08/22/19
	WBL7-T9	05/31/19	09/09/19		EBL7-D8	04/18/19	08/22/19
	WBL7-T10	06/03/19	09/09/19		EBL7-T9	04/22/19	08/22/19
	WBL7-T11	06/04/19	09/09/19		EBL7-T10	04/23/19	08/22/19
	WBL8-PD	06/05/19	09/10/19		EBL7-T11	04/24/19	08/22/19
WBL-8	WBL8-PU	06/04/19	09/10/19		EBL8-PD	07/02/19	08/23/19
	WBL8-T1	06/10/19	09/13/19	EBL-8	EBL8-PU	07/01/19	08/23/19
	WBL8-T2	06/12/19	09/13/19		EBL8-T1	04/11/19	08/29/19
	WBL8-T3	06/13/19	09/12/19		EBL8-T2	04/12/19	08/28/19
	WBL8-D4	06/14/19	09/12/19		EBL8-T3	04/13/19	08/28/19
	WBL8-T5	06/17/19	09/12/19		EBL8-D4	04/15/19	08/27/19
	WBL8-T6	06/18/19	09/12/19		EBL8-T5	04/16/19	08/27/19
	WBL8-T7	06/19/19	09/12/19		EBL8-T6	04/17/19	08/27/19
	WBL8-T8	06/20/19	09/12/19		EBL8-T7	04/18/19	08/27/19
	WBL8-T9	06/21/19	09/12/19		EBL8-T8	04/22/19	08/27/19
	WBL8-D10	06/25/19	09/11/19		EBL8-D9	04/23/19	08/27/19

	WBL8-T11	06/26/19	09/11/19		EBL8-T10	04/24/19	08/27/19
	WBL8-T12	06/27/19	09/11/19		EBL8-T11	04/25/19	08/27/19
	WBL9-ED	06/12/19	09/13/19		EBL8-T12	04/26/19	08/27/19
WBL-9	WBL9-EU	11/21/18	06/13/19		EBL9-PD	12/15/18	05/08/19
	WBL9-T1	01/28/19	06/12/19	EBL-9	EBL9-PU	12/12/18	05/08/19
	WBL9-T2	01/31/19	06/12/19		EBL9-T1	11/13/18	05/06/19
	WBL9-D3	02/01/19	06/12/19		EBL9-T2	11/15/18	05/06/19
	WBL9-T4	02/04/19	06/12/19		EBL9-T3	11/16/18	05/06/19
	WBL9-T5	02/05/19	06/12/19		EBL9-D4	11/19/18	05/06/19
	WBL9-T6	02/06/19	06/12/19		EBL9-T5	11/20/18	05/06/19
	WBL9-T7	02/07/19	06/12/19		EBL9-T6	11/21/18	05/07/19
	WBL9-T8	02/08/19	06/12/19		EBL9-T7	11/26/18	05/07/19
	WBL9-D9	02/09/19	06/12/19		EBL9-T8	11/27/18	05/07/19
	WBL9-T10	02/11/19	06/13/19		EBL9-T9	11/28/18	05/07/19
	WBL9-T11	02/13/19	06/13/19		EBL9-D10	11/29/18	05/07/19
	WBL9-T12	02/14/19	06/13/19		EBL9-T11	11/30/18	05/07/19
	WBL10-PD	08/14/18	06/13/19		EBL9-T12	12/04/18	05/07/19
WBL-10	WBL10-PU	08/04/18	06/17/19		EBL10-ED	02/25/19	05/08/19
	WBL10-T1	02/07/19	06/25/19	EBL-10	EBL10-EU	12/06/18	05/24/19
	WBL10-T2	02/08/19	06/17/19		EBL10-T1	04/17/18	05/16/19
	WBL10-T3	02/09/19	06/17/19		EBL10-T2	04/25/18	05/16/19
	WBL10-D4	02/11/19	06/17/19		EBL10-D3	05/07/18	05/16/19
	WBL10-T5	02/13/19	06/17/19		EBL10-T4	05/15/18	05/16/19
	WBL10-T6	02/14/19	06/17/19		EBL10-T5	05/21/18	05/16/19
	WBL10-T7	02/15/19	06/17/19		EBL10-T6	05/25/18	05/15/19
	WBL10-T8	02/16/19	06/17/19		EBL10-T7	06/02/18	05/15/19
	WBL10-D9	02/18/19	06/16/19		EBL10-T8	06/12/18	05/15/19
	WBL10-T10	02/19/19	06/16/19		EBL10-D9	06/19/18	05/15/19
	WBL10-T11	02/21/19	06/16/19		EBL10-T10	06/29/18	05/15/19
	WBL10-T12	02/22/19	06/16/19		EBL10-T11	07/11/18	05/15/19
	WBL11-PD	05/02/19	06/18/19		EBL10-T12	07/13/18	05/15/19
WBL-11	WBL11-PU	04/30/19	06/23/19		EBL11-PD	07/27/18	05/16/19
	WBL11-T1	03/20/18	06/30/19	EBL-11	EBL11-PU	05/09/19	05/21/19
	WBL11-T2	04/29/19	06/22/19		EBL11-T1	02/27/18	05/31/19
	WBL11-T3	04/30/19	06/22/19		EBL11-T2	03/06/18	05/20/19
	WBL11-D4	05/01/19	06/22/19		EBL11-T3	03/12/18	05/20/19
	WBL11-T5	05/02/19	06/21/19		EBL11-D4	04/12/18	05/20/19
	WBL11-T6	05/03/19	06/21/19		EBL11-T5	04/21/18	05/20/19
	WBL11-T7	05/06/19	06/21/19		EBL11-T6	04/30/18	05/20/19

	WBL11-T8	05/07/19	06/21/19		EBL11-T7	05/04/18	05/20/19
	WBL11-D9	05/08/19	06/21/19		EBL11-T8	05/10/18	05/20/19
	WBL11-T10	05/10/19	06/21/19		EBL11-D9	05/23/18	05/20/19
	WBL11-T11	05/13/19	06/21/19		EBL11-T10	06/05/18	05/20/19
	WBL11-T12	05/14/19	06/21/19		EBL11-T11	06/06/18	05/20/19
	WBL12-PD	05/01/19	06/22/19		EBL11-T12	06/07/18	05/20/19
WBL-12	WBL12-PU	04/29/19	06/24/19		EBL12-PD	08/10/18	05/21/19
	WBL12-T1	03/26/18	08/03/19	EBL-12	EBL12-PU	08/02/18	05/21/19
	WBL12-T2	05/02/19	08/03/19		EBL12-T1	04/06/18	07/11/19
	WBL12-T3	05/03/19	08/03/19		EBL12-T2	04/18/18	07/11/19
	WBL12-D4	05/06/19	08/03/19		EBL12-T3	04/24/18	07/11/19
	WBL12-T5	05/07/19	08/03/19		EBL12-D4	05/30/18	07/11/19
	WBL12-T6	05/08/19	08/04/19		EBL12-T5	06/21/18	07/11/19
	WBL12-T7	05/09/19	08/04/19		EBL12-T6	06/25/18	07/12/19
	WBL12-T8	05/10/19	08/04/19		EBL12-T7	06/29/18	07/12/19
	WBL12-T9	05/13/19	08/04/19		EBL12-T8	07/09/18	07/12/19
	WBL12-D10	05/14/19	08/04/19		EBL12-T9	07/13/18	07/12/19
	WBL12-T11	05/15/19	08/04/19		EBL12-D10	07/17/18	07/12/19
	WBL12-T12	05/16/19	08/04/19		EBL12-T11	07/20/18	07/12/19
	WBL13-ED	05/28/19	08/04/19		EBL12-T12	07/24/18	07/12/19
WBL-13	WBL13-EU	06/14/19	08/09/19		EBL13-ED	12/04/18	07/12/19
	WBL13-T1	03/24/18	08/09/19	EBL-13	EBL13-EU	05/10/19	07/23/19
	WBL13-T2	05/15/19	08/09/19		EBL13-T1	07/16/18	07/16/19
	WBL13-D3	05/16/19	08/10/19		EBL13-T2	07/18/18	07/16/19
	WBL13-T4	05/17/19	08/10/19		EBL13-D3	07/24/18	07/16/19
	WBL13-T5	05/20/19	08/10/19		EBL13-T4	07/26/18	07/16/19
	WBL13-T6	05/21/19	08/10/19		EBL13-T5	07/30/18	07/16/19
	WBL13-T7	05/22/19	08/10/19		EBL13-T6	08/01/18	07/16/19
	WBL13-T8	05/23/19	08/10/19		EBL13-T7	08/03/18	07/15/19
	WBL13-D9	05/24/19	08/10/19		EBL13-T8	08/06/18	07/15/19
	WBL13-T10	05/28/19	08/11/19		EBL13-D9	08/08/18	07/15/19
	WBL13-T11	05/29/19	08/11/19		EBL13-T10	08/10/18	07/15/19
	WBL13-T12	05/30/19	08/11/19		EBL13-T11	08/11/18	07/15/19
	WBL14-PD	06/25/19	08/11/19		EBL13-T12	08/13/18	07/15/19
WBL-14	WBL14-PU	06/24/19	08/17/19		EBL14-PD	06/15/19	07/16/19
	WBL14-T1	05/17/19	08/20/19	EBL-14	EBL14-PU	06/13/18	07/20/19
	WBL14-T2	05/20/19	08/18/19		EBL14-T1	08/08/18	07/26/19
	WBL14-T3	05/21/19	08/18/19		EBL14-T2	08/10/18	07/20/19
	WBL14-D4	05/22/19	08/18/19		EBL14-T3	08/11/18	07/20/19

	WBL14-T5	05/23/19	08/18/19		EBL14-D4	08/14/18	07/20/19
	WBL14-T6	05/24/19	08/18/19		EBL14-T5	08/16/18	07/20/19
	WBL14-T7	05/28/19	08/18/19		EBL14-T6	08/17/18	07/20/19
	WBL14-T8	05/29/19	08/18/19		EBL14-T7	08/18/18	07/20/19
	WBL14-D9	05/30/19	08/18/19		EBL14-T8	08/20/18	07/20/19
	WBL14-T10	05/31/19	08/17/19		EBL14-D9	08/22/18	07/20/19
	WBL14-T11	06/03/19	08/17/19		EBL14-T10	08/23/18	07/19/19
	WBL14-T12	06/04/19	08/17/19		EBL14-T11	08/24/18	07/19/19
	WBL15-PD	06/28/19	08/19/19		EBL14-T12	08/25/18	07/19/19
WBL-15	WBL15-PU	06/27/19	08/20/19		EBL15-PD	06/29/18	07/21/19
	WBL15-T1	06/19/19	09/17/19	EBL-15	EBL15-PU	06/18/19	07/22/19
	WBL15-T2	06/20/19	09/17/19		EBL15-T1	08/07/18	08/27/19
	WBL15-T3	06/21/19	09/17/19		EBL15-T2	08/08/18	08/27/19
	WBL15-D4	06/25/19	09/17/19		EBL15-T3	08/10/18	08/27/19
	WBL15-T5	06/26/19	09/17/19		EBL15-D4	08/13/18	08/27/19
	WBL15-T6	06/27/19	09/17/19		EBL15-T5	08/14/18	08/27/19
	WBL15-T7	06/28/19	09/18/19		EBL15-T6	08/15/18	08/27/19
	WBL15-T8	06/29/19	09/18/19		EBL15-T7	08/16/18	08/27/19
	WBL15-D9	07/01/19	09/18/19		EBL15-T8	08/17/18	08/27/19
	WBL15-T10	07/02/19	09/18/19		EBL15-D9	08/20/18	08/27/19
	WBL15-T11	07/03/19	09/18/19		EBL15-T10	08/21/18	08/27/19
	WBL15-T12	07/08/19	09/18/19		EBL15-T11	08/22/18	08/27/19
	WBL16-PD	07/30/19	09/18/19		EBL15-T12	08/23/18	08/28/19
WBL-16	WBL16-PU	07/27/19	09/20/19		EBL16-PD	06/01/19	08/28/19
	WBL16-T1	07/09/19	09/24/19	EBL-16	EBL16-PU	05/30/19	09/03/19
	WBL16-T2	07/08/19	09/21/19		EBL16-T1	04/18/18	09/08/19
	WBL16-T3	07/03/19	09/21/19		EBL16-T2	04/25/18	09/05/19
	WBL16-D4	07/02/19	09/21/19		EBL16-T3	05/05/18	09/04/19
	WBL16-T5	07/01/19	09/21/19		EBL16-D4	05/18/18	09/04/19
	WBL16-T6	06/29/19	09/21/19		EBL16-T5	06/30/18	09/04/19
	WBL16-T7	06/28/19	09/21/19		EBL16-T6	07/09/18	09/04/19
	WBL16-T8	06/27/19	09/21/19		EBL16-T7	07/11/18	09/04/19
	WBL16-T9	06/26/19	09/21/19		EBL16-T8	07/13/18	09/04/19
	WBL16-D10	06/25/19	09/21/19		EBL16-T9	07/17/18	09/04/19
	WBL16-T11	06/21/19	09/21/19		EBL16-D10	07/23/18	09/04/19
	WBL16-T12	03/15/18	09/20/19		EBL16-T11	07/25/18	09/04/19
	WBL17-ED	06/25/19	09/23/19		EBL16-T12	07/26/18	09/04/19
WBL-17	WBL17-EU	11/29/18	06/04/19		EBL17-ED	06/08/19	09/05/19
	WBL17-T1	01/18/19	06/04/19		EBL17-EU	01/26/19	04/01/19

	WBL17-T2	01/22/19	06/04/19		EBL17-T1	07/16/18	04/01/19
	WBL17-D3	01/24/19	06/04/19		EBL17-T2	07/17/18	04/01/19
	WBL17-T4	01/25/19	06/04/19		EBL17-D3	07/20/18	04/01/19
	WBL17-T5	01/26/19	06/05/19		EBL17-T4	07/24/18	04/01/19
	WBL17-T6	01/28/19	06/05/19		EBL17-T5	07/25/18	04/02/19
	WBL17-T7	01/31/19	06/05/19		EBL17-T6	07/26/18	04/02/19
	WBL17-T8	02/01/19	06/05/19	EBL-17	EBL17-T7	07/27/18	04/02/19
	WBL17-D9	02/02/19	06/05/19		EBL17-T8	07/30/18	04/02/19
	WBL17-T10	02/04/19	06/05/19		EBL17-D9	08/01/18	04/02/19
	WBL17-T11	02/05/19	06/05/19		EBL17-T10	08/02/18	04/02/19
	WBL17-T12	02/06/19	06/05/19		EBL17-T11	08/03/18	04/02/19
	WBL18-PD	04/02/19	06/15/19		EBL17-T12	08/06/18	04/03/19
	WBL18-PU	03/30/19	06/15/19		EBL18-PD	04/08/19	05/05/19
	WBL18-T1	01/17/19	06/25/19		EBL18-PU	04/04/19	05/05/19
	WBL18-T2	01/18/19	06/14/19		EBL18-T1	07/25/18	05/15/19
	WBL18-T3	01/22/19	06/14/19		EBL18-T2	07/26/18	04/06/19
	WBL18-D4	01/25/19	06/14/19		EBL18-T3	07/27/18	04/06/19
	WBL18-T5	01/26/19	06/14/19		EBL18-D4	07/30/18	04/06/19
WBL-18	WBL18-T6	01/28/19	06/14/19		EBL18-T5	08/01/18	04/05/19
	WBL18-T7	01/31/19	06/13/19	EBL-18	EBL18-T6	08/02/18	04/04/19
	WBL18-T8	02/01/19	06/13/19		EBL18-T7	08/03/18	04/04/19
	WBL18-D9	02/02/19	06/13/19		EBL18-T8	08/04/18	04/04/19
	WBL18-T10	02/04/19	06/13/19		EBL18-D9	08/07/18	04/04/19
	WBL18-T11	02/05/19	06/13/19		EBL18-T10	08/10/18	04/04/19
	WBL18-T12	02/06/19	06/13/19		EBL18-T11	08/11/18	04/04/19
	WBL19-PD	02/21/19	06/20/19		EBL18-T12	08/13/18	04/04/19
	WBL19-PU	02/18/19	06/20/19		EBL19-PD	07/25/18	05/15/19
	WBL19-T1	12/31/18	06/28/19		EBL19-PU	07/16/18	05/15/19
	WBL19-T2	01/02/19	06/18/19		EBL19-T1	07/17/18	05/29/19
	WBL19-T3	01/03/19	06/18/19		EBL19-T2	07/18/18	05/15/19
	WBL19-D4	01/04/19	06/18/19		EBL19-T3	07/20/18	05/15/19
	WBL19-T5	01/05/19	06/18/19		EBL19-D4	07/24/18	05/14/19
WBL-19	WBL19-T6	01/07/19	06/18/19	EBL-19	EBL19-T5	07/26/18	05/14/19
	WBL19-T7	01/08/19	06/17/19		EBL19-T6	07/27/18	05/14/19
	WBL19-T8	01/09/19	06/17/19		EBL19-T7	07/28/18	05/14/19
	WBL19-D9	01/10/19	06/17/19		EBL19-T8	07/30/18	05/14/19
	WBL19-T10	01/11/19	06/17/19		EBL19-D9	08/02/18	05/14/19
	WBL19-T11	01/12/19	06/17/19		EBL19-T10	08/03/18	05/13/19
	WBL19-T12	01/14/19	06/17/19		EBL19-T11	08/04/18	05/13/19

	WBL20-PD	02/07/19	06/25/19		EBL19-T12	08/06/18	05/13/19
WBL-20	WBL20-PU	02/05/19	06/25/19		EBL20-PD	04/01/19	05/25/19
	WBL20-T1	01/02/19	07/02/19	EBL-20	EBL20-PU	03/29/19	05/13/19
	WBL20-T2	01/03/19	06/26/19		EBL20-T1	07/25/18	05/30/19
	WBL20-T3	01/04/19	06/23/19		EBL20-T2	07/26/18	05/23/19
	WBL20-D4	01/07/19	06/23/19		EBL20-T3	07/30/18	05/23/19
	WBL20-T5	01/08/19	06/23/19		EBL20-D4	08/01/18	05/23/19
	WBL20-T6	01/09/19	06/23/19		EBL20-T5	08/03/18	05/23/19
	WBL20-T7	01/10/19	06/23/19		EBL20-T6	08/04/18	05/23/19
	WBL20-T8	01/11/19	06/22/19		EBL20-T7	08/07/18	05/23/19
	WBL20-T9	01/12/19	06/22/19		EBL20-T8	08/10/18	05/23/19
	WBL20-D10	01/14/19	06/22/19		EBL20-T9	08/11/18	05/23/19
	WBL20-T11	01/15/19	06/22/19		EBL20-D10	08/14/18	05/23/19
	WBL20-T12	01/16/19	06/22/19		EBL20-T11	08/16/18	05/23/19
	WBL21-ED	04/17/19	06/29/19		EBL20-T12	08/18/18	05/22/19
WBL-21	WBL21-EU	02/06/19	07/11/19		EBL21-ED	11/15/18	05/22/19
	WBL21-T1	12/11/18	07/10/19	EBL-21	EBL21-EU	04/03/19	07/22/19
	WBL21-T2	12/12/18	07/10/19		EBL21-T1	12/05/18	07/22/19
	WBL21-D3	12/14/18	07/10/19		EBL21-T2	01/04/19	07/22/19
	WBL21-T4	12/15/18	07/10/19		EBL21-D3	01/07/19	07/21/19
	WBL21-T5	12/17/18	07/10/19		EBL21-T4	01/08/19	07/21/19
	WBL21-T6	12/18/18	07/10/19		EBL21-T5	01/09/19	07/21/19
	WBL21-T7	12/19/18	07/10/19		EBL21-T6	01/10/19	07/21/19
	WBL21-T8	12/20/18	07/10/19		EBL21-T7	01/11/19	07/21/19
	WBL21-D9	12/22/18	07/09/19		EBL21-T8	01/12/19	07/21/19
	WBL21-T10	01/01/19	07/09/19		EBL21-D9	01/14/19	07/20/19
	WBL21-T11	01/02/19	07/09/19		EBL21-T10	01/15/19	07/20/19
	WBL21-T12	01/03/19	07/09/19		EBL21-T11	01/16/19	07/20/19
	WBL22-PD	02/20/19	07/15/19		EBL21-T12	01/17/19	07/20/19
WBL-22	WBL22-PU	02/16/19	07/15/19		EBL22-PD	02/26/19	08/02/19
	WBL22-T1	01/02/19	07/17/19	EBL-22	EBL22-PU	02/22/19	08/02/19
	WBL22-T2	01/03/19	07/02/19		EBL22-T1	01/09/19	08/05/19
	WBL22-T3	01/04/19	07/02/19		EBL22-T2	01/10/19	08/01/19
	WBL22-D4	01/07/19	07/02/19		EBL22-T3	01/11/19	07/31/19
	WBL22-T5	01/08/19	07/02/19		EBL22-D4	01/14/19	07/31/19
	WBL22-T6	01/09/19	07/02/19		EBL22-T5	01/15/19	07/31/19
	WBL22-T7	01/10/19	07/02/19		EBL22-T6	01/16/19	07/31/19
	WBL22-T8	01/11/19	07/02/19		EBL22-T7	01/17/19	07/31/19
	WBL22-D9	01/14/19	07/02/19		EBL22-T8	01/18/19	07/30/19

	WBL22-T10	01/15/19	07/01/19		EBL22-T9	01/22/19	07/30/19
	WBL22-T11	01/16/19	07/01/19		EBL22-D10	01/24/19	07/30/19
	WBL22-T12	01/17/19	07/01/19		EBL22-T11	01/25/19	07/30/19
	WBL23-PD	01/11/19	07/03/19		EBL22-T12	01/26/19	07/30/19
WBL-23	WBL23-PU	01/09/19	07/03/19		EBL23-ED	03/13/19	08/05/19
	WBL23-T1	01/31/19	07/19/19	EBL-23	EBL23-EU	03/16/19	08/08/19
	WBL23-T2	02/01/19	06/29/19		EBL23-T1	02/20/19	08/08/19
	WBL23-T3	02/02/19	06/29/19		EBL23-T2	02/21/19	08/08/19
	WBL23-D4	02/04/19	06/29/19		EBL23-D3	02/22/19	08/08/19
	WBL23-T5	02/05/19	06/29/19		EBL23-T4	02/23/19	08/08/19
	WBL23-T6	02/06/19	06/29/19		EBL23-T5	02/25/19	08/08/19
	WBL23-T7	02/07/19	06/29/19		EBL23-T6	02/26/19	08/08/19
	WBL23-T8	02/08/19	06/29/19		EBL23-T7	02/27/19	08/04/19
	WBL23-T9	02/09/19	06/29/19		EBL23-T8	02/28/19	08/04/19
	WBL23-D10	02/11/19	06/29/19		EBL23-D9	03/01/19	08/03/19
	WBL23-T11	02/13/19	06/28/19		EBL23-T10	03/02/19	08/03/19
	WBL23-T12	02/14/19	06/28/19		EBL23-T11	03/04/19	08/03/19
	WBL24-ED	02/14/19	07/18/19		EBL23-T12	03/05/19	08/03/19
WBL-24	WBL24-EU	05/04/19	08/17/19		EBL24-PD	03/13/19	08/24/19
	WBL24-T1	03/16/19	08/17/19	EBL-24	EBL24-PU	03/11/19	08/24/19
	WBL24-T2	03/18/19	08/17/19		EBL24-T1	04/10/19	09/11/19
	WBL24-D3	03/19/19	08/17/19		EBL24-T2	04/11/19	09/11/19
	WBL24-T4	03/20/19	08/17/19		EBL24-T3	04/12/19	09/11/19
	WBL24-T5	03/21/19	08/17/19		EBL24-D4	04/13/19	09/11/19
	WBL24-T6	03/22/19	08/17/19		EBL24-T5	04/15/19	09/11/19
	WBL24-T7	03/23/19	08/17/19		EBL24-T6	04/16/19	09/11/19
	WBL24-T8	03/25/19	08/17/19		EBL24-T7	04/17/19	09/11/19
	WBL24-D9	03/26/19	08/17/19		EBL24-T8	04/18/19	09/11/19
	WBL24-T10	03/27/19	08/17/19		EBL24-D9	04/22/19	09/11/19
	WBL24-T11	03/28/19	08/17/19		EBL24-T10	04/23/19	09/11/19
	WBL24-T12	03/29/19	08/17/19		EBL24-T11	04/24/19	09/11/19
	WBL25-PD	04/26/19	08/17/19		EBL24-T12	04/26/19	09/11/19
WBL-25	WBL25-PU	04/24/19	08/17/19		EBL25-PD	06/22/19	09/14/19
	WBL25-T1	03/25/19	08/20/19	EBL-25	EBL25-PU	05/22/19	09/14/19
	WBL25-T2	03/26/19	08/15/19		EBL25-T1	04/15/19	09/17/19
	WBL25-T3	03/27/19	08/15/19		EBL25-T2	04/16/19	09/13/19
	WBL25-D4	03/29/19	08/15/19		EBL25-T3	04/18/19	09/13/19
	WBL25-T5	03/30/19	08/15/19		EBL25-D4	04/22/19	09/13/19
	WBL25-T6	04/01/19	08/15/19		EBL25-T5	04/23/19	09/13/19

	WBL25-T7	04/02/19	08/15/19		EBL25-T6	04/24/19	09/13/19
	WBL25-T8	04/03/19	08/15/19		EBL25-T7	04/25/19	09/13/19
	WBL25-D9	04/04/19	08/15/19		EBL25-T8	04/26/19	09/13/19
	WBL25-T10	04/06/19	08/15/19		EBL25-T9	04/27/19	09/13/19
	WBL25-T11	04/08/19	08/14/19		EBL25-D10	04/29/19	09/12/19
	WBL25-T12	04/09/19	08/14/19		EBL25-T11	04/30/19	09/12/19
	WBL26-PD	05/07/19	05/16/19		EBL25-T12	05/01/19	09/12/19
WBL-26	WBL26-PU	05/06/19	05/15/19		EBL26-ED	05/21/19	09/14/19
	WBL26-T1	10/23/18	04/08/19	EBL-26	EBL26-EU	03/28/19	06/26/19
	WBL26-T2	10/25/18	04/08/19		EBL26-T1	02/13/19	06/26/19
	WBL26-T3	10/26/18	04/09/19		EBL26-T2	02/14/19	06/26/19
	WBL26-D4	10/29/18	04/09/19		EBL26-D3	02/15/19	06/25/19
	WBL26-T5	10/31/18	04/09/19		EBL26-T4	02/16/19	06/25/19
	WBL26-T6	11/01/18	04/09/19		EBL26-T5	02/18/19	06/25/19
	WBL26-T7	11/03/18	04/09/19		EBL26-T6	02/19/19	06/25/19
	WBL26-T8	11/05/18	04/09/19		EBL26-T7	02/21/19	06/25/19
	WBL26-T9	11/06/18	04/10/19		EBL26-T8	02/22/19	06/14/19
	WBL26-D10	11/08/18	04/10/19		EBL26-D9	02/23/19	06/14/19
	WBL26-T11	11/09/18	04/11/19		EBL26-T10	02/25/19	06/14/19
	WBL26-T12	11/13/18	04/12/19		EBL26-T11	02/26/19	06/14/19
	WBL27-ED	02/16/19	04/12/19		EBL26-T12	02/27/19	06/14/19
WBL-27	WBL27-EU	02/26/19	04/12/19		EBL27-PD	02/27/19	06/13/19
	WBL27-T1	09/14/18	04/13/19	EBL-27	EBL27-PU	02/25/19	06/13/19
	WBL27-T2	09/15/18	04/13/19		EBL27-T1	02/23/19	06/12/19
	WBL27-D3	09/17/18	04/13/19		EBL27-T2	02/25/19	06/21/19
	WBL27-T4	09/18/18	04/17/19		EBL27-T3	02/26/19	06/21/19
	WBL27-T5	09/19/18	04/17/19		EBL27-D4	02/27/19	06/21/19
	WBL27-T6	09/21/18	04/17/19		EBL27-T5	02/28/19	06/22/19
	WBL27-T7	09/25/18	04/17/19		EBL27-T6	03/01/19	06/22/19
	WBL27-T8	09/27/18	04/17/19		EBL27-T7	03/02/19	06/22/19
	WBL27-T9	09/28/18	04/18/19		EBL27-T8	03/04/19	06/23/19
	WBL27-D10	10/01/18	04/18/19		EBL27-D9	03/05/19	06/23/19
	WBL27-T11	10/02/18	04/18/19		EBL27-T10	03/06/19	06/23/19
	WBL27-T12	10/03/18	04/18/19		EBL27-T11	03/07/19	06/23/19
	WBL28-ED	02/22/19	04/12/19		EBL27-T12	03/08/19	06/23/19
WBL-28	WBL28-EU	06/22/19	08/02/19		EBL28-PD	03/08/19	06/24/19
	WBL28-T1	06/05/19	08/01/19	EBL-28	EBL28-PU	03/06/19	06/24/19
	WBL28-T2	06/06/19	08/01/19		EBL28-T1	05/02/19	07/18/19
	WBL28-D3	06/10/19	08/01/19		EBL28-T2	05/03/19	07/18/19

	WBL28-T4	06/11/19	08/01/19		EBL28-T3	05/06/19	07/18/19
	WBL28-T5	06/12/19	08/01/19		EBL28-D4	05/07/19	07/18/19
	WBL28-T6	06/13/19	08/01/19		EBL28-T5	05/08/19	07/18/19
	WBL28-T7	06/14/19	08/01/19		EBL28-T6	05/09/19	07/18/19
	WBL28-T8	06/17/19	08/01/19		EBL28-T7	05/10/19	07/18/19
	WBL28-D9	06/19/19	08/01/19		EBL28-T8	05/13/19	07/18/19
	WBL28-T10	06/20/19	08/01/19		EBL28-D9	05/14/19	07/18/19
	WBL28-T11	06/21/19	08/02/19		EBL28-T10	05/15/19	07/19/19
	WBL28-T12	06/25/19	08/02/19		EBL28-T11	05/16/19	07/19/19
	WBL29-PD	07/20/19	08/02/19		EBL28-T12	05/17/19	07/19/19
WBL-29	WBL29-PU	07/18/19	08/03/19		EBL29-PD	06/12/19	07/20/19
	WBL29-T1	06/05/19	08/15/19	EBL-29	EBL29-PU	06/11/19	07/20/19
	WBL29-T2	06/06/19	08/13/19		EBL29-T1	05/15/19	07/23/19
	WBL29-T3	06/07/19	08/13/19		EBL29-T2	05/17/19	07/23/19
	WBL29-D4	06/10/19	08/13/19		EBL29-T3	05/20/19	07/23/19
	WBL29-T5	06/11/19	08/13/19		EBL29-D4	05/21/19	07/23/19
	WBL29-T6	06/12/19	08/10/19		EBL29-T5	05/22/19	07/23/19
	WBL29-T7	06/13/19	08/10/19		EBL29-T6	05/23/19	07/23/19
	WBL29-T8	06/14/19	08/10/19		EBL29-T7	05/24/19	07/23/19
	WBL29-D9	06/17/19	08/10/19		EBL29-T8	05/28/19	07/23/19
	WBL29-T10	06/18/19	08/10/19		EBL29-D9	05/29/19	07/22/19
	WBL29-T11	06/19/19	08/10/19		EBL29-T10	05/30/19	07/22/19
	WBL29-T12	06/20/19	08/09/19		EBL29-T11	05/31/19	07/22/19
	WBL30-PD	07/18/19	08/13/19		EBL30-ED	06/11/19	07/23/19
WBL-30	WBL30-PU	07/16/19	08/13/19	EBL-30	EBL30-EU	06/26/19	08/27/19
	WBL30-T1	07/15/19	09/12/19		EBL30-T1	06/29/19	08/24/19
	WBL30-T2	07/16/19	09/12/19		EBL30-T2	07/01/19	08/24/19
	WBL30-T3	07/17/19	09/12/19		EBL30-D3	07/02/19	08/24/19
	WBL30-D4	07/18/19	09/12/19		EBL30-T4	07/03/19	08/24/19
	WBL30-T5	07/19/19	09/12/19		EBL30-T5	07/08/19	08/24/19
	WBL30-T6	07/20/19	09/12/19		EBL30-T6	07/09/19	08/24/19
	WBL30-T7	07/22/19	09/12/19		EBL30-D7	07/10/19	08/24/19
	WBL30-T8	07/23/19	09/12/19		EBL30-T8	07/11/19	08/24/19
	WBL30-D9	07/24/19	09/12/19		EBL30-T9	07/12/19	08/24/19
	WBL30-T10	07/25/19	09/12/19		EBL30-T10	07/13/19	08/24/19
	WBL30-T11	07/26/19	09/12/19		EBL31-PD	07/26/19	08/29/19
	WBL30-T12	07/29/19	09/12/19	EBL-31	EBL31-PU	07/24/19	08/29/19
	WBL31-PD	08/09/19	09/12/19		EBL31-T1	07/02/19	09/03/19
	WBL31-PU	08/07/19	09/12/19		EBL31-T2	07/03/19	08/30/19

WBL-31	WBL31-T1	07/20/19	09/16/19		EBL31-T3	07/08/19	08/30/19
	WBL31-T2	07/23/19	09/14/19		EBL31-D4	07/09/19	08/30/19
	WBL31-T3	07/24/19	09/14/19		EBL31-T5	07/10/19	08/30/19
	WBL31-D4	07/25/19	09/14/19		EBL31-T6	07/11/19	08/30/19
	WBL31-T5	07/26/19	09/14/19		EBL31-D7	07/13/19	08/30/19
	WBL31-T6	07/29/19	09/13/19		EBL31-T8	07/15/19	08/30/19
	WBL31-T7	07/30/19	09/13/19		EBL31-T9	07/16/19	08/30/19
	WBL31-D8	07/31/19	09/13/19		EBL31-T10	07/17/19	08/30/19
	WBL31-T9	08/01/19	09/13/19		EBL32-PD	10/17/18	05/26/19
	WBL31-T10	08/02/19	09/13/19	EBL-32	EBL32-PU	10/15/18	05/26/19
	WBL32-ED	07/11/19	09/14/19		EBL32-T1	01/18/19	05/25/19
WBL-32	WBL32-EU	05/08/19	08/22/19		EBL32-T2	01/22/19	05/25/19
	WBL32-T1	03/12/19	08/22/19		EBL32-T3	01/24/19	05/25/19
	WBL32-T2	03/13/19	08/22/19		EBL32-D4	01/25/19	05/27/19
	WBL32-D3	03/14/19	08/21/19		EBL32-T5	01/26/19	05/27/19
	WBL32-T4	03/15/19	08/21/19		EBL32-T6	01/28/19	05/27/19
	WBL32-T5	03/16/19	08/21/19		EBL32-D7	01/31/19	05/28/19
	WBL32-T6	03/18/19	08/21/19		EBL32-T8	02/01/19	05/28/19
	WBL32-T7	03/19/19	08/21/19		EBL32-T9	02/04/19	05/28/19
	WBL32-D8	03/20/19	08/21/19		EBL32-T10	02/05/19	05/28/19
	WBL32-T9	03/21/19	08/21/19		EBL33-PD	10/16/18	05/30/19
	WBL32-T10	03/22/19	08/21/19	EBL-33	EBL33-PU	10/13/18	05/30/19
	WBL32-T11	03/23/19	08/21/19		EBL33-T1	11/21/18	05/31/19
	WBL33-PD	04/16/19	08/02/19		EBL33-T2	11/26/18	05/31/19
WBL-33	WBL33-PU	04/15/19	08/02/19		EBL33-T3	11/27/18	06/01/19
	WBL33-T1	03/12/19	07/31/19		EBL33-D4	11/28/18	06/01/19
	WBL33-T2	03/13/19	07/31/19		EBL33-T5	11/29/18	06/01/19
	WBL33-T3	03/14/19	07/31/19		EBL33-T6	11/30/18	06/01/19
	WBL33-D4	03/15/19	07/31/19		EBL33-T7	12/04/18	06/01/19
	WBL33-T5	03/16/19	07/31/19		EBL33-D8	12/05/18	06/02/19
	WBL33-T6	03/18/19	07/31/19		EBL33-T9	12/06/18	06/02/19
	WBL33-T7	03/19/19	08/01/19		EBL33-T10	12/07/18	06/02/19
	WBL33-T8	03/20/19	08/01/19		EBL34-ED	02/21/19	06/02/19
	WBL33-D9	03/21/19	08/01/19	EBL-34	EBL34-EU	04/13/19	06/26/19
	WBL33-T10	03/22/19	08/01/19		EBL34-T1	11/20/18	06/22/19
	WBL33-T11	03/23/19	08/01/19		EBL34-T2	11/21/18	06/22/19
	WBL33-T12	03/25/19	08/01/19		EBL34-D3	11/26/18	06/22/19
	WBL34-PD	04/23/19	08/03/19		EBL34-T4	11/27/18	06/22/19
	WBL34-PU	04/18/19	08/03/19		EBL34-T5	11/28/18	06/23/19

WBL-34	WBL34-T1	04/10/19	08/05/19		EBL34-T6	11/29/18	06/23/19
	WBL34-T2	04/11/19	08/05/19		EBL34-T7	11/30/18	06/23/19
	WBL34-T3	04/12/19	08/05/19		EBL34-T8	12/04/18	06/23/19
	WBL34-D4	04/15/19	08/05/19		EBL34-D9	12/05/18	06/23/19
	WBL34-T5	04/16/19	08/05/19		EBL34-T10	12/06/18	06/23/19
	WBL34-T6	04/18/19	08/05/19		EBL34-T11	12/07/18	06/23/19
	WBL34-T7	04/22/19	08/05/19		EBL34-T12	12/10/18	06/23/19
	WBL34-D8	04/23/19	08/05/19		EBL35-PD	06/08/19	06/24/19
	WBL34-T9	04/24/19	08/05/19	EBL-35	EBL35-PU	06/07/19	06/26/19
	WBL34-T10	04/25/19	08/05/19		EBL35-T1	02/15/19	07/11/19
	WBL34-T11	04/26/19	08/06/19		EBL35-T2	02/16/19	07/11/19
	WBL35-PD	05/20/19	08/06/19		EBL35-T3	02/18/19	07/11/19
WBL-35	WBL35-PU	05/18/19	08/07/19		EBL35-D4	02/20/19	07/11/19
	WBL35-T1	05/01/19	09/28/19		EBL35-T5	02/21/19	07/12/19
	WBL35-T2	05/02/19	09/28/19		EBL35-T6	02/22/19	07/12/19
	WBL35-T3	05/03/19	09/28/19		EBL35-T7	02/23/19	07/20/19
	WBL35-D4	05/06/19	09/28/19		EBL35-T8	02/25/19	07/20/19
	WBL35-T5	05/07/19	09/28/19		EBL35-T9	02/26/19	07/20/19
	WBL35-T6	05/08/19	09/28/19		EBL35-D10	02/27/19	07/21/19
	WBL35-T7	05/10/19	09/28/19		EBL35-T11	02/28/19	07/21/19
	WBL35-T8	05/13/19	09/29/19		EBL35-T12	03/01/19	07/21/19
	WBL35-T9	05/14/19	09/29/19		EBL36-ED	04/24/19	07/23/19
	WBL35-D10	05/15/19	09/29/19	EBL-36	EBL36-EU	05/18/19	09/04/19
	WBL35-T11	05/16/19	09/29/19		EBL36-T1	03/29/19	09/04/19
	WBL35-T12	05/17/19	09/29/19		EBL36-T2	03/30/19	09/04/19
	WBL36-ED	06/04/19	09/29/19		EBL36-D3	04/01/19	09/04/19
WBL-36	WBL36-EU	07/10/19	10/14/19		EBL36-T4	04/02/19	09/04/19
	WBL36-T1	07/18/19	10/14/19		EBL36-T5	04/03/19	09/04/19
	WBL36-T2	07/19/19	10/14/19		EBL36-T6	04/04/19	09/04/19
	WBL36-D3	07/20/19	10/14/19		EBL36-T7	04/05/19	09/04/19
	WBL36-T4	07/22/19	10/14/19		EBL36-T8	04/06/19	09/06/19
	WBL36-T5	07/23/19	10/14/19		EBL36-D9	04/08/19	09/06/19
	WBL36-T6	07/24/19	10/14/19		EBL36-T10	04/09/19	09/06/19
	WBL36-T7	07/25/19	10/14/19		EBL36-T11	04/10/19	09/06/19
	WBL36-T8	07/26/19	10/13/19		EBL36-T12	04/11/19	09/06/19
	WBL36-D9	07/29/19	10/13/19		EBL37-PD	06/29/19	09/06/19
	WBL36-T10	07/30/19	10/13/19	EBL-37	EBL37-PU	06/27/19	09/06/19
	WBL36-T11	07/31/19	10/13/19		EBL37-T1	06/26/19	10/02/19
	WBL36-T12	08/01/19	10/13/19		EBL37-T2	06/27/19	10/02/19

	WBL37-PD	08/06/19	09/12/19		EBL37-T3	06/28/19	10/02/19
WBL-37	WBL37-PU	08/03/19	09/12/19		EBL37-D4	06/29/19	10/02/19
	WBL37-T1	07/20/19	09/12/19		EBL37-T5	07/02/19	10/01/19
	WBL37-T2	07/22/19	09/12/19		EBL37-T6	07/03/19	10/01/19
	WBL37-T3	07/23/19	09/12/19		EBL37-T7	07/08/19	10/01/19
	WBL37-D4	07/24/19	09/12/19		EBL37-T8	07/09/19	10/01/19
	WBL37-T5	07/25/19	09/11/19		EBL37-D9	07/10/19	10/01/19
	WBL37-T6	07/26/19	09/11/19		EBL37-T10	07/11/19	10/01/19
	WBL37-T7	07/29/19	09/10/19		EBL37-T11	07/12/19	10/01/19
	WBL37-D8	07/30/19	09/10/19		EBL37-T12	07/13/19	10/01/19
	WBL37-T9	07/31/19	09/10/19		EBL38-PD	01/22/19	06/08/19
	WBL37-T10	08/01/19	09/10/19	EBL-38	EBL38-PU	01/18/19	06/08/19
	WBL37-T11	08/02/19	09/10/19		EBL38-T1	01/22/19	06/06/19
	WBL38-PD	04/13/19	07/24/19		EBL38-T2	01/24/19	06/06/19
WBL-38	WBL38-PU	04/10/19	07/24/19		EBL38-T3	01/25/19	06/02/19
	WBL38-T1	02/28/19	07/19/19		EBL38-D4	01/26/19	06/02/19
	WBL38-T2	03/01/19	07/19/19		EBL38-T5	01/30/19	06/02/19
	WBL38-T3	03/02/19	07/19/19		EBL38-T6	01/31/19	06/02/19
	WBL38-D4	03/04/19	07/19/19		EBL38-T7	02/01/19	06/02/19
	WBL38-T5	03/05/19	07/19/19		EBL38-D8	02/02/19	06/02/19
	WBL38-T6	03/06/19	07/19/19		EBL38-T9	02/04/19	06/02/19
	WBL38-T7	03/07/19	07/19/19		EBL38-T10	02/05/19	06/02/19
	WBL38-D8	03/08/19	07/21/19		EBL38-T11	02/06/19	06/02/19
	WBL38-T9	03/09/19	07/21/19		EBL39-PD	01/24/19	06/08/19
	WBL38-T10	03/11/19	07/21/19	EBL-39	EBL39-PU	01/22/19	06/08/19
	WBL39-ED	04/16/19	07/21/19		EBL39-T1	04/27/19	09/11/19
WBL-39	WBL39-EU	04/18/19	08/28/19		EBL39-T2	04/29/19	09/11/19
	WBL39-T1	06/28/19	10/13/19		EBL39-T3	04/30/19	09/11/19
	WBL39-T2	06/29/19	10/13/19		EBL39-D4	05/01/19	09/11/19
	WBL39-D3	07/01/19	10/13/19		EBL39-T5	05/02/19	09/11/19
	WBL39-T4	07/02/19	10/13/19		EBL39-T6	05/03/19	09/11/19
	WBL39-T5	07/08/19	10/14/19		EBL39-T7	05/06/19	09/10/19
	WBL39-T6	07/09/19	10/14/19		EBL39-T8	05/07/19	09/10/19
	WBL39-T7	07/10/19	10/14/19		EBL39-T9	05/08/19	09/10/19
	WBL39-T8	07/11/19	10/14/19		EBL39-D10	05/10/19	09/10/19
	WBL39-D9	07/12/19	10/14/19		EBL39-T11	05/13/19	09/09/19
	WBL39-T10	07/13/19	10/14/19		EBL39-T12	05/14/19	09/09/19
	WBL39-T11	07/15/19	10/14/19		EBL40-ED	03/01/19	04/01/19
	WBL39-T12	07/16/19	10/14/19		EBL40-EU	03/06/19	04/01/19

	WBL40-PD	07/22/19	10/09/19		EBL40-T1	05/15/19	08/15/19
WBL-40	WBL40-PU	07/20/19	10/09/19		EBL40-T2	05/16/19	09/04/19
	WBL40-T1	07/03/19	10/08/19		EBL40-D3	05/17/19	09/04/19
	WBL40-T2	07/08/19	10/08/19		EBL40-T4	05/20/19	09/04/19
	WBL40-T3	07/09/19	10/08/19		EBL40-T5	05/21/19	09/04/19
	WBL40-D4	07/10/19	10/08/19	EBL-40	EBL40-T6	05/22/19	09/04/19
	WBL40-T5	07/11/19	10/08/19		EBL40-T7	05/23/19	09/04/19
	WBL40-T6	07/12/19	10/08/19		EBL40-T8	05/24/19	09/04/19
	WBL40-T7	07/13/19	10/08/19		EBL40-D9	05/28/19	09/05/19
	WBL40-T8	07/15/19	10/07/19		EBL40-T10	05/29/19	09/05/19
	WBL40-D9	07/16/19	10/07/19		EBL40-T11	05/30/19	09/05/19
	WBL40-T10	07/17/19	10/07/19		EBL40-T12	05/31/19	09/05/19
	WBL40-T11	07/18/19	10/07/19		EBL41-PD	11/17/18	06/16/19
	WBL40-T12	07/19/19	10/07/19		EBL41-PU	11/14/18	06/16/19
	WBL41-PD	04/11/19	09/20/19		EBL41-T1	11/03/18	06/15/19
WBL-41	WBL41-PU	04/09/19	09/19/19		EBL41-T2	11/05/18	06/15/19
	WBL41-T1	01/08/19	09/19/19		EBL41-T3	11/06/18	06/15/19
	WBL41-T2	01/10/19	09/19/19		EBL41-D4	11/08/18	06/15/19
	WBL41-T3	01/12/19	09/19/19		EBL41-T5	11/09/18	06/13/19
	WBL41-D4	01/16/19	09/19/19	EBL-41	EBL41-T6	11/13/18	06/11/19
	WBL41-T5	01/17/19	08/28/19		EBL41-T7	11/14/18	06/11/19
	WBL41-T6	01/18/19	08/23/19		EBL41-T8	11/15/18	06/11/19
	WBL41-T7	01/22/19	08/23/19		EBL41-D9	11/16/18	06/11/19
	WBL41-T8	01/24/19	08/23/19		EBL41-T10	11/17/18	06/11/19
	WBL41-T9	01/25/19	08/23/19		EBL41-T11	11/19/18	06/11/19
	WBL41-D10	01/26/19	08/23/19		EBL41-T12	11/20/18	06/11/19
	WBL41-T11	01/28/19	08/23/19		EBL42-PD	11/09/18	06/17/19
	WBL41-T12	01/31/19	08/22/19		EBL42-PU	11/06/18	06/17/19
	WBL42-ED	03/15/19	08/28/19		EBL42-T1	06/19/19	10/04/19
WBL-42	WBL42-EU	03/25/19	09/26/19		EBL42-T2	06/20/19	10/05/19
	WBL42-T1	02/01/19	09/27/19		EBL42-T3	06/21/19	10/05/19
	WBL42-D2	02/05/19	09/27/19		EBL42-D4	06/25/19	10/05/19
	WBL42-T3	02/06/19	09/27/19	EBL-42	EBL42-T5	06/26/19	10/05/19
	WBL42-D4	02/07/19	09/27/19		EBL42-T6	06/27/19	10/05/19
	WBL42-T5	02/09/19	09/27/19		EBL42-T7	06/28/19	10/05/19
	WBL43-ED	03/27/19	09/27/19		EBL42-D8	06/29/19	10/05/19
WBR-1	WBR1-EU	12/17/18	06/17/19		EBL42-T9	07/01/19	10/05/19
	WBR1-T1	08/15/18	06/16/19		EBL42-T10	07/02/19	10/05/19
	WBR1-T2	08/16/18	06/16/19		EBL43-ED	06/29/19	10/06/19

	WBR1-D3	08/18/18	06/15/19		EBR1-EU	05/07/19	06/05/19
	WBR1-T4	08/21/18	06/15/19		EBR1-T1	09/24/18	06/05/19
	WBR1-T5	08/22/18	06/15/19		EBR1-T2	09/25/18	06/05/19
	WBR1-T6	08/24/18	06/15/19		EBR1-D3	09/27/18	06/05/19
	WBR1-T7	08/27/18	06/15/19		EBR1-T4	09/28/18	06/04/19
	WBR1-D8	08/29/18	06/15/19		EBR1-T5	10/01/18	06/04/19
	WBR1-T9	08/30/18	06/15/19	EBR-1	EBR1-T6	10/02/18	06/04/19
	WBR1-T10	08/31/18	06/15/19		EBR1-T7	10/03/18	06/04/19
	WBR1-T11	09/05/18	06/14/19		EBR1-D8	10/05/18	06/04/19
	WBR2-PD	09/06/18	06/17/19		EBR1-T9	10/08/18	06/04/19
	WBR2-PU	08/29/18	06/17/19		EBR1-T10	10/09/18	06/04/19
	WBR2-T1	07/30/18	06/22/19		EBR1-T11	10/11/18	06/04/19
	WBR2-T2	08/01/18	06/22/19		EBR2-PD	05/16/19	05/21/19
	WBR2-T3	08/03/18	06/21/19		EBR2-PU	05/14/19	05/21/19
	WBR2-D4	08/07/18	06/21/19		EBR2-T1	10/01/18	03/28/19
	WBR2-T5	08/10/18	06/21/19		EBR2-T2	10/02/18	03/28/19
WBR-2	WBR2-T6	08/13/18	06/21/19		EBR2-T3	10/04/18	03/28/19
	WBR2-T7	08/15/18	06/21/19		EBR2-D4	10/06/18	03/27/19
	WBR2-D8	08/17/18	06/21/19		EBR2-T5	10/09/18	03/27/19
	WBR2-T9	08/20/18	06/21/19	EBR-2	EBR2-T6	10/11/18	03/27/19
	WBR2-T10	08/22/18	06/21/19		EBR2-T7	10/12/18	03/27/19
	WBR2-T11	08/24/18	06/21/19		EBR2-D8	10/16/18	03/27/19
	WBR3-PD	09/12/18	06/22/19		EBR2-T9	10/17/18	03/26/19
	WBR3-PU	09/07/18	06/22/19		EBR2-T10	10/18/18	03/26/19
	WBR3-T1	08/24/18	06/26/19		EBR2-T11	10/19/18	03/26/19
	WBR3-T2	08/25/18	06/19/19		EBR3-PD	05/07/19	05/14/19
	WBR3-T3	08/27/18	06/19/19		EBR3-PU	05/04/19	05/14/19
	WBR3-D4	08/29/18	06/19/19		EBR3-T1	10/04/18	03/23/19
	WBR3-T5	08/30/18	06/19/19		EBR3-T2	10/05/18	03/22/19
WBR-3	WBR3-T6	08/31/18	06/19/19		EBR3-T3	10/06/18	03/22/19
	WBR3-T7	09/04/18	06/18/19		EBR3-D4	10/08/18	03/22/19
	WBR3-D8	09/06/18	06/18/19		EBR3-T5	10/09/18	03/22/19
	WBR3-T9	09/07/18	06/18/19	EBR-3	EBR3-T6	10/11/18	03/22/19
	WBR3-T10	09/11/18	06/18/19		EBR3-T7	10/12/18	03/21/19
	WBR3-T11	09/12/18	06/18/19		EBR3-T8	10/13/18	03/21/19
	WBR4-PD	09/14/18	06/20/19		EBR3-D9	10/16/18	03/21/19
WBR-4	WBR4-PU	09/11/18	06/20/19		EBR3-T10	10/17/18	03/21/19
	WBR4-T1	08/21/18	07/26/19		EBR3-T11	10/18/18	03/20/19
	WBR4-T2	08/23/18	07/26/19		EBR4-ED	01/16/19	03/23/19

	WBR4-T3	08/25/18	07/26/19		EBR4-EU	04/06/19	07/10/19
	WBR4-D4	08/28/18	07/26/19		EBR4-T1	10/06/18	07/09/19
	WBR4-T5	08/30/18	07/26/19		EBR4-T2	10/08/18	07/09/19
	WBR4-T6	09/08/18	07/26/19		EBR4-D3	10/10/18	07/09/19
	WBR4-T7	09/11/18	07/26/19		EBR4-T4	10/11/18	07/09/19
	WBR4-T8	09/14/18	07/27/19		EBR4-T5	10/12/18	07/09/19
	WBR4-D9	09/19/18	07/27/19	EBR-4	EBR4-T6	10/13/18	07/09/19
	WBR4-T10	09/21/18	07/27/19		EBR4-T7	10/15/18	07/09/19
	WBR4-T11	09/24/18	07/27/19		EBR4-D8	10/16/18	07/09/19
	WBR5-ED	01/07/19	07/27/19		EBR4-T9	10/17/18	07/09/19
	WBR5-EU	12/19/18	08/04/19		EBR4-T10	10/18/18	07/10/19
	WBR5-T1	08/15/18	07/30/19		EBR4-T11	10/19/18	07/10/19
	WBR5-T2	08/17/18	07/30/19		EBR5-PD	06/17/19	07/10/19
	WBR5-D3	08/21/18	07/30/19		EBR5-PU	06/14/19	07/11/19
	WBR5-T4	08/23/18	07/30/19		EBR5-T1	10/12/18	07/17/19
WBR-5	WBR5-T5	08/24/18	07/30/19		EBR5-T2	10/13/18	07/13/19
	WBR5-T6	08/27/18	07/29/19		EBR5-T3	10/16/18	07/13/19
	WBR5-D7	08/28/18	07/29/19		EBR5-D4	10/17/18	07/12/19
	WBR5-T8	08/30/18	07/29/19	EBR-5	EBR5-T5	10/18/18	07/12/19
	WBR5-T9	08/31/18	07/29/19		EBR5-T6	10/19/18	07/12/19
	WBR5-T10	09/04/18	07/29/19		EBR5-D7	10/22/18	07/12/19
	WBR6-PD	09/20/18	07/30/19		EBR5-T8	10/24/18	07/12/19
	WBR6-PU	09/15/18	07/31/19		EBR5-T9	10/25/18	07/12/19
	WBR6-T1	08/14/18	08/07/19		EBR5-T10	10/26/18	07/12/19
	WBR6-T2	08/15/18	08/02/19		EBR6-PD	01/16/19	07/13/19
	WBR6-T3	08/16/18	08/02/19		EBR6-PU	06/19/19	07/13/19
	WBR6-D4	08/18/18	08/02/19		EBR6-T1	12/07/18	07/20/19
WBR-6	WBR6-T5	08/20/18	08/02/19		EBR6-T2	12/10/18	07/20/19
	WBR6-T6	08/21/18	08/01/19		EBR6-T3	12/12/18	07/19/19
	WBR6-D7	08/23/18	08/01/19		EBR6-D4	12/13/18	07/18/19
	WBR6-T8	08/25/18	08/01/19		EBR6-T5	12/14/18	07/18/19
	WBR6-T9	08/27/18	08/01/19	EBR-6	EBR6-T6	12/17/18	07/18/19
	WBR6-T10	08/27/18	08/01/19		EBR6-T7	12/18/18	07/18/19
	WBR7-PD	02/15/19	08/02/19		EBR6-T8	12/19/18	07/18/19
	WBR7-PU	02/13/19	08/06/19		EBR6-D9	12/20/18	07/18/19
	WBR7-T1	08/30/18	08/30/19		EBR6-T10	12/22/18	07/18/19
WBR-7	WBR7-T2	09/04/18	08/30/19		EBR6-T11	01/01/19	07/18/19
	WBR7-T3	09/06/18	08/30/19		EBR7-ED	03/26/19	07/19/19
	WBR7-D4	09/10/18	08/30/19		EBR7-EU	05/17/19	08/14/19

	WBR7-T5	09/12/18	08/30/19		EBR7-T1	03/16/19	08/13/19
	WBR7-T6	09/13/18	08/30/19		EBR7-T2	03/18/19	08/13/19
	WBR7-T7	09/15/18	08/30/19		EBR7-D3	03/19/19	08/13/19
	WBR7-D8	09/18/18	08/30/19		EBR7-T4	03/20/19	08/13/19
	WBR7-T9	09/19/18	08/30/19		EBR7-T5	03/21/19	08/13/19
	WBR7-T10	09/20/18	08/30/19	EBR-7	EBR7-T6	03/22/19	08/13/19
	WBR7-T11	09/21/18	08/30/19		EBR7-T7	03/23/19	08/13/19
	WBR8-PD	06/07/19	08/30/19		EBR7-D8	03/25/19	08/13/19
	WBR8-PU	06/04/19	09/04/19		EBR7-T9	03/26/19	08/13/19
	WBR8-T1	08/29/18	09/07/19		EBR7-T10	03/27/19	08/13/19
	WBR8-T2	08/30/18	09/06/19		EBR7-T11	03/28/19	08/13/19
	WBR8-T3	08/31/18	09/05/19		EBR8-PD	04/27/19	08/14/19
	WBR8-D4	09/05/18	09/05/19		EBR8-PU	04/26/19	08/15/19
	WBR8-T5	09/06/18	09/05/19		EBR8-T1	03/29/19	08/20/19
WBR-8	WBR8-T6	09/07/18	09/05/19		EBR8-T2	03/30/19	08/17/19
	WBR8-T7	09/08/18	09/05/19		EBR8-T3	04/01/19	08/17/19
	WBR8-T8	09/10/18	09/05/19		EBR8-D4	04/02/19	08/16/19
	WBR8-T9	09/12/18	09/05/19		EBR8-T5	04/03/19	08/16/19
	WBR8-D10	09/14/18	09/04/19	EBR-8	EBR8-T6	04/04/19	08/16/19
	WBR8-T11	09/15/18	09/04/19		EBR8-T7	04/05/19	08/16/19
	WBR8-T12	09/17/18	09/04/19		EBR8-T8	04/08/19	08/16/19
	WBR9-ED	06/05/19	09/06/19		EBR8-D9	04/09/19	08/16/19
	WBR9-EU	10/30/18	05/28/19		EBR8-T10	04/10/19	08/16/19
	WBR9-T1	08/28/18	05/24/19		EBR8-T11	04/11/19	08/16/19
	WBR9-T2	08/29/18	05/24/19		EBR8-T12	04/12/19	08/16/19
	WBR9-D3	08/31/18	05/24/19		EBR9-PD	12/19/18	04/04/19
	WBR9-T4	09/05/18	05/24/19		EBR9-PU	12/18/18	04/04/19
	WBR9-T5	09/06/18	05/24/19		EBR9-T1	09/27/18	04/01/19
WBR-9	WBR9-T6	09/07/18	05/25/19		EBR9-T2	09/28/18	04/01/19
	WBR9-T7	09/10/18	05/25/19		EBR9-T3	10/01/18	04/01/19
	WBR9-T8	09/11/18	05/25/19		EBR9-D4	10/04/18	04/02/19
	WBR9-D9	09/13/18	05/25/19		EBR9-T5	10/06/18	04/02/19
	WBR9-T10	09/14/18	05/25/19	EBR-9	EBR9-T6	10/08/18	04/02/19
	WBR9-T11	09/17/18	05/25/19		EBR9-T7	10/09/18	04/02/19
	WBR9-T12	09/18/18	05/25/19		EBR9-T8	10/11/18	04/02/19
	WBR10-PD	08/23/18	06/01/19		EBR9-T9	10/13/18	04/03/19
	WBR10-PU	08/17/18	06/01/19		EBR9-D10	10/16/18	04/03/19
WBR-10	WBR10-T1	04/09/18	06/10/19		EBR9-T11	10/18/18	04/03/19
	WBR10-T2	04/21/18	06/03/19		EBR9-T12	10/19/18	04/03/19

	WBR10-T3	04/30/18	06/03/19		EBR10-ED	01/25/19	04/03/19
	WBR10-D4	05/12/18	06/03/19		EBR10-EU	01/04/19	05/05/19
	WBR10-T5	05/16/18	06/03/19		EBR10-T1	09/19/18	05/05/19
	WBR10-T6	05/22/18	06/03/19		EBR10-T2	09/21/18	05/04/19
	WBR10-T7	05/24/18	06/03/19		EBR10-D3	04/18/19	04/27/19
	WBR10-T8	05/31/18	06/03/19		EBR10-T4	09/27/18	04/27/19
	WBR10-D9	06/05/18	06/03/19		EBR10-T5	09/28/18	04/10/19
	WBR10-T10	06/12/18	06/03/19	EBR-10	EBR10-T6	10/01/18	04/10/19
	WBR10-T11	06/14/18	06/03/19		EBR10-T7	10/02/18	04/10/19
	WBR10-T12	06/16/18	06/02/19		EBR10-T8	10/04/18	04/10/19
	WBR11-PD	08/24/18	06/03/19		EBR10-D9	10/06/18	04/10/19
	WBR11-PU	08/21/18	06/08/19		EBR10-T10	10/09/18	04/10/19
	WBR11-T1	02/21/18	06/15/19		EBR10-T11	10/11/18	04/10/19
	WBR11-T2	03/02/18	06/07/19		EBR10-T12	10/13/18	04/08/19
	WBR11-T3	03/07/18	06/07/19		EBR11-PD	12/13/18	04/26/19
	WBR11-D4	04/19/18	06/07/19		EBR11-PU	12/11/18	04/26/19
	WBR11-T5	04/27/18	06/07/19		EBR11-T1	11/15/18	05/13/19
WBR-11	WBR11-T6	05/03/18	06/07/19		EBR11-T2	11/17/18	04/16/19
	WBR11-T7	05/07/18	06/07/19		EBR11-T3	11/19/18	04/16/19
	WBR11-T8	05/09/18	06/07/19		EBR11-D4	11/20/18	04/16/19
	WBR11-D9	05/21/18	06/07/19		EBR11-T5	11/21/18	04/16/19
	WBR11-T10	05/23/18	06/07/19	EBR-11	EBR11-T6	11/26/18	04/16/19
	WBR11-T11	05/30/18	06/07/19		EBR11-T7	11/27/18	04/16/19
	WBR11-T12	05/31/18	06/07/19		EBR11-T8	11/28/18	04/15/19
	WBR12-PD	08/31/18	06/08/19		EBR11-D9	11/29/18	04/15/19
	WBR12-PU	08/28/18	06/08/19		EBR11-T10	12/04/18	04/15/19
	WBR12-T1	04/04/18	07/24/19		EBR11-T11	12/05/18	04/15/19
	WBR12-T2	04/17/18	07/24/19		EBR11-T12	12/06/18	04/15/19
	WBR12-T3	04/24/18	07/24/19		EBR12-PD	10/23/18	04/18/19
	WBR12-D4	05/05/18	07/24/19		EBR12-PU	10/19/18	04/19/19
	WBR12-T5	05/14/18	07/24/19		EBR12-T1	03/21/18	06/26/19
WBR-12	WBR12-T6	05/21/18	07/24/19		EBR12-T2	11/03/18	06/26/19
	WBR12-T7	06/20/18	07/24/19		EBR12-T3	11/05/18	06/26/19
	WBR12-T8	06/25/18	07/24/19	EBR-12	EBR12-D4	11/06/18	06/27/19
	WBR12-T9	06/29/18	07/24/19		EBR12-T5	11/08/18	06/27/19
	WBR12-D10	07/09/18	07/24/19		EBR12-T6	11/09/18	06/27/19
	WBR12-T11	07/13/18	07/24/19		EBR12-T7	11/13/18	06/27/19
	WBR12-T12	07/17/18	07/24/19		EBR12-T8	11/15/18	06/27/19
	WBR13-ED	12/11/18	07/25/19		EBR12-T9	11/16/18	06/27/19

WBR-13	WBR13-EU	11/07/18	08/05/19		EBR12-D10	11/19/18	06/27/19
	WBR13-T1	06/05/18	07/27/19		EBR12-T11	11/20/18	06/27/19
	WBR13-T2	06/06/18	07/27/19		EBR12-T12	11/26/18	06/27/19
	WBR13-D3	06/11/18	07/27/19		EBR13-ED	04/27/19	06/28/19
	WBR13-T4	06/13/18	07/27/19	EBR-13	EBR13-EU	05/03/19	07/03/19
	WBR13-T5	06/15/18	07/27/19		EBR13-T1	10/22/18	07/02/19
	WBR13-T6	06/18/18	07/27/19		EBR13-T2	10/24/18	07/02/19
	WBR13-T7	06/19/18	07/27/19		EBR13-D3	10/26/18	07/01/19
	WBR13-T8	06/22/18	07/27/19		EBR13-T4	10/29/18	07/01/19
	WBR13-D9	06/29/18	07/27/19		EBR13-T5	10/30/18	07/01/19
	WBR13-T10	07/09/18	07/27/19		EBR13-T6	10/31/18	07/01/19
	WBR13-T11	07/11/18	07/27/19		EBR13-T7	11/01/18	07/01/19
	WBR13-T12	07/13/18	07/26/19		EBR13-T8	11/02/18	07/01/19
	WBR14-PD	05/11/19	07/29/19		EBR13-D9	11/05/18	07/01/19
WBR-14	WBR14-PU	05/03/19	08/06/19		EBR13-T10	11/06/18	07/01/19
	WBR14-T1	06/13/18	08/14/19		EBR13-T11	11/08/18	07/01/19
	WBR14-T2	06/14/18	08/06/19		EBR13-T12	11/09/18	07/01/19
	WBR14-T3	06/15/18	08/06/19		EBR14-PD	03/27/19	07/02/19
	WBR14-D4	06/19/18	08/06/19	EBR-14	EBR14-PU	03/25/19	07/09/19
	WBR14-T5	06/21/18	08/06/19		EBR14-T1	10/22/18	07/13/19
	WBR14-T6	06/22/18	08/06/19		EBR14-T2	10/23/18	07/10/19
	WBR14-T7	06/26/18	08/06/19		EBR14-T3	10/24/18	07/10/19
	WBR14-T8	06/29/18	08/06/19		EBR14-D4	10/26/18	07/10/19
	WBR14-D9	07/09/18	08/06/19		EBR14-T5	10/29/18	07/10/19
	WBR14-T10	07/11/18	08/06/19		EBR14-T6	10/30/18	07/10/19
	WBR14-T11	07/13/18	08/06/19		EBR14-T7	10/31/18	07/10/19
	WBR14-T12	07/16/18	08/06/19		EBR14-T8	11/01/18	07/09/19
	WBR15-PD	06/26/19	08/06/19		EBR14-D9	11/02/18	07/09/19
WBR-15	WBR15-PU	06/25/19	08/08/19		EBR14-T10	11/03/18	07/09/19
	WBR15-T1	07/20/18	09/09/19		EBR14-T11	11/05/18	07/09/19
	WBR15-T2	07/24/18	09/10/19		EBR14-T12	11/06/18	07/09/19
	WBR15-T3	07/26/18	09/10/19		EBR15-PD	03/28/19	07/10/19
	WBR15-D4	07/30/18	09/10/19	EBR-15	EBR15-PU	03/26/19	07/11/19
	WBR15-T5	08/02/18	09/10/19		EBR15-T1	04/12/19	08/14/19
	WBR15-T6	08/06/18	09/10/19		EBR15-T2	04/13/19	08/14/19
	WBR15-T7	08/10/18	09/10/19		EBR15-T3	04/15/19	08/14/19
	WBR15-T8	08/14/18	09/10/19		EBR15-D4	04/16/19	08/14/19
	WBR15-D9	08/17/18	09/10/19		EBR15-T5	04/17/19	08/14/19
	WBR15-T10	08/21/18	09/10/19		EBR15-T6	04/22/19	08/15/19

	WBR15-T11	08/24/18	09/11/19		EBR15-T7	04/23/19	08/15/19
	WBR15-T12	08/28/18	09/11/19		EBR15-T8	04/24/19	08/15/19
	WBR16-PD	07/02/19	09/11/19		EBR15-D9	04/26/19	08/15/19
WBR-16	WBR16-PU	07/01/19	09/12/19		EBR15-T10	04/27/19	08/15/19
	WBR16-T1	06/20/18	09/16/19		EBR15-T11	04/29/19	08/15/19
	WBR16-T2	06/22/18	09/14/19		EBR15-T12	04/30/19	08/15/19
	WBR16-T3	06/26/18	09/14/19		EBR16-PD	05/29/19	08/15/19
	WBR16-D4	06/30/18	09/14/19	EBR-16	EBR16-PU	05/24/19	08/22/19
	WBR16-T5	07/09/18	09/14/19		EBR16-T1	04/25/19	08/29/19
	WBR16-T6	07/11/18	09/14/19		EBR16-T2	04/26/19	08/23/19
	WBR16-T7	07/12/18	09/14/19		EBR16-T3	04/27/19	08/23/19
	WBR16-T8	07/14/18	09/13/19		EBR16-D4	04/29/19	08/22/19
	WBR16-T9	07/17/18	09/13/19		EBR16-T5	04/30/19	08/22/19
	WBR16-D10	07/20/18	09/13/19		EBR16-T6	05/01/19	08/22/19
	WBR16-T11	07/23/18	09/13/19		EBR16-T7	05/02/19	08/22/19
	WBR16-T12	07/24/18	09/13/19		EBR16-T8	05/03/19	08/22/19
	WBR17-ED	06/15/19	09/14/19		EBR16-T9	05/06/19	08/22/19
WBR-17	WBR17-EU	10/02/18	05/21/19		EBR16-D10	05/07/19	08/22/19
	WBR17-T1	08/31/18	05/20/19		EBR16-T11	05/08/19	08/22/19
	WBR17-T2	09/05/18	05/20/19		EBR16-T12	05/09/19	08/22/19
	WBR17-D3	09/10/18	05/20/19		EBR17-ED	05/24/19	08/23/19
	WBR17-T4	09/12/18	05/21/19	EBR-17	EBR17-EU	01/02/19	03/12/19
	WBR17-T5	09/13/18	05/21/19		EBR17-T1	09/24/18	03/11/19
	WBR17-T6	09/17/18	05/21/19		EBR17-T2	09/25/18	03/11/19
	WBR17-T7	09/18/18	05/21/19		EBR17-D3	09/27/18	03/11/19
	WBR17-T8	09/20/18	05/21/19		EBR17-T4	10/01/18	03/12/19
	WBR17-D9	09/22/18	05/21/19		EBR17-T5	10/02/18	03/12/19
	WBR17-T10	09/25/18	05/21/19		EBR17-T6	10/03/18	03/13/19
	WBR17-T11	09/27/18	05/21/19		EBR17-T7	10/04/18	03/13/19
	WBR17-T12	09/29/18	05/21/19		EBR17-T8	10/05/18	03/13/19
	WBR18-PD	10/20/18	05/25/19		EBR17-D9	10/08/18	03/13/19
WBR-18	WBR18-PU	10/18/18	05/25/19		EBR17-T10	10/09/18	03/13/19
	WBR18-T1	12/07/18	06/01/19		EBR17-T11	10/11/18	03/13/19
	WBR18-T2	12/10/18	05/28/19		EBR17-T12	10/12/18	03/14/19
	WBR18-T3	12/12/18	05/28/19		EBR18-PD	09/21/18	03/14/19
	WBR18-D4	12/13/18	05/28/19	EBR-18	EBR18-PU	09/18/18	03/15/19
	WBR18-T5	12/14/18	05/28/19		EBR18-T1	09/06/18	03/23/19
	WBR18-T6	12/15/18	05/28/19		EBR18-T2	09/11/18	03/21/19
	WBR18-T7	12/17/18	05/28/19		EBR18-T3	09/12/18	03/21/19

	WBR18-T8	12/18/18	05/28/19		EBR18-D4	09/14/18	03/20/19
	WBR18-D9	12/19/18	05/26/19		EBR18-T5	09/17/18	03/20/19
	WBR18-T10	12/20/18	05/26/19		EBR18-T6	09/18/18	03/20/19
	WBR18-T11	12/21/18	05/26/19		EBR18-T7	09/20/18	03/20/19
	WBR18-T12	01/01/19	05/26/19		EBR18-T8	09/21/18	03/19/19
	WBR19-PD	01/01/19	06/02/19		EBR18-D9	09/25/18	03/19/19
	WBR19-PU	12/19/18	06/03/19		EBR18-T10	09/27/18	03/18/19
	WBR19-T1	12/15/18	06/10/19		EBR18-T11	09/28/18	03/18/19
	WBR19-T2	12/17/18	06/02/19		EBR18-T12	10/01/18	03/18/19
	WBR19-T3	12/18/18	06/02/19		EBR19-PD	09/29/18	03/19/19
	WBR19-D4	12/19/18	06/02/19		EBR19-PU	09/24/18	03/19/19
	WBR19-T5	12/20/18	06/01/19		EBR19-T1	11/05/18	03/30/19
WBR-19	WBR19-T6	12/22/18	06/01/19		EBR19-T2	11/06/18	03/30/19
	WBR19-T7	12/31/18	06/01/19		EBR19-T3	11/08/18	03/30/19
	WBR19-T8	01/01/19	06/01/19		EBR19-D4	11/09/18	03/30/19
	WBR19-D9	01/03/19	06/01/19		EBR19-T5	11/10/18	03/30/19
	WBR19-T10	01/04/19	06/01/19	EBR-19	EBR19-T6	11/13/18	03/30/19
	WBR19-T11	01/07/19	06/01/19		EBR19-T7	11/14/18	03/30/19
	WBR19-T12	01/08/19	06/01/19		EBR19-T8	11/16/18	03/30/19
	WBR20-PD	12/07/18	06/09/19		EBR19-D9	11/19/18	03/29/19
	WBR20-PU	05/24/19	06/09/19		EBR19-T10	11/20/18	03/29/19
	WBR20-T1	11/27/18	06/13/19		EBR19-T11	11/21/18	03/29/19
	WBR20-T2	11/28/18	06/08/19		EBR19-T12	11/26/18	03/29/19
	WBR20-T3	11/29/18	06/08/19		EBR20-PD	10/06/18	04/10/19
	WBR20-D4	12/04/18	06/08/19		EBR20-PU	10/03/18	04/10/19
	WBR20-T5	12/05/18	06/07/19		EBR20-T1	08/28/18	05/09/19
WBR-20	WBR20-T6	12/06/18	06/07/19		EBR20-T2	09/19/18	04/23/19
	WBR20-T7	12/07/18	06/07/19		EBR20-T3	09/21/18	04/23/19
	WBR20-T8	12/10/18	06/07/19		EBR20-D4	09/24/18	04/23/19
	WBR20-T9	12/11/18	06/07/19		EBR20-T5	09/25/18	04/22/19
	WBR20-D10	12/12/18	06/07/19	EBR-20	EBR20-T6	09/27/18	04/22/19
	WBR20-T11	12/13/18	06/07/19		EBR20-T7	09/28/18	04/22/19
	WBR20-T12	12/14/18	06/07/19		EBR20-T8	10/01/18	04/22/19
	WBR21-ED	03/23/19	06/15/19		EBR20-T9	10/02/18	04/22/19
	WBR21-EU	02/08/19	07/17/19		EBR20-D10	10/03/18	04/22/19
	WBR21-T1	02/07/19	07/15/19		EBR20-T11	10/04/18	04/19/19
WBR-21	WBR21-T2	02/08/19	07/15/19		EBR20-T12	10/05/18	04/19/19
	WBR21-D3	02/09/19	07/14/19		EBR21-ED	12/13/18	04/19/19
	WBR21-T4	02/11/19	07/14/19		EBR21-EU	03/30/19	08/08/19

	WBR21-T5	02/13/19	07/14/19		EBR21-T1	02/23/19	08/08/19
	WBR21-T6	02/14/19	07/14/19		EBR21-T2	02/25/19	08/08/19
	WBR21-T7	02/15/19	07/14/19		EBR21-D3	02/27/19	08/07/19
	WBR21-T8	02/16/19	07/14/19		EBR21-T4	02/28/19	08/07/19
	WBR21-D9	02/18/19	07/14/19		EBR21-T5	03/01/19	08/07/19
	WBR21-T10	02/19/19	07/14/19		EBR21-T6	03/02/19	08/06/19
	WBR21-T11	02/21/19	07/14/19	EBR-21	EBR21-T7	03/04/19	08/06/19
	WBR21-T12	02/22/19	07/14/19		EBR21-T8	03/05/19	08/06/19
	WBR22-PD	02/02/19	07/25/19		EBR21-D9	03/07/19	08/06/19
	WBR22-PU	01/31/19	07/25/19		EBR21-T10	03/08/19	08/06/19
	WBR22-T1	02/07/19	07/27/19		EBR21-T11	03/09/19	08/06/19
	WBR22-T2	02/08/19	07/23/19		EBR21-T12	03/11/19	08/06/19
	WBR22-T3	02/09/19	07/23/19		EBR22-PD	03/19/19	08/11/19
	WBR22-D4	02/11/19	07/23/19		EBR22-PU	03/15/19	08/11/19
	WBR22-T5	02/13/19	07/23/19		EBR22-T1	03/01/19	08/13/19
WBR-22	WBR22-T6	02/14/19	07/23/19		EBR22-T2	03/02/19	08/10/19
	WBR22-T7	02/15/19	07/23/19		EBR22-T3	03/04/19	08/10/19
	WBR22-T8	02/16/19	07/23/19		EBR22-D4	03/06/19	08/10/19
	WBR22-D9	02/18/19	07/23/19		EBR22-T5	03/07/19	08/10/19
	WBR22-T10	02/21/19	07/23/19	EBR-22	EBR22-T6	03/08/19	08/09/19
	WBR22-T11	02/22/19	07/23/19		EBR22-T7	03/09/19	08/09/19
	WBR22-T12	02/23/19	07/23/19		EBR22-T8	03/11/19	08/09/19
	WBR23-PD	02/04/19	07/28/19		EBR22-T9	03/12/19	08/09/19
	WBR23-PU	02/01/19	07/28/19		EBR22-D10	03/13/19	08/09/19
	WBR23-T1	03/06/19	07/30/19		EBR22-T11	03/14/19	08/09/19
	WBR23-T2	03/07/19	07/27/19		EBR22-T12	03/15/19	08/09/19
	WBR23-T3	03/08/19	07/27/19		EBR23-ED	04/12/19	08/12/19
	WBR23-D4	03/11/19	07/26/19		EBR23-EU	04/23/19	09/07/19
	WBR23-T5	03/12/19	07/26/19		EBR23-T1	03/02/19	09/07/19
WBR-23	WBR23-T6	03/13/19	07/26/19		EBR23-T2	03/04/19	09/07/19
	WBR23-T7	03/14/19	07/26/19		EBR23-D3	03/05/19	09/07/19
	WBR23-T8	03/15/19	07/26/19		EBR23-T4	03/06/19	09/07/19
	WBR23-T9	03/16/19	07/26/19	EBR-23	EBR23-T5	03/07/19	09/07/19
	WBR23-D10	03/18/19	07/26/19		EBR23-T6	03/08/19	09/06/19
	WBR23-T11	03/19/19	07/26/19		EBR23-T7	03/09/19	09/06/19
	WBR23-T12	03/20/19	07/26/19		EBR23-T8	03/11/19	09/06/19
	WBR24-ED	03/08/19	07/27/19		EBR23-D9	03/12/19	09/06/19
WBR-24	WBR24-EU	05/31/19	08/22/19		EBR23-T10	03/13/19	09/06/19
	WBR24-T1	04/13/19	08/22/19		EBR23-T11	03/14/19	09/06/19

	WBR24-T2	04/15/19	08/22/19		EBR23-T12	03/15/19	09/05/19
	WBR24-D3	04/16/19	08/22/19		EBR24-PD	04/06/19	09/11/19
	WBR24-T4	04/17/19	08/22/19	EBR-24	EBR24-PU	04/03/19	09/11/19
	WBR24-T5	04/18/19	08/22/19		EBR24-T1	05/01/19	09/20/19
	WBR24-T6	04/22/19	08/21/19		EBR24-T2	05/02/19	09/20/19
	WBR24-T7	04/23/19	08/21/19		EBR24-T3	05/03/19	09/20/19
	WBR24-T8	04/24/19	08/21/19		EBR24-D4	05/06/19	09/20/19
	WBR24-D9	04/26/19	08/21/19		EBR24-T5	05/07/19	09/20/19
	WBR24-T10	04/27/19	08/21/19		EBR24-T6	05/08/19	09/20/19
	WBR24-T11	04/29/19	08/21/19		EBR24-T7	05/09/19	09/19/19
	WBR24-T12	04/30/19	08/21/19		EBR24-T8	05/10/19	09/19/19
	WBR25-PD	06/13/19	09/03/19		EBR24-D9	05/13/19	09/19/19
WBR-25	WBR25-PU	06/11/19	09/03/19		EBR24-T10	05/14/19	09/19/19
	WBR25-T1	03/30/19	09/06/19		EBR24-T11	05/15/19	09/19/19
	WBR25-T2	04/01/19	09/03/19		EBR24-T12	05/16/19	09/19/19
	WBR25-T3	04/02/19	09/03/19		EBR25-PD	06/01/19	09/21/19
	WBR25-D4	04/03/19	09/03/19	EBR-25	EBR25-PU	05/30/19	09/21/19
	WBR25-T5	04/04/19	09/03/19		EBR25-T1	05/17/19	09/26/19
	WBR25-T6	04/06/19	08/30/19		EBR25-T2	05/20/19	09/24/19
	WBR25-T7	04/08/19	08/30/19		EBR25-T3	05/21/19	09/24/19
	WBR25-T8	04/09/19	08/30/19		EBR25-D4	05/22/19	09/24/19
	WBR25-D9	04/10/19	08/30/19		EBR25-T5	05/23/19	09/24/19
	WBR25-T10	04/11/19	08/30/19		EBR25-T6	05/24/19	09/24/19
	WBR25-T11	04/12/19	08/30/19		EBR25-T7	05/28/19	09/24/19
	WBR25-T12	04/13/19	08/30/19		EBR25-T8	05/29/19	09/23/19
	WBR26-PD	01/28/19	06/19/19		EBR25-T9	05/30/19	09/23/19
WBR-26	WBR26-PU	01/25/19	06/19/19		EBR25-D10	05/31/19	09/23/19
	WBR26-T1	10/19/18	06/19/19		EBR25-T11	06/03/19	09/23/19
	WBR26-T2	10/22/18	06/18/19		EBR25-T12	06/04/19	09/23/19
	WBR26-T3	10/23/18	06/18/19		EBR26-ED	05/22/19	09/24/19
	WBR26-D4	10/24/18	06/18/19	EBR-26	EBR26-EU	05/11/19	07/30/19
	WBR26-T5	10/25/18	06/18/19		EBR26-T1	03/09/19	07/02/19
	WBR26-T6	10/26/18	06/18/19		EBR26-T2	03/11/19	07/02/19
	WBR26-T7	10/27/18	06/18/19		EBR26-D3	03/12/19	07/02/19
	WBR26-T8	10/29/18	06/17/19		EBR26-T4	03/13/19	07/02/19
	WBR26-T9	10/30/18	06/17/19		EBR26-T5	03/14/19	07/02/19
	WBR26-D10	10/31/18	05/23/19		EBR26-T6	03/15/19	07/02/19
	WBR26-T11	11/01/18	05/23/19		EBR26-T7	03/16/19	07/01/19
	WBR26-T12	11/02/18	05/23/19		EBR26-T8	03/18/19	07/01/19

	WBR27-ED	02/05/19	05/22/19		EBR26-D9	03/19/19	07/01/19
WBR-27	WBR27-EU	02/19/19	05/22/19		EBR26-T10	03/20/19	07/01/19
	WBR27-T1	10/22/18	05/21/19		EBR26-T11	03/21/19	07/01/19
	WBR27-T2	10/23/18	05/21/19		EBR26-T12	03/22/19	07/01/19
	WBR27-D3	10/24/18	05/23/19		EBR27-PD	04/17/19	07/02/19
	WBR27-T4	10/25/18	06/07/19	EBR-27	EBR27-PU	04/16/19	07/02/19
	WBR27-T5	10/26/18	06/07/19		EBR27-T1	03/25/19	07/06/19
	WBR27-T6	10/27/18	06/07/19		EBR27-T2	03/26/19	07/06/19
	WBR27-T7	10/29/18	06/07/19		EBR27-T3	03/27/19	07/06/19
	WBR27-T8	10/30/18	06/07/19		EBR27-D4	03/29/19	07/06/19
	WBR27-T9	10/31/18	06/08/19		EBR27-T5	03/30/19	07/06/19
	WBR27-D10	11/01/18	06/08/19		EBR27-T6	04/01/19	07/06/19
	WBR27-T11	11/02/18	06/08/19		EBR27-T7	04/02/19	07/06/19
	WBR27-T12	11/03/18	06/09/19		EBR27-T8	04/03/19	07/07/19
	WBR28-ED	02/13/19	06/09/19		EBR27-D9	04/04/19	07/07/19
WBR-28	WBR28-EU	06/20/19	07/26/19		EBR27-T10	04/06/19	07/07/19
	WBR28-T1	05/20/19	07/25/19		EBR27-T11	04/08/19	07/07/19
	WBR28-T2	05/21/19	07/25/19		EBR27-T12	04/09/19	07/07/19
	WBR28-D3	05/22/19	07/25/19		EBR28-PD	05/20/19	07/08/19
	WBR28-T4	05/23/19	07/25/19	EBR-28	EBR28-PU	05/17/19	07/09/19
	WBR28-T5	05/24/19	07/25/19		EBR28-T1	04/16/19	07/13/19
	WBR28-T6	05/29/19	07/25/19		EBR28-T2	04/17/19	07/12/19
	WBR28-T7	05/30/19	07/25/19		EBR28-T3	04/18/19	07/12/19
	WBR28-T8	05/31/19	07/25/19		EBR28-D4	04/22/19	07/12/19
	WBR28-D9	06/04/19	07/25/19		EBR28-T5	04/23/19	07/12/19
	WBR28-T10	06/05/19	07/26/19		EBR28-T6	04/24/19	07/12/19
	WBR28-T11	06/06/19	07/26/19		EBR28-T7	04/25/19	07/12/19
	WBR28-T12	06/07/19	07/26/19		EBR28-T8	04/26/19	07/11/19
	WBR29-PD	07/11/19	07/26/19		EBR28-D9	04/27/19	07/11/19
WBR-29	WBR29-PU	07/09/19	07/26/19		EBR28-T10	04/29/19	07/11/19
	WBR29-T1	06/03/19	07/29/19		EBR28-T11	04/30/19	07/11/19
	WBR29-T2	06/04/19	07/29/19		EBR28-T12	05/01/19	07/11/19
	WBR29-T3	06/05/19	07/29/19		EBR29-PD	05/22/19	07/13/19
	WBR29-D4	06/06/19	07/29/19	EBR-29	EBR29-PU	05/21/19	07/13/19
	WBR29-T5	06/07/19	07/29/19		EBR29-T1	04/27/19	07/16/19
	WBR29-T6	06/10/19	07/29/19		EBR29-T2	04/29/19	07/15/19
	WBR29-T7	06/11/19	07/29/19		EBR29-T3	04/30/19	07/15/19
	WBR29-T8	06/12/19	07/27/19		EBR29-D4	05/01/19	07/15/19
	WBR29-D9	06/13/19	07/27/19		EBR29-T5	05/02/19	07/15/19

	WBR29-T10	06/14/19	07/27/19		EBR29-T6	05/03/19	07/15/19
	WBR29-T11	06/17/19	07/27/19		EBR29-T7	05/06/19	07/15/19
	WBR29-T12	06/18/19	07/27/19		EBR29-T8	05/07/19	07/15/19
	WBR30-PD	07/17/19	07/30/19		EBR29-T9	05/08/19	07/15/19
	WBR30-PU	07/13/19	07/30/19		EBR29-D10	05/10/19	07/15/19
	WBR30-T1	07/10/19	09/05/19		EBR29-T11	05/13/19	07/15/19
	WBR30-T2	07/11/19	09/05/19		EBR29-T12	05/14/19	07/15/19
	WBR30-T3	07/12/19	09/05/19		EBR30-ED	06/01/19	07/16/19
	WBR30-D4	07/15/19	09/05/19		EBR30-EU	06/22/19	08/19/19
	WBR30-T5	07/16/19	09/05/19		EBR30-T1	06/18/19	08/17/19
WBR-30	WBR30-T6	07/17/19	09/05/19		EBR30-T2	06/19/19	08/17/19
	WBR30-T7	07/18/19	09/06/19		EBR30-D3	06/20/19	08/17/19
	WBR30-T8	07/19/19	09/06/19		EBR30-T4	06/21/19	08/17/19
	WBR30-D9	07/22/19	09/06/19	EBR-30	EBR30-T5	06/25/19	08/17/19
	WBR30-T10	07/23/19	09/06/19		EBR30-T6	06/26/19	08/17/19
	WBR30-T11	07/24/19	09/06/19		EBR30-D7	06/27/19	08/17/19
	WBR30-T12	07/25/19	09/06/19		EBR30-T8	06/28/19	08/18/19
	WBR31-PD	07/31/19	09/06/19		EBR30-T9	06/29/19	08/18/19
	WBR31-PU	07/29/19	09/07/19		EBR30-T10	07/01/19	08/18/19
	WBR31-T1	07/17/19	09/12/19		EBR31-PD	07/25/19	08/19/19
	WBR31-T2	07/18/19	09/09/19		EBR31-PU	07/23/19	08/19/19
	WBR31-T3	07/19/19	09/09/19		EBR31-T1	06/21/19	08/22/19
	WBR31-D4	07/20/19	09/09/19		EBR31-T2	06/25/19	08/21/19
WBR-31	WBR31-T5	07/22/19	09/09/19		EBR31-T3	06/26/19	08/21/19
	WBR31-T6	07/23/19	09/09/19		EBR31-D4	06/27/19	08/21/19
	WBR31-T7	07/24/19	09/09/19	EBR-31	EBR31-T5	06/28/19	08/21/19
	WBR31-D8	07/25/19	09/09/19		EBR31-T6	06/29/19	08/21/19
	WBR31-T9	07/26/19	09/09/19		EBR31-D7	07/01/19	08/21/19
	WBR31-T10	07/29/19	09/09/19		EBR31-T8	07/02/19	08/21/19
	WBR32-ED	07/03/19	09/09/19		EBR31-T9	07/03/19	08/21/19
	WBR32-EU	04/30/19	08/14/19		EBR31-T10	07/08/19	08/21/19
	WBR32-T1	02/25/19	08/14/19		EBR32-PD	09/27/18	05/08/19
	WBR32-T2	02/26/19	08/13/19		EBR32-PU	09/22/18	05/08/19
	WBR32-D3	02/28/19	08/13/19		EBR32-T1	07/14/18	04/24/19
WBR-32	WBR32-T4	03/01/19	08/13/19		EBR32-T2	07/17/18	04/24/19
	WBR32-T5	03/02/19	08/13/19	EBR-32	EBR32-T3	07/20/18	04/24/19
	WBR32-T6	03/04/19	08/13/19		EBR32-D4	07/26/18	04/24/19
	WBR32-T7	03/05/19	08/13/19		EBR32-T5	07/30/18	04/24/19
	WBR32-D8	03/06/19	08/13/19		EBR32-T6	08/01/18	04/25/19

	WBR32-T9	03/07/19	08/13/19		EBR32-D7	08/04/18	04/25/19
	WBR32-T10	03/08/19	08/13/19		EBR32-T8	08/07/18	04/25/19
	WBR32-T11	03/09/19	08/13/19		EBR32-T9	08/10/18	04/25/19
	WBR33-PD	03/22/19	07/18/19		EBR32-T10	08/13/18	04/26/19
WBR-33	WBR33-PU	03/20/19	07/18/19		EBR33-PD	10/04/18	05/09/19
	WBR33-T1	03/04/19	07/15/19	EBR-33	EBR33-PU	10/02/18	05/09/19
	WBR33-T2	03/05/19	07/15/19		EBR33-T1	11/05/18	05/02/19
	WBR33-T3	03/06/19	07/15/19		EBR33-T2	11/06/18	05/02/19
	WBR33-D4	03/07/19	07/16/19		EBR33-T3	11/07/18	05/02/19
	WBR33-T5	03/08/19	07/16/19		EBR33-D4	11/08/18	05/02/19
	WBR33-T6	03/09/19	07/16/19		EBR33-T5	11/09/18	05/02/19
	WBR33-T7	03/11/19	07/16/19		EBR33-T6	11/10/18	05/02/19
	WBR33-D8	03/12/19	07/16/19		EBR33-T7	11/13/18	04/30/19
	WBR33-T9	03/13/19	07/16/19		EBR33-D8	11/15/18	04/30/19
	WBR33-T10	03/14/19	07/17/19		EBR33-T9	11/16/18	04/30/19
	WBR33-T11	03/15/19	07/17/19		EBR33-T10	11/19/18	04/30/19
	WBR34-PD	03/23/19	07/19/19		EBR34-ED	02/09/19	05/20/19
WBR-34	WBR34-PU	03/21/19	07/19/19	EBR-34	EBR34-EU	02/27/19	06/10/19
	WBR34-T1	03/16/19	07/29/19		EBR34-T1	12/05/18	06/09/19
	WBR34-T2	03/18/19	07/29/19		EBR34-T2	12/10/18	06/09/19
	WBR34-T3	03/19/19	07/29/19		EBR34-D3	12/12/18	06/09/19
	WBR34-D4	03/20/19	07/29/19		EBR34-T4	12/14/18	06/09/19
	WBR34-T5	03/21/19	07/29/19		EBR34-T5	12/15/18	06/09/19
	WBR34-T6	03/22/19	07/29/19		EBR34-T6	12/17/18	06/10/19
	WBR34-T7	03/23/19	07/29/19		EBR34-T7	12/18/18	06/10/19
	WBR34-T8	03/25/19	07/29/19		EBR34-T8	12/19/18	06/10/19
	WBR34-D9	03/26/19	07/29/19		EBR34-D9	12/21/18	06/10/19
	WBR34-T10	03/27/19	07/30/19		EBR34-T10	01/01/19	06/10/19
	WBR34-T11	03/29/19	07/30/19		EBR34-T11	01/02/19	06/10/19
	WBR34-T12	03/30/19	07/30/19		EBR34-T12	01/03/19	06/10/19
	WBR35-PD	05/10/19	07/30/19		EBR35-PD	02/14/19	06/13/19
WBR-35	WBR35-PU	05/02/19	07/30/19	EBR-35	EBR35-PU	02/11/19	06/13/19
	WBR35-T1	03/26/19	09/24/19		EBR35-T1	01/09/19	06/20/19
	WBR35-T2	03/29/19	09/24/19		EBR35-T2	01/10/19	06/15/19
	WBR35-T3	03/30/19	09/24/19		EBR35-T3	01/11/19	06/15/19
	WBR35-D4	04/01/19	09/24/19		EBR35-D4	01/14/19	06/15/19
	WBR35-T5	04/02/19	09/24/19		EBR35-T5	01/15/19	06/15/19
	WBR35-T6	04/03/19	09/24/19		EBR35-T6	01/17/19	06/15/19
	WBR35-T7	04/04/19	09/24/19		EBR35-T7	01/18/19	06/15/19

	WBR35-T8	04/05/19	09/24/19		EBR35-T8	01/22/19	06/15/19
	WBR35-T9	04/06/19	09/25/19		EBR35-T9	01/24/19	06/14/19
	WBR35-D10	04/08/19	09/25/19		EBR35-D10	01/25/19	06/14/19
	WBR35-T11	04/09/19	09/25/19		EBR35-T11	01/28/19	06/14/19
	WBR35-T12	04/10/19	09/25/19		EBR35-T12	01/30/19	06/14/19
	WBR36-ED	05/15/19	09/25/19		EBR36-ED	03/20/19	06/21/19
WBR-36	WBR36-EU	06/28/19	10/10/19	EBR-36	EBR36-EU	06/18/19	07/22/19
	WBR36-T1	07/09/19	10/10/19		EBR36-T1	05/29/19	07/22/19
	WBR36-T2	07/10/19	10/10/19		EBR36-T2	05/30/19	08/18/19
	WBR36-D3	07/11/19	10/10/19		EBR36-D3	05/31/19	08/18/19
	WBR36-T4	07/12/19	10/09/19		EBR36-T4	06/03/19	08/18/19
	WBR36-T5	07/13/19	10/09/19		EBR36-T5	06/04/19	08/18/19
	WBR36-T6	07/15/19	10/09/19		EBR36-T6	06/05/19	08/18/19
	WBR36-T7	07/16/19	10/09/19		EBR36-D7	06/06/19	08/19/19
	WBR36-D8	07/17/19	10/09/19		EBR36-T8	06/07/19	08/21/19
	WBR36-T9	07/18/19	10/09/19		EBR36-T9	06/10/19	08/21/19
	WBR36-T10	07/19/19	10/09/19		EBR36-T10	06/11/19	08/21/19
	WBR36-T11	07/20/19	10/09/19		EBR37-PD	06/22/19	08/21/19
	WBR37-PD	08/05/19	09/21/19	EBR-37	EBR37-PU	06/20/19	08/22/19
WBR-37	WBR37-PU	08/01/19	09/21/19		EBR37-T1	06/03/19	09/25/19
	WBR37-T1	07/15/19	09/21/19		EBR37-T2	06/04/19	09/25/19
	WBR37-T2	07/16/19	09/21/19		EBR37-T3	06/05/19	09/25/19
	WBR37-T3	07/17/19	09/21/19		EBR37-D4	06/06/19	09/25/19
	WBR37-D4	07/18/19	09/21/19		EBR37-T5	06/07/19	09/25/19
	WBR37-T5	07/19/19	09/20/19		EBR37-T6	06/10/19	09/25/19
	WBR37-T6	07/20/19	09/20/19		EBR37-T7	06/11/19	09/26/19
	WBR37-T7	07/22/19	09/20/19		EBR37-D8	06/12/19	09/26/19
	WBR37-T8	07/23/19	09/20/19		EBR37-T9	06/13/19	09/26/19
	WBR37-D9	07/25/19	09/20/19		EBR37-T10	06/15/19	09/26/19
	WBR37-T10	07/26/19	09/20/19		EBR37-T11	06/18/19	09/26/19
	WBR37-T11	07/29/19	09/20/19		EBR38-PD	11/29/18	05/20/19
	WBR37-T12	07/30/19	09/20/19	EBR-38	EBR38-PU	11/27/18	05/10/19
	WBR38-PD	02/09/19	07/09/19		EBR38-T1	12/15/18	05/10/19
WBR-38	WBR38-PU	02/06/19	07/09/19		EBR38-T2	12/17/18	05/10/19
	WBR38-T1	02/06/19	07/02/19		EBR38-T3	12/18/18	05/10/19
	WBR38-T2	02/07/19	07/02/19		EBR38-D4	12/19/18	05/11/19
	WBR38-T3	02/08/19	07/02/19		EBR38-T5	12/20/18	05/12/19
	WBR38-D4	02/09/19	07/02/19		EBR38-T6	12/22/18	05/12/19
	WBR38-T5	02/11/19	07/03/19		EBR38-T7	12/31/18	05/12/19

	WBR38-T6	02/13/19	07/03/19		EBR38-T8	01/01/19	05/12/19
	WBR38-T7	02/14/19	07/03/19		EBR38-D9	01/03/19	05/12/19
	WBR38-D8	02/15/19	07/03/19		EBR38-T10	01/04/19	05/12/19
	WBR38-T9	02/16/19	07/03/19		EBR38-T11	01/07/19	05/12/19
	WBR38-T10	02/18/19	07/03/19		EBR38-T12	01/08/19	05/12/19
	WBR39-ED	04/02/19	07/10/19		EBR39-PD	11/28/18	05/13/19
WBR-39	WBR39-EU	04/09/19	08/29/19	EBR-39	EBR39-PU	11/21/18	05/13/19
	WBR39-T1	06/05/19	10/03/19		EBR39-T1	03/11/19	08/13/19
	WBR39-T2	06/06/19	10/03/19		EBR39-T2	03/12/19	08/13/19
	WBR39-D3	06/07/19	10/04/19		EBR39-T3	03/14/19	08/13/19
	WBR39-T4	06/10/19	10/04/19		EBR39-D4	03/15/19	08/13/19
	WBR39-T5	06/11/19	10/04/19		EBR39-T5	03/16/19	08/13/19
	WBR39-T6	06/12/19	10/05/19		EBR39-T6	03/18/19	08/12/19
	WBR39-T7	06/13/19	10/05/19		EBR39-T7	03/20/19	08/12/19
	WBR39-T8	06/14/19	10/05/19		EBR39-T8	03/21/19	08/12/19
	WBR39-D9	06/17/19	10/05/19		EBR39-T9	03/22/19	08/12/19
	WBR39-T10	06/18/19	10/05/19		EBR39-D10	03/25/19	08/12/19
	WBR39-T11	06/19/19	10/05/19		EBR39-T11	03/26/19	08/12/19
	WBR39-T12	06/20/19	10/05/19		EBR39-T12	03/27/19	08/12/19
	WBR40-PD	07/15/19	09/17/19		EBR40-ED	03/05/19	04/02/19
WBR-40	WBR40-PU	07/13/19	09/16/19	EBR-40	EBR40-EU	03/02/19	04/02/19
	WBR40-T1	06/12/19	09/16/19		EBR40-T1	04/01/19	07/11/19
	WBR40-T2	06/13/19	09/16/19		EBR40-T2	04/02/19	07/11/19
	WBR40-T3	06/14/19	09/16/19		EBR40-D3	04/03/19	07/12/19
	WBR40-D4	06/17/19	09/16/19		EBR40-T4	04/04/19	07/12/19
	WBR40-T5	06/18/19	09/15/19		EBR40-T5	04/06/19	07/13/19
	WBR40-T6	06/19/19	09/15/19		EBR40-T6	04/08/19	07/13/19
	WBR40-T7	06/20/19	09/15/19		EBR40-T7	04/09/19	07/13/19
	WBR40-T8	06/21/19	09/15/19		EBR40-T8	04/10/19	07/13/19
	WBR40-D9	06/25/19	09/15/19		EBR40-D9	04/11/19	07/13/19
	WBR40-T10	06/26/19	09/15/19		EBR40-T10	04/12/19	07/13/19
	WBR40-T11	06/27/19	09/15/19		EBR40-T11	04/13/19	07/13/19
	WBR40-T12	06/28/19	09/15/19		EBR40-T12	04/15/19	07/13/19
	WBR41-PD	06/20/19	08/02/19		EBR41-PD	11/20/18	06/01/19
WBR-41	WBR41-PU	03/02/19	08/01/19	EBR-41	EBR41-PU	11/16/18	06/01/19
	WBR41-T1	12/10/18	08/01/19		EBR41-T1	11/27/18	06/01/19
	WBR41-T2	12/12/18	08/01/19		EBR41-T2	11/28/18	06/01/19
	WBR41-T3	12/14/18	08/01/19		EBR41-T3	11/29/18	06/01/19
	WBR41-D4	12/17/18	07/29/19		EBR41-D4	12/04/18	06/01/19

	WBR41-T5	12/19/18	07/29/19		EBR41-T5	12/05/18	05/29/19
	WBR41-T6	12/20/18	07/29/19		EBR41-T6	12/06/18	05/29/19
	WBR41-T7	12/22/18	07/28/19		EBR41-T7	12/07/18	05/29/19
	WBR41-T8	12/31/18	07/28/19		EBR41-T8	12/10/18	05/29/19
	WBR41-D9	01/02/19	07/28/19		EBR41-D9	12/11/18	05/29/19
	WBR41-T10	01/04/19	07/27/19		EBR41-T10	12/12/18	05/29/19
	WBR41-T11	01/05/19	07/26/19		EBR41-T11	12/13/18	05/28/19
	WBR42-ED	03/12/19	07/31/19		EBR41-T12	12/14/18	05/28/19
WBR-42	WBR42-EU	03/18/19	09/30/19		EBR42-PD	12/06/18	06/04/19
	WBR42-T1	08/02/19	09/30/19	EBR-42	EBR42-PU	12/04/18	06/04/19
	WBR42-D2	08/01/19	09/30/19		EBR42-T1	07/09/19	10/12/19
	WBR42-T3	02/14/19	09/30/19		EBR42-T2	07/10/19	10/12/19
	WBR42-D4	02/15/19	09/30/19		EBR42-T3	07/11/19	10/13/19
	WBR42-T5	02/16/19	10/01/19		EBR42-D4	07/12/19	10/13/19
	WBR43-ED	03/21/19	10/01/19		EBR42-T5	07/13/19	10/13/19
B26-1	B26-1-EU	05/01/19	09/18/19		EBR42-T6	07/15/19	10/14/19
	B26-1-T1	03/21/19	09/17/19		EBR42-T7	07/16/19	10/14/19
	B26-1-T2	03/22/19	09/17/19		EBR42-D8	07/17/19	10/14/19
	B26-1-D3	03/25/19	09/17/19		EBR42-T9	07/18/19	10/14/19
	B26-1-T4	03/26/19	09/17/19		EBR42-T10	07/19/19	10/14/19
	B26-1-T5	03/27/19	09/17/19		EBR43-ED	07/02/19	10/14/19
	B26-1-T6	03/29/19	09/17/19	B22-1	B22-1-EU	01/30/19	03/28/19
	B26-1-T7	03/30/19	09/18/19		B22-1-T1	11/08/18	03/28/19
	B26-1-T8	04/01/19	09/18/19		B22-1-T2	11/13/18	03/28/19
	B26-1-D9	04/02/19	09/18/19		B22-1-D3	11/15/18	03/28/19
	B26-1-T10	04/03/19	09/18/19		B22-1-T4	11/16/18	03/28/19
	B26-1-T11	04/04/19	09/18/19		B22-1-T5	11/19/18	03/29/19
	B26-1-T12	04/05/19	09/18/19		B22-1-T6	11/20/18	03/29/19
	B26-2-PD	04/24/19	09/20/19		B22-1-T7	11/26/18	03/29/19
B26-2	B26-2-PU	04/22/19	09/20/19		B22-1-T8	11/27/18	03/29/19
	B26-2-T1	05/10/19	09/26/19		B22-1-T9	11/28/18	03/29/19
	B26-2-T2	05/13/19	09/26/19		B22-1-D10	12/04/18	03/29/19
	B26-2-T3	05/14/19	09/26/19		B22-1-T11	12/05/18	03/29/19
	B26-2-D4	05/15/19	09/26/19		B22-1-T12	12/07/18	03/30/19
	B26-2-T5	05/16/19	09/26/19		B22-2-ED	02/01/19	03/30/19
	B26-2-T6	05/17/19	09/26/19				
	B26-2-T7	05/20/19	09/26/19				
	B26-2-T8	05/21/19	09/26/19				
	B26-2-D9	05/22/19	09/26/19				

	B26-2-T10	05/23/19	09/25/19	
	B26-2-T11	05/24/19	09/25/19	
	B26-2-T12	05/28/19	09/25/19	
	B26-3-PD	07/11/19	10/01/19	
B26-3	B26-3-PU	07/09/19	10/01/19	
	B26-3-T1	05/31/19	10/03/19	
	B26-3-T2	06/03/19	10/03/19	
	B26-3-T3	06/04/19	10/03/19	
	B26-3-D4	06/05/19	10/03/19	
	B26-3-T5	06/06/19	10/03/19	
	B26-3-T6	06/07/19	10/02/19	
	B26-3-T7	06/10/19	10/02/19	
	B26-3-T8	06/11/19	10/02/19	
	B26-3-T9	06/12/19	10/02/19	
	B26-3-D10	06/13/19	10/02/19	
	B26-3-T11	06/14/19	10/02/19	
	B26-3-T12	06/17/19	10/02/19	
	B26-4-ED	06/08/19	10/03/19	